Rainfall may not be enough to end hydrological drought pp. 680 & 745

Improve indoor air quality to reduce airborne infections p. 689

Examining genetic effects of Chernobyl pp. 705 & 725

Science

$15
14 MAY 2021
sciencemag.org

AAAS

RIVER DANCE

Why rivers leap from their channels in deadly avulsions p. 676

Left to right: Marcelo Rebelo de Sousa, president of Portugal; Santiago Zelenay and Caetano Reis e Sousa, winners of the BIAL Award in Biomedicine 2019; Luís Portela, chairman of the BIAL Foundation

BIAL Foundation funds a unique award with a focus on teamwork

The BIAL Foundation, created in 1994 by the pharmaceutical company BIAL in collaboration with the Council of Rectors of Portuguese Universities, seeks to support outstanding discoveries in the biomedical field.

The BIAL Award in Biomedicine, created in 2018, honors "the most remarkable and relevant discoveries in that field," according to the description on its website. This €300,000 prize "takes a broad look at all biomedical research over the past decade and identifies a specific published study—rather than a person," explains Ralph Adolphs, Bren Professor of Psychology, Neuroscience, and Biology at the California Institute of Technology and president of the jury for this year's BIAL Award in Biomedicine. "It is distinguished by requiring both a large advance in basic science, and translational relevance."

The inaugural BIAL Award in Biomedicine (2019) was given to a report on some of the molecular mechanisms behind cancer's evasion of immune attacks—a project led by Caetano Reis e Sousa, head of the immunobiology laboratory at the Francis Crick Institute in London. In this work, Sousa and his colleagues explored the connection between inflammation and the development of cancer. In particular, these scientists studied an enzyme, cyclooxygenase (COX), which plays a role in producing a lipid compound, prostaglandin E2, that can support the growth of a tumor. The key finding is that blocking COX might expose the cancer to an attack by a patient's immune system. Although Sousa and his colleagues performed this work on mice, they noted that similar COX-related activity arises in human tumors.

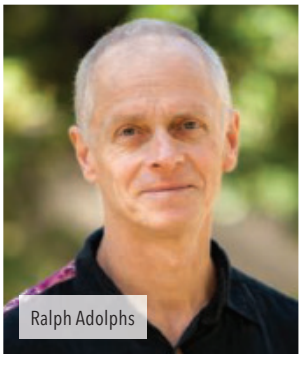
Ralph Adolphs

IMAGE: PHOTOGRAPHS PROVIDED BY THE BIAL FOUNDATION

Nonetheless, this research remains preclinical, and much work remains to be done before any of the conclusions of this study can impact human health. "To actually recognize what was effectively preclinical work—very much at the fundamental end of the research spectrum—was very visionary on the part of the jury," Sousa says. "I think the intention is to recognize the whole spectrum and the whole breadth of medical research."

Being Portuguese himself, Sousa took added pleasure in his team's work winning the BIAL Award in Biomedicine. As he says, "Actually winning a prize from my home country makes it even more special."

In fact, the format of the prize—rewarding a paper rather than a person—expands just how important this award can be. In thinking back on the award presentation, Sousa says, "I was accepting it on behalf of our team, and it was distributed among the team members." He adds, "One of the nicest things about it has been to see that everyone in the team shared in the accolades and that they can all put it on their CV and effectively gain something from it."

Consequently, the BIAL Award in Biomedicine reflects one of the field's crucial elements, which is teamwork. Although not yet at the level of fields like particle physics, biomedical advances rely increasingly on the collaboration of groups of scientists. A dozen scientists working at several colleges, institutes, and universities earned a place as an author on the paper that won the first award.

Many teams of scientists will likely be in the running for this year's award. Participants already envision an exciting process for 2021. Adolphs says, "I look forward to reviewing all of the submissions we will receive, and to vigorous discussions about their merits with my colleagues on the jury for the BIAL Award in Biomedicine." When the results are announced during the first quarter of 2022, a new team will enjoy the accolades.

The BIAL Foundation is soliciting nominations for the BIAL Award in Biomedicine. Proposals must be sent by June 30, 2021 to fundacao@bial.com. www.fundacaobial.com

Sponsored by

FUNDAÇÃO Bial

Instituição de utilidade pública

Institution of public utility

CONTENTS

14 MAY 2021 • VOLUME 372 • ISSUE 6543

676
A sediment-laden river in Indonesia is prone to shifting course.

NEWS

IN BRIEF

IN DEPTH

FEATURES

INSIGHTS

PERSPECTIVES

694

PHOTOS: (TOP) CONTAINS MODIFIED ESA/COPERNICUS SENTINEL DATA (2019), COPYRIGHT SAM BROOKE AND VAMSI GANTI (2021); (BOTTOM) MARIO SUAREZ PORRAS/MINDEN PICTURES

ON THE COVER

The meandering channels of the Mississippi River, carved and silted up over centuries, are shown in a 1944 map. The map highlights the site of the present-day Old River Control Structure, where engineers fight the river's natural urge to jump in an avulsion into the Atchafalaya River—once the Mississippi's main route. Researchers say that levees and control structures will only hasten the next avulsion. See page 676. *Credit: US Army Corps of Engineers*

ILLUSTRATION: ROBERT NEUBECKER

SCIENCE (ISSN 0036-8075) is published weekly on Friday, except last week in December, by the American Association for the Advancement of Science, 1200 New York Avenue, NW, Washington, DC 20005. Periodicals mail postage (publication No. 484460) paid at Washington, DC, and additional mailing offices.

Domestic individual membership, including subscription (12 months): $165 ($74 allocated to subscription). Domestic institutional subscription (51 issues): $2148; Foreign postage extra: Air assist delivery: $98. First class, airmail, student, and emeritus rates on request. Canadian rates with GST available upon request, GST #125488122. Publications Mail Agreement Number 1069624. **Printed in the U.S.A.**
Change of address: Allow 4 weeks, giving old and new addresses and 8-digit account number. **Postmaster:** Send change of address to AAAS, P.O. Box 96178, Washington, DC 20090–6178. **Single-copy sales:** $15 each plus shipping and handling available from backissues.sciencemag.org; bulk rate on request. **Authorization to reproduce** material for internal or personal use under circumstances not falling within the fair use provisions of the Copyright Act can be obtained through the Copyright Clearance Center (CCC), www.copyright.com. The identification code for *Science* is 0036-8075. *Science* is indexed in the *Reader's Guide to Periodical Literature* and in several specialized indexes.

Science AAAS

Editor-in-Chief Holden Thorp, hthorp@aaas.org

Executive Editor Monica M. Bradford

Editors, Research Valda Vinson, Jake S. Yeston **Editor, Insights** Lisa D. Chong

DEPUTY EDITORS Julia Fahrenkamp-Uppenbrink (UK), Stella M. Hurtley (UK), Phillip D. Szuromi, Sacha Vignieri **SR. EDITORIAL FELLOW** Andrew M. Sugden (UK) **SR. EDITORS** Gemma Alderton (UK), Caroline Ash (UK), Brent Grocholski, Pamela J. Hines, Di Jiang, Marc S. Lavine (Canada), Yevgeniya Nusinovich, Ian S. Osborne (UK), Beverly A. Purnell, L. Bryan Ray, H. Jesse Smith, Keith T. Smith (UK), Jelena Stajic, Peter Stern (UK), Valerie B. Thompson, Brad Wible, Laura M. Zahn **ASSOCIATE EDITORS** Michael A. Funk, Priscilla N. Kelly, Tage S. Rai, Seth Thomas Scanlon (UK), Yury V. Suleymanov **LETTERS EDITOR** Jennifer Sills **LEAD CONTENT PRODUCTION EDITORS** Harry Jach, Lauren Kmec **CONTENT PRODUCTION EDITORS** Amelia Beyna, Jeffrey E. Cook, Chris Filiatreau, Julia Katris, Nida Masiulis, Suzanne M. White **SR. EDITORIAL COORDINATORS** Carolyn Kyle, Beverly Shields **EDITORIAL COORDINATORS** Aneera Dobbins, Joi S. Granger, Jeffrey Hearn, Lisa Johnson, Maryrose Madrid, Ope Martins, Shannon McMahon, Jerry Richardson, Hilary Stewart (UK), Alana Warnke, Alice Whaley (UK), Anita Wynn **PUBLICATIONS ASSISTANTS** Jeremy Dow, Alexander Kief, Ronmel Navas, Brian White **EXECUTIVE ASSISTANT** Jessica Slater **ASI DIRECTOR, OPERATIONS** Janet Clements (UK) **ASI SR. OFFICE ADMINISTRATOR** Jessica Waldock (UK)

News Editor Tim Appenzeller

NEWS MANAGING EDITOR John Travis **INTERNATIONAL EDITOR** Martin Enserink **DEPUTY NEWS EDITORS** Elizabeth Culotta, Lila Guterman, David Grimm, Eric Hand (Europe), David Malakoff **SR. CORRESPONDENTS** Daniel Clery (UK), Jon Cohen, Jeffrey Mervis, Elizabeth Pennisi **ASSOCIATE EDITORS** Jeffrey Brainard, Catherine Matacic **NEWS REPORTERS** Adrian Cho, Jennifer Couzin-Frankel, Jocelyn Kaiser, Rodrigo Pérez Ortega (Mexico City), Kelly Servick, Robert F. Service, Erik Stokstad, Paul Voosen, Meredith Wadman **INTERN** Sofia Moutinho **CONTRIBUTING CORRESPONDENTS** Warren Cornwall, Andrew Curry (Berlin), Ann Gibbons, Sam Kean, Eli Kintisch, Kai Kupferschmidt (Berlin), Andrew Lawler, Mitch Leslie, Eliot Marshall, Virginia Morell, Dennis Normile (Tokyo), Elisabeth Pain (Careers), Charles Piller, Michael Price, Tania Rabesandratana (Barcelona), Joshua Sokol, Emily Underwood, Gretchen Vogel (Berlin), Lizzie Wade (Mexico City) **CAREERS** Donisha Adams, Rachel Bernstein (Editor), Katie Langin (Associate Editor) **COPY EDITORS** Julia Cole (Senior Copy Editor), Cyra Master (Copy Chief) **ADMINISTRATIVE SUPPORT** Meagan Weiland

Creative Director Beth Rakouskas

DESIGN MANAGING EDITOR Marcy Atarod **GRAPHICS MANAGING EDITOR** Alberto Cuadra **PHOTOGRAPHY MANAGING EDITOR** William Douthitt **WEB CONTENT STRATEGY MANAGER** Kara Estelle-Powers **MULTIMEDIA MANAGING PRODUCER** Joel Goldberg **DESIGN EDITOR** Chrystal Smith **DESIGNER** Christina Aycock **GRAPHICS EDITOR** Nirja Desai **INTERACTIVE GRAPHICS EDITOR** Kelly Franklin **SENIOR SCIENTIFIC ILLUSTRATORS** Valerie Altounian, Chris Bickel **SENIOR GRAPHICS SPECIALISTS** Holly Bishop, Nathalie Cary **SENIOR PHOTO EDITOR** Emily Petersen **PHOTO EDITOR** Kaitlyn Dolan **WEB DESIGNER** Jennie Pajerowski **SOCIAL MEDIA STRATEGIST** Jessica Hubbard **VIDEO PRODUCER** Meagan Cantwell **SENIOR PODCAST PRODUCER** Sarah Crespi

Chief Executive Officer and Executive Publisher Sudip Parikh

Publisher, Science Family of Journals Bill Moran

DIRECTOR, BUSINESS SYSTEMS AND FINANCIAL ANALYSIS Randy Yi **DIRECTOR, BUSINESS OPERATIONS & ANALYSIS** Eric Knott **DIRECTOR OF ANALYTICS** Enrique Gonzales **MANAGER, BUSINESS OPERATIONS** Jessica Tierney **SENIOR BUSINESS ANALYST** Cory Lipman, Meron Kebede **FINANCIAL ANALYST** Alexander Lee **ADVERTISING SYSTEM ADMINISTRATOR** Tina Burks **SENIOR SALES COORDINATOR** Shirley Young **DIGITAL/PRINT STRATEGY MANAGER** Jason Hillman **SENIOR MANAGER, PUBLISHING AND CONTENT SYSTEMS** Marcus Spiegler **ASSISTANT MANAGER DIGITAL/PRINT** Rebecca Doshi **SENIOR CONTENT SPECIALISTS** Steve Forrester, Jacob Hedrick, Antoinette Hodal, Lori Murphy **PRODUCTION SPECIALIST** Kristin Wowk **DIGITAL PRODUCTION MANAGER** Lisa Stanford **CONTENT SPECIALIST** Kimberley Oster **ADVERTISING PRODUCTION OPERATIONS MANAGER** Deborah Tompkins **DESIGNER, CUSTOM PUBLISHING** Jeremy Huntsinger **SR. TRAFFIC ASSOCIATE** Christine Hall **SPECIAL PROJECTS ASSOCIATE** Sarah Dhere

ASSOCIATE DIRECTOR, BUSINESS DEVELOPMENT Justin Sawyers **GLOBAL MARKETING MANAGER** Allison Pritchard **DIGITAL MARKETING MANAGER** Aimee Aponte **JOURNALS MARKETING MANAGER** Shawana Arnold **MARKETING ASSOCIATES** Tori Velasquez, Mike Romano, Ashley Hylton **DIGITAL MARKETING SPECIALIST** Asleigh Rojanavongse **SENIOR DESIGNER** Kim Huynh

DIRECTOR AND SENIOR EDITOR, CUSTOM PUBLISHING Sean Sanders **ASSISTANT EDITOR, CUSTOM PUBLISHING** Jackie Oberst

DIRECTOR, PRODUCT & PUBLISHING DEVELOPMENT Chris Reid **DIRECTOR, BUSINESS STRATEGY AND PORTFOLIO MANAGEMENT** Sarah Whalen **ASSOCIATE DIRECTOR, PRODUCT MANAGMENT** Kris Bishop **PRODUCT DEVELOPMENT MANAGER** Scott Chernoff **PUBLISHING TECHNOLOGY MANAGER** Michael Di Natale **SR. PRODUCT ASSOCIATE** Robert Koepke **SPJ ASSOCIATE** Samantha Bruno Fuller

DIRECTOR, INSTITUTIONAL LICENSING Iquo Edim **ASSOCIATE DIRECTOR, RESEARCH & DEVELOPMENT** Elisabeth Leonard **MARKETING MANAGER** Kess Knight **SENIOR INSTITUTIONAL LICENSING MANAGER** Ryan Rexroth **INSTITUTIONAL LICENSING MANAGER** Marco Castellan **MANAGER, AGENT RELATIONS & CUSTOMER SUCCESS** Judy Lillibridge **SENIOR OPERATIONS ANALYST** Lana Guz **FULFILLMENT COORDINATOR** Melody Stringer **SALES COORDINATOR** Josh Haverlock

DIRECTOR, GLOBAL SALES Tracy Holmes **US EAST COAST AND MID WEST SALES** Stephanie O'Connor **US WEST COAST SALES** Lynne Stickrod **US SALES MANAGER, SCIENCE CAREERS** Claudia Paulsen-Young **US SALES REP, SCIENCE CAREERS** Tracy Anderson **ASSOCIATE DIRECTOR, ROW** Roger Goncalves **SALES REP, ROW** Sarah Lelarge **SALES ADMIN ASSISTANT, ROW** Bryony Cousins **DIRECTOR OF GLOBAL COLLABORATION AND ACADEMIC PUBLISHING RELATIONS, ASIA** Xiaoying Chu **ASSOCIATE DIRECTOR, INTERNATIONAL COLLABORATION** Grace Yao **SALES MANAGER** Danny Zhao **MARKETING MANAGER** Kilo Lan **ASCA CORPORATION, JAPAN** Kaoru Sasaki (Tokyo), Miyuki Tani (Osaka) **COLLABORATION/CUSTOM PUBLICATIONS/JAPAN** Adarsh Sandhu

DIRECTOR, COPYRIGHT, LICENSING AND SPECIAL PROJECTS Emilie David **RIGHTS AND LICENSING COORDINATOR** Jessica Adams **RIGHTS AND PERMISSIONS ASSOCIATE** Elizabeth Sandler **CONTRACTS AND LICENSING ASSOCIATE** Lili Catlett

MAIN HEADQUARTERS
Science/AAAS
1200 New York Ave. NW
Washington, DC 20005

SCIENCE INTERNATIONAL
Clarendon House
Clarendon Road
Cambridge, CB2 8FH, UK

SCIENCE CHINA
Room 1004, Culture Square
No. 59 Zhongguancun St.
Haidian District, Beijing, 100872

SCIENCE JAPAN
ASCA Corporation
Sibaura TY Bldg. 4F, 1-14-5
Shibaura Minato-ku
Tokyo, 108-0073 Japan

EDITORIAL
science_editors@aaas.org

NEWS
science_news@aaas.org

INFORMATION FOR AUTHORS
sciencemag.org/authors/science-information-authors

REPRINTS AND PERMISSIONS
sciencemag.org/help/reprints-and-permissions

MEDIA CONTACTS
scipak@aaas.org

MULTIMEDIA CONTACTS
SciencePodcast@aaas.org
ScienceVideo@aaas.org

INSTITUTIONAL SALES AND SITE LICENSES
sciencemag.org/librarian

PRODUCT ADVERTISING & CUSTOM PUBLISHING
advertising.sciencemag.org/products-services
science_advertising@aaas.org

CLASSIFIED ADVERTISING
advertising.sciencemag.org/science-careers
advertise@sciencecareers.org

JOB POSTING CUSTOMER SERVICE
employers.sciencecareers.org
support@sciencecareers.org

MEMBERSHIP AND INDIVIDUAL SUBSCRIPTIONS
sciencemag.org/subscriptions

MEMBER BENEFITS
aaas.org/membercentral

Science serves as a forum for discussion of important issues related to the advancement of science by publishing material on which a consensus has been reached as well as including the presentation of minority or conflicting points of view. Accordingly, all articles published in *Science*—including editorials, news and comment, and book reviews—are signed and reflect the individual views of the authors and not official points of view adopted by AAAS or the institutions with which the authors are affiliated.

EDITORIAL

Israel's COVID-19 endgame

As several countries now confront COVID-19 surges, Israel may be crossing over to other side of the pandemic. Whereas 5.5 million new severe acute respiratory syndrome coronavirus 2 (SARS-CoV-2) infections were reported globally last week, Israel reported only 398 (compared with >50,000 in January). Already, 54% of Israel's 9.2 million citizens have been fully vaccinated, considerably more than in most other countries. In the coming months, as restrictions continue to ease, the country should be optimistic, yet cautious, as risks of resurgence persist. Israel thus may well be an early case study for favorable outcomes of a mass-vaccination campaign.

In January 2021, faced with a third pandemic wave driven by the newly dominant B.1.1.7 variant, Israel enforced a 4-week strict lockdown in conjunction with rapid mass vaccination. By early February, 38% of the population had received at least one vaccine dose (80% of those over age 50), and an additional 7.5% had documented past infection (thought to confer some protection). In view of high vaccine uptake rates, and because interim analyses of a large local cohort showed high (>90%) vaccine effectiveness, the risk of resurgence and its expected burden was deemed sufficiently hedged. The lockdown was therefore lifted, despite a stagnated high incidence (over 8000 daily infections).

> "...mass-vaccination... could serve as a model strategy for other countries."

Exceeding predictions, a sharp 90-day continuous decline in new infections followed—a >100-fold decrease in documented infections and a >50-fold decrease in severe cases—despite gradual removal of most restrictions. Several indications suggest that this was driven mainly by the vaccination campaign rather than seasonality or residual lockdown effects. The decline in severe cases was first evident among the elderly (earliest-vaccinated group) and only weeks later among younger, mostly unvaccinated age groups. By late March, over 55% of daily COVID-19 mortality occurred among a small (<1.6%) subgroup—unvaccinated adults over 60 years old.

It is difficult to extrapolate from the Israeli experience a universally "safe" vaccine uptake threshold at which countries can safely reopen their economies, because such a threshold is likely setting-specific. By mid-April, the United Kingdom had experienced a similar decline in infections after a single vaccine dose campaign, whereas Chile and Seychelles experienced a surge of COVID-19 despite relatively high vaccine uptake (48, 39, and 67%, respectively, of each country's population having received at least one dose).

Israel's rapid vaccination campaign reaped the benefits of a decades-long investment in its community-focused universal health care system, including its digital health infrastructure. Led by Israel's four public nonprofit health organizations, hundreds of vaccination clinics administered vaccines for up to 2.5% of Israel's population daily. Their preparedness highlights several best practices: proactive outreach through call-centers and easy-to-use mobile device apps; electronic health records to expedite intake at vaccination sites; and offering vaccines left over at the end of each day to people of all ages so that doses did not go to waste.

Vaccine hesitancy hindered early vaccination efforts, particularly in ultra-Orthodox and Arab communities. Opening vaccination sites in these communities and encouraging respectful discussions between health experts and community leaders have helped increase uptake. Israel's COVID-19 National Expert Advisory Panel has suggested that Israel consider proactive steps to increase vaccine access to the Palestinian Authority population, and Israel has, thus far, vaccinated over 100,000 Palestinian workers employed in Israel.

With nearly 40% of the total population still unvaccinated—mostly younger than 16, plus 15% of vaccine-eligible age groups—Israel will likely not reach herd immunity soon. Interrupting viral transmission by mass vaccination ("indirect protection") has thus far sustained a continuous decline in incidence rates in all age groups. But as the remaining nonpharmaceutical interventions—indoor masks, quarantining, and a vaccination certificate policy (which limits access to high-risk indoor settings to vaccinated and recovered individuals only)—are gradually removed, the risk of COVID-19 resurgence will persist. In the absence of these interventions, outbreaks could be driven by increased vulnerability in low–vaccine uptake localities, as well as by viral variants that could partially evade the protective effects of vaccines. Even in one of the most vaccinated nations, the pandemic is not yet over, and Israel must remain vigilant. Its mass-vaccination success should not be squandered and could serve as a model strategy for other countries.

–Ran D. Balicer and Reut Ohana

Ran D. Balicer is founding director at the Clalit Research Institute and Chief Innovation Officer, Clalit Health Services, Tel Aviv, Israel; a professor at the School of Public Health, Ben Gurion University of the Negev, Be'er Sheva, Israel; and the chairman of Israel's COVID-19 National Expert Advisory Panel. rbalicer@clalit.org.il

Reut Ohana is deputy director at the Clalit Research Institute, Innovation Division, Clalit Health Services, Tel Aviv, Israel. reut.ohana@clalit.org.il

10.1126/science.abj3858

NEWS

Limited doses of China's Sinopharm COVID-19 vaccine have gone to Pakistan (including at a Lahore health facility, above) and other countries, but use may now widen.

IN BRIEF

Edited by **Jeffrey Brainard**

DISPATCHES FROM THE PANDEMIC

WHO authorizes Chinese vaccine

COVID-19 | In a move that promises to increase the meager supply of COVID-19 vaccines in poorer countries, the World Health Organization (WHO) last week gave a Chinese-made product the green light. Sinopharm, which makes its vaccine by chemically inactivating the pandemic coronavirus, received an Emergency Use Listing (EUL), a designation WHO gives after reviewing efficacy, safety, and manufacturing practices. It allows the COVID-19 Vaccines Global Access (COVAX) Facility, a global consortium promoting equity in vaccine distribution, to purchase and distribute Sinopharm's vaccine. COVAX and Sinopharm are still negotiating a price, and the company says it can increase production. More than 65 million doses have already been administered in 45 countries that have authorized its use. COVAX has struggled to buy affordable vaccines that have EULs—most are too expensive, or supplies were prepurchased by other countries. To date, COVAX has shipped fewer than 60 million doses.

U.S. supports patent waivers

VACCINES | After a protracted internal debate, the Biden administration last week said it supports a proposed international agreement to waive patents on the intellectual property used to make COVID-19 vaccines. The move was hailed by advocates of increased vaccine access and fairness in their distribution, who contend that it will attract new companies to help alleviate a global shortage and reduce costs. But many health officials and vaccinemakers caution that it will not increase supply for many months and that newcomers who want to produce the vaccines face bottlenecks including a lack of technical know-how and widespread shortage of raw materials.

Shot OK'd for 12- to 15-year-olds

PUBLIC HEALTH | U.S. regulators on 10 May authorized Pfizer and BioNTech's COVID-19 vaccine for use in children ages 12 to 15, expanding availability beyond older teens and adults. The go-ahead is the first in the United States for this age group and a key step in restarting in-person schooling, team sports, and other group activities. The decision by the U.S. Food and Drug Administration (FDA) was expected after the companies announced in March results from a trial of 2260 adolescents in that age group; 18 who received a placebo developed COVID-19 versus none who received the vaccine. Pfizer has said it expects to obtain safety and efficacy data from clinical trials studying children ages 2 to 11 by September, when it plans to ask FDA to permit use in that age group. A small fraction of all Americans who have died from COVID-19 were under age 18, and children who contract COVID-19 tend to have milder symptoms, but some face long-term health problems. However, many U.S. parents remain hesitant to vaccinate their children because of misinformation and because FDA has only authorized COVID-19 vaccines for emergency use, not given them full approval.

WHO flags new variant of concern

VIROLOGY | The World Health Organization (WHO) on 10 May designated as a variant of concern a version of the pandemic coronavirus first identified in India in February. Evidence suggests the variant, B.1.617, now found in about 40 countries, is more transmissible than original strains of SARS-CoV-2, WHO said. It is the fourth variant to receive this WHO designation, following ones first found in Brazil, South Africa, and the United Kingdom.

A call for pandemic precautions

GOVERNANCE | To be better prepared for the next pandemic, the world needs a Global Health Threats Council akin to the United Nations Security Council, which would bring together country leaders from different regions along with representatives of the

PHOTO: ARIF ALI/AFP/GETTY IMAGES

private sector and civil society, according to the first comprehensive review of the global response to COVID-19, released on 12 May. The 13-member Independent Panel for Pandemic Preparedness and Response, which was commissioned by the World Health Organization, also proposes creating an International Pandemic Financing Facility with annual funding of $5 billion to $10 billion and giving WHO a bigger budget, more independence, and new powers to investigate outbreaks anywhere in the world, among many other recommendations. The panel was led by two former heads of state, Ellen Johnson Sirleaf of Liberia and Helen Clark of New Zealand, and included public health specialists, diplomats, and economists. "Pandemics pose potential existential threats to humanity and must be elevated to the highest level," says the report, *COVID-19: Make it the Last Pandemic*.

Vaccine passports? It depends

PUBLIC ATTITUDES | U.S. adults voice varying support for rules by governments and businesses that could require people to prove they received a COVID-19 vaccine before certain in-person activities, such as attending crowded events or entering their office, a Gallup poll reported last week. Most of the 3731 respondents surveyed in April favored proof to travel by airplane (57%) and attend large events such as concerts (55%). But support dipped below a majority for requiring proof to enter one's workplace (45%) or dine indoors at a restaurant (40%). Responses differed by political party affiliation and willingness to be vaccinated.

Top CDC official resigns

LEADERSHIP | Nancy Messonnier, a top official at the U.S. Centers for Disease Control and Prevention (CDC) who drew the ire of former President Donald Trump in February 2020 for her unvarnished public warning about the impending coronavirus pandemic, will leave the agency on 14 May, she told colleagues last week in an email. Two weeks before the email, she had been reassigned from heading CDC's COVID-19 task force, *Politico* reported. She will join the Skoll Foundation as executive director for pandemics and health systems. At CDC since 1995, Messonnier led the launch of a low-cost meningitis vaccine in Africa and rose to head the agency's National Center for Immunization and Respiratory Diseases. After she warned at a press conference 15 months ago that the pandemic might severely sicken many Americans, stock markets plunged, and she did not appear at any subsequent White House briefings.

PHOTO: ALAN MURPHY/MINDEN PICTURES

The belted kingfisher is among the species covered by the Migratory Bird Treaty Act.

CONSERVATION

Biden plans to restore fines for killing birds

President Joe Biden's administration moved last week to overturn a regulation adopted by his predecessor that eliminated sanctions against companies whose operations accidentally kill migratory birds. Trump administration officials had said the fines should be reserved for intentional deaths—an interpretation that broke with long-standing policy and would have prevented, for example, any penalties against the companies responsible for the 2010 *Deepwater Horizon* oil spill in the Gulf of Mexico that killed as many as 1 million birds. Wildlife biologists have said the original, broader enforcement was essential to curtail steep declines in populations of 1100 bird species covered by the federal Migratory Bird Treaty Act. Biden's administration would replace Trump's regulation with a new one, which could take months to finalize. Conservation advocates have long proposed a permitting program that would protect companies from legal action for accidental deaths if they adopt practices and technology shown to prevent most bird deaths.

Seismic array winds down

SEISMOLOGY | One of the largest seismic research projects in history, used to study structures in Earth's crust and mantle as deep as 3000 kilometers, is ending its run. Begun in 2004 and funded by the U.S. National Science Foundation, the several hundred seismic stations of the Transportable Array collected earthquake data as a way of peering deep inside Earth. The stations were deployed at first in the western states and then were moved east across the country every few years. In 2017, the project's final phase began when the network was transported to Alaska. Pandemic-related delays prompted an extra year of operation, but in early May, more than 80 stations went dark, awaiting collection this summer. Another 100 will remain in

ENERGY

During pandemic, renewables grew while coal slumped

Electricity production from renewable sources, led by solar photovoltaics and wind, continued years of steady growth globally during the COVID-19 pandemic, a report says. The production grew 7% in 2020, even as overall demand for electricity dropped and generation from fossil fuels declined. This year, as social restrictions ease and demand climbs, renewable electricity is expected to increase by 8%, the International Energy Agency said last month in its *Global Energy Review 2021*. Overall, production from renewables, especially in China, is forecast to provide half the total increase in electricity this year. But power from fossil fuels will grow as well, and analysts say the switch away from coal and other carbon-emitting energy sources is not happening fast enough to reduce the effects of global warming.

A tailwind for alternative energy

Coal showed a steep drop in 2019–20 globally, in part because U.S. plants switched to cheaper natural gas. But a rebound is expected as China and India use more coal.

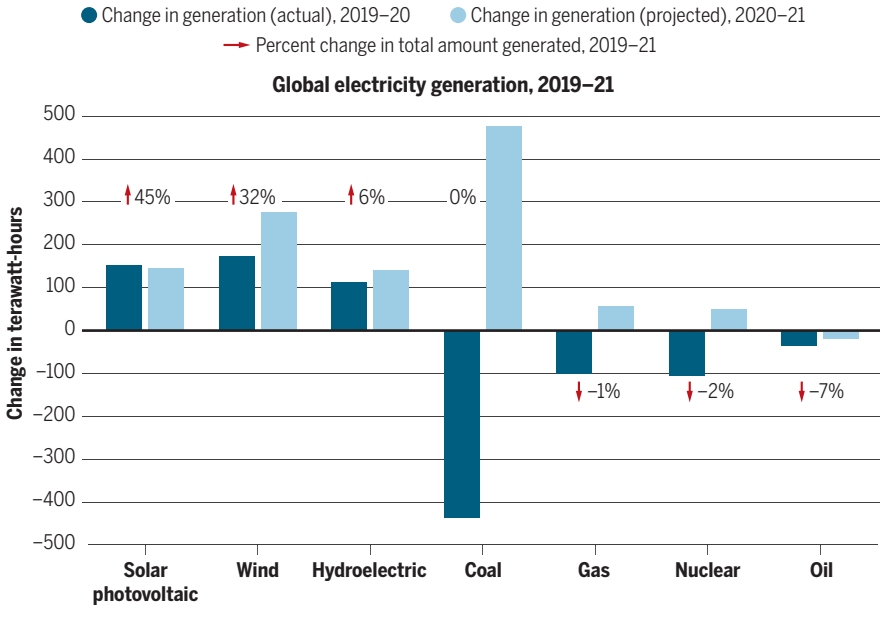

Alaska, many of them in remote, previously unmonitored regions, filling gaps in the state's seismic coverage.

Ecstasy passes clinical test

DRUG DEVELOPMENT | A psychedelic drug has passed a major milestone by showing evidence of benefit as a supplement to talk therapy for post-traumatic stress disorder (PTSD), researchers report this week. The results came from the first phase 3 clinical trial combining psychotherapy with the drug 3,4-methylenedioxymethamphetamine (MDMA), popularly called ecstasy, for people with severe, chronic PTSD. The study, sponsored by the Multidisciplinary Association for Psychedelic Studies (MAPS), recruited 90 people to receive talk therapy during 15 sessions, including three "experimental" ones in which they received either MDMA or a placebo. The MDMA group saw significantly greater improvements on a PTSD symptom scale, the researchers said in *Nature Medicine*. Two months after the final experimental session, 67% of those who got MDMA no longer met the diagnostic criteria for PTSD, versus 32% of those who got a placebo. MAPS aims to confirm those benefits in a 100-person trial now enrolling volunteers and, in 2023, to seek approval from the U.S. Food and Drug Administration for MDMA-assisted therapy.

Scientists seek whale safeguards

CONSERVATION | Researchers are pressing Chile's government to increase protections for whales along its coast against deadly ship collisions. After three whales were found dead during just 8 days in April, 65 Chilean marine mammal specialists issued a public plea for the government to act. They called for rerouting ships away from sensitive regions, setting speed limits, and establishing an alert system to warn vessel pilots of nearby whales. Hundreds of vessels plying Chilean waters pose significant threats to the estimated 40% of the world's cetacean species that frequent them, researchers say. In 2008, Chile declared its entire 6500-kilometer-long coastline a whale sanctuary. But the country's protections for marine mammals still exist only on paper or lack details. The government says it is working to increase safety measures. But researchers say it must commit adequate funding to succeed.

Space scope, rock return on deck

SPACE SCIENCE | NASA marked two milestones this week—the final tests on Earth of its next marquee space telescope, and the start of a long journey home for a trove of asteroid rocks. NASA engineers are wrapping up testing on the giant gold-tinted mirror of the James Webb Space Telescope. Afterward, the long-delayed, $9 billion observatory will be shipped off to French Guiana for launch on 31 October. Also this week, NASA's OSIRIS-REx probe began its 2-year flight back to Earth from the asteroid Bennu, carrying up to 400 grams of rocky chunks the spacecraft collected from its surface. It will be the largest U.S. haul of rocks collected in space since the Apollo program, and NASA's first from an asteroid.

Fish expert wins food prize

AQUACULTURE | Nutrition expert Shakuntala Haraksingh Thilsted was awarded the World Food Prize this week for research that used aquaculture to improve the diets of millions of people across Asia and Africa. Thilsted, who began her career at Trinidad and Tobago's Ministry of Agriculture, Land & Fisheries, now heads nutrition research at WorldFish, a nonprofit research center in Penang state in Malaysia. In Bangladesh, she studied small, native fish species widely eaten by farmers. Thilsted identified micronutrients the fish contain and their valuable role in the healthy development of infants and toddlers; adding these fish also helps the body absorb other micronutrients in rice and vegetables. She developed ways to cheaply raise fish, combining large and small species in ponds, which increases production. These methods have helped make Bangladesh one of the world's top aquaculture producers.

SCIENCEMAG.ORG/NEWS
Read more news from *Science* online.

CREDITS: (GRAPHIC) N. CARY/*SCIENCE*; (DATA) *GLOBAL ENERGY REVIEW 2021*, IEA

Former winner and member of the Prize Jury advocates diversity and inclusion in science

eppendorf & Science PRIZE FOR NEUROBIOLOGY

Marlene Cohen, Ph.D. is now Professor in the Department of Neuroscience and Center for the Neural Basis of Cognition at the University of Pittsburgh. Marlene Cohen's lab will be moving to the University of Chicago in 2022.

Marlene Cohen was awarded the Eppendorf & Science Prize for Neurobiology in 2012. She uses the responses of groups of neurons to get a snapshot of an animal's cognitive state at any moment. Her approach provides a new way to study how our mental activity affects what we perceive and how cognitive processes such as attention are controlled. Since winning the prize at the start of her first year as Assistant Professor, Marlene's lab has expanded in the number of people and in the breadth of research.

"I have been lucky to attract people who have different backgrounds, ideas and interests. Our new research directions have grown out of those differences. We have been experimenting with new behaviors, new stimuli, recordings from new (to us) brain areas, new cognitive processes, new translational approaches, and new models. The exciting part for me is how these varied approaches have informed and improved each other. The breadth has allowed us to extract relatively simple general principles about the relationships between neurons and behavior that we might have missed if we restricted ourselves to our standard behaviors and experiments."

Marlene says, "I tell people considering joining the lab that those happiest here are those who like learning new things. No two days are the same. You can expect a mix of biology, psychology, math, engineering and medicine, with some chaos thrown in!"

Marlene adds that increasing diversity in the scientific community makes science fairer for researchers, for the diverse set of people whose tax dollars fund the work, and simply better. She says, "It's incumbent on all of us to work hard to improve equity and inclusion in science."

Marlene, herself a former winner of the Eppendorf & Science Prize, was a member of the 2020 Prize Jury. She was extraordinarily impressed by the huge number of terrific scientists who applied and she learned a lot about the brain from these essays.

"One of the favorite parts of this prize is that it rewards both scientific discovery and communication. Winning the award encouraged me to work even harder at communicating about my research. Our discoveries don't mean much if we don't communicate them to the scientific community and to the public."

If you are thinking about applying for the prize in 2021, Marlene advises you to, "Go for it! For me, writing about my work in essay format influenced the way I think and talk about it. And you just might win!"

Eppendorf & Science Prize for Neurobiology

This annual international research prize of US$25,000 is awarded to one young scientist for their outstanding contributions to neurobiological research based on methods of molecular and cell biology. Researchers who are not older than 35 years are invited to apply by June 15, 2021.

www.eppendorf.com/prize

eppendorf

Science AAAS

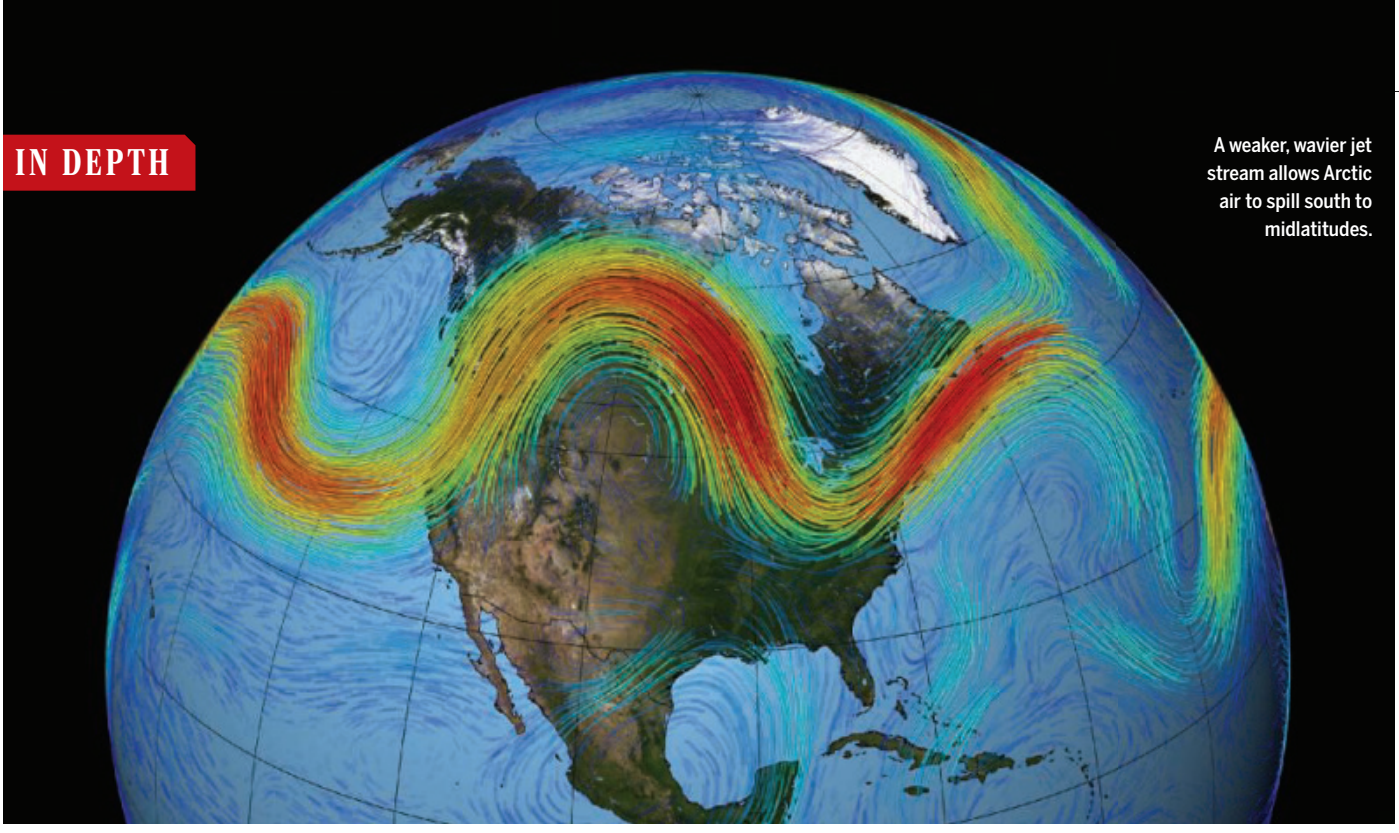

A weaker, wavier jet stream allows Arctic air to spill south to midlatitudes.

IMAGE: NASA/GODDARD SPACE FLIGHT CENTER SCIENTIFIC VISUALIZATION STUDIO

CLIMATE CHANGE

Arctic ice loss not a big culprit in harsh winters

Models find few links between sea ice loss and cold weather from weakened jet stream

By **Paul Voosen**

Every time severe winter weather strikes the United States or Europe, reporters are fond of saying that global warming may be to blame. The paradox goes like this: As Arctic sea ice melts and the polar atmosphere warms, the swirling winds that confine cold Arctic air weaken, letting it spill farther south. But this idea, popularized a decade ago, has long faced skepticism from many atmospheric scientists, who found the proposed linkage unconvincing and saw little evidence of it in simulations of the climate.

Now, the most comprehensive modeling investigation into this link has delivered the heaviest blow yet: Even after the massive sea ice loss expected by midcentury, the polar jet stream will only weaken by tiny amounts—at most only 10% of its natural swings. And in today's world, the influence of ice loss on winter weather is negligible, says James Screen, a climate scientist at the University of Exeter and co-leader of the investigation, which presented its results last month at the annual meeting of the European Geosciences Union. "To say the loss of sea ice has an effect over a particular extreme event, or even over the last 20 years, is a stretch."

The idea that Arctic sea ice loss could influence midlatitude winter weather first gained traction in 2012, in a paper by two climate scientists, Jennifer Francis, now at the Woodwell Climate Research Center, and Stephen Vavrus at the University of Wisconsin, Madison (*Science*, 18 April 2014, p. 250). It started with a simple observation: The Arctic is warming nearly three times faster than the rest of the world. At the time, sea ice loss was thought to be the primary accelerant for this amplification: As bright, reflective ice is replaced by dark, sunlight-absorbing water, the Arctic heats up, causing more ice loss, and more warming in turn.

The warming, Francis and Vavrus proposed, would inflate the height of the polar troposphere—the lowest layer of the atmosphere and home to its weather. That would decrease the pressure differences between polar and midlatitude air that drive the polar jet stream, which separates the air masses and keeps cold air collared around the pole. The jet would grow weaker and wavier, allowing cold air to intrude farther south. In their paper, Francis and Vavrus argued such a trend was visible in weather records and worsening with Arctic warming and ice loss.

A lot has changed since then, Francis now says. "Like all things, as you dig into them, they become more complicated." Most significantly, the 25-year trend that she and others had identified in observations from the late 1980s to early 2010s has weakened after another decade of observations. Although sea ice loss has continued, there are few signs of colder winters in Eurasia or North America, more cold extremes, or more frequent weakening or waviness in the jet stream. The new computer modeling matches the observations, says Doug Smith, a climate scientist at the United Kingdom's Met Office and another co-leader of the modeling effort. "There's not an inconsistency."

In the yearslong investigation, called the Polar Amplification Model Intercomparison Project (PAMIP), researchers ran more than a dozen climate models 100 times each. One set of model runs simulated the Arctic atmosphere without pronounced sea ice loss, using ocean temperatures and sea ice extent from 2000. The other kept the ocean temperatures the same, but reduced the ice coverage to the extent expected decades from now, after 2°C of global warming, when the Arctic could be ice free in the summer. Keeping the oceans the same should highlight the influence—if any—of sea ice loss.

In addition to finding only a tiny effect of sea ice loss on the polar jet stream, the models also found no coherent sign of a second proposed effect of reduced sea ice: more frequent disruptions of the stratospheric polar vortex—a second set of swirling winds, much higher up. Such disruptions, which occur every 2 years on average, ultimately allow cold air lower in the atmosphere to spill southward, causing extreme winter storms, including the cold that gripped Texas this past winter.

Judah Cohen, director of seasonal forecasting at Atmospheric and Environmental Research, has long argued that increased snow cover and diminished sea ice in Siberia favor weather patterns that propagate energy into the stratosphere, making the high-altitude disruptions more frequent. But although some model runs show this happening, on average "there is no clear response," says Yannick Peings, a climate scientist at the University of California (UC), Irvine.

Cohen isn't convinced, noting that the models also forecast unrealistically warm winter weather in the midlatitudes, making other predictions suspect. "There's clearly something missing." And Francis says the PAMIP experiment may be too simplistic, now that "we know there's a lot more to Arctic amplification than sea ice loss." Satellites and weather balloons have shown that the high troposphere in the tropics is warming fast because of tremendous storms that shoot hot, humid air upward. The Arctic is much less stormy, but many scientists now believe so-called atmospheric rivers regularly deliver this warm tropical air to the Arctic—a mechanism that PAMIP ignored.

Several PAMIP scientists, including Peings, tried to address this shortcoming in a paper last year in *Geophysical Research Letters*. They compared simulations that accounted just for sea ice loss, which tended to warm only the surface, with models in which tropical air warmed the whole Arctic atmosphere. Those models showed a striking effect of a warmer Arctic: At lower latitudes in Siberia, temperatures dropped 2°C by 2060. "That was a big eye opener for everybody," Francis says. It made the focus on just sea ice seem like "kind of a waste of time," she says. Gudrun Magnusdottir, a climate scientist at UC Irvine and co-author of the study, agrees. "It's dangerous to emphasize just one area and one point," she says.

The debate is far from over. Indeed, new evidence from weather records, published last month in the *Journal of Geophysical Research*, suggests the jet stream actually has gotten slightly wavier since the 1950s. The true cause of it—and the influence of global warming—remains to be seen. ■

DEMOGRAPHY

China's population still growing, census shows—but barely

Looming turning point triggers calls to raise retirement ages and create a "fertility-friendly society"

By **Dennis Normile**

Ending months of speculation about what its 2020 census would find, China reported on 11 May that preliminary data show its population is still growing. But major demographic challenges loom. China's population will start to shrink in the next few years, the trends suggest, meaning fewer and fewer people in their working prime will have to support a rapidly growing cadre of elderly. That has triggered discussions about how to increase the country's birth rate, which is far below the replacement level.

"China's population will peak in the future, but there remains uncertainty as to when," National Bureau of Statistics head Ning Jizhe said at a press conference in Beijing.

China is now home to 1.411 billion people, according to the decadal census, up from 1.339 billion in 2010. The number of citizens increased by an annual average of 0.53% over the past decade, a drop from the 0.57% rate recorded between 2000 and 2010. It was the lowest rate of growth since the early 1960s, when famine caused the population to decline. Those age 60 and over now make up 18.70% of the population, an increase of 5.44 percentage points since 2010. The census also showed that illiteracy decreased, the sex ratio at birth became slightly less skewed toward boys, and the number of years in school and the number of university graduates increased.

> **"China's population will peak in the future, but there remains uncertainty as to when."**
> **Ning Jizhe**, National Bureau of Statistics

The top-heavy age pyramid has policymakers worried that China may grow old before it grows rich. In many economic sectors, male employees can retire at 60; female office staff can retire at 55 and female blue-collar workers at 50. Those ages were set in the early 1950s, when life expectancy was less than 45; it has since risen to about 77. Previous efforts to make people work longer foundered because of public opposition. Now, there are "real discussions to push for a retirement age change," says Yong Cai, a demographer at the University of North Carolina, Chapel Hill.

What to do at the other end of the demographic equation is more contentious. China's total fertility dropped precipitously in the 1970s, from 5.8 births per woman in 1970 to 2.8 in 1979. The one-child policy, which took effect in 1980, drove fertility down further but also made it difficult to establish the exact rate because births were underreported. Estimates were "all over the place," Cai says. There is general agreement that fertility dropped below 2.1, the rate at which a population remains stable, in the early 1990s. In a 2013 study in *Population and Development Review*, Cai figured the total fertility rate in 2010 was 1.5 or lower. Now, the statistics bureau estimates it at 1.3 in 2020. And unlike the United States and Europe, China has next to no immigration to offset low fertility.

Since 2016, Chinese couples can have two children, and a new 5-year plan adopted in March calls for reducing the burdens of having, raising, and educating children by improving child care services and parental leave policies. Parents still face fines if they have more than two children, but there is now talk of allowing parents to have as many kids as they want.

Some would go further. Entrepreneur Liang Jianzhang, who's also an applied economist at Peking University, has long warned a shrinking population will lose its innovative prowess. In a May 2020 op-ed in *China Daily* he recommended building "a fertility-friendly society" using monthly child care subsidies, tax incentives, and subsidized housing for families with multiple children.

But such incentives are unlikely to reverse what is a worldwide trend toward fewer children, says Zhongwei Zhao, a demographer at the Australian National University. He takes comfort from another new statistic: 15.5% of Chinese people now have a tertiary education, up from 8.9% in 2010. This huge increase in human capital "is going to drive socioeconomic development," Zhao says. ■

Since 2016, the canopylike New Safe Confinement has sealed off and protected the ruined Chernobyl reactor.

NUCLEAR LEGACY

Fission reactions are smoldering again at Chernobyl

Neutrons from remnant fuel raise accident concerns

By **Richard Stone**

Thirty-five years after the Chernobyl Nuclear Power Plant in Ukraine exploded in the world's worst nuclear accident, fission reactions are smoldering again in uranium fuel masses deep inside a mangled reactor hall. "It's like the embers in a barbecue pit," says Neil Hyatt, a nuclear materials chemist at the University of Sheffield. Now, Ukrainian scientists are scrambling to learn whether the reactions will wink out—or require extraordinary steps to avert another accident.

Sensors are tracking a rising number of neutrons, a signal of fission, streaming from one inaccessible room, Anatolii Doroshenko of the Institute for Safety Problems of Nuclear Power Plants (ISPNPP) in Kyiv, Ukraine, reported last month during discussions about dismantling the reactor. "There are many uncertainties," says ISPNPP's Maxim Saveliev. "But we can't rule out the possibility of [an] accident." The neutron counts are rising slowly, Saveliev says, suggesting managers still have a few years to figure out how to stifle the threat. Any remedy will be of keen interest to Japan, which is coping with the aftermath of its own nuclear disaster 10 years ago at Fukushima, Hyatt notes. "It's a similar magnitude of hazard."

The specter of self-sustaining fission, or criticality, in the nuclear ruins has long haunted Chernobyl. When part of the Unit Four reactor's core melted down on 26 April 1986, uranium fuel rods and their zirconium cladding, graphite blocks, and sand dumped on the core to try to extinguish the fire melted together into a lava. It flowed into basement rooms and hardened into formations called fuel-containing materials (FCMs), laden with about 170 tons of irradiated uranium—95% of the original fuel.

The concrete-and-steel sarcophagus called the Shelter, erected 1 year after the accident to house Unit Four's remains, allowed rainwater to seep in. Because water slows, or moderates, neutrons and thus enhances their odds of striking and splitting uranium nuclei, heavy rains sometimes sent neutron counts soaring. After a downpour in June 1990, a "stalker"—a scientist at Chernobyl who risks radiation exposure to venture into the damaged reactor hall—dashed in and sprayed gadolinium nitrate solution, which absorbs neutrons, on an FCM that scientists feared might go critical. Several years later, the Shelter was equipped with gadolinium nitrate sprinklers. But the spray can't effectively penetrate some basement rooms.

Chernobyl officials presumed any criticality risk would fade when the massive New Safe Confinement (NSC) was slid over the Shelter in November 2016. The €1.5 billion structure was meant to seal off the Shelter so it could be stabilized and eventually dismantled. It also keeps out the rain, and since its emplacement, neutron counts in much of the Shelter have been stable or are declining.

But they began to edge up in a few spots, nearly doubling over 4 years in room 305/2, which contains tons of FCMs buried under debris. ISPNPP modeling suggests the drying of the fuel is somehow making neutrons ricocheting through it more, rather than less, effective at splitting uranium nuclei. "It's believable and plausible data," Hyatt says. "It's just not clear what the mechanism might be."

The threat can't be ignored. As water continues to recede, the fear is that "the fission reaction accelerates exponentially," Hyatt says, leading to "an uncontrolled release of nuclear energy." There's no chance of a repeat of 1986, when the explosion and fire sent a radioactive cloud over Europe. A runaway fission reaction in an FCM could sputter out after heat from fission boils off the remaining water. Still, Saveliev notes, although any explosive reaction would be contained, it could threaten to bring down unstable parts of the rickety Shelter, filling the NSC with radioactive dust.

Addressing the newly unmasked threat is a daunting challenge. Radiation levels in 305/2 preclude installing sensors. And spraying gadolinium nitrate on the nuclear debris there is not an option, as it's entombed under concrete. One idea is to develop a robot that can withstand the intense radiation for long enough to drill holes in the FCMs and insert boron cylinders, which would function like reactor control rods and sop up neutrons. In the meantime, ISPNPP intends to step up monitoring of two other areas where FCMs have the potential to go critical.

The resurgent fission reactions are not the only challenge facing Chernobyl's keepers. Besieged by intense radiation and high humidity, the FCMs are disintegrating—spawning even more radioactive dust that complicates plans to dismantle the Shelter. Early on, an FCM formation called the Elephant's Foot was so hard scientists had to use a Kalashnikov rifle to shear off a chunk for analysis. "Now it more or less has the consistency of sand," Saveliev says.

Ukraine has long intended to remove the FCMs and store them in a geological repository. By September, with help from European Bank for Reconstruction and Development, it aims to have a comprehensive plan for doing so. But with life still flickering within the Shelter, it may be harder than ever to bury the reactor's restless remains. ■

Richard Stone is senior science editor at the Howard Hughes Medical Institute's Tangled Bank Studios.

MICROBIOME

Ancient poop reveals extinction in gut bacteria

First DNA from paleofeces shows diverse microbes in people 1000 years ago in U.S., Mexico

By **Andrew Curry**

Every meal you eat is digested with the help of the bountiful bacteria thronging your intestines. When you're done digesting, those bacteria are also part of what's excreted. Now, 1000-year-old piles of dried-out poop are offering insights into how the billions-strong bacterial ecosystems in the human gut have been altered by sanitation, processed foods, and antibiotics.

In a study published in *Nature* this week, researchers analyzed ancient DNA from coprolites, or preserved feces, found at the back of rock shelters in Utah and Mexico. The data give scientists their first good look at ancient gut bacterial communities, says Stanford University biologist Justin Sonnenburg. "These paleofeces are the equivalent of a time machine."

They suggest that over the past millennium, the human gut has experienced an "extinction event," losing dozens of species and becoming significantly less diverse, says lead author and Harvard Medical School microbiologist Aleksandar Kostic. "These are things we don't get back."

Previous studies have used the gut bacteria of today's hunter-gatherers and herders as a proxy for the ancient microbiome. Their microbial diversity far exceeds that of people in industrial societies, and researchers have linked low diversity to higher rates of "diseases of civilization," including diabetes, obesity, and allergies. But it wasn't clear how much today's nonindustrial people have in common with ancient humans. "We really wanted to be able to go back in time and see when those changes [in the modern gut microbiome] came about, and what's causing them," says Harvard University geneticist Christina Warinner, a co-author on the paper. "Is it food itself? Is it processing, is it antibiotics, is it sanitation?"

An international team analyzed eight ancient coprolites preserved by dryness and stable temperatures in three rock shelters in Mexico and the southwestern United States. Researchers radiocarbon dated the samples, some of which were excavated almost 100 years ago and stored in a museum, to between 0 C.E. and 1000 C.E. Meradeth Snow, an archaeologist at the University of Montana, Missoula, then rehydrated tiny bits of feces, recovering longer DNA strands than previous paleofeces analyses.

Earlier attempts to analyze the ancient gut microbiome had been thwarted by the challenge of sorting ancient gut bacterial DNA from that of microbes invading from the surrounding soil, says Marsha Wibowo, a Ph.D. student at Harvard's Joslin Diabetes Center, who analyzed the DNA. She singled out the ancient gut species by focusing on DNA that had been damaged by time, and on sequences from bacteria known to be associated with the mammalian gut. Some of the ancient DNA was unfamiliar, however, evidently representing never-before-seen kinds of extinct bacteria.

Coprolites from near the Turkey Pen site in Utah reveal ancient diets.

PHOTO: RUSS BISHOP/ALAMY STOCK PHOTO

The coprolites yielded 181 genomes that were both ancient and likely came from a human gut. Many resembled those found in nonindustrial gut samples today, including species associated with high-fiber diets. Bits of food in the samples confirmed that the ancient people's diet included maize and beans, typical of early North American farmers. Samples from a site in Utah suggested a more eclectic, fiber-rich "famine diet" including prickly pear, ricegrass, and grasshoppers.

But the ancient microbiomes also stood apart from their modern counterparts, for example lacking markers for antibiotic resistance. And they were notably more diverse, including dozens of unknown species. "In just these eight samples from a relatively confined geography and time period, we found 38% novel species," Kostic says.

Treponema bacteria, for instance, are virtually unknown in the industrialized gut microbiome and appear only occasionally in people living nonindustrial lifestyles today. But, "They're present in every single one of the paleofeces, across all the geographic sites," Kostic says. "That suggests it's not purely diet that's shaping things." He hopes future experiments on coprolites from other time periods will make it possible to isolate when the biggest shifts took place and what prompted them.

The findings echo another study of much older samples by Warinner and colleagues published this week, which reported DNA from previously unidentified microbes on the teeth of Neanderthals and early modern humans.

The new data from old poop show no one on the planet today has been spared changes to their microbiome. "Nonindustrial populations, including their microbiomes, shouldn't be considered proxies for our ancestors," says Massachusetts Institute of Technology geneticist Mathieu Groussin.

The findings also suggest we've lost a lot of microbial helpers in the recent past, and our bodies may not have had time to adapt. "This study gives us a gold standard to check on what species we've lost," Sonnenburg says.

Because feces aren't considered human remains under U.S. law, Warinner says, there was little discussion early on about the ethics of the research. But when the group reached out to several dozen tribes in the Southwest, some said the samples were a link to their ancestors and were upset they hadn't been consulted earlier. The study now includes an ethics statement, a first for a paleofeces paper.

University of California, San Diego, geneticist Keolu Fox says the team didn't go far enough. Insights into the ancient gut could someday inform commercial efforts to reshape modern microbiomes, he says. That raises complex questions of who owns such data. "It's supposedly waste, but it contains DNA and profiles of microbial diversity. Maybe that poop is literally gold," Fox says. "We're getting into a whole new gray area." ■

POLLUTION

Shipping rule cleans the air but dirties the water

Growing use of ship exhaust scrubbers has increased marine discharge of compounds

By **Erik Stokstad**

In an unwelcome twist, a global effort to curb pollution from the heavy fuel oil burned by most big ships appears to be encouraging water pollution instead. A 2020 regulation aimed at cutting sulfur emissions from ship exhaust is prompting many owners to install scrubbing systems that capture pollutants in water and then dump some or all of the waste into the sea.

Some 4300 scrubber-equipped ships are already releasing at least 10 gigatons of such wastewater each year, often in ports and sometimes near sensitive coral reefs, researchers reported last month in the first effort to quantify and map the releases worldwide. The shipping industry says pollutants in the waste don't exceed national and international limits, and that there's no evidence of harm. But some researchers fear scrubber water, which includes toxic metals such as copper and carcinogenic compounds called polycyclic aromatic hydrocarbons, poses a rapidly growing threat, and they want to see such systems outlawed.

"There's definitely reason for concern," says Ida-Maja Hassellöv, a maritime environmental scientist at the Chalmers University of Technology who studies the issue. "A ban of the scrubbers is most urgent."

The emerging debate is the result of a 2020 regulation put into place by the International Maritime Organization (IMO), an arm of the United Nations that works with 174 member states to develop common rules for international shipping. By banning the use of sulfur-heavy fuel oil, the rule intended to reduce pollutants that contribute to acid rain and smog. IMO estimated the rule would slash sulfur emissions by 77% and prevent tens of thousands of premature deaths from air pollution in ports and coastal communities.

But cleaner fuel can cost up to 50% more than the sulfur-rich kind, and the rule allows ship owners to continue to burn the cheaper fuel if they install scrubbers. In 2015, fewer than 250 ships had scrubbers (often to comply with local regulations); last year, that number grew to more than 4300, according to industry figures.

A scrubber system sends exhaust through a meters-tall metal cylinder, where it is sprayed with seawater or freshwater, depending on the type, at rates comparable to gushing fire hydrants, to capture pollutants. In the most popular systems, called open loop scrubbers, seawater is discharged to the ocean after little or no treatment. Other systems retain sludge for disposal on land and release much smaller (but more concentrated) amounts while at sea.

To come up with its estimate of annual discharges, a group led by environmental policy researcher Bryan Comer of the International Council on Clean Transportation (ICCT), a nonprofit think tank, analyzed roughly 3600 scrubber-equipped ships. The 10 gigatons a year they calculated is likely an underestimate, Comer says, because more ships are adding scrubbers and many have discharge rates higher than the IMO estimates used in the study.

The ICCT study, released on 29 April, also examined the routes taken by the ships in 2019 and found that scrubber discharge is concentrated where shipping traffic is dense, such as the North Sea and the Straits of Malacca. But it also spans the exclusive economic zones of many nations, which extend 370 kilometers out to sea. "Our mapping shocked even me," Comer says, because it wasn't obvious that so many kinds of ships, operating all over the world, would opt to install exhaust scrubbers.

Researchers are particularly worried about discharges in areas that IMO has designated as ecologically sensitive. The Great Barrier Reef, for example, receives about 32 million tons of scrubber effluent per year because it's near a major shipping route for coal. Ships also release scrubber water around the Galápagos Islands.

Ports see substantial discharges, too. Cruise ships dominate those releases, contributing some 96% of discharges in seven of the 10 most discharge-rich ports (see map, below). Cruise ships typically need to burn fuel in port to continue to operate their casinos, heated pools, air conditioning, and other amenities. Most ports have shallow water, so pollutants are less diluted and can accumulate more rapidly.

Smoke in the water

Vessels equipped with exhaust scrubbers often discharge the resulting wastewater while in port. Some ships, such as this ferry off Corsica (right), keep their engines running in port, potentially increasing releases of both air and water pollutants.

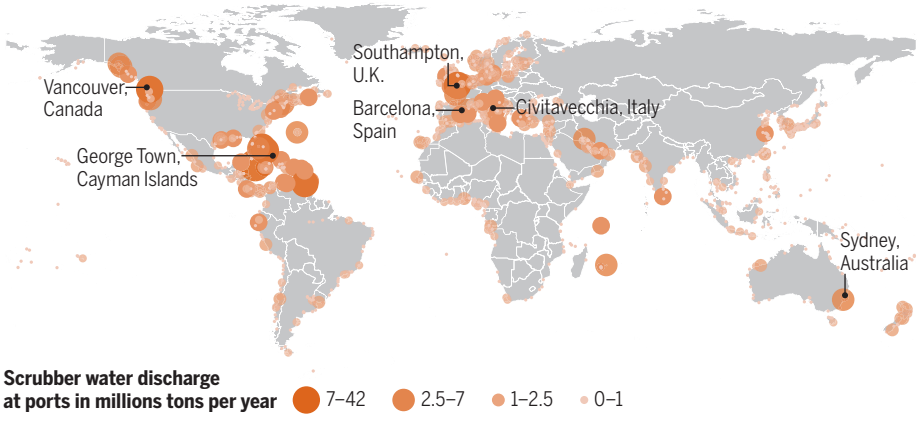

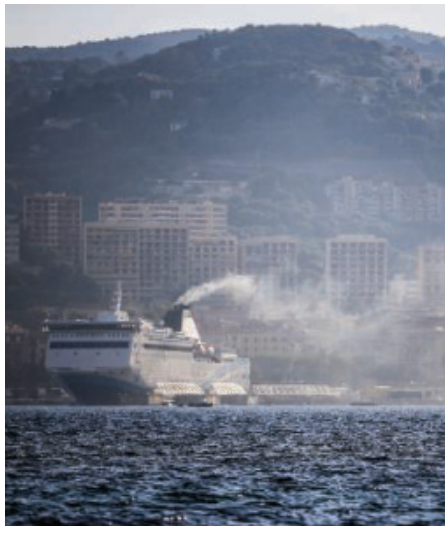

CREDITS: (MAP) OSIPOVA *ET AL.*, *GLOBAL SCRUBBER WASHWATER DISCHARGES UNDER IMO'S 2020 FUEL SULFUR LIMIT*. INTERNATIONAL COUNCIL ON CLEAN TRANSPORTATION, 2021; ADAPTED BY N. DESAI/*SCIENCE*; (PHOTO) PASCAL POCHARD-CASABIANCA/AFP VIA GETTY IMAGES

Industry organizations, including one called the Clean Shipping Alliance 2020, say the discharge figures are misleading. They argue, for example, that it is the waste's possible toxicity that matters, not its volume.

So far, few researchers have tested scrubber water on marine life. One laboratory study, published last month in *Environmental Science & Technology*, found that samples from three North Sea ships harmed the development of a common copepod (*Calanus helgolandicus*), a tiny crustacean that is a key part of Atlantic Ocean food webs. At very low doses, young copepods stopped molting, and the animals died at rates three times that found in the wild. Such impacts could be "a big deal" for food webs in the real world, says co-author Peter Thor, a marine ecologist now with the Swedish University of Agricultural Sciences.

"We were surprised that we saw effects at such low concentrations," says Kerstin Magnusson, a co-author and a marine ecotoxicologist with the Swedish Environmental Research Institute. None of the measured pollutants alone occurred at what seemed to be a harmful concentration; instead, the mixture could be to blame, and it's possible that scrubbers generate new compounds.

Next, the researchers, who are participating in a €7.5 million European effort to study shipping pollution called EMERGE, would like to study how scrubber water affects fish larvae, which are likely more sensitive than copepods to scrubber pollutants.

But shippers have become hesitant to share samples and data with scientists. "We're reluctant to give it to organizations which we know have already an established agenda," says Mike Kaczmarek, chairman of the Clean Shipping Alliance 2020. The group will work with "science-based organizations where we think that [the data will] get an objective treatment." He points to studies that predict no harm from scrubber discharges, and says that, so far, there's no evidence of actual damage. "Show me the harm," Kaczmarek says. "There isn't any." Comer, however, says those studies have methodological lapses that make it impossible to know whether they used samples that meet existing guidelines.

The ultimate solution, he and others say, is to require ships to use the cleanest fuel, called marine gas oil. In the meantime, 16 countries as well as some localities have banned the most common scrubbers. Those bans have reduced discharges by 4%, Comer says. "There needs to be a global fix on top of that," he says. "That's going to take a long time," he concedes, given that it can take years for nations to agree on new shipping rules, especially when they increase costs. ■

PHOTO: ISTOCK.COM/MIODRAG IGNJATOVIC

Some conferences will convene partially in-person this year as "hybrid" meetings.

COVID-19

As U.S. pandemic subsides, conferences explore 'hybrids'

Societies aim to harness the best of in-person and virtual meetings, but it won't be easy

By **Katie Langin**

Last year, the COVID-19 pandemic upended the conference experience for researchers around the globe as scientific societies canceled in-person meetings and scrambled to hold virtual events in their place—with varying success. Now, as vaccines become more widely available, particularly in the United States, some of those societies are grappling with a new challenge: when and how to safely get conference attendees into the same room again while maintaining the accessibility and wide reach virtual meetings afford.

Many are opting to stay virtual. But this summer and fall, a handful of U.S. societies are taking the plunge and planning "hybrid" meetings, which will convene in a physical location and also allow for virtual participation. It's a significant undertaking, often involving two separate planning teams and greater expense—and the risk that virtual attendees won't get the full benefit of the meeting. But many are optimistic it will pay off. "We're going to take the best of both worlds and try and smash them together in a way that makes sense," says Nate Wambold, director of meetings and conferences for the American Anthropological Association (AAA). (For its 2022 annual meeting, AAAS, *Science*'s publisher, will also adopt a hybrid format.)

If these hybrids succeed, they could serve as a model for what scientific conferences could look like in years to come. "All the organizations that run meetings … will have to revise the concept," says Guy Brasseur, a group leader at the Max Planck Institute for Meteorology who is serving as the program committee chair for the American Geophysical Union's (AGU's) annual meeting, scheduled to convene in New Orleans in December. He likens the situation to the digital publishing shakeup: "When we went from paper publication to electronic publication, that was a revolution for the community. Now we are in the middle of thinking, 'What is going to be the conferences of the future?'"

Plans for meetings' in-person components are still being ironed out. But persistent COVID-19 spread makes it likely they'll look much different than in years past. Current proposed policies include

Science's COVID-19 reporting is supported by the Heising-Simons Foundation.

requiring masks when attendees aren't eating or drinking and promoting social distancing, for instance by spacing lecture hall seats 2 meters apart and breaking up poster sessions into more exhibit halls than previously. Attendees may also be barred from serving their own coffee. "It's really important for our attendees to not only be safe … but [also] for them to feel safe," says Wambold, who is organizing AAA's first ever hybrid meeting in Baltimore in November. None of the conference organizers *Science* spoke with have currently decided to require proof of vaccination for in-person attendance, although some are considering taking that step.

At the same time, "The virtual audience can't be second class citizens—they have to be included," says Lauren Parr, vice president of meetings for AGU. The current plan is that all scientific sessions at the AGU meeting will be open to virtual attendees, either through livestreaming or by recording the sessions and making them available online. Organizers are also exploring the idea of organizing "watch parties" for virtual attendees who live in the same area—"to bring them together too so they get a bit of both," Parr says.

> **"We're going to take the best of both worlds and try and smash them together."**
> **Nate Wambold**, American Anthropological Association

Other societies are taking a different approach. "What hybrid means to us is there's an in-person meeting and then there's a virtual meeting, and there's a little bit of … digital overlap," says Robin Preston, director of meeting operations for the American Chemical Society, which is scheduled to host a hybrid conference in Atlanta in August. Virtual attendees will pay a reduced registration fee, but they won't have access to all in-person events. "We're not, from a cost standpoint, able to livestream everything," Preston says.

AAA is planning something similar. "We're doing all we can to blend those spaces and blend those experiences in creative ways," Wambold says—noting that organizers are planning a series of "live from Baltimore" events, which will include moderated questions from the online audience. But, "To do that for every one of our sessions in 30 meeting rooms … would be cost prohibitive for us."

AAA's virtual attendees will benefit from lessons learned during the society's virtual "test" in 2020, when it canceled its annual meeting and held a series of virtual events instead. "We knew that reading papers on a Zoom call would be about as entertaining as watching paint dry," Wambold says, so "we wanted to get people away from the normal ways of thinking about how to engage with their work and engage with one another." The society ended up holding a series of roundtable discussions, debates, and interviews. Those types of sessions will be incorporated into this year's meeting—both on-site and virtual—and will likely continue for the society's meetings going forward.

By offering a virtual option, societies hope to ease attendance for people like Laura Na Liu, a physics professor at Heidelberg University in Germany. She would love to attend this year's fall meeting of the Materials Research Society—a hybrid meeting in Boston that she is co-chairing—in person. She'll be fully vaccinated by then. But she's not sure she'll be able to because she has a 1-year-old daughter at home. "It's difficult to balance the traveling and then this entire crisis." So, she may be part of the virtual audience. As for the likelihood of hybrid or in-person meetings closer to home, she points to the slower vaccination in most of Europe as the major hurdle. "We will have to wait a little bit more."

Divya Persaud, a Ph.D. student at University College London who has a chronic illness that makes conference attendance challenging, hopes the virtual format outlasts the pandemic. She co-authored an opinion piece in October 2020 arguing that virtual options ease attendance for many scientists, including those with caregiving responsibilities, disabilities, and limited funds. "I really, really hope that we continue to have the conversation about what virtual can bring," she says.

For the foreseeable future, AGU organizers plan to stick to the hybrid format; they think a virtual option will boost international attendance and appeal to researchers at the edge of what the society specializes in. "AGU wants to be … more interdisciplinary," Brasseur says. "So that's an opportunity." For instance, an economist who is interested in global change might not have time to travel to an in-person meeting, he says. But if they can attend virtually, it may lower the bar enough for them to participate.

Conversations about how to enable virtual meeting attendance aren't new. AGU, for instance, started those discussions long before the pandemic because many of its members expressed an interest in greater accessibility and reducing the annual meeting's carbon footprint. "That was always in our plan," Parr says, "and the pandemic was a huge accelerator and a disrupter." ■

COVID-19

Do coronavirus genes slip into human chromosomes?

Further evidence supports challenged claim, but significance remains unclear

By **Jon Cohen**

A team of prominent scientists has doubled down on its controversial hypothesis that genetic bits of the pandemic coronavirus can integrate into our chromosomes and stick around long after the infection is over. If they are right—skeptics have argued that their results are likely lab artifacts—the insertions could explain the rare finding that people can recover from COVID-19 but then test positive for SARS-CoV-2 again months later. The team, however, doesn't yet have direct evidence of the integrations in infected people or any data indicating such events harm a person's health.

Stem cell biologist Rudolf Jaenisch and gene regulation specialist Richard Young of the Massachusetts Institute of Technology, who led the work, triggered a Twitter storm in December 2020, when their team first presented evidence for this phenomenon in a preprint on bioRxiv. The researchers emphasized that viral integration did not mean people who recovered from COVID-19 remain infectious. But critics charged them with stoking unfounded fears that COVID-19 vaccines based on messenger RNA (mRNA) might somehow alter human DNA. (Jaenisch and Young stress that their results, both original and new, in no way imply that those vaccines integrate their sequences into our DNA.)

Researchers also presented a brace of scientific criticisms, some of which the team addresses in a paper released online last week by the *Proceedings of the National Academy of Sciences* (*PNAS*). "We now have unambiguous evidence that coronavirus sequences can integrate into the genome," Jaenisch says.

SARS-CoV-2, the virus that causes COVID-19, has genes composed of RNA, and Jaenisch, Young, and co-authors contend that on rare occasions an enzyme in hu-

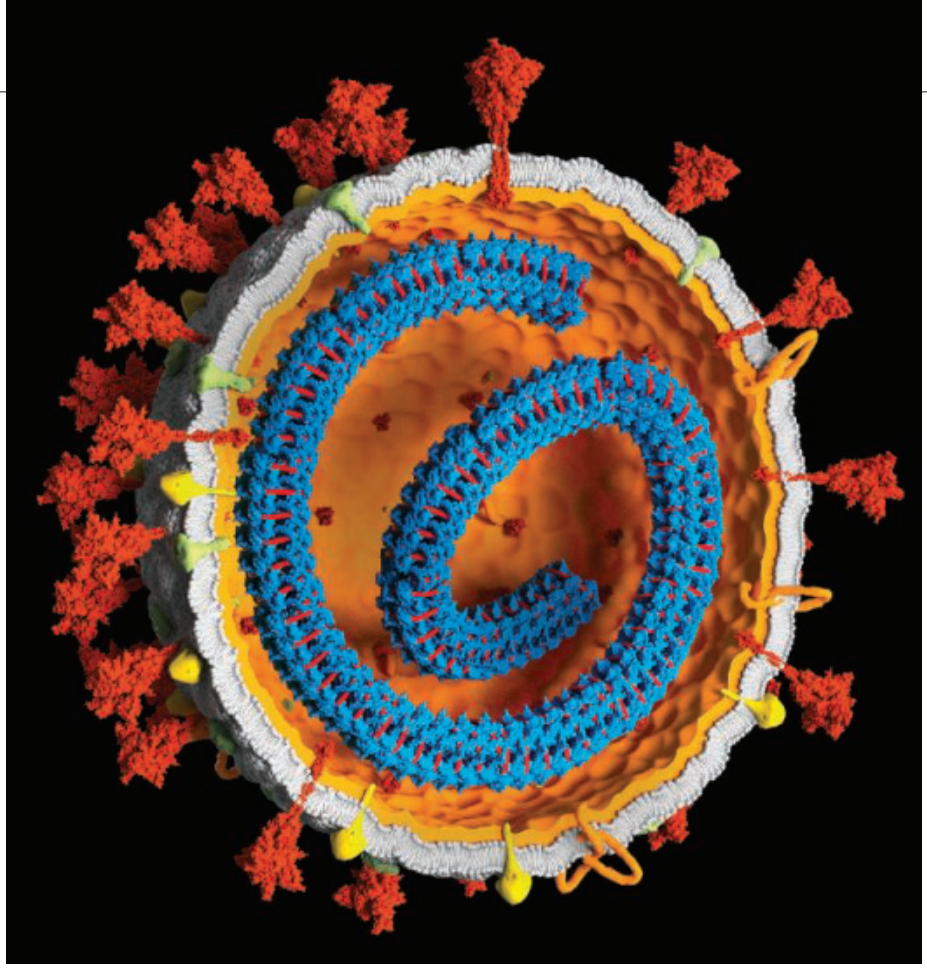

Lab studies of genetically engineered human cells suggest segments of the RNA (blue in virus illustration) of SARS-CoV-2 could convert to DNA in infected people and slip into their chromosomes.

PHOTO: CLAUS LUNAU/SCIENCE SOURCE

man cells may copy the viral sequences into DNA, allowing them to slip into our chromosomes. The enzyme, reverse transcriptase, is encoded by LINE-1 elements, sequences that litter 17% of the human genome and represent artifacts of ancient infections by retroviruses. In their original preprint, the researchers presented test tube evidence that when human cells spiked with extra LINE-1 elements were infected with the coronavirus, DNA versions of SARS-CoV-2's sequences nestled into the cells' chromosomes.

Many researchers who specialize in LINE-1 elements and other "retrotransposons" thought the data were too thin to support the claim. "If I would have had this data, I would have not submitted to any publication at that point," says Cornell University's Cedric Feschotte, who studies endogenous retrovirus chunks in the human genome. He and others also said they expected higher quality work coming from scientists of the caliber of Jaenisch and Young.

In two subsequent studies, both posted on bioRxiv, critics presented evidence that the supposed chimeras of human and viral sequences can be created by the very technique the group used to scan for them in chromosomes. As one report concluded, the human-virus sequences "are more likely to be a methodological product, than the result of genuine reverse transcription, integration, and expression."

In the new, peer-reviewed publication, Jaenisch, Young, and colleagues acknowledge that the technique they used accidentally creates human-viral chimeras. "I think it's a valid point," Jaenisch says.

He adds that when they first submitted the paper to a journal, they knew it needed stronger data, which they hoped to add during the review process. But the journal, like many, requires authors to immediately post all COVID-19 results to a preprint server. "I probably should have said screw you, I won't put it on bioRxiv. It was a misjudgment," Jaenisch says.

In the *PNAS* paper, the team provides evidence that artifacts alone can't explain the detected levels of virus-human chimeric DNA. The scientists also show that portions of LINE-1 elements flank the integrated viral genetic sequence, further supporting their hypothesis. And they have collaborated with one of the original skeptics, Stephen Hughes of the National Cancer Institute, who suggested an experiment to clarify whether the integration was real or noise, based on the orientation of the integrated viral sequences relative to the human ones. The results support the original hypothesis, says Hughes, a co-author of the new paper. "That analysis has turned out to be important," he says.

Others agree. "The integration data in cell culture is much more convincing than what was presented in the preprint, but it's still not totally clean," says Feschotte, who now calls Jaenisch's and Young's hypothesis "plausible." (SARS-CoV-2, he notes, can also persist in a person for months without integrating its genes.)

The real question is whether the cell culture data have any relevance to human health or diagnostics. "In the absence of evidence of integration in patients, the most I can take away from these data is that it is possible to detect SARS-CoV-2 RNA retroposition events in infected cell lines where LINE-1 is overexpressed," Feschotte says. "The clinical or biological significance of these observations, if any, is a matter of pure speculation at this point."

Jaenisch's and Young's team do report hints of SARS-CoV-2 integration in tissue from living and autopsied COVID-19 patients. Specifically, the researchers found high levels of a type of RNA that is only produced by integrated viral DNA as the cell reads its sequence to make proteins. But, Young acknowledges, "We do not have direct evidence for that yet."

Harmit Malik, a specialist in ancient viruses in the human genome at the Fred Hutchinson Cancer Research Center, says it's a "legitimate question" to ask why people who should have cleared the virus sometimes have positive polymerase chain reaction tests for its sequences. But he also remains unconvinced that the explanation is integrated virus. "Under normal circumstances, there is so little reverse transcription machinery available" in human cells, Malik says.

The controversy has grown decidedly more civil since December. Both Young and Jaenisch say they received more intense criticism for their preprint than any studies in their careers, in part because some researchers worried it played into the hands of vaccine skeptics spreading false claims about the newly authorized mRNA vaccines. "If there ever was a preprint that should be deleted, it is this one! It was irresponsible to even put it up as a preprint, considering the complete lack of relevant evidence. This is now being used by some to spread doubts about the new vaccines," Marie-Louise Hammarskjöld, a microbiologist at the University of Virginia, posted in a comment on bioRxiv at the time.

And what of the original journal submission? "They rejected it," Jaenisch says. ■

Science's COVID-19 reporting is supported by the Heising-Simons Foundation.

WHEN THE LEVEES BREAK

Researchers are learning where, when, and why rivers leap from their channels in deadly avulsions

By **Fred Pearce**

After a 2008 avulsion on the Kosi River, floodwaters overran the Indian state of Bihar, displacing millions of people.

PHOTO: PRASHANTH VISHWANATHAN/BLOOMBERG/GETTY IMAGES

Rumors that the Kosi River was about to burst were spreading fast in Kusaha, a Nepalese village on the border with India. The river's levees, towering over the village, were being eroded quickly by the cresting waters. At 2 p.m. on 18 August 2008, the east bank ruptured. People ran for their lives as the breach grew. Soon, the entire river, one of the largest tributaries of the Ganges River, had overrun Kusaha and was spilling into India, drowning farm after farm in search of a faster path to the sea.

Eventually, the rampaging river found a long-abandoned channel, where it flowed for 4 months before engineers wrenched it back to its old course. In the end, the flood destroyed some 800 farming villages, killed more than 400 people, and displaced a further 3 million. At one point, half of the Indian state of Bihar was underwater.

At the time, government officials and scientists blamed the deluge on heavy monsoon rains and poor maintenance of the levees. Both played a role, but this event was triggered by something else, says Rajiv Sinha, a river morphologist at the Indian Institute of Technology, Kanpur, who has studied it in detail.

The Kosi is one of the siltiest rivers in the world, carrying an annual load of some 100 million tons of sediment eroded from its catchment in the Himalayas. Near Kusaha the river hits the flat plain at the foot of the mountains, where it slows, dropping much of its load in the riverbed. As the channel's carrying capacity diminishes over time, the river eventually seeks a new route. For cen-

turies, the Kosi has burst its banks in this region every few decades—a phenomenon known to geographers as an avulsion.

Avulsions are often called the "earthquakes of rivers," because they are so sudden and catastrophic. But over the past decade, research has revealed that they are also somewhat predictable. Computer analyses and laboratory models of rivers and deltas have yielded insights into where major rivers tend to avulse—and when. "Ten years ago, we didn't know what was driving avulsions," says Vamsi Ganti, a geomorphologist at the University of California, Santa Barbara (UCSB). "Now we can model the processes and start to identify hot spots."

Yet just as researchers are gaining foresight into these rhythmic cataclysms, human activity is undermining it. Upstream deforestation and development is adding silt to rivers in unpredictable ways. Levees and dams are altering flows and paths, sometimes worsening the threat. After the Kosi flood, for example, Bihar began to build even more flood protection levees. But levees force a river to drop silt within a constrained channel, hastening the next avulsion, Sinha says. "If [engineers] don't understand the underlying dynamics," he says, "they are doomed to fail."

Climate change is another wild card: Rising seas are shifting avulsion hot spots that occur on coastal deltas, another place where rivers slow down, drop silt, and raise riverbeds, "Humans are now the big instigators of avulsions on rivers," says Jaia Syvitski, a hydrogeologist at the University of Colorado, Boulder.

FOR ALL THEIR destructiveness, avulsions bring benefits to both nature and society. They unleash regular floods that nourish many of the world's great wetlands. For example, the vast Pantanal, in the heart of South America, is kept rich and muddy by the avulsing Taquari River.

And by smearing fresh sediment across flood plains and deltas, avulsions fertilize lands that have nurtured some of the planet's great civilizations. The interlinked flood plains of the Tigris and Euphrates rivers in Iraq bear the imprints of 11 major avulsions over the past 7000 years. Ancient Mesopotamians converted some abandoned channels into irrigation canals; at other times the rivers themselves took over irrigation canals.

It is no surprise that to this day, avulsion zones are among the most densely populated places on Earth. River deltas, where avulsions are frequent, occupy just 0.5% of the world's land, but are home to 4.5% of its population. Those dense populations, drawn by the fertility that avulsions foster, are also in the path of their destructive force. Not for nothing are great avulsing rivers such as the Kosi or the Yellow River (Huang He) in China known as their peoples' "joy and sorrow."

Avulsions are not just rare catastrophes. An unpublished analysis of satellite images by Sam Brooke of UCSB has identified about 100 abrupt river jumps in the past 50 years: about 40 on coastal deltas and 60 on inland alluvial fans where rivers exit mountain valleys. Many avulsions cluster on rainy, mountainous islands in the tropics that erode quickly, such as Madagascar and Java—something Brooke says the analysis, the first of its kind, drew attention to.

In the aftermath of the Kosi disaster, Douglas Jerolmack, a sedimentologist at the University of Pennsylvania, was one of a handful of researchers to look more closely at the dynamics of avulsions. Often in the past, researchers had claimed avulsions were triggered by earthquakes or extreme floods. But Jerolmack's experiments confirmed a growing suspicion that avulsions happened naturally—and predictably. "Rivers are perturbed all the time but only avulse if they are set up by enough deposition," he says. Typically, he says, this happens once the riverbed rises above the land outside its banks or levees, so the entire volume of the river is "perched," as happened with the Kosi.

> **"Humans are now the big instigators of avulsions on rivers."**
>
> **Jaia Syvitski**, University of Colorado, Boulder

Jerolmack and his colleagues used a humble laboratory tool for mimicking river avulsions: a stream table, basically a large tank filled with sand and water. At one end of the stream table, the researchers could turn a "river" tap on and off and change the concentrations of sediment in the flow. By varying the steepness of the table, they created miniature mountain streams disgorging into fan-shaped flood plains and bird's-foot deltas.

Geographers had already noticed that rivers tend to avulse at the foot of mountains, where slopes change dramatically and sediment settles out, silting up the bed. The miniature rivers of the stream table allowed the team to quantify how often the avulsions occurred. "The time scale was basically the time it took the channel to fill with sediment," Jerolmack says.

He and his colleagues also found that the river kept reoccupying a small number of channels. "Old channel paths remained topographically smooth, and so low-resistance pathways to the sea," Jerolmack says. So if an avulsing river encounters an old channel, he says, it is likely to colonize it.

While Jerolmack was learning about the periodicity and quasi-predictability of avulsions inland, Michael Lamb, a geomorphologist at the California Institute of Technology, wanted to understand the mystery of recurrent avulsions downstream, in river deltas. In deltas, unlike at the foot of mountains, there is almost no slope change to slow a river and cause sediment to build up.

Lamb and his colleagues investigated by setting up not a steep stream table, but a languid laboratory delta, with a gradient of just one in 100,000 and a river spilling into a 3-meter-wide "ocean." In cycles of floods and gentle flows, they sent water and sediment—low-density crushed walnut shells—into the basin. They again found that the river spontaneously switched pathways to the ocean, and that the avulsions almost always occurred at the head of the delta.

Why that was happening turned out to be more complex than expected. Tides, by slowing the river so that it unloads sediment as it enters the delta, are one factor. But in deltas, scouring from floods is almost as important as deposition in creating avulsion conditions. Floods tend to flush sediment away from the lower part of the delta, Lamb says, preventing avulsions from occurring there. This leads to an avulsion-prone spot one "backwater length" from the mouth of the delta—a distance that can be calculated from basic river parameters.

The theory suggested that on the Mississippi River, an avulsion point should fall some 500 kilometers upstream from its delta mouth. The real world agrees: The Mississippi has avulsed in central Louisiana about once every 1400 years, creating large delta lobes across the Gulf Coast. The researchers also found evidence for repeated avulsions one backwater length up from the mouth of the Yellow, Rhine, Danube, Orinoco, and Nile rivers. "The discovered tie between avulsion location and backwater hydrodynamics has been a game changer," Jerolmack says.

Some rivers are less predictable, however. Last year, Lamb and colleagues published an investigation into a cluster of recent avulsions on short, steep, and sediment-rich streams in Madagascar. They found avulsions happening as much as 20 times farther upstream than predicted by the backwater length alone. They concluded that scouring from floods penetrates farther upstream on these streams because they deposit unusually fine sediments, which floods can sweep away more easily. "It's a special case, but still conforms to the theory that scour length is determining avulsion location," Lamb says.

Why rivers get jumpy

Avulsions occur naturally, when rivers jump from their courses and seek a faster way to the sea, often recolonizing remnant channels. They tend to occur in two hot spots where rivers slow down.

1 Upland hot spot
When rivers exit mountains, they slow down and spread sediment in alluvial fans. The frequency of avulsions depends on how silty the rivers are.

2 Delta hot spot
Rivers also slow down and drop silt at the heads of deltas, where they feel the effects of tides. Rising seas from climate change may not only shift avulsions upstream, but also increase their frequency.

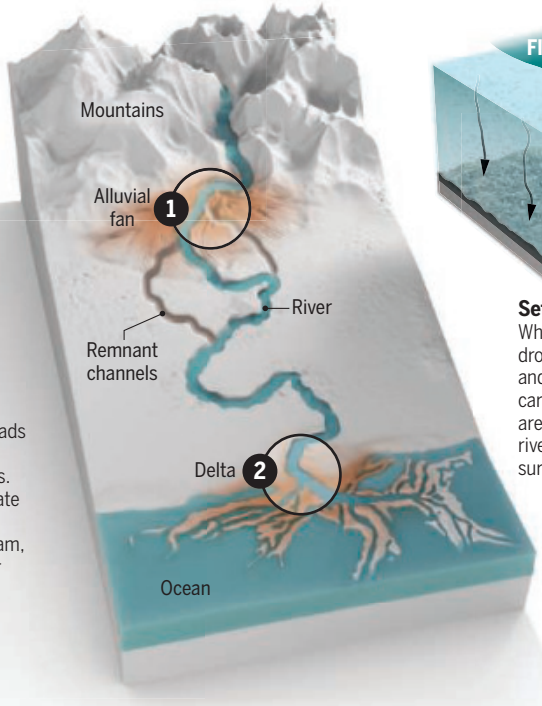

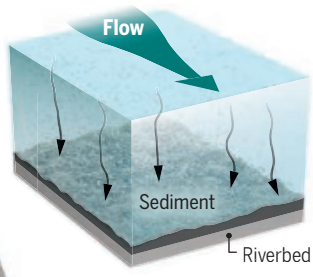

Settle down
When rivers slow down, they drop sediment that settles and reduces their channels' carrying capacity. Avulsions are most likely when riverbeds are perched above surrounding flood plains.

Deadly diversions

In 2010, a pair of textbook avulsions unleashed deadly floods along the Indus River in Pakistan, killing thousands and impacting millions. The events were captured by an instrument on NASA's Terra satellite.

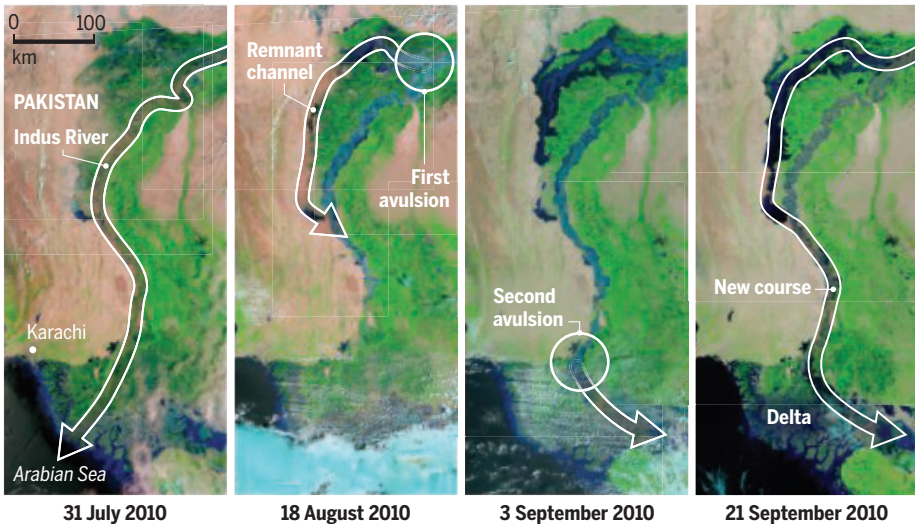

31 July 2010 | 18 August 2010 | 3 September 2010 | 21 September 2010

ALTHOUGH AVULSIONS will never be wholly predictable, the day is nearing where engineers can know where and when the dangers are at their greatest. Adrian Hartley, a rivers researcher at the University of Aberdeen, is pleased with how far the field has come. "We are getting much closer to understanding avulsions." But he warns that just as researchers begin to grasp these natural river cycles, human influences are altering them. "Few river systems are without significant human influence anymore, so simple generic models, however good they are, won't do all the job needed to predict avulsions."

Some anthropogenic effects are unsurprising. For instance, deforestation and soil erosion can make rivers siltier. That increases the pace at which they fill up their channels and reach the point of avulsion. But other factors are less obvious. Dams can trap sediment, preventing its flow downstream—and so they would seem to reduce the risk of avulsions. But Ganti says dams selectively capture coarse sediment, while allowing finer silt to continue downstream. Paradoxically, the resulting rivers "can carry exceptionally high volumes of sediment," Ganti says. Those loads, eventually dropped, should increase the frequency of avulsions, he predicts.

Meanwhile, coastal deltas are facing rising seas. By eroding the coastline and pushing tides farther upstream, they cause rivers to dump more sediment farther inland, shifting the entire backwater reach upstream, along with the avulsion hot spot. Ganti says their frequency increases as well, because the invading tides ensure that less of the sediment reaches. As tides push farther into deltas, they slow down rivers; less of the sediment gets into the ocean and more ends up in the delta where it causes avulsions. "We are turning the knob the wrong way," Ganti says. "We should brace ourselves for more avulsions."

If models are to keep up with such a fast-changing environment, they need more and better field data to show when and where tipping points are approaching, Lamb says. "Collecting data on the world's riverbeds is more important than ever." But that information is difficult to gather remotely and painstaking to collect in person or by boat, Lamb says. "For most of the world's rivers, we lack any data set for river bottom elevations," he says. "It's actually a major gap in our understanding of the geography of the Earth."

IGNORANT OF what is happening underwater, many river engineers continue to make bad situations worse by sticking with conventional methods of trying to hold back floods. For them, ever higher levees are the solution, whereas river scientists say they are the problem.

At the natural avulsion point some 500 kilometers up from the mouth of the Mississippi delta, the U.S. Army Corps of Engineers has for a century fought the river's urge to flow into the Atchafalaya River, which was the Mississippi's main channel until a few thousand years ago. In 1963, the Corps acted to prevent a full-scale avulsion. It completed a floodgate system, known as the Old River Control Structure, that kept most of the river's flow—and sediment—in the main channel. "Without this engineering, the Atchafalaya would have captured the majority of the flow from the Mississippi by now," Ganti says.

But half a century on, the Old River Control Structure's effectiveness is dwindling. It allows the Mississippi to send 30% of its water into the Atchafalaya while holding onto most of its sediment. As a result, the riverbed just downstream of Old River Control has risen by about 1.5 meters, according to Bo Wang, a fluvial geomorphologist now at Brown University. The sediment buildup increases the risk that a future flood will back up, overwhelm Old River Control, and

To avoid avulsions, China has tested discharging water from the Yellow River reservoirs to flush sediment from the riverbed downstream and send it to the ocean.

surge down the Atchafalaya. Such an avulsion would be catastrophic for trade on the Mississippi River, and could overrun many low-lying regions of the Atchafalaya. But Lamb says the rush of sediment would be an ecological boon for the delta regions of coastal Louisiana now sinking to the ocean. "Many would be nourished straight away if the river went down the Atchafalaya," he says (*Science*, 23 April, p. 334).

The stakes may be even higher in northern China, where some 90 million people live in a flood zone downstream of an avulsion hot spot on the Yellow River. But China is taking a more sophisticated approach to mitigating the risk, which it knows well from recent, tragic history.

On the right bank of the river, close to the city of Zhengzhou, is a modest stone plaque. It commemorates events on the morning of 9 June 1938, when the great river burst its banks, flooded the country's breadbasket, and found a new outlet to the sea, 650 kilometers south of the river's former mouth. Imagine the Mississippi heading east to enter the Atlantic Ocean in Georgia. The vast avulsion killed up to 1 million people and made refugees of up to 10 million more. It took engineers 9 years to coerce the river back to its former course.

This was no natural avulsion, however. The river's banks were dynamited on the orders of the country's leader Chiang Kai-shek, to hold back Japanese invaders during the Second Sino-Japanese War. It is reckoned to be humanity's single most deadly act of war, although most of the dead were Chinese, and the Japanese troops were held up for less than a month.

Whatever the military folly, the engineers knew what they were doing. They breached the bank at Huayuankou, a known avulsion hot spot where the river slackens as it emerges from the Loess Plateau and dumps its sediment. For the past 2500 years, the Yellow River has changed course here roughly once a century. If it were to happen again, "it would be a disaster of global importance, by affecting the Chinese economy," Syvitski warns.

Today, as the river rises as much as 10 meters above the surrounding flood plain, China is testing out new tactics in the vigil to avoid an avulsion. It has reduced sediment loads through soil conservation projects on the Loess Plateau. And it tested using fast flows of sediment-depleted water from dammed reservoirs to flush out sediment from the riverbed downstream and deliver it to the ocean, says Jeff Nittrouer, a hydrologist whose team at Rice University has been studying China's efforts to tame the Yellow River.

Chinese engineers are also intervening at the second avulsion point downstream, at the head of the Yellow River delta, where seven avulsions have occurred between 1855 and 1930. Since then, engineers have stopped trying to prevent channel switches. Instead, they induce them with dynamite and digging. Apart from making avulsions more predictable, the idea is to move sediment deposition to parts of the delta where the created land could be economically useful, such as for aquaculture or exploiting oil and gas reserves, Nittrouer says.

In 1938, China triggered an avulsion on the Yellow River to repel Japanese invaders—thought to be humanity's deadliest act of war.

The first major diversion was in 1976. Then in 1996, workers blocked the 20-year-old Qingshuigou channel as it filled with sediment, and forced the river down an old natural channel to enter the ocean 20 kilometers from its former mouth. Nature took the lead again in 2005, when the river cut a crevasse into its left bank, forming a new channel that has now taken over.

"The Yellow River delta is no longer by any stretch a natural delta," Syvitski says. Even so, the river's urge to shift its route to the ocean never abates. The price of safety on its banks is eternal vigilance. ■

Fred Pearce is a journalist in London.

PHOTOS: (TOP TO BOTTOM) XINHUA/LI AN/GETTY IMAGES; BETTMANN/CONTRIBUTOR/GETTY IMAGES

INSIGHTS

PERSPECTIVES

WATER SYSTEMS

River basins on the edge of change

Water scarcity after the Millennium Drought reveals the finite resilience of water systems

By **Flavia Tauro**

Ecological systems can switch into qualitatively different states after small perturbations (*1*). Climate change and anthropic activities are dominant drivers of such ecological shifts, which affect the ability of these systems to recover from future disturbance (*2*). Such finite resilience in complex and dynamic natural systems has been predicted and documented (*3*). However, whether abrupt transitions have occurred or will occur in the water cycle is an unsolved problem (*4*). The possibility for river basins to achieve thresholds at which tiny perturbations alter their state and lead to chronic water scarcity or excessive water bears substantial implications for the sustainable use of water resources in extreme climate conditions (*5*). On page 745 of this issue, Peterson *et al.* (*6*) demonstrate that river systems exhibit a finite resilience to perturbations and that climate may indeed drive river basins between alternative states.

To assess multistability in hydrological systems, Peterson *et al.* statistically investigated annual and seasonal precipitation and runoff records of more than 160 river basins in Victoria, Australia, before, during, and

PHOTO: ASHLEY COOPER/CONSTRUCTION PHOTOGRAPHY/AVALON/GETTY IMAGES

Most of Victoria and New South Wales in Australia experienced the Millennium Drought. River levels dropped, and reservoirs were at a fraction of their capacity. In 2010, the Lake Eildon reservoir in Victoria was at 29% capacity.

after the Millennium Drought (2001–2009), the worst drought ever recorded for southeast Australia (*7*). River basins are networks of channels and ridges that convey water to a common outlet. The studied river basins had neither major reservoirs nor water extractions, and runoff changes were not correlated to remotely sensed changes of Earth's surface cover. Seven years after the meteorological drought ended (that is, when dry weather ceased to dominate), more than a third of the river basins had not returned to previous runoff conditions, and most of them showed no signs of recovering soon. Conversely, basins that did shift back to a normal runoff state had shown warning signs in the 3 years before recovery. Unlike hydrological models that assume an infinite resilience of river systems, these findings imply that river basins do not always recover from droughts and that returning to predrought runoff conditions is not just a matter of time. Rather, the onset of positive feedbacks in hydrological systems, such as increased transpiration in nonrecovered basins, may amplify the impacts of climate change and, alarmingly, reduce the probability of switching back to a normal runoff state.

Among basins switching back to predrought conditions, runoff recovery was not simply explained by increased soil moisture or groundwater recharge, as estimated by exploring basin wetness during shifts between multiple states. Hydrological recovery may instead have been driven by complex interactions of vegetation and soil hydraulics, which demands further research.

Although climate shifts are predicted to alter water processes over widespread regions (*8*), the existence of multiple equilibrium points in the water cycle has focused on small subcontinental scales. Positive feedbacks between precipitation and soil moisture have suggested the emergence of preferential states in soil moisture dynamics and the persistence of droughts in the state of Illinois in the United States (*9*).

Bistability was also demonstrated in coupled salt-vegetation dynamics at the basin scale, where gradual changes of salt concentration in irrigation water led to abrupt and irreversible changes in land productivity (*10*). Bistability was also identified in urban settings, where more frequent floods, droughts, population growth, and competition for resources may challenge the resilience of water supply systems and lead worldwide cities toward poverty (*11*).

The conclusion of Peterson *et al.*—that river basins may irreversibly enter a persistent water scarcity state after severe meteorological droughts—challenges the comforting assumption that water systems naturally tend to absorb disturbances. This emphasizes the necessity to change the way global water processes are conceptualized.

Assessing the existence of multiple equilibrium points in a natural water system and accounting for feedback mechanisms will likely help improve understanding of the hydrological response of river basins in drying regions and the development of appropriate water management adaptation strategies to climate change. However, the intrinsic heterogeneity of water systems and the stochastic nature of meteorological forcing (such as temperature, precipitation, and wind) raise questions about the possibility that all river basins have multiple equilibrium points (*12*). Further research is needed to identify the critical tipping points at which river basins switch to alternative states as well as the early warning signals of change in their resilience. This requires long-term monitoring of river basins that not only experience climate disturbances up and beyond critical thresholds but also do not undergo notable land-use change. Unfortunately, screening dynamic water processes is an actual challenge, and substantial limitations in current monitoring systems hamper systematic basin-scale hydrological investigations.

Observations through standard equipment are still inadequate to fully grasp natural processes (*13*). They offer limited spatial coverage and generally involve high maintenance costs, which hinder implementation in many parts of the world, such as remote environments and developing countries (*14*). Although classical hydrological observations have been consistently decreasing worldwide since the 1980s, the recent use of innovative and unintended technology (such as low-cost electronics and participatory sensing) is providing opportunities for sensing the water cycle at even higher spatiotemporal resolutions (*15*). Dense and accurate monitoring of the hydrological response of and within river basins coupled with advanced data interpretation are necessary steps toward disentangling the complex interactions between basin morphological and functional attributes and hydroclimatic drivers in a changing world. ■

Department for Innovation in Biological, Agro-food and Forest Systems, University of Tuscia, Viterbo 01100, Italy. Email: flavia.tauro@unitus.it

REFERENCES AND NOTES

1. M. Scheffer, S. Carpenter, J. A. Foley, C. Folke, B. Walker, *Nature* **413**, 591 (2001).
2. B. Walker, C. S. Holling, S. R. Carpenter, A. Kinzig, *Ecol. Soc.* **9**, (2004).
3. R. M. May, *Nature* **269**, 471 (1977).
4. G. Blöschl *et al.*, *Hydrol. Sci. J.* **64**, 1141 (2019).
5. T. R. Ault, *Science* **368**, 256 (2020).
6. T. J. Peterson, M. Saft, M. C. Peel, A. John, *Science* **372**, 745 (2021).
7. . A. I. J. M. van Dijk *et al.*, *Water Resour. Res.* **49**, 1040 (2013).
8. J. S. Caplan *et al.*, *Sci. Adv.* **5**, eaau6635 (2019).
9. P. D'Odorico, A. Porporato, *Proc. Natl. Acad. Sci. U.S.A.* **101**, 8848 (2004).
10. C. W. Runyan, P. D'Odorico, *Water Resour. Res.* **46**, W11561 (2010).
11. E. H. Krueger *et al.*, *Earths Future* **7**, 1167 (2019).
12. T. J. Peterson, A. W. Western, *Water Resour. Res.* **50**, 2993 (2014).
13. A. K. Mishra, P. Coulibaly, *Rev. Geophys.* **47**, RG2001 (2009).
14. N. van de Giesen, R. Hut, J. Selker, *Wiley Interdiscip. Rev. Water* **1**, 341 (2014).
15. F. Tauro *et al.*, *Hydrol. Sci. J.* **63**, 169 (2018).

10.1126/science.abi8770

EVOLUTIONARY ECOLOGY

The footprint of evolution in seed dispersal interactions

The evolutionary stability of fruit-eating birds is linked to their role in dispersing seeds

By **Carolina Bello**[1] *and* **Elisa Barreto**[1,2]

Mutually beneficial interactions between plants and frugivorous birds have evolved for at least 80 million years (*1*). Now, more than 70% of flowering plants rely on birds to disperse their seeds, and about 56% of bird families consume fruits as part of their diet (*2*, *3*). Plants often have more than one seed disperser, and birds consume different types of fruits from different plant species, thus establishing a complex network of interactions. These networks can change considerably across space and time (*4*). Over short time spans, seed-dispersal interactions are dynamic and change in response to factors such as competition or abundance of the interacting partner (*5*, *6*). However, the effects of evolutionary processes that take place over deep time are not clear (*7*). On page 733 of this issue, Burin *et al.* (*8*) suggest that evolutionary stability is associated with the specific role of the bird species in seed-dispersal networks.

[1]Swiss Federal Research Institute WSL, Zürcherstrasse 111, 8903 Birmensdorf, Switzerland. [2]Laboratório de Ecologia Teórica e Síntese, Universidade Federal de Goiás (UFG), Goiânia, Goiás, Brazil. Email: carolina.bello@wsl.ch

The role of each bird species depends on the number of interactions it establishes with potential partner plant species and how it links different parts of the larger bird-plant network (*9*). These interactions are the result of a set of evolutionary factors, such as coevolution, trait convergence, and diversification (*10*, *11*). Now, Burin *et al.* add one more factor by demonstrating that birds with a central role in a network (that is, they interact with more plants) tend to have greater persistence through evolutionary time. A bird lineage persists longer through time if it has lower extinction rates and/or higher speciation rates, which the authors refer to as "macroevolutionary stability." Having a low extinction rate implies longer longevities through evolutionary time, which in turn facilitates the establishment of more connections within the network because bird species have more time to coevolve with plants, whereas having high speciation rates suggests the accumulation of more sister species that are expected to have similar traits and play similar roles in the network and can therefore act as a replacement if a species goes extinct (see the figure).

Understanding how evolutionary dynamics influence species interactions is a challenge that has persisted for a long time, given the disparity in temporal scale between the observed networks and the macroevolutionary processes. Most studies on the assembly of seed-dispersal networks are centered at ecological time scales—that is, the time of a change in the environment that affects the relationships of organisms with each other (tens to thousands of years). These studies have shown that the cores of seed dispersal networks are stable to annual fluctuations in fruit availability or the presence of specific bird species (*12*). Conversely, studies that focused on evolutionary aspects of seed-dispersal networks (time scale of thousands to millions of years) are primarily centered on reconstructing trait evolution of the interacting species as a proxy to detect coevolution (*13*). Accurately estimating speciation, and particularly extinction rates, from phylogenies composed solely of extant species is still a challenge (*14*, *15*), making it hard to detect the footprint of evolutionary dynamics on species interactions. Although these methods are still controversial, Burin *et al.* take the leap to merge macroevolution and interaction networks and find a consistent and robust effect, even when accounting for the uncertainty of the rate estimates and the phylogenetic hypothesis.

Merging macroevolution and species interactions to understand the historical drivers of network assembly raises new questions in both evolutionary and ecological contexts. The direction and causality between macroevolutionary stability and the central role of a species in a network is still not understood. It is unclear whether bird species that persist over deep time become central in the interaction networks because they had more time to coevolve with the plants or whether bird species

Central to a network and stable over time

Birds disperse the seeds of fruiting plants. These bird-plant interactions form a network that evolves through time. Birds that play a central role in a network (i.e., interact with more plants) persist for longer and/or generate more sister species over deep time. These more evolutionarily stable bird species have a higher probability of being replaced by a sister species if they go extinct. The evolutionary stability of bird species within the network (shown by the color of the bird) is estimated from a phylogenetic tree.

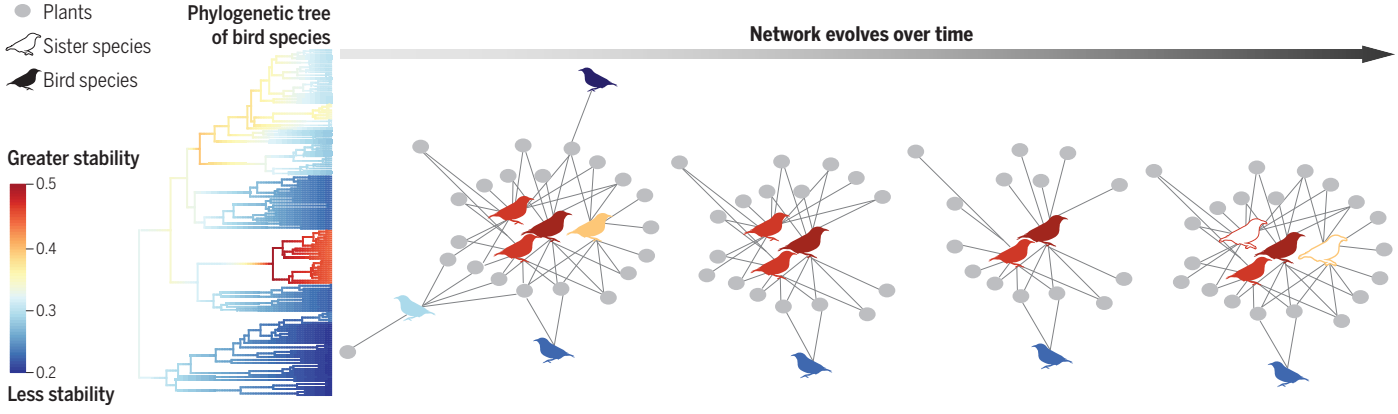

GRAPHIC: N. CARY/*SCIENCE*

with a central role in interaction networks are more resilient to temporal changes in the availability of resources and therefore have greater evolutionary stability. Or is it a combination of the two? Moreover, exploring the processes underlying the relationship between macroevolution and species interactions improves understanding of current ecological processes. For example, it is unknown whether evolutionary stability is related to a species' ability to become invasive, because invasive species generally interact with many species and occupy central positions in the networks. There is also the question of which species traits are related to macroevolutionary stability and a species role in the network. In addition, it is not known whether interactions between species with different rates of speciation and extinction are volatile under new climate scenarios. The findings of Burin *et al.* and open a new avenue for the field of interaction network research. This should help forecast the dynamics of network under new ecological conditions, especially given the current rates of climate change and ecosystem transformation. ■

"...birds with a central role in a network (that is, they interact with more plants) tend to have greater persistence through evolutionary time."

REFERENCES AND NOTES

1. O. Eriksson, *Biol. Rev. Camb. Philos. Soc.* **91**, 168 (2016).
2. T. H. Fleming, W. J. Kress, *Acta Oecol.* **37**, 521 (2011).
3. P. Jordano, in *Seeds: The Ecology of Regeneration in Plant Communities*, M. Fenner, Ed. (CABI, 2000), pp. 125–165.
4. P. J. CaraDonna *et al.*, *Ecol. Lett.* **24**, 149 (2021).
5. B. Rumeu, M. Álvarez-Villanueva, J. M. Arroyo, J. P. González-Varo, *Oecologia* **190**, 605 (2019).
6. D. P. Vázquez *et al.*, *Oikos* **116**, 1120 (2007).
7. P. Jordano, *Evo. Edu. Outreach* **3**, 40 (2010).
8. G. Burin, P. R. Guimarães Jr., T. B. Quental, *Science* **372**, 733 (2021).
9. P. Jordano *et al.*, *Biol. Lett.* **7**, 321 (2011).
10. C. I. Donatti *et al.*, *Ecol. Lett.* **14**, 773 (2011).
11. S. Chamberlain, D. P. Vázquez, L. Carvalheiro, E. Elle, J. C. Vamosi, *J. Ecol.* **102**, 1234 (2014).
12. M. Plein *et al.*, *Ecology* **94**, 1296 (2013).
13. G. Peralta, *Funct. Ecol.* **30**, 1917 (2016).
14. D. L. Rabosky, *Evolution* **64**, 1816 (2010).
15. S. Louca, M. W. Pennell, *Nature* **580**, 502 (2020).

ACKNOWLEDGMENTS

We acknowledge funding from the European Research Council under the European Union's Horizon 2020 research and innovation program (grant 787638) and the Swiss National Science Foundation (grant 173342), both awarded to C. Graham. We thank D. Karger for valuable comments.

10.1126/science.abi8160

IMMUNOLOGY

De-stressing the T cells in need

Protection of transfer RNAs from fragmentation avoids overstressing T cells

By **Zhangli Su** *and* **Anindya Dutta**

When exposed to external antigens, T cells are rapidly activated to proliferate and differentiate. A genetic screen identified a mutation called *elektra* that causes immunodeficiency in mice through a single loss-of-function missense mutation in the Schlafen 2 (*Slfn2*) gene (*1*). *Slfn2* mutation was associated with impaired T cell activation. However, whether *Slfn2* regulates T cell function directly, and how, was unclear. On page 703 of this issue, Yue *et al.* (*2*) report that SLFN2 safeguards T cells from excessive stress during activation and thus facilitates the necessary up-regulation of protein translation. SLFN2 binds and shields transfer RNAs (tRNAs), essential adaptor molecules in translation of messenger RNAs (mRNAs), from stress-activated fragmentation. Without SLFN2, excessive tRNA fragmentation lowers global translation and specifically decreases the translation of key cytokine receptor proteins important for T cell activation. This study expands the role of tRNA fragmentation and implicates SLFN2 in preventing fragmentation to enable immune function.

During T cell activation, quiescent T cells turn on cellular machineries to ramp up metabolism, which demands an increase in protein synthesis. SLFN2 is a member of the Schlafen gene family, mostly present in mammals. The family was first identified in 1998 through the screening of regulators for thymocyte development (*3*). Owing to a lack of homology with other protein families, the functions and mechanisms of action of the Schlafen proteins are still mostly elusive. Yue *et al.* found that signaling in response to the cytokine interleukin-2 (IL-2) was impaired by *Slfn2* deficiency in T cells. IL-2 receptors (IL-2Rs) are expressed on activated T cells, and binding to IL-2 induces gene expression and metabolic programs that are important for T cell activation (*4*, *5*). Expression of IL-2Rβ and IL-2Rγ, but not the IL-2Rα subunit, is decreased, most likely as a result of decreased translation, when *Slfn2* is absent. A global proteomics study showed that translation is highly dynamic during T cell activation, with both rapid turnover of select proteins and idling ribosomes poised for new synthesis (*6*). A similar analysis will clarify which proteins, besides IL-2Rβ and IL-2Rγ, are specifically protected for translation by SLFN2 during T cell activation.

In addition to specific IL-2R proteins, global translation was lowered by *Slfn2* deficiency (*2*). This decrease was observed both in quiescent T cells and after T cell activation. The connection between SLFN2 and translation is perhaps not completely unexpected. Other Schlafen family members, human SLFN11 and SLFN13, can recognize and cleave tRNAs during HIV infection (*7*, *8*). Yue *et al.* find that SLFN2 also binds tRNA. However, unlike SLFN11 and SLFN13, SLFN2 does not cleave tRNAs because of two missing acidic residues important for the ribonuclease (RNase) activity, but instead shields the tRNAs from cleavage into 30- to 40-nucleotide RNA fragments (tRNAs are 79 to 90 nucleotides).

tRNA fragmentation is known to repress global protein translation, repress translation of specific target mRNAs by microRNA-like action, and regulate mRNA stability. tRNA-derived fragments (tRFs), particularly the subclass that is nearly half a tRNA in size, are often generated upon stress and form stress granules, cytoplasmic RNA-protein complexes that repress global translation by sequestering translation initiation factors (*9*). What is causing tRNA cleavage during T cell activation? Paradoxically, rapid T cell proliferation is also accompanied by increased concentrations of reactive oxygen species (ROS). ROS arise as by-products from amplified mitochondrial metabolism and activate important transcription factors during T cell activation (*10*, *11*). However, ROS have other downstream effects during T cell activation: tRNA cleavage, translation inhibition, and stress-granule formation. These stress responses are hyperactivated in *Slfn2*-deficient T cells, despite similar ROS concentrations, suggesting that *Slfn2* deficiency exacerbates ROS sensing. The increased stress response and defective proliferation in *Slfn2*-deficient T cells are counteracted by antioxidant (*N*-acetylcysteine) treatment. Together, this suggests that increased ROS trigger excessive tRNA cleavage and suppress translation in the absence of SLFN2. Thus, SLFN2 sets the threshold for determining whether T cells should proliferate or be inactivated by

Department of Genetics, University of Alabama, Birmingham, AL 35233, USA. Email: duttaa@uab.edu

Protecting T cells from stress

T cell activation is accompanied by increased amounts of reactive oxygen species (ROS). Schlafen 2 (SLFN2) protects transfer RNAs (tRNAs) from ROS-induced cleavage to maintain the increased translation that is necessary for T cell activation. When SLFN2 is absent, this tRNA protection is removed, and T cells are more sensitive to ROS amounts and thus more likely to undergo cell death.

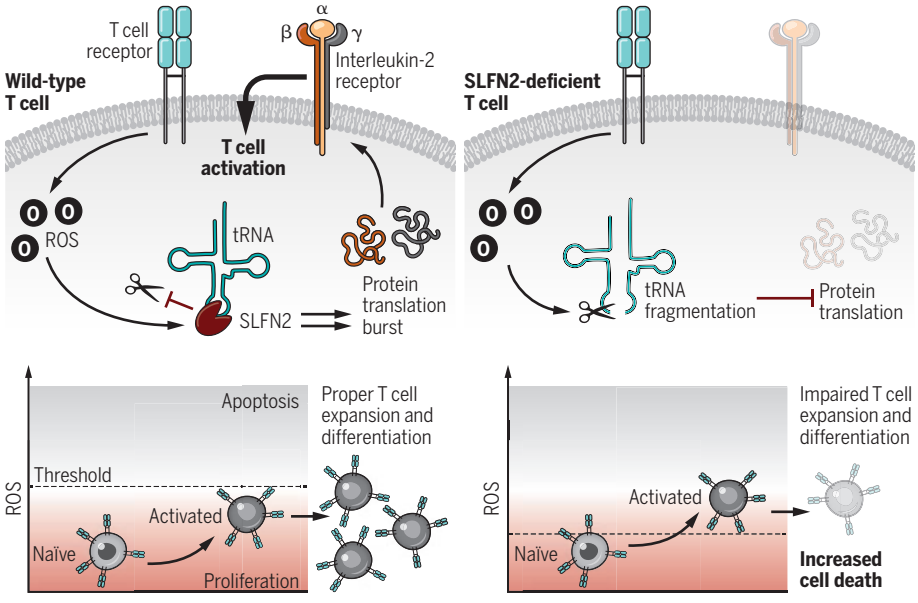

the stress response when the cells recognize antigen (see the figure).

Angiogenin (ANG) is a potent RNase that cleaves the tRNA anticodon loop to produce the half-molecule type of tRFs (*9*). Yue *et al.* found that SLFN2 protects tRNAs from ANG cleavage, and lower ANG expression restored tRNA amounts, protein translation, and cell proliferation of *Slfn2*-deficient T cells. *Ang* mRNA and protein expression are upregulated by T cell activation, which can be reversed by antioxidant. This represents a newly identified mechanism to trigger tRNA cleavage by directly regulating RNase expression. Further investigation is needed to understand whether the tRNA-protective function of SLFN2 also exists in other cell types.

The study by Yue *et al.* reveals an intricate regulation of ROS sensing and translation by SLFN2 during T cell activation. This mechanism may be relevant in autoimmunity because SLFN2 is important in a mouse model of multiple sclerosis (*2*). Notably, Schlafen family functions are not completely understood (*12*). This study opens several future directions in Schlafen family research. Is the regulation of RNA metabolism and translation a common theme of Schlafen function? It is unknown whether Schlafen proteins can bind to (and protect or cleave) other cellular RNAs or viral RNAs. Additionally, whether there is redundancy of function between members of the family awaits further research.

Growing evidence shows that tRNA fragments are not random degradation products, but rather they have biological functions (*9*). Because tRNA fragmentation can repress translation by decreasing the pool of tRNAs, or through direct inhibitory effects of tRNA fragments on the translation machinery through stress-granule formation or microRNA-like action, it will be interesting to determine which mechanism, if not all, are contributing to translation repression in SLFN2-deficient T cells. Additionally, RNases other than ANG mediate tRNA fragmentation (*9*), and in other contexts, tRNA fragments are generated efficiently even after *Ang* deletion (*13*). This suggests that although Yue *et al.* characterize ANG as the major tRNase during T cell activation, the mechanism may be generalizable to other RNases, whose activities could be regulated by other SLFN2-like tRNA-protective proteins in other biological contexts or cell lineages. ■

REFERENCES AND NOTES

1. M. Berger *et al.*, *Nat. Immunol.* **11**, 335 (2010).
2. T. Yue *et al.*, *Science* **372**, aba4220 (2021).
3. D. A. Schwarz *et al.*, *Immunity* **9**, 657 (1998).
4. C. Ye *et al.*, *Signal Transduct. Target. Ther.* **3**, 2 (2018).
5. S. H. Ross, D. A. Cantrell, *Annu. Rev. Immunol.* **36**, 411 (2018).
6. T. Wolf *et al.*, *Nat. Immunol.* **21**, 927 (2020).
7. M. Li *et al.*, *Nature* **491**, 125 (2012).
8. J. Y. Yang *et al.*, *Nat. Commun.* **9**, 1165 (2018).
9. Z. Su *et al.*, *Annu. Rev. Genet.* **54**, 47 (2020).
10. L. A. Sena *et al.*, *Immunity* **38**, 225 (2013).
11. D. G. Franchina *et al.*, *Trends Immunol.* **39**, 489 (2018).
12. E. Mavrommatis, E. N. Fish, L. C. Platanias, *J. Interferon Cytokine Res.* **33**, 206 (2013).
13. Z. Su *et al.*, *J. Biol. Chem.* **294**, 16930 (2019).

ACKNOWLEDGMENTS

Work in the authors' laboratory is supported by R01 AR067712 from the National Institutes of Health.

10.1126/science.abi7265

NEUROSCIENCE

Neurobiology of novelty seeking

Neurons in the subthalamic "zone of uncertainty" assign intrinsic value to novel experiences

By **Zahra Z. Farahbakhsh** *and* **Cody A. Siciliano**

The human brain adapts with experience to learn and motivate future behaviors. But what drives motivation before learning? Attraction to the unknown, or curiosity, is a prerequisite for higher-order knowledge. Innate attraction to novelty is thought to be an evolutionary prerequisite for complex learning and guides organisms toward acquisition of adaptive behavioral repertoires (*1*). Indeed, heightened novelty exploration has been linked with augmented learning rates in mice and humans. Additionally, novel stimuli without any clear rewarding or biologically beneficial attributes can function as positive reinforcers, highlighting their powerful motivational properties (*2*). Heightened novelty-seeking phenotypes are premorbid risk factors for several neuropsychiatric disorders, such as addiction and bipolar disorder (*3*), relationships that are recapitulated in rodent models (*4*). On page 704 of this issue, Ahmadlou *et al.* (*5*) identify a population of neurons in the medial zona incerta (ZIm) that integrates arousal state and familiarity of stimuli in the environment to drive investigation of novelty in mice.

In search of explanations for innate motivations, psychologists at the turn of the 20th century developed methods for quantifying behaviors produced by physiological need states, such as hunger and thirst, in laboratory animals. Later formalized in "drive theory," these studies demonstrated that adaptive behaviors such as exploration and foraging could be predictably evoked regardless of prior experience (*6*). During these early investigations, researchers noted that similar behaviors occurred in novel contexts—for example, if animals were not habituated to the experimental apparatus. Initially noted as a confounding variable in hunger studies

Department of Pharmacology, Vanderbilt Brain Institute, Vanderbilt Center for Addiction Research, Vanderbilt University, Nashville, TN 37232, USA.
Email: cody.siciliano@vanderbilt.edu

GRAPHIC: KELLIE HOLOSKI/*SCIENCE*

(*7*), later work demonstrated that attraction toward novelty can be strong enough to override hunger, thirst, and even pain (*8*, *9*).

Although the underlying psychological constructs are still debated, well-validated procedures have been developed for quantifying novelty-driven behaviors, such as exploratory activity in a novel arena, novelty-induced place preference, and novel-object investigation. Like other motivated behaviors, responses to novelty follow a temporal time course and can be satiated by exposure and augmented by deprivation (*10*, *11*). That said, precisely identifying the neurobiological substrates of novelty-driven behaviors separate from confounding motivational drives poses several challenges, and without tempered interpretation, spurious conclusions are common (*10*). Specifically, the structure of novelty assays makes it difficult to distinguish neural encoding of novelty as opposed to general locomotor activity, goal-based exploration, habituation, and other cooccurring processes (*12*). These limitations have made it difficult to uncover neurobiological substrates with specialized roles in novelty seeking.

Ahmadlou *et al.* used a free-access double-choice task in which mice were placed in an arena with a familiar and a novel object. Objects were sequentially replaced, so that novelty-induced investigation and subsequent habituation was observed many times throughout the session. Video analysis and statistical modeling revealed that animals interacted more with novel stimuli, and with stereotypic action sequences (such as bite, grab, and carry), which diverged on the basis of familiarity. When mice approached and sniffed objects, the probability of subsequently biting was greater when the object was novel, and the sniff-to-bite transition marked the onset of long bouts of continuous investigation. This allowed for interaction bouts to be separated into "deep" investigations, when sniff-bite was the first transition, or "shallow" when it was not. To parse novelty-induced investigation from general locomotion and interactions with familiar objects, the authors probed the neural mechanisms that allow novelty to briefly imbue otherwise neutral stimuli with positive reinforcing properties.

The zona incerta—Latin for "zone of uncertainty"—is a subthalamic nucleus with diverse connectivity throughout the brain and spinal cord that had been largely overlooked until recent years (*13*). Through innovative experiments, Ahmadlou *et al.* found that ZIm γ-aminobutyric acid (GABA) neurons are preferentially activated during deep investigation compared with shallow investigation, and that manipulating these neurons bidirectionally modulated time spent interacting with novel objects. Photoactivation of ZIm GABAergic neurons also acted as a positive reinforcer in an intercranial self-stimulation task, suggesting that endogenous activity observed during deep investigation may drive the reinforcing properties of novel stimuli.

Upstream projections from prelimbic cortex to ZIm were activated during both deep and shallow investigation, and their activity was highly correlated with arousal. Photoactivation of prelimbic inputs increased pupil diameter and downstream activity of GABAergic ZIm neurons, and inhibition of these synapses in ZIm attenuated novel object investigation. Together, this suggests that although prelimbic inputs to ZIm do not distinguish between novel and familiar stimuli, they provide excitatory drive necessary for novelty-induced increases in investigatory behavior. The authors speculate that sensory representations of stimuli converge with arousal-driven activity from prelimbic inputs within the ZIm to augment preference and depth of investigation when the stimulus is novel. They go on to show that modulation of investigation depth is mediated by a subset of ZIm neurons expressing tachykinin-1 (TAC1), a precursor of the neuropeptides substance P and neurokinin A. These TAC1-expressing neurons receive monosynaptic inputs from prelimbic cortex and send output projections to the lateral periaqueductal gray area. This implies a mechanism by which arousal-related information is transferred from cortex to the ZIm, where signals converge with encoding of stimulus features in TAC1^{+} ZIm neurons. In turn, these neuorns provide inhibitory drive to the lateral periaqueductal gray to determine whether a stimulus is treated as novel or familiar (see the figure).

Ahmadlou *et al.* detail a mechanism for assigning intrinsic reinforcing properties to novel stimuli. Further work will be required to understand how upstream sensory inputs identify novelty and how they interact with circuits involved in recall, reward, and fear to drive investigatory decision-making. Probing these systems may clarify the mechanisms that allow novelty encoding to influence learning and other motivated behaviors. The discovery of this cortico-subthalamic-hindbrain circuit may also reveal why novelty-seeking phenotypes confer neuropsychiatric disease vulnerability (*3*, *4*). The field is a step closer to understanding one of the most ubiquitous and influential innate drivers of human and animal behavior. ■

Circuitry involved in novelty-driven investigation

The prelimbic cortex carries motivational and arousal related information to the medial zona incerta (ZIm), which is putatively integrated with information from sensory inputs. Approaching an object or social target leads to activation of tachykinin-1 (TAC1)–expressing neurons in the ZIm, which scales with stimulus novelty. If sufficient activation of TAC1 neurons projecting to the lateral periaqueductal gray is reached, the object is treated as novel and investigated with specific behavioral sequences (sniffing and biting).

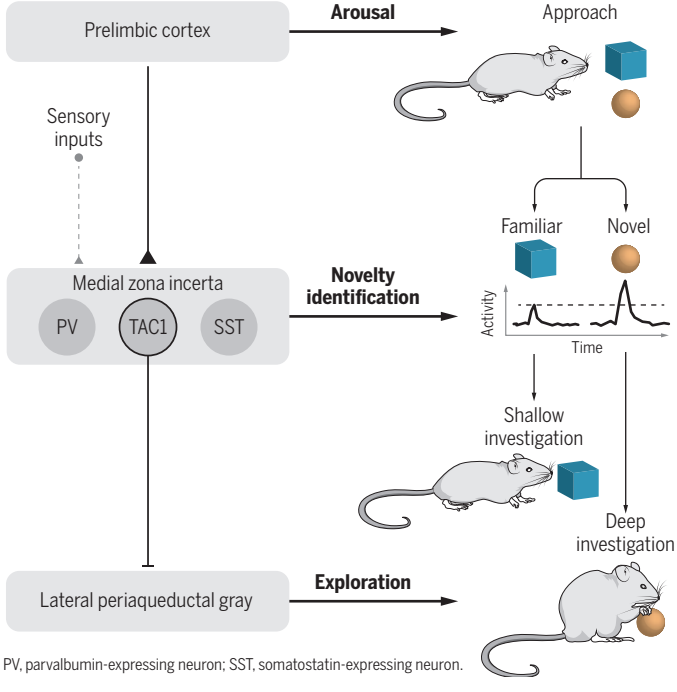

PV, parvalbumin-expressing neuron; SST, somatostatin-expressing neuron.

GRAPHIC: N. DESAI/*SCIENCE*

REFERENCES AND NOTES

1. C. Mettke-Hofmann, H. Winkler, B. Leisler, *Ethology* **108**, 249 (2002).
2. C. M. Olsen, D. G. Winder, *Neuropsychopharmacology* **34**, 1685 (2009).
3. M. Zuckerman, *Behavioral Expressions and Biosocial Bases of Sensation Seeking* (Cambridge Univ. Press, 1994).
4. F. Dellu *et al.*, *Neuropsychobiology* **34**, 136 (1996).
5. M. Ahmadlou *et al.*, *Science* **372**, eabe9681 (2021).
6. C. L. Hull, *Principles of Behavior: An Introduction to Behavior Theory* (D. Appleton-Century Company, 1943).
7. J. F. Dashiell, *J. Comp. Psychol.* **5**, 205 (1925).
8. D. E. Berlyne, *Br. J. Psychol.* **41**, 68 (1950).
9. H. W. Nissen, *Pedagog. Semin. J. Genet. Psychol.* **37**, 361 (1930).
10. A. E. Kelley, *Methods Behav. Pharmacol.* **10**, 499 (1993).
11. R. E. Lubow, A. U. Moore, *J. Comp. Physiol. Psychol.* **52**, 415 (1959).
12. A. S. Lewis, E. S. Calipari, C. A. Siciliano, *eNeuro* ENEURO.0498-20.2021 (2021).
13. A. Forel, *Archiv f. Psychiatrie* (Stuttg.) **7**, 393 (1877).

10.1126/science.abi7270

INFECTIOUS DISEASE

Preventing respiratory syncytial virus (RSV) disease in children

After many decades, promising strategies for RSV immunization are on the horizon

By **Ruth A. Karron**

In 1957, a virus recovered from infants with lower respiratory tract illness (LRTI) was named respiratory syncytial virus (RSV) for its ability to form multinucleated cells (syncytia) in cell culture (*1*). Early epidemiologic studies in high-income countries described the spectrum of RSV disease, including pneumonia, bronchiolitis (a characteristic wheezing LRTI), otitis media (middle ear infection), and apnea (pauses in breathing) in very young infants. Later studies demonstrated that RSV infection causes substantial disease in young children globally and that the burden of RSV in high-income countries is only a small fraction of the global burden. There is an urgent and universal need to develop products to reduce child mortality and morbidity through prevention of RSV disease. Fortunately, substantial progress has been made in the development of several promising RSV vaccines and monoclonal antibodies (mAbs) to achieve this goal.

RSV is the leading cause of hospitalization for pneumonia and other LRTI in young children (*2*). Annual RSV epidemics typically occur seasonally during cooler months in temperate climates but may be nearly year-round in tropical equatorial climates. Approximately 33 million cases of LRTI and up to 59,600 deaths worldwide annually are attributed to RSV, with more than 90% occurring in low- and middle-income countries (*3*). Although very young infants are at increased risk of RSV morbidity and mortality, >80% of RSV-associated LRTI and more than half of RSV deaths occur in children aged 6 months and older (*3*). In addition, RSV infection in infancy may predispose to recurrent wheezing and impaired lung function in early life (*4*).

RSV only became a priority for vaccine development in the 21st century, likely for at least two reasons. Although pneumonia has long been recognized as a major cause of early childhood disease and death, it was only after the widespread deployment of highly effective vaccines for the leading bacterial causes of pneumonia, *Haemophilus influenzae* type B and *Streptococcus pneumoniae*, that RSV was recognized as a leading contributor to the residual childhood pneumonia burden. An even more important obstacle was the legacy of RSV vaccine–associated disease enhancement, which stymied RSV vaccine development for decades.

In the 1960s, Lot 100 formalin-inactivated (FI) RSV vaccine was administered to infants and children at several US trial sites. RSV-experienced children were unaffected, but RSV-naïve children experienced a marked increase in severe disease and hospitalization when they encountered RSV in the winter following vaccination. In one study, 80% of RSV-infected children who had received the FI-RSV vaccine were hospitalized, compared with 5% of RSV-infected children in the control group (*5*). Tragically, a 14-month-old and a 16-month-old died, children who were well outside the age range normally associated with RSV mortality. For the remainder of the 20th century, considerable effort was put into understanding the pathogenesis of this catastrophe, through development of animal models and evaluation of the limited human samples available (*6*). Enhanced RSV disease was associated with high titers of poorly functioning (non-neutralizing) antibodies, T helper 2 (T_H2)–biased $CD4^+$ T cell responses, and immune complex deposition, likely related to the nonfunctional conformation of the fusion (F) protein in the inactivated RSV vaccine (*6*).

From a vaccine development standpoint, the practical consequence of these findings has been to tailor the immunization platform to the target pediatric population, avoiding administration of subunit (nonreplicating protein) vaccines to RSV-naïve infants and children. For infants younger than 4 to 6 months, the goal has been to provide passive immunity, either through direct administration of extended half-life RSV F-specific mAbs or through administration of an RSV F subunit vaccine to pregnant women to promote transplacental transfer of RSV-neutralizing antibodies. For RSV-naïve infants over 6 months and young children, the goal has been to provide active immunity through administration of replicating vectored or live-attenuated vaccines (*7*) (see the figure).

The strategy of protecting young infants against RSV LRTI through delivery of RSV-neutralizing antibodies is rooted in epidemiologic data demonstrating an association between neutralizing antibody titers and protection against RSV LRTI (*8*), and in the development of two products that have protected preterm infants against RSV LRTI: intravenous immunoglobulin containing high titers of RSV-neutralizing antibodies (RSV-IGIV), and an RSV F mAb (palivizumab) with potent neutralizing activity (*9*). Although palivizumab is used in very premature infants in high-income countries, its high cost and the need for monthly dosing have precluded wider use. However, nirsevimab, MK-1654, and RSM-01 are mAbs with modifications to the Fc region to prolong antibody half-life. These extended half-life mAbs have been termed "vaccine-like" because they could be given as a single dose and provide protection for several months. The development of these highly potent next-generation RSV F-specific mAbs, as well as new RSV maternal vaccines, was made possible by a critical advance: determining the crystal structure of the RSV F glycoprotein in its key conformations before and after it mediates viral membrane fusion with host cells (*10*).

RSV F exists in a metastable prefusion (pre-F) conformation and stable postfusion (post-F) state. Triggering of RSV pre-F induces a conformational transition to a stable post-F state; this rearrangement is required to drive viral entry into a target cell (*10*). RSV pre-F contains the six major antigenic sites (∅ through V) that have been mapped to the fusion protein, and most neutralizing activity in human sera is directed toward RSV pre-F (*6*). Nirsevimab, which binds to site ∅, has more than 50-fold greater neutralizing activity than palivizumab. A phase 2B study of nirsevimab in preterm infants demonstrated 70.1% efficacy against all RSV-LRTI and 78.4% efficacy against hospitalization for RSV-LRTI (*11*). These promising results also set expectations for the efficacy of passive immunization against RSV in young infants, whether through mAb administration or maternal immunization. It was recently announced that the phase 3 MELODY trial of nirsevimab in late preterm and full-term infants (NCT03979313) reached its primary endpoint, with significant reduction in LRTI. RSM-01, which is also a site ∅–specific mAb, is expected to enter clinical trials later this year, and MK-1654, a site IV–specific mAb, is currently being evaluated in a phase 1/2 trial in healthy preterm and full-term infants (NCT03524118).

Center for Immunization Research, Department of International Health, Johns Hopkins Bloomberg School of Public Health, Baltimore, MD, USA. Email: rkarron@jhu.edu

Maternal immunization to boost RSV-neutralizing antibodies is an alternative strategy for passive immunization of young infants (see the figure). The largest maternal immunization trial completed to date evaluated the baculovirus-expressed RSV F nanoparticle vaccine in 4636 pregnant women (*12*). The RSV F nanoparticle vaccine does not contain engineered mutations to stabilize the pre-F state and most closely resembles post-F (*7*). The overall efficacy of this vaccine against medically significant RSV LRTI and against RSV hospitalization was 39.4% and 44.4%, respectively (*12*). Although this landmark study failed to meet its primary efficacy endpoint for prevention of RSV LRTI in the first 90 days of life, it provided important lessons to guide subsequent maternal immunization studies with other candidate vaccines. Two RSV maternal vaccines containing engineered stabilized RSV pre-F are in phase 3 clinical development; both induce substantial neutralizing antibodies against RSV. The MATISSE trial of RSVpreF (NCT04424316) began in 2020 and is expected to enroll 6900 pregnant women over several RSV seasons. The GRACE trial of RSVpreF3 (NCT04605159) also began in 2020 and will enroll up to 10,000 pregnant women. In both of these multicountry trials, medically attended or assessed RSV LRTI and severe RSV LRTI in infants up to 6 months of age are primary endpoints.

Based on the outcomes of these trials, countries and funders may ultimately be able to choose between mAb administration and maternal immunization to protect young infants against RSV disease. In addition to the efficacy of individual products, each strategy has potential biologic advantages and disadvantages. mAbs are given directly to infants and would be unaffected by conditions that could influence transplacental antibody transfer (prematurity, HIV infection, hypergammaglobulinemia, administration late in pregnancy). However, mAbs are epitope-specific, and the emergence of escape mutants could threaten efficacy over time. Successful maternal immunization would induce high titers of polyclonal RSV-neutralizing antibodies, which should prevent immune escape, but transfer from mother to infant could be affected by the aforementioned conditions. Duration of protection, cost, and country-specific concerns such as the strength of maternal and neonatal health systems and of the Expanded Program on Immunization platform will also be important considerations.

Passive and active immunization

Immunization against respiratory syncytial virus (RSV) is based on the fusion (F) protein. Young infants can be protected with F-specific antibodies, either administered directly to the infant as monoclonal antibodies (mAbs) or acquired through transplacental transfer from mother to infant following maternal immunization. Older infants and young children will be protected against RSV disease through vaccination with live-attenuated virus or adenoviruses expressing F.

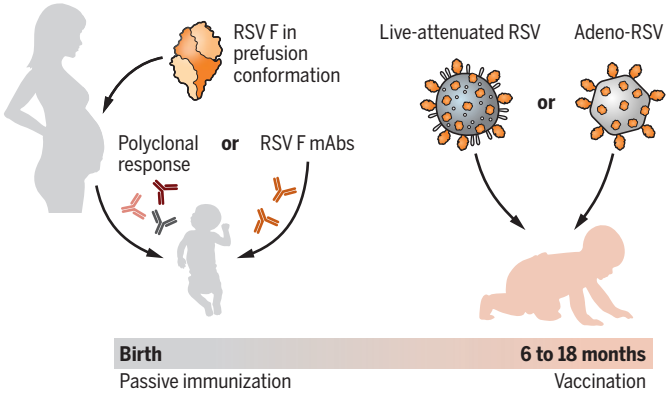

GRAPHIC: KELLIE HOLOSKI/*SCIENCE*

Replicating vaccines for young children should generate immunity in a manner that avoids the aberrant immune response seen with the FI-RSV vaccine. Vectored and live-attenuated vaccines are being evaluated in phase 1/2 clinical trials. These studies typically require sequential evaluation in adults, RSV-experienced (seropositive) young children, and RSV-naïve (seronegative) infants, who are the target population. Vectored vaccines include Sendai virus expressing RSV F, evaluated in adults (NCT03473002), and adenovirus vectors expressing either RSV pre-F (Ad26.RSV.preF), evaluated in RSV-seropositive toddlers (NCT03303625) and now in RSV-seronegative toddlers (NCT03606512), or RSV F, nucleocapsid (N), and the transcription antitermination protein M2-1 (ChAd155-RSV), previously evaluated in toddlers (NCT02927873) and currently in 6- to 7-month-old infants (NCT03636906). Intranasal human parainfluenza virus type 3 (HPIV3) expressing RSV preF could offer protection against both RSV and HPIV3 (*13*) but awaits clinical evaluation.

Live-attenuated intranasal RSV vaccines are likely to induce durable local and systemic immune responses, including B and T cell responses, because they contain internal and surface viral proteins. Codon deoptimization (use of suboptimal codons to decrease gene expression) is one approach to attenuation, and a vaccine candidate with deoptimized expression of the viral interferon antagonists nonstructural protein 1 (NS1) and NS2, RSV G, and deletion of the small hydrophobic (*SH*) gene (MV-012-968 vaccine) was evaluated in adults and will be evaluated in RSV-seropositive children (NCT04444284). An alternative approach has been deletion of *NS1*, *NS2*, or of *M2-2*, which regulates viral RNA synthesis. Several of these vaccines have been evaluated in phase 1 trials in RSV-seronegative infants; the most promising induce durable immunity and prime for potent immune memory responses with substantial increases in neutralizing antibodies after natural exposure to RSV. In a preliminary post hoc pooled analysis, these vaccines protected against any medically attended RSV-associated respiratory illness, as well as RSV-LRTI (*14*). Further development of these vaccines is under way. Other approaches, including messenger RNA (mRNA) vaccines, are in early-stage clinical development.

Advances in structural biology and understanding of gene function have led to substantial progress in RSV vaccine and mAb development. Within the next decade, it is likely that more than one product will be available to protect the youngest infants. The severe acute respiratory syndrome coronavirus 2 (SARS-CoV-2) pandemic created particular challenges for progress during 2020, not least because RSV seasons were nearly absent in some settings (*15*) and markedly shifted in others. However, the high efficacy of SARS-CoV-2 vaccines, combined with the promising preliminary data from RSV products in development (*11, 14*), allows us to imagine similar results for RSV vaccines and mAbs in young children. Ultimately, global and equitable deployment of safe and effective vaccines and mAbs will allow us to fully appreciate and mitigate the burden of RSV disease in children. ■

REFERENCES AND NOTES

1. R. Chanock, L. Finberg, *Am. J. Hyg.* **66**, 291 (1957).
2. PERCH Study Group, *Lancet* **394**, 757 (2019).
3. T. Shi *et al.*, *Lancet* **390**, 946 (2017).
4. H. J. Zar *et al.*, *Lancet Glob. Health* **8**, e1316 (2020).
5. H. W. Kim *et al.*, *Am. J. Epidemiol.* **89**, 422 (1969).
6. T. J. Ruckwardt, K. M. Morabito, B. S. Graham, *Immunity* **51**, 429 (2019).
7. RSV Vaccine and mAb Snapshot, www.path.org/resources/rsv-vaccine-and-mab-snapshot/.
8. W. P. Glezen *et al.*, *Am. J. Dis. Child.* **140**, 543 (1986).
9. The IMpact-RSV study group, *Pediatrics* **102**, 531 (1998).
10. J. S. McLellan *et al.*, *Science* **340**, 1113 (2013).
11. M. P. Griffin *et al.*, *N. Engl. J. Med.* **383**, 415 (2020).
12. S. A. Madhi *et al.*, *N. Engl. J. Med.* **383**, 426 (2020).
13. B. Liang *et al.*, *J. Virol.* **95**, e01512 (2020).
14. R. A. Karron *et al.*, *Am. J. Respir. Crit. Care Med.* **203**, 594 (2021).
15. P. N. Britton *et al.*, *Lancet Child Adolesc. Health* **4**, e42 (2020).

ACKNOWLEDGMENTS

Thoughtful review of the manuscript by A. Moscona and B. Graham is gratefully acknowledged. The author has received funding from the NIH (HHS 272200900010C), Sanofi-Pasteur, and the Bill and Melinda Gates Foundation.

10.1126/science.abf9571

NANOMATERIALS

Is chiral crystal shape inherited or acquired?

Reaction kinetics drives chiral nanocrystal formation from helically bonded tellurium atoms

By **Inna Popov**

A glove fits only one of our hands because the mirror images of gloves (and our hands) cannot be superimposed. Molecules or crystals that have this property are said to be chiral. Since the work of Pasteur on the separation of the sodium ammonium salts of racemic tartaric acid into right- and left-handed crystals (*1*), how and whether molecular chirality is necessary for formation of chiral crystals has been explored. Even atoms such as tellurium (Te) (*2*) can form chiral crystals because their chemical bonding can create helices (see the figure, top) that are right- or left-handed, although such helices can also pack to form achiral crystals. On page 729 of this issue, Ben-Moshe *et al.* (*3*) explored what determines the formation of chiral Te nanocrystals through controlled colloidal synthesis and advanced electron microscopy. Chiral crystals grew at medium supersaturation, apparently driven by screw dislocations in the crystal nuclei.

Although compositionally identical, the chiral forms of the same entity (enantiomers) are dissimilar in that they polarize light in opposite directions (*4*). Most biological molecules are chiral. For reasons yet to be understood, natural amino acids are almost exclusively left-handed, but sugars are right-handed (*5*). The biological activity of enantiomers can differ. Some enantiomers are perceived as different odors (*6*), and for drug molecules, usually only one of several enantiomers is active, and some inactive forms can be unsafe. However, different enantiomers of a chiral molecule spontaneously crystallizing into separate crystals from a racemic mixture, as seen by Pasteur, is rare. Indeed, unlike its salt, the higher melting form of tartaric acid ("racemic acid") grows achiral crystals, with the right- and left-handed molecules packing together (*7*).

Chirality of crystals can also be induced. Amino acid binding induces chirality in the growth of calcite, which has no intrinsic chirality (*8*). Chiral biomolecules can bind as shape-controlling ligands in the reductive synthesis of selenium and Te nanocrystals where the atoms pack helically (*9*). Crystal shape changes (such as twisting) and lattice impurities can be correlated (*10*).

To explore the role of ligands and impurities directing crystallization versus the role of the intrinsically chiral helical atomic arrangement, Ben-Moshe *et al.* prepared Te crystals by reducing its oxide with various amounts of hydrazine in the presence of either chiral L- or D-penicillamine or achiral mercaptopropionic acid. They created and structurally characterized ensembles of 100- to 300-nm size particles (see the figure, middle). Crystals obtained at medium supersaturation (slower kinetics) grew chirally no matter which ligand was used (see the figure, middle), but Te nanocrystals obtained at high supersaturation rate (fast growth) acquired an achiral shape even in the presence of chiral ligands (see the figure, bottom). Ben-Moshe *et al.* that reaction kinetics played a key role and that the intrinsic lattice chirality of Te is only a prerequisite for the chiral morphology.

From helices to crystals

Ben-Moshe *et al.* show that kinetics determines whether chiral tellurium (Te) nanocrystals form.

Right and left helices

The 2. 9-Å long bond in elemental Te forms helices.

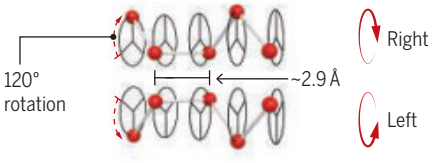

Chiral and achiral crystals

(**Top**) At medium supersaturation (slower kinetics), M (left-handed) and P (right-handed) crystals formed, as assigned by outlined regions. (**Bottom**) Higher supersaturation formed symmetric crystals.

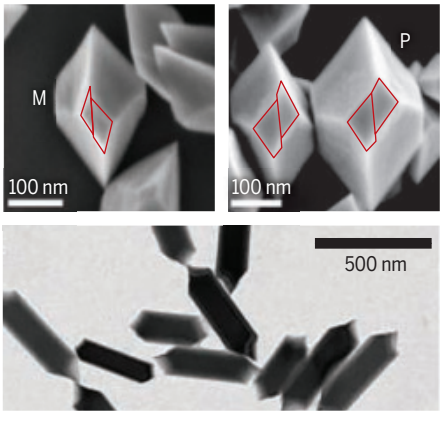

The authors clarified how chiral ligands affect the crystal shape by quantifying morphology in populations of Te nanocrystals grown separately with different ligands. Although equal fractions of each shape's handedness grew with the achiral ligand, the populations grown with the chiral ligand of one handedness contained larger fractions of crystals shaped in the same sense. They conclude that being able to bias the relative abundance of mirror-image chiral ligands is neither necessary nor sufficient for chiral shape formation. For a few nanocrystals, the authors could determine both shape- and lattice-handedness. As in Pasteur's experiments, the crystal lattice and shape had the same chiral sense.

Unlike the achiral shapes, chirally shaped Te crystallites are structurally imperfect. They are twisted, contain voids, and show structural signatures of one-dimensional lattice defects, namely screw dislocations. Ben-Moshe *et al.* suggest that these screw dislocations in the crystal nuclei obtained at medium saturation rates cause chiral crystal shapes, but additional experimental work is needed to prove the mechanism providing.

The study of Ben-Moshe *et al.* of achiral and chiral Te nanocrystals also has potential technological applications. Their systematically planned experiment with a model material allowed them to separate and develop a hierarchy of the factors affecting the crystal shape. This process could be repeated with other materials that possess lattice chirality and used to manufacture enantiopure materials. In the Te system itself, the lattice arrangement in achirally shaped crystals is still unknown and could include atomic helixes of both senses (*7*). It will be of interest to see how each morphology type affects the energy landscape of crystalline Te. ■

The Center for Nanoscience and Nanotechnology, the Hebrew University of Jerusalem, Jerusalem 9190410, Israel. Email: innap@savion.huji.ac.il

REFERENCES AND NOTES

1. L. Pasteur, *Ann. Chim. Phys.* **24**, 442 (1848).
2. B. Escaig, *J. Phys. Colloq.* **35**, C7 (1974).
3. A. Ben-Moshe *et al.*, *Science* **372**, 729 (2021).
4. M. Hentschel *et al.*, *Sci. Adv.* **3**, e1602735 (2017).
5. B. L. Feringa, *Science* **292**, 2021 (2001).
6. L. Friedman, J. G. Miller, *Science* **172**, 1044 (1971).
7. A. Collet, L. Ziminski, C. Garcia, F. Vigne-Maeder, in *Supramolecular Stereochemistry*, J. S. Siegel, Ed. (Kluwer Academic, 1995), pp. 91–110.
8. C. A. Orme *et al.*, *Nature* **411**, 775 (2001).
9. A. Ben-Moshe *et al.*, *Nat. Commun.* **5**, 4302 (2014).
10. A. G. Shtukenberg *et al.*, *Angew. Chem. Int. Ed.* **53**, 672 (2014).

ACKNOWLEDGMENTS

The author acknowledges the financial support of the Hebrew University Center for Nanoscience and Nanotechnology.

10.1126/science.abh1213

GRAPHIC: C. BICKEL/*SCIENCE*; (IMAGES) BEN-MOSHE *ET AL.* (3)

POLICY FORUM

INFECTIOUS DISEASE

A paradigm shift to combat indoor respiratory infection

Building ventilation systems must get much better

By **Lidia Morawska, Joseph Allen, William Bahnfleth, Philomena M. Bluyssen, Atze Boerstra, Giorgio Buonanno, Junji Cao, Stephanie J. Dancer, Andres Floto, Francesco Franchimon, Trisha Greenhalgh, Charles Haworth, Jaap Hogeling, Christina Isaxon, Jose L. Jimenez, Jarek Kurnitski, Yuguo Li, Marcel Loomans, Guy Marks, Linsey C. Marr, Livio Mazzarella, Arsen Krikor Melikov, Shelly Miller, Donald K. Milton, William Nazaroff, Peter V. Nielsen, Catherine Noakes, Jordan Peccia, Kim Prather, Xavier Querol, Chandra Sekhar, Olli Seppänen, Shin-ichi Tanabe, Julian W. Tang, Raymond Tellier, Kwok Wai Tham, Pawel Wargocki, Aneta Wierzbicka, Maosheng Yao**

There is great disparity in the way we think about and address different sources of environmental infection. Governments have for decades promulgated a large amount of legislation and invested heavily in food safety, sanitation, and drinking water for public health purposes. By contrast, airborne pathogens and respiratory infections, whether seasonal influenza or COVID-19, are addressed fairly weakly, if at all, in terms of regulations, standards, and building design and operation, pertaining to the air we breathe. We suggest that the rapid growth in our understanding of the mechanisms behind respiratory infection transmission should drive a paradigm shift in how we view and address the transmission of respiratory infections to protect against unnecessary suffering and economic losses. It starts with a recognition that preventing respiratory infection, like reducing waterborne or foodborne disease, is a tractable problem.

Two factors in particular may contribute to our relatively weak approach to fighting airborne transmission of infectious diseases compared to waterborne and foodborne transmission. First, it is much harder to trace airborne infections. Food and water contamination nearly always come from an easily identifiable point source with a discrete reservoir, such as a pipe, well, or package of food. Its impact on human health is early if not immediate in terms of characteristic signs and symptoms, so that diligent epidemiology can track and identify the source relatively easily. Over the years, this has led to the current public health structures in well-resourced countries. Standards have been enacted for all aspects of food and water processing, as well as wastewater and sewage. Public health officials, environmental health officers, and local councils are trained in surveillance, sampling, and investigation of clusters of potential food and waterborne outbreaks, often alerted by local microbiology laboratories. There are published infection rates for a large range of pathogens, with morbidity and mortality risks now well established. By contrast, airborne studies are much more difficult to conduct because air as a contagion medium is nebulous, widespread, not owned by anybody, and uncontained. Buildings and their airflows are complicated, and measurement methods for such studies are complex and not generally standardized.

"...healthy indoor environments with a substantially reduced pathogen count are essential for public health."

Second, a long-standing misunderstanding and lack of research into airborne transmission of pathogens has negatively affected recognition of the importance of this route (*1*). Most modern building construction has occurred subsequent to a decline in the belief that airborne pathogens are important. Therefore, the design and construction of modern buildings make few if any modifications for this airborne risk (other than for specialized medical, research, or manufacturing facilities, for example). Respiratory outbreaks have been repeatedly "explained away" by invoking droplet transmission or inadequate hand hygiene. For decades, the focus of architects and building engineers was on thermal comfort, odor control, perceived air quality, initial investment cost, energy use, and other performance issues, whereas infection control was neglected. This could in part be based on the lack of perceived risk or on the assumption that there are more important ways to control infectious disease, despite ample evidence that healthy indoor environments with a substantially reduced pathogen count are essential for public health.

It is now known that respiratory infections are caused by pathogens emitted through the nose or mouth of an infected person and transported to a susceptible host. The pathogens are enclosed in fluid-based particles aerosolized from sites in the respiratory tract during respiratory activities such as breathing, speaking, sneezing, and coughing. The particles encompass a wide size range, with most in the range of submicrometers to a few micrometers (*1*).

Although the highest exposure for an individual is when they are in close proximity, community outbreaks for COVID-19 infection in particular most frequently occur at larger distances through inhalation of airborne virus–laden particles in indoor spaces shared with infected individuals (*2*). Such airborne transmission is potentially the dominant mode of transmission of numerous respiratory infections. There is also strong evidence on disease transmission—for example, in restaurants, ships, and schools—suggesting that the way buildings are designed, operated, and maintained influences transmission.

Yet, before COVID-19, to the best of our knowledge, almost no engineering-based measures to limit community respiratory infection transmission had been employed in public buildings (excluding health care facilities) or transport infrastructure anywhere in the world, despite the frequency of such infections and the large health burden and economic losses they cause (*3*). The key engineering measure is ventilation, supported by air filtration and air disinfection (*4*). In this context, ventilation includes a minimum amount of outdoor air combined with recirculated air that is cleaned using effective filtration and disinfection.

VENTILATION OF THE FUTURE

There are ventilation guidelines, standards, and regulations to which architects and building engineers must adhere. Their objectives are to address the issues of odor, and occupant-generated bioeffluents [indicated by the concentrations of occupant-generated carbon dioxide (CO_2)], by specifying minimum ventilation rates and other measures to provide an acceptable indoor air quality (IAQ) for most occu-

Affiliations are listed in the supplementary materials.
Email: l.morawska@qut.edu.au

pants. Similarly, there are other guidelines and regulations to ensure thermal comfort. To achieve this, the amount of outdoor air delivered to indoor spaces is recommended or mandated in terms of set values of air change rate per hour, or liters of air per person per second. Threshold values of CO_2 and a range of indoor air temperatures and relative humidity have also been prescribed.

There are also some health-based indoor air quality guidelines. The most important are the World Health Organization (WHO) IAQ guidelines, providing values for benzene, carbon monoxide, formaldehyde, and other chemicals, based on the duration of exposure (*5*). There are, however, no ventilation guidelines or standards to specifically control the concentration of these pollutants indoors. None of the documents provide recommendations or standards for mitigating bacteria or viruses in indoor air, originating from human respiratory activities. Therefore, it is necessary to reconsider the objective of ventilation to also address air pollutants linked to health effects and airborne pathogens.

One challenge is that ventilation rates required to protect against infection transmission cannot be derived in the same way as rates for other pollutants. First, infection-focused ventilation rates must be risk-based rather than absolute, considering pathogen emission rates and the infectious dose [for which there exist data for a number of diseases, including influenza (*6*), severe acute respiratory syndrome coronavirus (SARS-CoV), Middle East respiratory syndrome, tuberculosis, SARS-CoV-2, and measles]. There is often limited knowledge of viral emission rates, and rates differ depending on the physiology of the respiratory tract (which varies with age, for example), the stage of the disease, and the type of respiratory activity (e.g., speaking, singing, or heavy breathing during exercise). The infectious dose may differ depending on the mode of transmission. This is well established for influenza A, for which the infectious dose is smaller with an aerosol inoculum than with nasal instillation (*7*). Some infectious agents display "anisotropy," in which the severity of disease varies according to the mode of transmission (*7*).

Second, future ventilation systems with higher airflow rates and that distribute clean, disinfected air so that it reaches the breathing zone of occupants must be demand controlled and thus flexible (see the figure). The ventilation rate will differ for different venues according to the activities conducted there (e.g., higher ventilation rates for exercising in gyms than for resting in movie theaters). There are already models enabling assessments of ventilation rates and their effective distribution in the occupant microenvironments (*8*), and in general this is a rapidly expanding field.

Demand control and flexibility are necessary not only to control risk but also to address other requirements, including the control of indoor air pollution originating from inside and outside sources and, especially, to control energy use: Ventilation should be made adequate on demand but not unreasonably high. Buildings consume over one-third of energy globally, much of it expended on heating or cooling outdoor air as it is brought indoors. Therefore, although building designs should optimize indoor environment quality in terms of health and comfort, they should do so in an energy-efficient way in the context of local climate and outdoor air pollution.

Third, in some settings, it will not be possible to increase ventilation to the point of reducing the risk to an acceptable level, regardless of the quality of the ventilation system. This refers to individual risk of infection for each susceptible occupant, to the event reproduction number (the expected number of new infections arising from a single infectious occupant at an event), and to the reality that ventilation has less of an impact for near-field exposure. Management of the event reproduction number is important for the control of an epidemic, especially for indoor spaces with a high density of people, high emission rate (vocalization or exercising), and long periods of shared time. Spaces like this will require air-cleaning measures, including air filtration and disinfection. Air filtration can be achieved by incorporating filters into the building heating, ventilation, and air conditioning system or by portable air cleaners, and air disinfection can be achieved by using ultraviolet devices (*4*) while avoiding unproven technologies. The necessity of such measures and their effective per-person additional removal rate, and thus their efficacy in risk reduction, can be incorporated into risk assessment and prospectively modeled.

None of this means that every indoor space should become a biosafety facility. It means that a building should be designed and operated according to its purpose and the activities conducted there, so that air-

Flexible ventilation systems, dependent on the building's purpose

Ventilation airflow rates must be controlled by the number of occupants in the space and their activity.

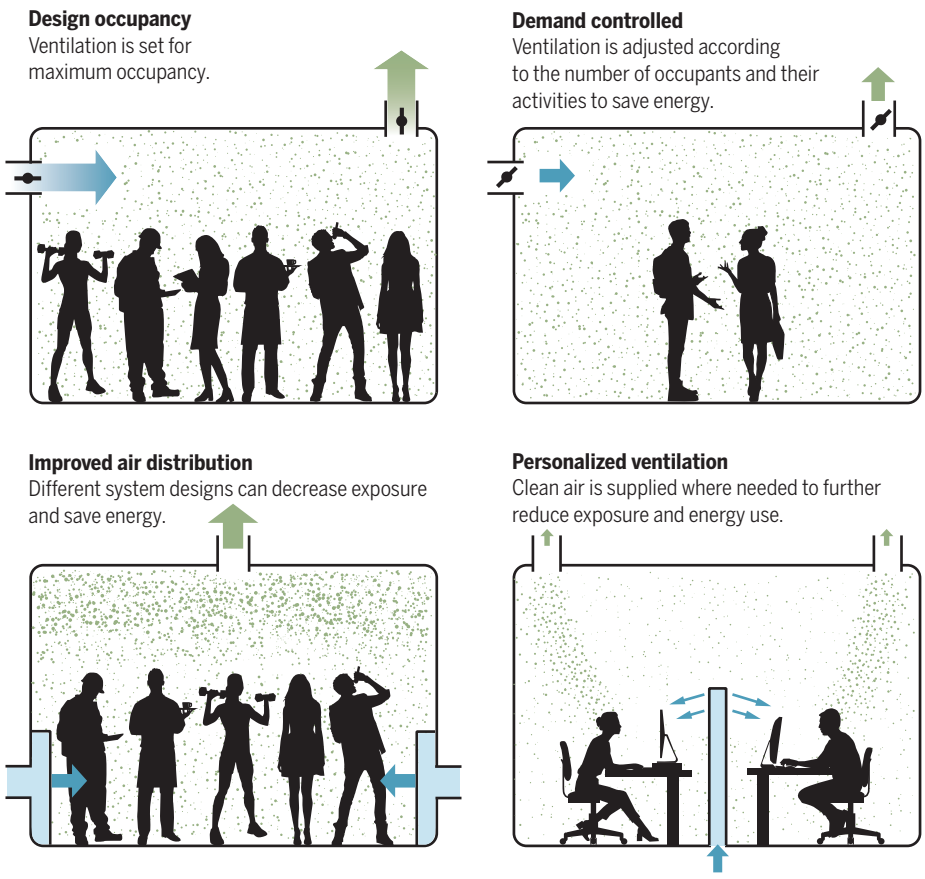

GRAPHIC: N. CARY/*SCIENCE*

borne infection risk is maintained below an acceptable level. Such measures cannot easily be taken during the current pandemic because most building systems have not been designed for limiting respiratory infection, building owners and operators were not trained to operate the systems during the pandemic, and ad hoc measures are often not sufficient. Such training, and appropriate measures, should form a part of national strategies to prevent the spread of airborne diseases and infections.

The only types of public buildings where airborne infection control exists are health care facilities, where requirements for ventilation rates are typically much higher than for other public buildings (*9*). However, although modern hospitals comply with relevant standards set to control infection, this may not always be the case for some hospitals located in very old buildings. Comparing health care ventilation requirements with those for non–health care venues suggests that non–health care rates should be higher for effective infection control or that more recirculation with better filtration should be used.

There needs to be a shift in the perception that we cannot afford the cost of control, because economic costs of infections can be massive and may exceed initial infrastructure costs to contain them. The global monthly harm from COVID-19 has been conservatively assessed at $1 trillion (*10*), but there are massive costs of common respiratory infections as well. In the United States alone, the yearly cost (direct and indirect) of influenza has been calculated at $11.2 billion (*11*); for respiratory infections other than influenza, the yearly cost stood at $40 billion (*12*).

It is not known exactly what fraction of infections could be prevented if all building and transport ventilation systems on the planet were ideal (in terms of controlling airborne infections), or the cost of design and retrofitting to make them ideal. However, the airborne transmission route is potentially the dominant mode of transmission (*1, 2, 13*). Estimates suggest that necessary investments in building systems to address airborne infections would likely result in less than a 1% increase in the construction cost of a typical building (*14*). For the vast inventory of existing buildings, although economic estimations are more complex, there are numerous cost-effective, performance-enhancing solutions to minimize the risk of infection transmission. Although detailed economic analyses remain to be done, the existing evidence suggests that controlling airborne infections can cost society less than it would to bear them.

The costs of infections are paid from different pockets than building and operating costs or health care costs, and there is often resistance to higher initial expenditure. But ultimately, society pays for all the costs, and costs and benefits are never evenly distributed. Investment in one part of the system may generate savings in a different part of the system, so cross-system reallocation of budgets must be facilitated. The benefits extend beyond infectious disease transmission. An improvement in indoor air quality may reduce absenteeism in the workplace from other, noninfectious causes, such as sick building syndrome and allergic reactions, to the extent that the reduction in productivity losses may cover the cost of any ventilation changes.

A PATH FORWARD

We encourage several critical steps. First and foremost, the continuous global hazard of airborne respiratory infection must be recognized so the risk can be controlled. This has not yet been universally accepted, despite strong evidence to support it and no convincing evidence to refute it.

Global WHO IAQ guidelines must be extended to include airborne pathogens and to recognize the need to control the hazard of airborne transmission of respiratory infections. This includes recommendations on preventive measures addressing all modes of respiratory infection transmission in a proper and balanced way, based on state-of-the-art science. The recently published WHO Ventilation Roadmap (*15*) is an important step but falls short of recognizing the hazard of airborne respiratory infection transmission and, in turn, the necessity of risk control.

National comprehensive IAQ standards must be developed, promulgated, and enforced by all countries. Some countries have IAQ standards, but none are comprehensive enough to include airborne pathogens. In most countries that have IAQ standards, there are no enforcement procedures. Most countries do not have any IAQ standards.

Comprehensive ventilation standards must be developed by professional engineering bodies. Organizations such as the American Society of Heating, Refrigerating and Air-Conditioning Engineers and the Federation of European Heating, Ventilation and Air Conditioning Associations have ventilation standards, and during the COVID-19 pandemic, they have proposed building and system-related control actions and design improvements to mitigate risk of infection. However, standards must be improved to explicitly consider infection control in their statements of purpose and definitions. New approaches must be developed to encourage implementation of standards (e.g., "ventilation certificates" similar to those that exist for food hygiene certification for restaurants).

Wide use of monitors displaying the state of IAQ must be mandated. At present, members of the general public are not well aware of the importance of IAQ and have no means of knowing the condition of the indoor spaces that they occupy and share with others. Sensor technologies exist to display numerous parameters characterizing IAQ (most commonly, but not exclusively, CO_2). Existing IAQ sensor technologies have limitations, and more research is needed to develop alternative indicator systems. However, visible displays will help keep building operators accountable for IAQ and will advance public awareness, leading to increased demand for a safe environment.

The COVID-19 pandemic has revealed how unprepared the world was to respond to it, despite the knowledge gained from past pandemics. A paradigm shift is needed on the scale that occurred when Chadwick's *Sanitary Report* in 1842 led the British government to encourage cities to organize clean water supplies and centralized sewage systems. In the 21st century, we need to establish the foundations to ensure that the air in our buildings is clean with a substantially reduced pathogen count, contributing to the building occupants' health, just as we expect for the water coming out of our taps. ■

REFERENCES AND NOTES

1. L. Morawska, D. K. Milton, *Clin. Infect. Dis.* **6**, ciaa939 (2020).
2. M. Kriegel *et al.*, *medRxiv* 10.1101/2020.10.08.20209106 (2020).
3. W. J. Fisk, A. H. Rosenfeld, *Indoor Air* **7**, 158 (1997).
4. L. Morawska *et al.*, *Environ. Int.* **142**, 105832 (2020).
5. WHO, "Guidelines for Indoor Air Quality, Selected Pollutants" (World Health Organization, Geneva, 2010).
6. T. Watanabe, T. A. Bartrand, T. Omura, C. N. Haas, *Risk Anal.* **32**, 555 (2012).
7. R. Tellier, *Emerg. Infect. Dis.* **12**, 1657 (2006).
8. G. Buonanno, L. Morawska, L. Stabile, *Environ. Int.* **145**, 106112 (2020).
9. American Society of Heating, Refrigerating and Air-Conditioning Engineers, "Ventilation of health care facilities: ANSI/ASHRAE/ASHE Standard 170-2021" (2021).
10. J. C. Castillo *et al.*, *Science* **371**, 1107 (2021).
11. W. C. W. S. Putri, D. J. Muscatello, M. S. Stockwell, A. T. Newall, *Vaccine* **36**, 3960 (2018).
12. A. M. Fendrick, A. S. Monto, B. Nightengale, M. Sarnes, *Arch. Intern. Med.* **163**, 487 (2003).
13. T. Greenhalgh *et al.*, *Lancet* (2021). 10.1016/S0140-6736(21)00869-2
14. P. Wargocki *et al.*, "Indoor climate and productivity in offices," REHVA Guidebook (2016).
15. WHO, "Roadmap to improve and ensure good indoor ventilation in the context of COVID-19 (World Health Organization, 2021).

SUPPLEMENTARY MATERIALS

science.sciencemag.org/content/372/6543/689/suppl/DC1

10.1126/science.abg2025

BOOKS *et al.*

FILM

The hunt for habitable planets gets a new tool

A new documentary captures the lead-up to the long-awaited launch of the James Webb telescope

By **Sarah Rugheimer**

Several astronomers confer at the Lick Observatory in a scene from *The Hunt for Planet B*.

When asked if she believes there is life beyond Earth in the new documentary film *The Hunt for Planet B*, American astronomer Jill Tarter, who has dedicated her life to finding signs of intelligence in the cosmos, pointedly replies, "Whatever I think about life beyond Earth doesn't matter a bit…We're not doing religion here, we're doing science." Yet humans have long dreamed of finding another planet like Earth, if only to prove that we are not alone.

The Hunt for Planet B, directed by Nathaniel Kahn, tells the story of the scientists searching for signs of extraterrestrial life and is organized around the building of the NASA-led James Webb Space Telescope (JWST), the high-powered Hubble successor scheduled to launch in late 2021. The film provides a behind-the-scenes view of the technical complexities, personalities, and politics that go into building a multidecade space mission.

In a historically male-dominated field, women are at the forefront of habitable exoplanet research. This film weaves together scenes from their personal and professional lives as they lead this effort. Featured in the film are the mother-daughter astrophysics duo Natalie and Natasha Batalha, who are spearheading efforts to detect habitable worlds and model them; quantum astrochemist Clara Sousa-Silva, who is developing techniques to determine the molecular components of exoplanet atmospheres; and astronomer Sara Seager, who leads a team whose goal is to discover new biosignatures and to build instruments that, for example, help block out a host star's light, helping researchers to see planets of interest. The film even includes glimpses into the researchers' lives outside work. Astronomer Maggie Turnbull paddles her canoe as she discusses the nuances of planetary habitability, while systems engineer Amy Lo, who leads the alignment of the JWST, reveals a passion for race cars.

The Hunt for Planet B
Nathaniel Kahn, director
Crazy Boat Pictures, 2021. 93 min.

The JWST—which is so powerful it could detect from Earth the heat of a bumble bee on the Moon—will allow scientists to look further back in our Universe's history than ever before. Owing to its large size, it will be folded up for launch and unfurled in space, at which time repairs will be impossible. Much like the so-called "7 minutes of terror" experienced by NASA personnel in February 2021 during the Perseverance Mars landing, the JWST crew is in for some tense moments. For them, however, the suspense will last for weeks, as each of the telescope's nearly 400 assembly steps are completed.

The original launch date for the JWST was planned for 2007, but the telescope's complexities have resulted in a number of delays. The film gives viewers a good sense of the frustrations the team has experienced as they worked to overcome new technical challenges, and it successfully conveys the pressure felt by all involved to make sure the $10 billion mission will succeed.

The women and men working on JWST who were interviewed for this film spoke of the call to explore, to be a part of something bigger than what any individual, or even any individual nation, can accomplish. JWST is a multinational effort, a collaboration of the space agencies of the US, Canada, and Europe, and astronomers worldwide are already applying for observing time. This will be the first telescope capable of detecting biosignatures in an exoplanet atmosphere, bringing us one step closer to answering the age-old question "Are we alone in the Universe?" The exoplanet community is excited and prepared.

Near the end of the film, climate activist Greta Thunberg is shown encouraging an audience not to forget about Earth in our haste to find other habitable planets. "We demand a safe future, is that too much to ask?" she implores. For the foreseeable technological future, humans will remain bound to the Solar System. Even Mars, the most habitable planet in our Solar System besides Earth, makes winter in Antarctica look like a summer beach resort.

Still, the prospect of finding life—even microbial life—on another world beckons. Amid a hundred billion galaxies, each with hundreds of billions of stars and planets, it is absurd to think we are alone. ■

The reviewer is at Jesus College, University of Oxford, Oxford OX1 3DW, UK. Email: sarah.rugheimer@physics.ox.ac.uk

10.1126/science.abh3822

PHOTO: COURTESY OF CRAZY BOAT PICTURES

PSYCHOLOGY

Promoting a culture of climate care

Neoliberalism has led to a society impervious to climate reality, argues a psychologist

By **Deborah R. Coen**

Climate scientists have been getting some tough questions lately, not about their data but about their feelings. How does it feel to study such a badly damaged planet? To be condemned by opponents who refuse to engage with the evidence you have put forward? It is not often that scientists are asked to talk about their feelings, but many of those studying climate change seem grateful for opportunities to do so. They have admitted to experiencing anger, frustration, and despair, along with varying degrees of hope.

The psychoanalyst Sally Weintrobe believes that we all need more opportunities to share our feelings about climate change. In *Psychological Roots of the Climate Crisis*, she explores the forces that conspire to distract us from doing so.

Weintrobe's diagnosis centers on neoliberalism, a slippery term that gains contour and traction from her analysis. For Weintrobe, neoliberalism is more than a deregulated form of capitalism—it is a mindset. The problem is not simply that free-market ideologues have captured state power and undermined the authority of science since the 1980s; worse, neoliberalism has invaded the psyches of those living in the global north.

Every human being has both a caring and an uncaring side, Weintrobe explains. When the caring part dominates, the individual manages to rein in unruly desires out of concern for others. Neoliberalism, she argues, feeds the uncaring part of the human psyche and silences the caring part.

The result is a population of what Weintrobe calls "Exceptions," individuals whose sense of entitlement is impervious to reality checks. Exceptions cannot tolerate evidence of their dependence on other people or on the physical environment. They refuse to acknowledge their own vulnerability, so they resort to denial—including the denial of scientific evidence. Like the heroes of Ayn Rand's novels, Exceptions are immune to feelings of concern, guilt, or shame.

Weintrobe backs up these claims with vivid examples drawn from history, fiction, the media, daily life, and clinical practice, presented in short chapters with punchy prose. She shows, for instance, how advertisers have goaded us into seeking fulfillment in unsustainable habits of consumption, from sexy cigarettes to fast cars; they have even borrowed Freud's insights to devise their ruses. She illustrates the predicament of the Exception with a vignette of a patient who believes himself to be perfect yet at night dreams of descending from his home at the top of a high-rise, betraying his desire to regain contact with reality. Her critical eye exposes the subtle machinations of the culture of "uncare," such as the euphemistic language that allows corporations and the press to talk about environmental harms while evading questions of moral responsibility.

What will it take to replace neoliberalism with a culture of care? Government has a large role to play, Weintrobe argues. Genuine democracy and social welfare empower people to care by making them feel cared about. But a transformation is necessary at the individual level as well.

Facing climate reality means owning up to our vulnerability and our dependence on the people and environments we exploit. It means working through the feelings of anxiety and grief that may come with this recognition. Weintrobe argues that a proper culture of care can empower individuals to come to terms with their "inner exception," the part of the psyche that resists unpleasant truths.

Among the signs of an emerging "culture of care," Weintrobe points to a "paradigm shift underway in science." This new science understands "the environment" to be composed of physical, social, and "psychic" systems: "Each requires frameworks of care and sustainable life depends on stability in them all." She points to growing attention to the psychological cost of climate adaptation as one harbinger of this shift.

Beyond attention to mental health, Weintrobe sees potential in scientific approaches that prize humility and a diversity of ways of knowing. She suggests that science might further contribute to the new culture of care by mustering evidence against corporate perpetrators of ecocide, a crime that she suggests should be codified in international law.

Among the lessons Weintrobe's book holds for climate scientists is that human vulnerability to climate change cannot be measured on a simple quantitative scale running from the most vulnerable populations to the most resilient. To be sure, the risks of climate change are distributed highly unevenly, with poor, marginalized communities likely to suffer the worst effects. Yet, for the privileged readers to whom Weintrobe addresses this book, vulnerability is not the opposite of resilience. Rather, feeling vulnerable is the first step toward building sustainable relationships. ■

We must stop thinking of ourselves as "Exceptions," separate from other people and from nature, argues Weintrobe.

PHOTO: CHAN LONG HEI/SOPA IMAGES/LIGHTROCKET VIA GETTY IMAGES

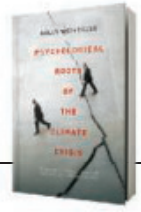

Psychological Roots of the Climate Crisis
Sally Weintrobe
Bloomsbury Academic, 2021. 344 pp.

The reviewer is chair of the Program in the History of Science and Medicine, Yale University, New Haven, CT 06520, USA, and the author of *Climate in Motion: Science, Empire, and the Problem of Scale* (University of Chicago Press, 2018). Email: deborah.coen@yale.edu

10.1126/science.abi7088

LETTERS

Edited by **Jennifer Sills**

Investigate the origins of COVID-19

On 30 December 2019, the Program for Monitoring Emerging Diseases notified the world about a pneumonia of unknown cause in Wuhan, China (*1*). Since then, scientists have made remarkable progress in understanding the causative agent, severe acute respiratory syndrome coronavirus 2 (SARS-CoV-2), its transmission, pathogenesis, and mitigation by vaccines, therapeutics, and non-pharmaceutical interventions. Yet more investigation is still needed to determine the origin of the pandemic. Theories of accidental release from a lab and zoonotic spillover both remain viable. Knowing how COVID-19 emerged is critical for informing global strategies to mitigate the risk of future outbreaks.

In May 2020, the World Health Assembly requested that the World Health Organization (WHO) director-general work closely with partners to determine the origins of SARS-CoV-2 (*2*). In November, the Terms of Reference for a China–WHO joint study were released (*3*). The information, data, and samples for the study's first phase were collected and summarized by the Chinese half of the team; the rest of the team built on this analysis. Although there were no findings in clear support of either a natural spillover or a lab accident, the team assessed a zoonotic spillover from an intermediate host as "likely to very likely," and a laboratory incident as "extremely unlikely" [(*4*), p. 9]. Furthermore, the two theories were not given balanced consideration. Only 4 of the 313 pages of the report and its annexes addressed the possibility of a laboratory accident (*4*). Notably, WHO Director-General Tedros Ghebreyesus commented that the report's consideration of evidence supporting a laboratory accident was insufficient and offered to provide additional resources to fully evaluate the possibility (*5*).

As scientists with relevant expertise, we agree with the WHO director-general (*5*), the United States and 13 other countries (*6*), and the European Union (*7*) that greater clarity about the origins of this pandemic is necessary and feasible to achieve. We must take hypotheses about both natural and laboratory spillovers seriously until we have sufficient data. A proper investigation should be transparent, objective, data-driven, inclusive of broad expertise, subject to independent oversight, and responsibly managed to minimize the impact of conflicts of interest. Public health agencies and research laboratories alike need to open their records to the public. Investigators should document the veracity and provenance of data from which analyses are conducted and conclusions drawn, so that analyses are reproducible by independent experts.

Finally, in this time of unfortunate anti-Asian sentiment in some countries, we note that at the beginning of the pandemic, it was Chinese doctors, scientists, journalists, and citizens who shared with the world crucial information about the spread of the virus—often at great personal cost (*8*, *9*). We should show the same determination in promoting a dispassionate science-based discourse on this difficult but important issue.

Jesse D. Bloom[1,2], Yujia Alina Chan[3], Ralph S. Baric[4], Pamela J. Bjorkman[5], Sarah Cobey[6], Benjamin E. Deverman[3], David N. Fisman[7], Ravindra Gupta[8], Akiko Iwasaki[9,2], Marc Lipsitch[10], Ruslan Medzhitov[9,2], Richard A. Neher[11], Rasmus Nielsen[12], Nick Patterson[13], Tim Stearns[14], Erik van Nimwegen[11], Michael Worobey[15], David A. Relman[16,17]*

[1]Basic Sciences and Computational Biology, Fred Hutchinson Cancer Research Center, Seattle, WA 98109, USA. [2]Howard Hughes Medical Institute, Chevy Chase, MD 20815, USA. [3]Stanley Center for Psychiatric Research, Broad Institute of Massachusetts Institute of Technology and Harvard University, Cambridge, MA 02142, USA. [4]Department of Epidemiology and Department of Microbiology & Immunology, University of North Carolina at Chapel Hill, Chapel Hill, NC 27599, USA. [5]Division of Biology and Biological Engineering, California Institute of Technology, Pasadena, CA 91125, USA. [6]Department of Ecology and Evolution, University of Chicago, Chicago, IL 60637, USA. [7]Dalla Lana School of Public Health, University of Toronto, Toronto, ON M5S 1A8, Canada. [8]Cambridge Institute of Therapeutic Immunology & Infectious Disease, Cambridge, UK. [9]Department of Immunobiology, Yale University School of Medicine, New Haven, CT 06519, USA. [10]Department of Immunology and Infectious Diseases and Center for Communicable Disease Dynamics, Department of Epidemiology, Harvard T. H. Chan School of Public Health, Boston, MA 02115, USA. [11]Biozentrum, University of Basel and Swiss Institute of Bioinformatics, Basel, Switzerland. [12]Department of Integrative Biology and Department of Statistics, University of California, Berkeley, CA 94720, USA. [13]Department of Human Evolutionary Biology, Harvard University, Cambridge, MA 02138, USA. [14]Department of Biology and Department of Genetics, Stanford University, Stanford, CA 94305, USA. [15]Department of Ecology and Evolutionary Biology, University of Arizona, Tucson, AZ 85721, USA. [16]Department of Medicine and Department of Microbiology & Immunology, Stanford University School of Medicine, Stanford, CA 94305, USA. [17]Center for International Security and Cooperation, Stanford University, Stanford, CA 94305, USA.
*Corresponding author. Email: relman@stanford.edu

REFERENCES AND NOTES

1. "Undiagnosed pneumonia—China (Hubei): Request for information," ProMED post (2019); https://promedmail.org/promed-post/?id=6864153.
2. World Health Assembly Resolution 73.1: COVID-19 response (2020); https://apps.who.int/gb/ebwha/pdf_files/WHA73/A73_R1-en.pdf.
3. WHO, "WHO-convened global study of the origins of SARS-CoV-2" (2020); www.who.int/publications/m/item/who-convened-global-study-of-the-origins-of-sars-cov-2.
4. WHO, "WHO-convened global study of origins of SARS-CoV-2: China part" (2021); www.who.int/publications/i/item/who-convened-global-study-of-origins-of-sars-cov-2-china-part.
5. WHO, "WHO director-general's remarks at the Member State Briefing on the report of the international team studying the origins of SARS-CoV-2" (2021); www.who.int/director-general/speeches/detail/who-director-general-s-remarks-at-the-member-state-briefing-on-the-report-of-the-international-team-studying-the-origins-of-sars-cov-2.
6. US Department of State, "Joint statement on the WHO-Convened COVID-19 origins study" (2021); www.state.gov/joint-statement-on-the-who-convened-covid-19-origins-study/.
7. Delegation of the European Union to the UN and other International Organizations in Geneva "EU statement on the WHO-led COVID-19 origins study" (2021); https://eeas.europa.eu/delegations/un-geneva/95960/eu-statement-who-led-covid-19-origins-study_en.
8. J. Hollingsworth, Y. Xiong, "The truthtellers: China created a story of the pandemic. These people revealed details Beijing left out," *CNN* (2021).
9. A. Green, L. Wenliang, *Lancet* **395**, 682 (2020).

10.1126/science.abj0016

PHOTO: MARIO SUAREZ PORRAS/MINDEN PICTURES

Ban veterinary use of diclofenac in Europe

In Europe, vulture recovery has been an important conservation success story (*1*). This success may now be jeopardized by the use of diclofenac in Europe's pastoral landscapes. Although diclofenac had already caused a rapid and catastrophic 95% decline in Asian vulture populations (*2*), the non-steroidal anti-inflammatory drug was approved for veterinary use in Spain in 2013 (*3*). Although measures for the safe disposal of carcasses of livestock treated with diclofenac are supposed to prevent avian scavengers from feeding on contaminated carrion (*4*), a Spanish cinereous vulture (*Aegypius monachus*) was found dead,

A Spanish cinereous vulture (*Aegypius monachus*) was found poisoned by diclofenac in September 2020.

poisoned with diclofenac (*5*), in September 2020. European regulatory authorities should permanently ban diclofenac use in livestock before the tragedy met by Asian vultures repeats itself in Europe.

Vulture breeding populations in Spain represent more than 90% of the total European vulture population (*6*). Diclofenac use in livestock could contribute an additional annual mortality rate of 0.9% to 7.7% in Spanish griffon vultures (*7*). The vulture discovered in September was tracked by GPS tag. Given that untagged birds are harder to find, it is likely that more vultures have been poisoned by diclofenac but have not been found. The genus of the recently discovered bird is also ominous; previous diclofenac deaths have only affected species of the genus *Gyps* (*2*, *8*).

If bold measures are not immediately taken throughout Europe, the consequences for European vultures could be severe. In addition to posing an indirect threat, the legal availability of diclofenac may provide a highly efficient weapon to lawbreakers who wish vultures harm. European and national decision-makers should embrace a precautionary approach that promotes treating livestock with cost-effective, vulture-safe alternatives to diclofenac, such as meloxicam (*9*). These decisions would protect European avian scavengers and align with the new European Green Deal action plan for restoring biodiversity (*10*).

Antoni Margalida[1]*, Rhys E. Green[2], Fernando Hiraldo[3], Guillermo Blanco[4], José A. Sánchez-Zapata[5], Andrea Santangeli[6], Olivier Duriez[7], José A. Donázar[3]

[1]Instituto de Investigación en Recursos Cinegéticos, Consejo Superior de Investigaciones Científicas (CSIC), Universidad de Castilla–La Mancha, E-13005 Ciudad Real, Spain. [2]Department of Zoology, University of Cambridge, Cambridge CB2 3EJ, UK. [3]Estación Biológica de Doñana, CSIC, E-41092 Sevilla, Spain. [4]Museo Nacional de Ciencias Naturales, CSIC, E-28006 Madrid, Spain. [5]Universidad Miguel Hernández, E-03202 Elche, Spain. [6]Research Centre for Ecological Change, Organismal and Evolutionary Biology Research Programme, University of Helsinki, 00014 Helsinki, Finland. [7]Centre d'Ecologie Fonctionnelle et Evolutive, University of Montpellier, Centre National de la Recherche Scientifique, École Pratique des Hautes Études, Institut de Recherche pour le Développement, University of Paul Valéry Montpellier 3, Montpellier, France.
*Corresponding author. Email: a.margalida@csic.es

REFERENCES AND NOTES

1. R. Safford *et al.*, *Bird Conserv. Int.* **29**, 1 (2019).
2. J. L. Oaks *et al.*, *Nature* **427**, 630 (2004).
3. A. Margalida *et al.*, *Science* **346**, 1296 (2014).
4. M. J. I. Chaudhry *et al.*, *Bird Conserv. Int.* **22**, 389 (2012).
5. M. Herrero-Villar *et al.*, *Sci. Tot. Environ.* **782**, 146890 (2021).
6. A. Margalida *et al.*, *J. Appl. Ecol* **47**, 931 (2010).
7. R. E. Green *et al.*, *J. Appl. Ecol.* **53**, 993 (2016).
8. R. E. Green *et al.*, *J. Appl. Ecol.* **41**, 793 (2004).
9. D. Swarup *et al.*, *Anim. Conserv.* **10**, 192 (2007).
10. European Commission, A European Green Deal (https://ec.europa.eu/info/strategy/priorities-2019-2024/european-green-deal_en).

10.1126/science.abj0131

Salmon aquaculture threatens Patagonia

In March, a massive die-off of farmed salmon sent more than 2.2 million kilos of rotting fish biomass into the fjords and channels of the Pacific Patagonian wilderness (*1*), critical areas for biodiversity conservation. The mass mortality event is part of a pattern in which industrial salmon farming increases eutrophication and boosts harmful micro-algae blooms (*2*), which enter gills and suffocate fish (*3*). In turn, decomposition of salmon carcasses leads to increased dissolved organic matter, which, in combination with human-induced ocean warming, facilitates the occurrence of more algal blooms (*4*). With a new constitutional act under discussion, Chile should seize this opportunity to add regulations that will stop the cycle and protect the valuable Patagonian region.

Pacific Patagonia remained mostly pristine until the 1980s (*5*). The region served as one of the last territories of thriving blue whales (*5*) and provided non-breeding habitat for long-distance migratory shorebirds breeding as far away as Alaska (*6*). Salmon aquaculture markedly changed this vast coastal landscape from Chiloé Archipelago to Tierra del Fuego, affecting even remote channels without any previous signs of human activity other than from Indigenous cultures (*7*). Despite repeated warnings regarding socio-environmental impacts (*8*), salmon aquaculture surpassed 1,000,000 tons in 2020 and is now one of the largest economic activities in Chile, the second-largest salmon producer in the world (*9*). In addition to pollution generated by the industry, the regular escape of farmed salmon from broken cages adds non-native mesopredators to food-webs and affects wildlife by transferring aquaculture-associated diseases (*10*) and antibiotic resistant bacteria and genes, which can take hold in wild animals (*11*).

The international community, which serves as the market for Chile's salmon, can leverage its economic power to convince Chile to take action to protect this unique biodiversity hotspot from the environmental effects of salmon aquaculture. Existing government regulations and industry standards must be strengthened. For example, current sustainable aquaculture labelling schemes label some salmon operations as "sustainable" without fully evaluating impacts to wildlife and the surrounding environment (*6*, *11*). The United Nations should push the Chilean government to halt the current expansion of salmon industry toward southern latitudes, especially in the Magallanes region, one of the last bastions of the Patagonian wilderness. Furthermore, a comprehensive monitoring program should be put in place to conduct annual reviews, give

warnings to the industry where necessary, and dismantle aquaculture operations that violate the regulations.

The United Nations should take advantage of the socio-political momentum in Chile. In October 2020, 79% of voters approved the creation of a new constitutional act for Chile, with the potential to address a variety of issues, including a wide range of environmental regulations (*12*). The proposed legislation presents an opportunity to place much-needed limits on aquaculture development. The act will take shape with the input of independent candidates rather than the current parliamentarians and senators who have contributed to the precarious aquaculture cycle. After three decades of salmon industry development, this process could finally lead to policies that protect the Pacific Patagonian wilderness.

Juan G. Navedo[1,2,3]* and Luis Vargas-Chacoff[3,4,5]
[1]Estación Experimental Quempillén (Chiloé), Facultad de Ciencias, Universidad Austral de Chile, Chile. [2]Bird Ecology Lab, Instituto de Ciencias Marinas y Limnológicas, Universidad Austral de Chile, Chile. [3]Instituto de Ciencias Marinas y Limnológicas, Facultad de Ciencias, Universidad Austral de Chile, Casilla 567, Valdivia, Chile. [4]Centro FONDAP de Investigaciones en Dinámica de Ecosistemas Marinos de Altas Latitudes, Universidad Austral de Chile, Casilla 567, Valdivia, Chile. [5]Integrative Biology Group, Universidad Austral de Chile, Valdivia, Chile.
*Corresponding author. Email: jgnavedo@uach.cl

REFERENCES AND NOTES

1. Ecoceános, "Millions of salmon die in a new sanitary-environmental disaster in the fjords and channels of Chiloe and Aysen" (2021); www.ecoceanos.cl/2021/04/millions-of-salmon-die-in-a-new-sanitary-environmental-disaster-in-the-fjords-and-channels-of-chiloe-and-aysen/.
2. C. Folke, N. Kautsky, M. Troell, *J. Environ. Manage.* **40**, 173 (1994).
3. J. León-Muñoz *et al.*, *Sci. Rep.* **8**, 1330 (2018).
4. H. W. Paerl, J. Huisman, *Science* **320**, 57 (2008).
5. R. Hucke-Gaete, P. Lo Moro, J. Ruiz, Eds., "Conservando el mar de Chiloé, Palena y Guaitecas" (Universidad Austral de Chile, 2010) [in Spanish].
6. J. G. Navedo, V. Araya, C. Verdugo, *Sci. Tot. Environ.* **777**, 146004 (2021).
7. P. A. Marquet *et al.*, *Science* **370**, 669 (2021).
8. J. R. Barton, A. Floysand, *Glob. Environ. Chang.* **20**, 739 (2010).
9. Servicio Nacional de Pesca, "Informe sobre uso de antimicrobianos en la salmonicultura nacional: Año 2020" (Gobierno de Chile, 2021) [in Spanish].
10. C. Vargas-Lagos *et al.*, *Fish Shellfish Immunol.* **90**, 1 (2020).
11. F. C. Cabello, H. P. Godfrey, A. H. Buschmann, H. J. Dölz, *Lancet Infect. Dis.* **126**, 127 (2016).
12. Gob.cl, Proceso Constituyente (www.gob.cl/procesoconstituyente/) [in Spanish].

10.1126/science.abj1044

ERRATA

Erratum for the Report "Manta-like planktivorous sharks in Late Cretaceous oceans" by R. Vullo *et al.*, *Science* **372**, eabi9203 (2021). Published online 16 April 2021; 10.1126/science.abi9203

Thank you.

Bruce M. and Betty Alberts

David R. and Patricia D. Atkinson Foundation

Neal Baer, M.D.

Kathleen Stassen Berger

Mani L. Bhaumik

Fred A. and Diane F. Blum

The Boger Family Foundation

Ann and Doug Bostrom

Janet Chen

Keith C. Cheng

Steven and Jean Chu

Mary E. Clutter*

Joyce B. Cowin

Kenneth and Helen Cowin

Elizabeth Crown and Bill Wallace

Roy Curtiss and Josephine Clark-Curtiss

Troy E. and Leslie Daniels

Joseph and Carol Danks

Gary and Denise David

Ken Davis, M.D. and Bonnie Davis, M.D.

The Delta Foundation

Martin Djos Family Foundation

Deborah Donnell

Neil J. Dorans

Elizabeth E. Ehrenfeld

Vincent A. and Marcie Elder

Stephen and Janelle Fodor

Claire M. Fraser

James I. Garrels and Joan E. Brooks

Alison Gopnik and Alvy Ray Smith

Marc Haas Foundation

Benjamin C. and Ruth Hammett

Daniel A. Hitchcock and Linda Arvin

Rush Holt and Margaret Lancefield

Michael W. Hunkapiller

Joan Morthland Hutchins

David W. Ignat

Irving S. and Alwyn N. Johnson*

Sadie E. Kendall

Pauline P. Lee, in memory of Bernard S. Lee

Alan I. and Agnes Leshner

Li Lu Humanitarian Foundation

Robert B. and Bethany Millard

Leo Model Foundation

Gordon E. and Betty I. Moore

Thomas P. and Lydia Moran

Sherie L. and Donald Morrison

Kathryn Murdoch

Edith D. Neimark

Gilbert S. Omenn and Martha A. Darling

Sudip S. Parikh

Bruce B. Parker

Marion B. Patton Trust*

Mark E. Peeples and Rebecca Brumberg Peeples

Daniel Pinkel

Carol Raugust Trust*

William and Eleanor Revelle

Charles M. Rice III

David A. and Janet H. Rice

Juan and Beatriz Roederer

John W. Rowe, M.D.

Sapere Aude Fund

Raymond F. Schinazi

Sara L. Schupf

Bret Snyder

Leslie Sternlieb

David M. Stonner

Holden and Patti Thorp

Daniel and Dianne E. Vapnek

Dan Vickery and Carolyn Myers

Jan and Marica Vilcek

Dyann F. and Peter K. Wirth

Daniel L. Wulff

Philip J. and Carolyn V. Wyatt

Zakaria Family Foundation

These donors' pledges and contributions were received between January 1, 2020 and December 31, 2020.

**Donor is a member of the AAAS 1848 Society. Gift is a bequest through a will or trust.*

The **American Association for the Advancement of Science** gratefully thanks the individuals listed here whose leadership in giving fuels our work on behalf of science and society — including publishing the world's most advanced, innovative research and engaging in the issues that matter locally, nationally and around the world.

To learn more about how a gift to AAAS can advance science and serve society, visit us at **www.aaas.org/support**.

AAAS

AMERICAN ASSOCIATION FOR THE ADVANCEMENT OF SCIENCE

RESEARCH

IN *SCIENCE* JOURNALS

Edited by **Michael Funk**

ATMOSPHERIC CHEMISTRY

Cleaning in a flash

Hydroxyl radicals (OH) are the most important oxidizing species in the atmosphere and provide much of its ability to cleanse itself. It is known that nitric oxide production by lightning leads to the formation of OH and other atmospheric oxidants, such as ozone and hydroperoxyl radicals (HO_2), through a variety of chemical reactions. Brune *et al.* used airborne measurements of OH and HO_2 to show that lightning also produces them directly and in amounts much greater than expected. They found that this mechanism may be responsible for as much as one-sixth of the oxidizing capacity of Earth's atmosphere. —HJS *Science*, this issue p. 711

Lightning generates an abundance of reactive species in the atmosphere.

CELL DIFFERENTIATION

Metabolic pathway regulates cell fate

Lineage-specific regulators direct cell fate decisions, but the precise mechanisms are not well known. Using an in vivo chemical suppressor screen of a bloodless zebrafish mutant, Rossmann *et al.* show that the lineage-specific chromatin factor *tif1*γ directly regulates mitochondrial genes to drive red blood cell differentiation. Loss of *tif1*γ reduces coenzyme Q synthesis and function, impeding mitochondrial respiration and leading to epigenetic alterations and repression of erythropoiesis. The loss of blood in the mutant fish can be rescued by the addition of coenzyme Q. This work establishes a mechanism by which a chromatin factor tunes a metabolic pathway in a tissue-specific manner. —BAP

Science, this issue p. 716

NUCLEAR ASTROPHYSICS

Natural plutonium from supernovae

The rapid neutron capture process (r-process) produces many of the heavy chemical elements, but the astrophysical settings where it occurs remain unclear. Leading candidates are neutron star mergers and some types of supernovae. Wallner *et al*. analyzed the plutonium content of a deep-sea crust sample, identifying a few dozen atoms of the r-process isotope plutonium-244 that were delivered to Earth within the past few million years. There was a simultaneous signal of iron-60, which is known to be produced in supernovae. Comparing the ratios of these isotopes constrains the relative contributions of supernovae and neutron star mergers to r-process nucleosynthesis. —KTS

Science, this issue p. 742

CORONAVIRUS

Kids armed with anti-coronavirus B cells

It remains unclear whether B cell repertoires against coronaviruses and other pathogens differ between adults and children and how important these distinctions are. Yang *et al*. analyzed blood samples from young children and adults, as well as tissues from deceased organ donors, characterizing the B cell receptor (BCR) repertoires specific to six common pathogens and two viruses that they had not seen before: Ebola virus and severe acute respiratory syndrome coronavirus 2 (SARS-CoV-2). Children had higher frequencies of B cells with convergent BCR heavy chains against previously encountered pathogens and higher frequencies of class-switched convergent B cell

PHOTO: A. T. WILLETT/ALAMY STOCK PHOTO

clones against SARS-CoV-2 and related coronaviruses. These findings suggest that encounters with coronaviruses in early life may produce cross-reactive memory B cell populations that contribute to divergent COVID-19 susceptibilities. —STS

Science, this issue p. 738

ALZHEIMER'S DISEASE

Developing an immunotherapy for AD

Hyperphosphorylated tau aggregates contribute to neurodegeneration in patients with Alzheimer's disease (AD), and reducing tau accumulation has had therapeutic effects in preclinical models. Ayalon *et al*. generated and characterized a humanized anti-tau monoclonal antibody called semorinemab, which they tested in mice and nonhuman primates and in a phase 1 clinical trial in humans. Semorinemab was able to bind all six human tau isoforms and had therapeutic effects in vivo in AD mice by reducing tau accumulation. In patients with AD, semorinemab crossed the blood–brain barrier and showed evidence of target engagement without evident side effects. These results support the idea that immunotherapies targeting tau might be effective in reducing tau pathology in AD. —MM

Sci. Transl. Med. **13**, eabb2639 (2021).

MUCOSAL IMMUNOLOGY

Building back colonic crypts

Restoration of the colonic epithelium after mucosal injury depends on cell renewal initiated by intestinal stem cells (ISCs) and their progeny. Stromal cells near the base of colonic crypts secrete trophic factors for ISCs, but regulation of this process by proinflammatory mediators is not well understood. Cox *et al.* used mouse models of pathogen- or chemical-induced epithelial damage to investigate the contribution of interleukin-1 (IL-1) and its receptor (IL-1R1) to epithelial restitution. IL-1 release set off a signaling pathway supporting ISC renewal and proliferation and promoted innate lymphoid cell production of IL-22, a cytokine supporting colonocyte proliferation. These findings illustrate the need to consider the desirable regenerative properties of IL-1 when designing therapeutic approaches for chronic inflammatory diseases. —IRW

Sci. Immunol. **6**, eabe8856 (2021).

PLANT SCIENCE

Computational analysis of cell walls

Layers of intertwined fibers make up plant cell walls. The various types of fibers respond differently to deformation. Cellulose microfibrils, for example, can stretch or curve, changing their end-to-end length, and can also slide past each other, reorient relative directions, and bundle with neighboring microfibrils. Zhang *et al*. developed a computational model based on observations of onion skin epidermis that describes how these complex changes in space govern cell wall mechanics. The results inform ways to engineer multifunctional fibrous materials. —PJH

Science, this issue p. 706

SUPERCONDUCTIVITY

Controlling interfacial superconductivity

The interface between the oxides $LaAlO_3$ and $KTaO_3$(111) has been shown to superconduct at temperatures up to 2 Kelvin. Chen *et al*. show that this superconductivity can be controlled with electric fields. As they tuned the gating voltage, the researchers observed a dome-shaped variation of the superconducting critical temperature. This variation could not be ascribed to the change in carrier density, but rather seemed to reflect the change in the mobility of the carriers. —JS

Science, this issue p. 721

IN OTHER JOURNALS

Edited by **Caroline Ash** *and* **Jesse Smith**

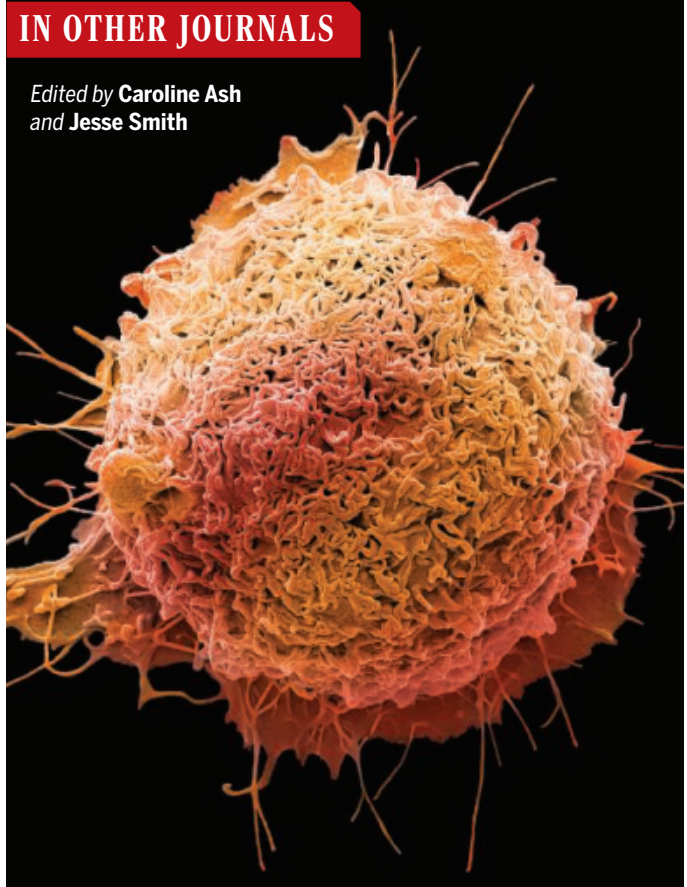

SIGNAL TRANSDUCTION

Imaging cancer cell by cell

Experience in treating colorectal cancer shows that inhibition of the oncogene-activated mitogen-activated protein kinase (MAPK) signaling pathway is often more effective if the activity of the epidermal growth factor receptor, which acts upstream to activate the pathway, is also inhibited. To help clarify how such combined treatment might work, Ponsioen *et al.* used single-cell imaging of activity of the MAPK extracellular signal–regulated kinase (ERK) in patient-derived organoids. Oncogene-induced signaling showed that oscillations in ERK activity were amplified by epidermal growth factor signaling. The results help to explain how improved clinical practices in colorectal cancer treatment have been achieved. —LBR

Nat. Cell Biol. **23**, 377 (2021).

Colored scanning electron micrograph of a colon cancer cell

DNA REPAIR

Costs of moving stem cells

Adult stem cells travel long distances to a wound to repair the damaged tissue. The potential cost of migration has been revealed in in vitro studies of cancer cell lines, dendritic cells, and primary stem cells. If these cells have to squeeze into wounds, then this constriction may cause DNA damage. Sahu *et al.* show that adult stem cells in *Schmidtea mediterranea*, a highly regenerative planarian flatworm, accumulate DNA

IMAGE: STEVE GSCHMEISSNER/SCIENCE SOURCE

A steam-blast (phreatic) eruption from Mount Ontake, Japan

VOLCANOLOGY

A pre-eruptive fever

Determining when volcanoes will erupt is important but difficult and often relies on measuring seismicity or deformation. Girona *et al.* added surface heat to that list, suggesting that a thermal signal precedes eruption by years. The increase in surface heat is subtle and likely due to underground hydrothermal activity, but it also can be detected with satellite observations and may allow early detection for the eruption of different types of volcanoes. This could be particularly important for phreatic eruptions that often occur with little to no warning. —BG

Nat. Geosci. **14**, 238 (2021).

damage as they migrate. The flatworm's stem cells actively repair the migration-inflicted DNA damage en route. The authors propose that during migration, the stem cells go through a "migration-damage-repair-migration" cycle as they home into a wound. —DJ

eLife **10**, e63779 (2021).

NEURODEVELOPMENT

Building bridges in the brain

Some 200 million axons connect the right hemisphere to the left through the brain's corpus callosum. A malformed or absent corpus callosum causes neurological or cognitive deficits. During development, astroglia build a substrate for axons to use in crossing the interhemispheric fissure. Signaling by Netrin 1 (NTN1) and its receptor, Deleted in Colorectal Carcinoma (DCC), guides axons to the midline. Morcom *et al.* show that NTN1 and DCC function even earlier to clear the path by regulating astroglial morphology and function. Without NTN1 and DCC function, astroglia that would normally build bridges across the interhemispheric fissure are unable to do so, and thus axons, no matter how well guided, struggle to build the corpus callosum. —PJH

eLife **10**, e61769 (2021)

ENZYME ENGINEERING

Risk and replacement

Much like the gears and chain of a well-used bicycle, a cell's metabolic enzymes age and collect damage and occasionally suffer catastrophic failure related to use. The rate of replacement required to maintain cellular function is determined by a combination of factors and differs for each enzyme. Hanson *et al*. analyzed protein turnover in bacteria, yeast, and plants and found associations among replacement rate, abundance, and metabolic flux. Up to 50% of metabolic enzymes may undergo self-inflicted, irreversible damage. Studying how to minimize these reactions without reducing activity could yield better catalysts for synthetic biology. —MAF

Proc. Natl. Acad. Sci. U.S.A. **118**, e2023348118 (2021).

AUTOIMMUNE DIVERSITY

Population-level lupus

Autoimmune diseases often show polygenic inheritance, making the identification of potential causal genetic variants difficult, especially across ancestrally divergent populations. Andreoletti *et al.* examined the transcriptomes of bulk immune cells from 120 systematic lupus erythematosus (SLE) patients of Asian and European ancestry. Disease-specific genetic signatures were revealed, as well as ancestrally associated differences in SLE molecular pathways and the role of gene expression variation in disease severity. Because SLE severity differs among populations, this study highlights the need to examine disease genetics in multiethnic cohorts for underlying differences and to explore the clinical treatment options for individuals of differing ancestries. —LMZ

Commun. Biol. **4**, 488 (2021).

MAGNETISM

A twist on the Ising model

The material $CoNb_2O_6$ contains loosely bound zigzag chains of magnetic cobalt ions and is considered to be a model system for the so-called one-dimensional transverse field Ising model (TFIM). In this iconic model of quantum criticality, a string of particles with spin ½ orders with all of the spins pointing in the same direction, this ferromagnetic state melts at a critical value of an external transverse magnetic field. Morris *et al.* re-examined the applicability of this model to $CoNb_2O_6$ using time–domain terahertz spectroscopy and found that some of their results could not be explained by TFIM. Instead, the data fit what the authors dubbed a twisted Kitaev chain model, in which the Ising direction alternates along the chain. —JS

Nat. Phys. 10.1038/s41567-021-01208-0 (2021).

PHOTO: AP PHOTO/KYODO NEWS

REVIEW SUMMARY

ORGANIC CHEMISTRY

Arene diversification through distal C(sp^2)–H functionalization

Uttam Dutta†, Sudip Maiti†, Trisha Bhattacharya, Debabrata Maiti*

BACKGROUND: Organic synthetic chemistry has facilitated the production of medicines, agrochemicals, food, polymers, dyes, and more through step- and atom-economical pathways. Most of these value-added products consist of complex molecular frameworks that can be constructed from simple starting materials by either functional group interconversion or installation of new functionality or coupling units. Incorporation of new functionality through direct replacement of a C–H bond, the most common constituent of organic molecules, has emerged as an attractive synthetic tool, particularly for its atom economy. However, to be useful, the process has to be highly regioselective to avoid costly time- and energy-intensive separations of similar product isomers.

For aromatic and heteroaromatic ring substrates, regioselective C–H functionalization implies the installation of a functional group selectively at *ortho*-, *meta*-, or *para*-positions one, two, or three carbons away from a substituent that is already present. Traditional approaches to achieving this goal have relied on subtle reactivity differences arising from steric and electronic effects associated with each substituent. Although electronically controlled C–H functionalization of arenes by Friedel-Crafts reactions has been known for over a century, such methods often suffer from poor selectivity and limited substrate scope. A quest to find a putative reaction path that would override intrinsic electronic or steric bias is therefore an active research area. In the last three decades, there have been notable advances in the realm of proximal *ortho*-C–H functionalization with the assistance of a coordinating directing group. However, accessing distal *meta*- and *para*-C–H functionalization of electronically and sterically unbiased arenes remained elusive until much more recently. The development of suitable synthetic methods that enable distal *meta*- or *para*-C–H functionalization with prominent selectivity remains an active challenge for researchers in the synthetic chemistry field.

ADVANCES: Steric and/or electronic influences can be manipulated through the design of suitable catalysts, ligands, or reagents that alter the traditional patterns of regioselectivity. Several approaches have been implemented in the past decade for the selective functionalization of *meta* and *para*-C–H bonds along these lines. These include (i) σ-bond activation–assisted remote C–H functionalization, in which initial ortho-cycloruthenation plays a crucial role; (ii) template-assisted remote C–H functionalization; (iii) the use of a bifunctional template for remote C–H activation of heteroarenes; and (iv) remote C–H functionalization enabled by noncovalent interactions such as ion pairing and hydrogen bonding. Pairing palladium with a transient mediator in conjunction with a precise directing group has also emerged as a viable approach. Finally, nondirected remote C–H activation protocols that rely on cooperative catalysis, ligand, or reagent control of regioselectivity have been reported.

OUTLOOK: Emergence of the aforementioned distal C–H functionalization techniques has recast numerous synthetic routes to producing value-added chemicals. One of the major challenges associated with increasing the practicality of this chemistry is to discover more environmentally benign, cost-effective, scalable, and sustainable catalytic systems with very high turnover number. Expanding the catalytic toolbox in this fashion will enable the synthetic modification of hitherto inaccessible sites of organic molecules and enhance the discovery and manufacture of pharmaceuticals, agrochemicals, and other desired materials. ■

Indian Institute of Technology Bombay, Powai, Mumbai 400076, India.
†These authors contributed equally to this work.
*Corresponding author. Email: dmaiti@iitb.ac.in
Cite this article as U. Dutta *et al.*, *Science* **372**, eabd5992 (2021). DOI: 10.1126/science.abd5992

READ THE FULL ARTICLE AT
https://doi.org/10.1126/science.abd5992

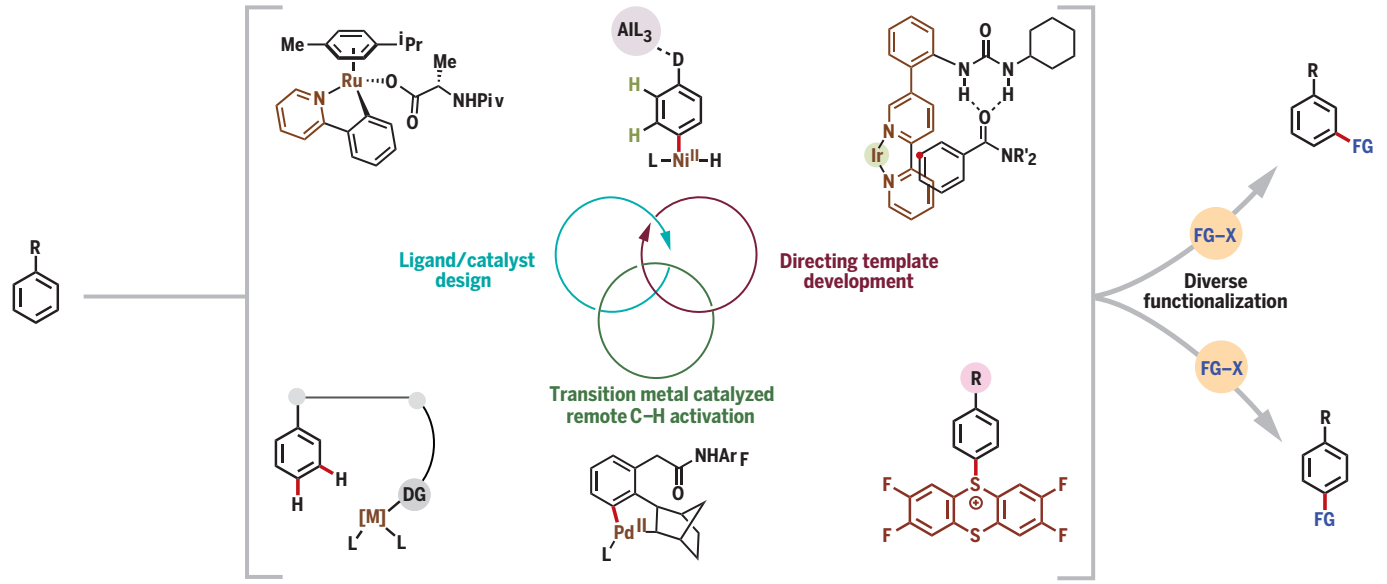

Distal C–H functionalization of arenes. Transition metal catalysts paired with an optimal ligand, directing group (DG), and/or mediator can add a functional group (FG) two or three carbons away from an existing group (R) on an aryl ring.

RESEARCH ARTICLE SUMMARY

CANCER GENOMICS

A prometastatic splicing program regulated by SNRPA1 interactions with structured RNA elements

Lisa Fish†, Matvei Khoroshkin†, Albertas Navickas†, Kristle Garcia, Bruce Culbertson, Benjamin Hänisch, Steven Zhang, Hoang C. B. Nguyen, Larisa M. Soto, Maria Dermit, Faraz K. Mardakheh, Henrik Molina, Claudio Alarcón, Hamed S. Najafabadi, Hani Goodarzi*

INTRODUCTION: Alternative splicing is a post-transcriptional regulatory mechanism critical for transcriptome and proteome diversity. By increasing complexity at the protein level, alternative splicing can induce functional changes in the cell. It is well established that RNA structural elements play a critical role in post-transcriptional regulatory processes, including alternative splicing. Therefore, the role of regulatory information encoded by RNA secondary structure that governs alternative splicing decisions is of particular interest. Changes in alternative splicing patterns have been shown to govern cancer progression and metastasis, and therefore drivers of this process are of clinical interest.

RATIONALE: Pathological changes in alternative splicing patterns are considered a hallmark of cancer, yet the underlying regulatory programs that control this process remain largely unknown. A major obstacle to better understanding these programs is that the bioinformatic strategies commonly used for the discovery of cis-regulatory elements fail to capture the contribution of RNA secondary structure to regulatory information. To address this, we had previously developed the computational framework TEISER (Tool for Eliciting Informative Structural Elements in RNA), which uses both RNA structural and sequence information to identify cis-regulatory elements that are informative of transcriptomic changes. Here, we introduce pyTEISER (pythonic TEISER), which incorporates experimentally derived and additional computationally predicted RNA structural information to investigate the RNA sequence and structural code that governs a broader range of RNA-related processes, including splicing and RNA processing, in addition to steady-state gene expression.

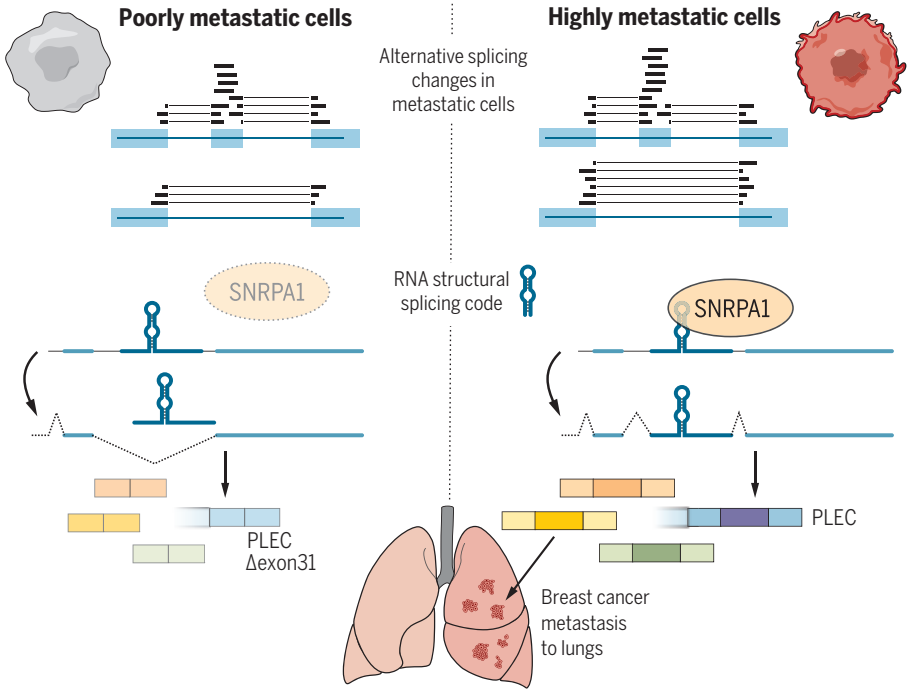

SNRPA1 uses an RNA structural code to drive a prometastatic alternative splicing program in breast cancer. Higher SNRPA1 expression in highly metastatic breast cancer cell lines and clinical samples increases the retention of a set of alternative cassette exons, driven by SNRPA1-associated structural splicing enhancer elements. PLEC is a functional target of SNRPA1, whose rod domain–containing isoform increases cancer cell invasion and promotes metastasis.

RESULTS: By applying pyTEISER to data from cell line and patient-derived xenograft models of breast cancer metastasis, as well as measurements in matched clinical samples from primary breast tumors and metastases, we have discovered and functionally characterized a previously unknown RNA structural element that acts as a splicing enhancer. We find that this structural element drives aberrant alternative splicing in highly metastatic breast cancer, and that the RNA-binding protein SNRPA1 (small nuclear ribonucleoprotein polypeptide A′) mediates this alternative splicing pathway through direct interactions with these structural elements, which we have named SNRPA1-associated structural splicing enhancers (S3Es). These elements are located near cassette exons that exhibit increased inclusion in cells with higher SNRPA1 expression. While SNRPA1 is a core component of the U2 snRNP, we provide evidence that SNRPA1 modulates the splicing of S3E-containing exons independently of its spliceosomal function. We identify the functional sequence and structure requirements for SNRPA1-S3E interactions in vitro and in vivo and demonstrate that this previously unknown SNRPA1-S3E regulatory pathway is up-regulated in highly metastatic breast cancer cells. We show that modulating SNRPA1 expression has a significant effect on the metastatic capacity of breast cancer cells by affecting their invasiveness. In contrast, SNRPA1 expression levels are not associated with changes in cell proliferation or primary tumor growth. Importantly, we identify *PLEC* as a target of SNRPA1-mediated alternative splicing and find that this SNRPA1-regulated alternatively spliced plectin isoform is also up-regulated in metastatic tumors. We show that correction of *PLEC* splicing using antisense morpholinos can reduce the metastatic capacity of breast cancer cells by down-regulating their invasiveness.

CONCLUSION: Our results establish a non-canonical function for SNRPA1 and a previously unknown RNA structural code that regulates alternative splicing, and we find that this SNRPA1-mediated pathway acts as a promoter of breast cancer metastasis. ■

The list of author affiliations is available in the full article online.
†These authors contributed equally to this work.
*Corresponding author. Email: hani.goodarzi@ucsf.edu
Cite this article as L. Fish *et al.*, *Science* **372**, eabc7531 (2021). DOI: 10.1126/science.abc7531

READ THE FULL ARTICLE AT
https://doi.org/10.1126/science.abc7531

RESEARCH ARTICLE SUMMARY

IMMUNOLOGY

SLFN2 protection of tRNAs from stress-induced cleavage is essential for T cell–mediated immunity

Tao Yue, Xiaoming Zhan, Duanwu Zhang, Ruchi Jain, Kuan-wen Wang, Jin Huk Choi, Takuma Misawa, Lijing Su, Jiexia Quan, Sara Hildebrand, Darui Xu, Xiaohong Li, Emre Turer, Lei Sun, Eva Marie Y. Moresco, Bruce Beutler*

INTRODUCTION: Naïve T cells activated by cognate antigens and costimulation proliferate and differentiate to effector T cells. The shift from a resting to a proliferative state entails profound changes in cellular metabolism, in particular increases in glycolysis, glutaminolysis, and mitochondrial metabolism, to produce high levels of adenosine 5′-triphosphate (ATP). T cells depend on a translational burst to produce the metabolic enzymes that support an increase in metabolism and to produce the protein components of clonal T cell progeny and their cytokines. Paradoxically, the metabolic processes that provide energy for growth and expansion also produce reactive oxygen species (ROS). These are capable of inducing oxidative stress, which leads to the repression of translation. On the other hand, ROS function as second messengers in T cell receptor (TCR) signaling and are essential for proliferation and development of effector function. This suggests that to preserve the signaling activities of ROS, protective mechanisms against oxidative stress may occur at multiple levels beyond simply reducing ROS levels in T cells.

RATIONALE: From a mouse-forward genetic screen for mutations affecting immunity, we previously identified a recessive mutation in the Schlafen 2 (*Slfn2*) gene, which leads to elevated susceptibility to bacterial and viral infections and to diminished numbers of T cells that failed to proliferate in response to infection and diverse proliferative stimuli. Here, we aimed to investigate the molecular function of SLFN2 in T cells by generating mice with a T cell–specific deletion of *Slfn2*.

RESULTS: T cell–specific SLFN2-deficient mice displayed compromised humoral and cellular immune responses to immunization with a T cell–dependent antigen and to infection with mouse cytomegalovirus, respectively. These defects stemmed from impaired $CD4^+$ and $CD8^+$ T cell proliferative responses to TCR stimulation, despite normal induction of TCR signaling events in SLFN2-deficient T cells. Interleukin-2 (IL-2) production by SLFN2-deficient T cells was normal after TCR stimulation, but these cells failed to proliferate in response to exogenous IL-2, which suggests that interleukin-2 receptor (IL-2R) signaling was defective. The abrogation of the mitogenic effects of IL-2 was a result of a failure to translationally up-regulate the β and γ chains of the IL-2 receptor. There was a globally dampened translational response to TCR activation in SLFN2-deficient T cells both in vitro and in vivo.

The cellular oxidative stress response includes translation repression by transfer RNA (tRNA) fragments generated by angiogenin (ANG), a stress-induced tRNA-directed ribonuclease (RNase). ANG cleaves tRNAs within their anticodon loops, yielding 30- to 40-nucleotide tRNA fragments (tiRNAs). In response to TCR activation, SLFN2-deficient T cells accumulated tiRNA, which could be reduced by antioxidant treatment or by knockdown or inhibition of ANG. Moreover, global translation rates in activated SLFN2-deficient T cells could be rescued by antioxidant treatment or by ANG knockdown. SLFN2 directly bound to tRNAs, but it exerted no nucleolytic activity toward them, unlike other SLFN proteins. Binding of SLFN2 to tRNAs blocked tRNA cleavage by ANG, thereby averting tiRNA accumulation and tiRNA-mediated translation repression.

CONCLUSION: We describe a protective mechanism by which SLFN2 shields tRNA from oxidative stress–induced cleavage, thereby preventing the translation inhibitory effects of ROS produced in response to T cell activation. Notably, SLFN2 acts downstream of ROS production itself, leaving ROS functions in T cell metabolism and signaling intact. We identify ANG as a stress-activated RNase whose effects are opposed by SLFN2 in T cells. Our data provide further support for a key role of SLFN family members in the regulation of RNA and translation. ■

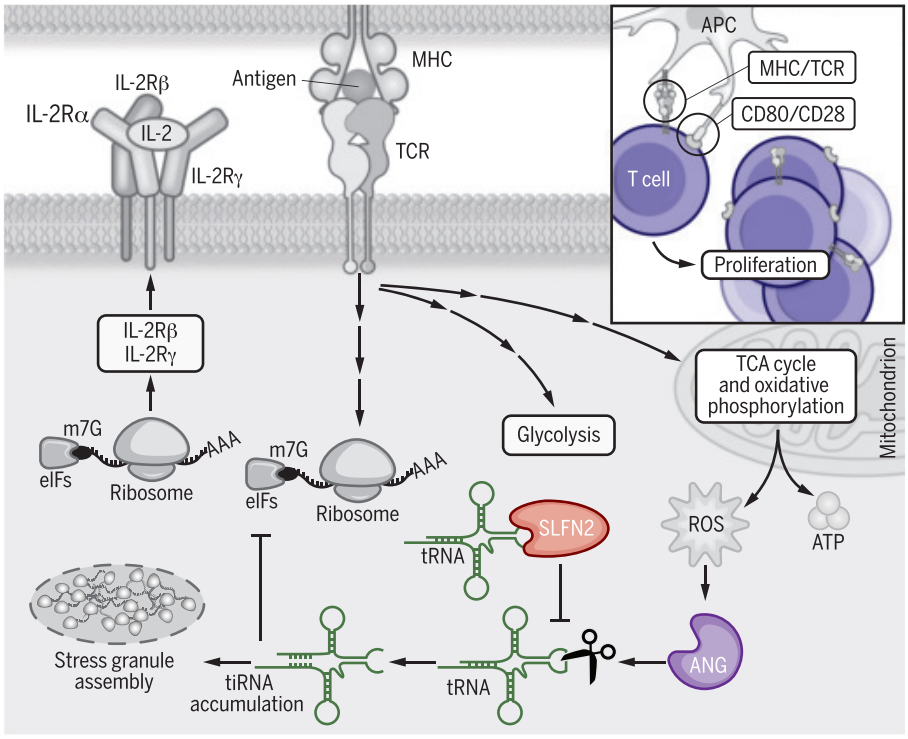

SLFN2 protects tRNA from oxidative stress–induced cleavage, precluding translation inhibition by tRNA fragments (tiRNA). T cell–specific SLFN2 deficiency results in excessive tRNA cleavage mediated by the oxidative stress–activated ribonuclease ANG during the metabolic reprograming phase of activated T cells. Accumulated tiRNA promotes stress-granule assembly and inhibits translation by displacing eukaryotic initiation factors (eIFs) from mRNA. SLFN2-deficient T cells fail to translationally up-regulate IL-2Rβ and IL-2Rγ. MHC, major histocompatibility complex; APC, antigen-presenting cell; TCA, tricarboxylic acid.

The list of author affiliations is available in the full article online.
*Corresponding author. Email: bruce.beutler@utsouthwestern.edu
Cite this article as T. Yue *et al.*, *Science* **372**, eaba4220 (2021). DOI: 10.1126/science.aba4220

READ THE FULL ARTICLE AT
https://doi.org/10.1126/science.aba4220

RESEARCH ARTICLE SUMMARY

NEUROSCIENCE

A cell type–specific cortico-subcortical brain circuit for investigatory and novelty-seeking behavior

Mehran Ahmadlou*, Janou H. W. Houba, Jacqueline F. M. van Vierbergen, Maria Giannouli, Geoffrey-Alexander Gimenez, Christiaan van Weeghel, Maryam Darbanfouladi, Maryam Yasamin Shirazi, Julia Dziubek, Mejdy Kacem, Fred de Winter, J. Alexander Heimel*

INTRODUCTION: Motivational drives are internal states that can be different even in similar interactions with external stimuli. Curiosity as the motivational drive for novelty-seeking and investigating the surrounding environment is for survival as essential and intrinsic as hunger. Curiosity, hunger, and appetitive aggression drive three different goal-directed behaviors—novelty seeking, food eating, and hunting—but these behaviors are composed of similar actions in animals. This similarity of actions has made it challenging to study novelty seeking and distinguish it from eating and hunting in nonarticulating animals. The brain mechanisms underlying this basic survival drive, curiosity, and novelty-seeking behavior have remained unclear.

RATIONALE: In spite of having well-developed techniques to study mouse brain circuits, there are many controversial and different results in the field of motivational behavior. This has left the functions of motivational brain regions such as the zona incerta (ZI) still uncertain. Not having a transparent, nonreinforced, and easily replicable paradigm is one of the main causes of this uncertainty. Therefore, we chose a simple solution to conduct our research: giving the mouse freedom to choose what it wants—double free-access choice. By examining mice in an experimental battery of object free-access double-choice (FADC) and social interaction tests—using optogenetics, chemogenetics, calcium fiber photometry, multichannel recording electrophysiology, and multicolor mRNA in situ hybridization—we uncovered a cell type–specific cortico-subcortical brain circuit of the curiosity and novelty-seeking behavior.

RESULTS: We analyzed the transitions within action sequences in object FADC and social interaction tests. Frequency and hidden Markov model analyses showed that mice choose different action sequences in interaction with novel objects and in early periods of interaction with novel conspecifics compared with interaction with familiar objects or later periods of interaction with conspecifics, which we categorized as deep and shallow investigation, respectively. This finding helped us to define a measure of depth of investigation that indicates how much a mouse prefers deep over shallow investigation and reflects the mouse's motivational level to investigate, regardless of total duration of investigation.

Optogenetic activation of inhibitory neurons in medial ZI (ZIm), ZIm^{GAD2} neurons, showed a dramatic increase in positive arousal level, depth of investigation, and duration of interaction with conspecifics and novel objects compared with familiar objects, crickets, and food. Optogenetic or chemogenetic deactivation of these neurons decreased depth and duration of investigation. Moreover, we found that ZIm^{GAD2} neurons are more active during deep investigation as compared with during shallow investigation.

We found that activation of prelimbic cortex (PL) axons into ZIm increases arousal level, and chemogenetic deactivation of these axons decreases the duration and depth of investigation. Calcium fiber photometry of these axons showed no difference in activity between shallow and deep investigation, suggesting a nonspecific motivation.

Optogenetic activation of ZIm^{GAD2} axons into lateral periaqueductal gray (lPAG) increases the arousal level, whereas chemogenetic deactivation of these axons decreases duration and depth of investigation. Calcium fiber photometry of these axons showed high activity during deep investigation and no significant activity during shallow investigation, suggesting a thresholding mechanism.

Last, we found a new subpopulation of inhibitory neurons in ZIm expressing tachykinin 1 (TAC1) that monosynaptically receive PL inputs and project to lPAG. Optogenetic activation and deactivation of these neurons, respectively, increased and decreased depth and duration of investigation.

CONCLUSION: Our experiments revealed different action sequences based on the motivational level of novelty seeking. Moreover, we uncovered a new brain circuit underlying curiosity and novelty-seeking behavior, connecting excitatory neurons of PL to lPAG through TAC1^{+} inhibitory neurons of ZIm. ■

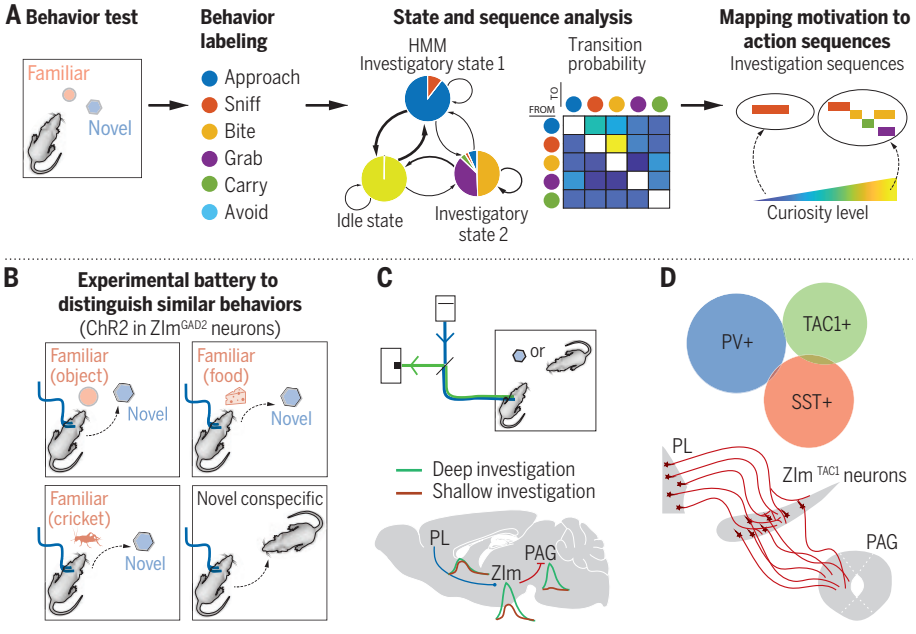

Brain mechanism of curiosity. (**A**) How we mapped motivational level to action sequences. (**B**) Experimental battery to distinguish novelty-seeking behavior from food eating and hunting in mice with photoactivation of ZIm^{GAD2} neurons. (**C**) Schematic of calcium activity in PL→ZIm, ZIm, and ZIm→PAG during shallow and deep investigation. (**D**) TAC1^{+} neurons as a subpopulation of ZIm^{GAD2} neurons receive input from PL and project to PAG. HMM, hidden Markov model.

The list of author affiliations is available in the full article online.
*Corresponding author. Email: m.ahmadlou@nin.knaw.nl (M.A.); a.heimel@nin.knaw.nl (J.A.H.)
Cite this article as M. Ahmadlou *et al.*, *Science* **372**, eabe9681 (2021). DOI: 10.1126/science.abe9681

RESEARCH ARTICLE SUMMARY

CANCER

Radiation-related genomic profile of papillary thyroid carcinoma after the Chernobyl accident

Lindsay M. Morton*†, Danielle M. Karyadi†, Chip Stewart†, Tetiana I. Bogdanova‡, Eric T. Dawson‡, Mia K. Steinberg‡, Jieqiong Dai, Stephen W. Hartley, Sara J. Schonfeld, Joshua N. Sampson, Yosef E. Maruvka, Vidushi Kapoor, Dale A. Ramsden, Juan Carvajal-Garcia, Charles M. Perou, Joel S. Parker, Marko Krznaric, Meredith Yeager, Joseph F. Boland, Amy Hutchinson, Belynda D. Hicks, Casey L. Dagnall, Julie M. Gastier-Foster, Jay Bowen, Olivia Lee, Mitchell J. Machiela, Elizabeth K. Cahoon, Alina V. Brenner, Kiyohiko Mabuchi, Vladimir Drozdovitch, Sergii Masiuk, Mykola Chepurny, Liudmyla Yu. Zurnadzhy, Maureen Hatch, Amy Berrington de Gonzalez, Gerry A. Thomas§, Mykola D. Tronko§, Gad Getz§, Stephen J. Chanock*§

INTRODUCTION: The 1986 Chernobyl (Chornobyl in Ukrainian) nuclear power plant accident exposed millions of individuals in the surrounding region to radioactive contaminants, resulting in increased papillary thyroid carcinoma (PTC) incidence in radioactive iodine (^{131}I)–exposed children. Currently, no reliable biomarkers for radiation-induced cancers have been identified, and large-scale genomic characterizations of human tumors after radiation exposure are lacking.

RATIONALE: To investigate the contribution of environmental radiation to the genomic characteristics of PTC and gain further insight into radiation-induced carcinogenesis, we analyzed 440 pathologically confirmed fresh-frozen PTCs from Ukraine (359 with estimated childhood or in utero ^{131}I exposure, 81 from unexposed children born after March 1987; mean age at PTC = 28.0 years, range 10.0 to 45.6) and matched normal tissue (nontumor thyroid tissue and/or blood). Our genomic characterization included whole-genome, mRNA, and microRNA sequencing; DNA methylation profiling; and genotyping arrays.

RESULTS: The mean estimated radiation dose among ^{131}I-exposed individuals was 250 mGy (range, 11.0 to 8800). In multivariable models adjusted for age at PTC and sex, we observed radiation dose–dependent increases in small deletions ($P = 8.0 \times 10^{-9}$) and simple/balanced structural variants ($P = 1.2 \times 10^{-14}$) but no association with single-nucleotide variants or insertions. Further analyses demonstrated stronger radiation-related associations for clonal—but not subclonal—small deletions and simple/balanced structural variants that bore hallmarks of nonhomologous end-joining repair (deletions, $P = 4.9 \times 10^{-31}$; simple/balanced structural variants, $P = 5.5 \times 10^{-19}$). In contrast, radiation dose was not associated with locally templated insertions characteristic of alternative end-joining repair.

Candidate drivers were identified for 433 tumors (98.4%), of which 401 had only a single candidate driver, illustrating the parsimonious nature of PTC carcinogenesis. More than half of the drivers ($n = 253$) were mutations, occurring commonly ($n = 194$) in *BRAF*. Fusions accounted for the remaining drivers, frequently involving *RET* ($n = 73$) or other receptor tyrosine kinase genes ($n = 64$). In total, 401 PTCs had drivers in the mitogen-activated protein kinase (MAPK) pathway. In multivariable models adjusted for age at PTC and sex, we observed radiation dose–dependent enrichment of fusion versus mutation drivers ($P = 6.6 \times 10^{-8}$), whereas the radiation dose distribution did not differ substantially by driver.

The effects of radiation on genomic alterations (fusion drivers, deletions, or structural variants) were more pronounced for individuals who were younger at exposure. Analyses were consistent with a linear dose response for most radiation-associated molecular characteristics. Individuals with PTC who were unexposed to ^{131}I or had lower doses had higher genetic risk ($P = 4.7 \times 10^{-4}$) according to a 12-locus polygenic risk score. Analyses of transcriptomic and epigenomic features demonstrated strong associations with the PTC driver gene but not with radiation dose.

CONCLUSION: Our large-scale integrated genomic landscape analysis of PTCs after the Chernobyl accident with detailed dose estimation points to DNA double-strand breaks as early carcinogenic events that subsequently enable PTC growth after environmental radiation exposure. Tumor epigenomic and transcriptomic profiles reflected the PTC driver and did not identify a reliable set of biomarkers for radiation-induced carcinogenesis. Nonhomologous end-joining was consistently implicated as the key repair mechanism for the observed radiation dose–associated DNA double-strand breaks, leading to more fusion drivers as a result of increasing radiation dose. Linear increases in radiation-associated damage, especially for exposure at younger ages, underscore the potential deleterious consequences of ionizing radiation exposure. ■

The list of author affiliations is available in the full article online.
†These authors contributed equally to this work.
‡These authors contributed equally to this work.
§These authors contributed equally to this work.
*Corresponding author. Email: chanocks@mail.nih.gov (S.J.C.); mortonli@mail.nih.gov (L.M.M.)
Cite this article as L. M. Morton *et al.*, *Science* **372**, eabg2538 (2021). DOI: 10.1126/science.abg2538

READ THE FULL ARTICLE AT
https://doi.org/10.1126/science.abg2538

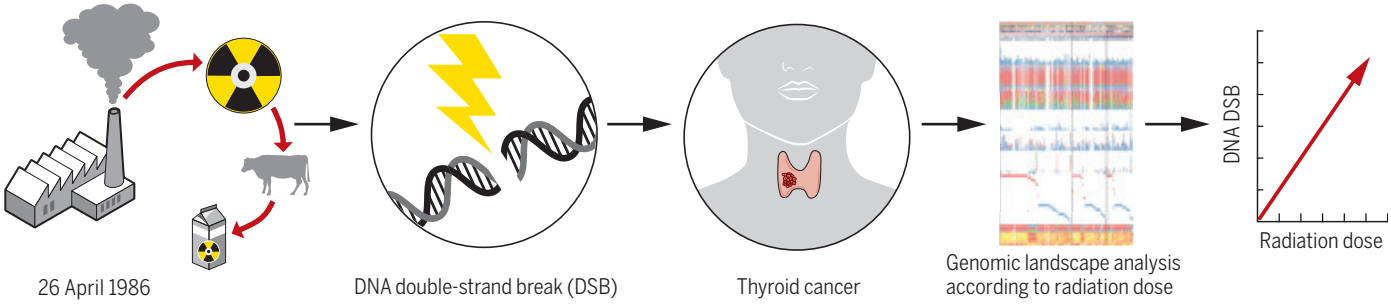

Genomic profiling of post-Chernobyl thyroid cancers reveals clonal DNA double-strand breaks repaired by nonhomologous end-joining. Radioactive iodine deposited on surrounding pastures after the Chernobyl nuclear power plant explosion increased thyroid cancer risk, particularly for childhood exposure. Comprehensive genomic profiling of post-Chernobyl thyroid tumors revealed radiation dose–dependent increases in clonal DNA double-strand breaks but no dose relationship with transcriptomic or epigenomic characteristics, highlighting environmental radiation exposure as an early carcinogenic event.

RESEARCH ARTICLES

PLANT SCIENCE

Molecular insights into the complex mechanics of plant epidermal cell walls

Yao Zhang[1], Jingyi Yu[1], Xuan Wang[1], Daniel M. Durachko[1], Sulin Zhang[2]*, Daniel J. Cosgrove[1]*

Plants have evolved complex nanofibril-based cell walls to meet diverse biological and physical constraints. How strength and extensibility emerge from the nanoscale-to-mesoscale organization of growing cell walls has long been unresolved. We sought to clarify the mechanical roles of cellulose and matrix polysaccharides by developing a coarse-grained model based on polymer physics that recapitulates aspects of assembly and tensile mechanics of epidermal cell walls. Simple noncovalent binding interactions in the model generate bundled cellulose networks resembling that of primary cell walls and possessing stress-dependent elasticity, stiffening, and plasticity beyond a yield threshold. Plasticity originates from fibril-fibril sliding in aligned cellulose networks. This physical model provides quantitative insight into fundamental questions of plant mechanobiology and reveals design principles of biomaterials that combine stiffness with yielding and extensibility.

The primary cell wall physically controls many key features of growing plant cells, including size, shape, growth, water/turgor relations, mechanical strength, and defense against pathogens (*1*). Comprising three distinctive polysaccharides (cellulose, hemicelluloses, and pectins), the wall is often organized as a multilayer nanostructure, particularly conspicuous in epidermal walls that physically protect and limit growth of leaves and stems (*2*, *3*). Within individual layers (lamellae), stiff cellulose fibrils (~3 nm wide, traditionally called microfibrils) form a reticulated, noncovalent network aligned in a common direction that varies among lamellae, while hemicelluloses bind noncovalently to cellulose and well-hydrated pectins form a gel-like matrix hosting the stiff cellulose network. This cross-lamellate architecture contrasts with the network structures of soft and highly stretchable animal skins (*4*), brick-and-mortar structures in tough nacres (*5*), Bouligand (helicoidal) structures in impact-resistant cuticles of crustaceans (*6*), and many fiber-based biogels (*7*). Studies of such biomaterials have revealed how microstructures contribute to macroscale material properties (*7*–*9*), but this level of structure-function understanding has not yet been achieved for plant primary cell walls. An understanding of force distribution, microfibril movements, and reshaping of wall structure in response to mechanical forces can provide molecular insights into the mechanobiology of plant growth (*10*–*12*), responses to environmental and biotic stresses (*13*), and engineering of multifunctional materials (*14*, *15*).

Tensile tests of growing cell walls typically distinguish reversible (elastic) and irreversible (plastic) deformations (*16*–*18*). These empirical measurements lack a quantitative framework to connect macroscale mechanics to microscale responses. The development of this framework has been hindered by uncertainties of wall structure and by the difficulties of mechanical modeling of complex organs with heterogeneous cell walls. Here, we focused on the outer epidermal wall of onion scale as a primary cell wall with key advantages (*19*). It can be isolated as centimeter-wide peels that are large and strong enough for mechanical testing, yet are only one cell wall thick (~7 μm), offering a simplified material for structural and mechanical analyses (fig. S1). Imaging by atomic force microscopy (AFM) revealed its cross-lamellate organization and documented complex nanoscale motions of cellulose microfibrils during stretching and enzymatic loosening (*19*–*21*).

To bridge the gap between macroscale mechanical behaviors and microscale microfibril motions, we turned to mesoscale coarse-grained molecular dynamics (CGMD) simulations. In contrast to continuum and finite-element models of cell walls (which generally lack dynamic polymer behaviors) and atomistic simulations (which cannot capture wall mechanical behaviors because of length-scale limitations), CGMD simulations encompass molecular-scale behaviors with computational efficiency (*22*). Because CGMD models lump multiple atomic interactions between molecules, they can simulate wall-stretching experiments (*23*), thereby offering multiscale insights into wall mechanics. We combined this modeling approach with tensile testing of epidermal walls to generate insights into the microstructural bases for the complex nonlinear response of primary cell walls to tensile force. The model simulated aspects of wall assembly, uncovered the physical basis for wall plasticity, and revealed the uneven distribution of tensile stresses within epidermal walls; these stresses have been hypothesized to modulate cytoskeletal dynamics and morphogenesis (*10*–*12*).

Design and assembly of the model wall

Our model is based on the cross-lamellate onion epidermal wall (Fig. 1A) (*19*–*21*). Cellulose microfibrils and matrix polysaccharides (xyloglucan, the main hemicellulose, and homogalacturonan, the dominant pectin) were represented by chains of beads tuned to best estimates of their corresponding physical properties (*24*). Homo-bead interaction potentials were set to match the axial and bending stiffnesses of the corresponding polysaccharides (table S1), whereas interbead interaction potentials captured the noncovalent binding interactions between polysaccharides based on atomistic simulations (table S2) (*24*, *25*). The full simulation consisted of four lamellae with initial dimensions of 900 nm × 900 nm × 160 nm and with varied cellulose orientations (Fig. 1). Wall composition matched that of the onion epidermal wall (*24*).

To generate a wall-like structure, we initially placed cellulose microfibrils into a common orientation midplane of each lamella (Fig. 1B), mimicking surface deposition by synthase complexes (*26*) under cellular guidance (*27*). Cellulose orientations varied among lamellae. Xyloglucan and pectin chains were randomly dispersed in the simulation domain, roughly mimicking the result of exocytosis of matrix polysaccharides. The system was dynamically equilibrated, allowing spontaneous movements and interactions of all polymers. Cellulose microfibrils within lamellae self-assembled into coherent two-dimensional networks resembling, to a first approximation, the bundled cellulose organization observed by AFM (*20*) (compare Fig. 1, A and C). In further simulations, microfibril crossover as observed by AFM was mimicked by dispersing 20% of the microfibrils within each lamella at a divergent angle (Fig. 1, D to K, and fig. S2). After equilibration, xyloglucans adhered to cellulose microfibrils as extended chains and random coils (Fig. 1, F to K), resembling actual xyloglucan chains observed in onion walls (*28*). Pectins were distributed throughout the space and made extensive but weak contacts with cellulose surfaces, consistent with results from solid-state nuclear magnetic resonance (*29*), AFM (*19*, *20*), and binding studies. Cellulose networks in the four lamellae remained physically distinct (Fig. 1G). These equilibration results—based on minimal assumptions of the physical properties, deposition patterns, and interactions of wall polymers—demonstrate that

[1]Department of Biology, Pennsylvania State University, University Park, PA 16802, USA. [2]Department of Engineering Science and Mechanics and Department of Biomedical Engineering, Pennsylvania State University, University Park, PA 16802, USA.
*Corresponding author. Email: suz10@psu.edu (S.Z.); dcosgrove@psu.edu (D.J.C.)

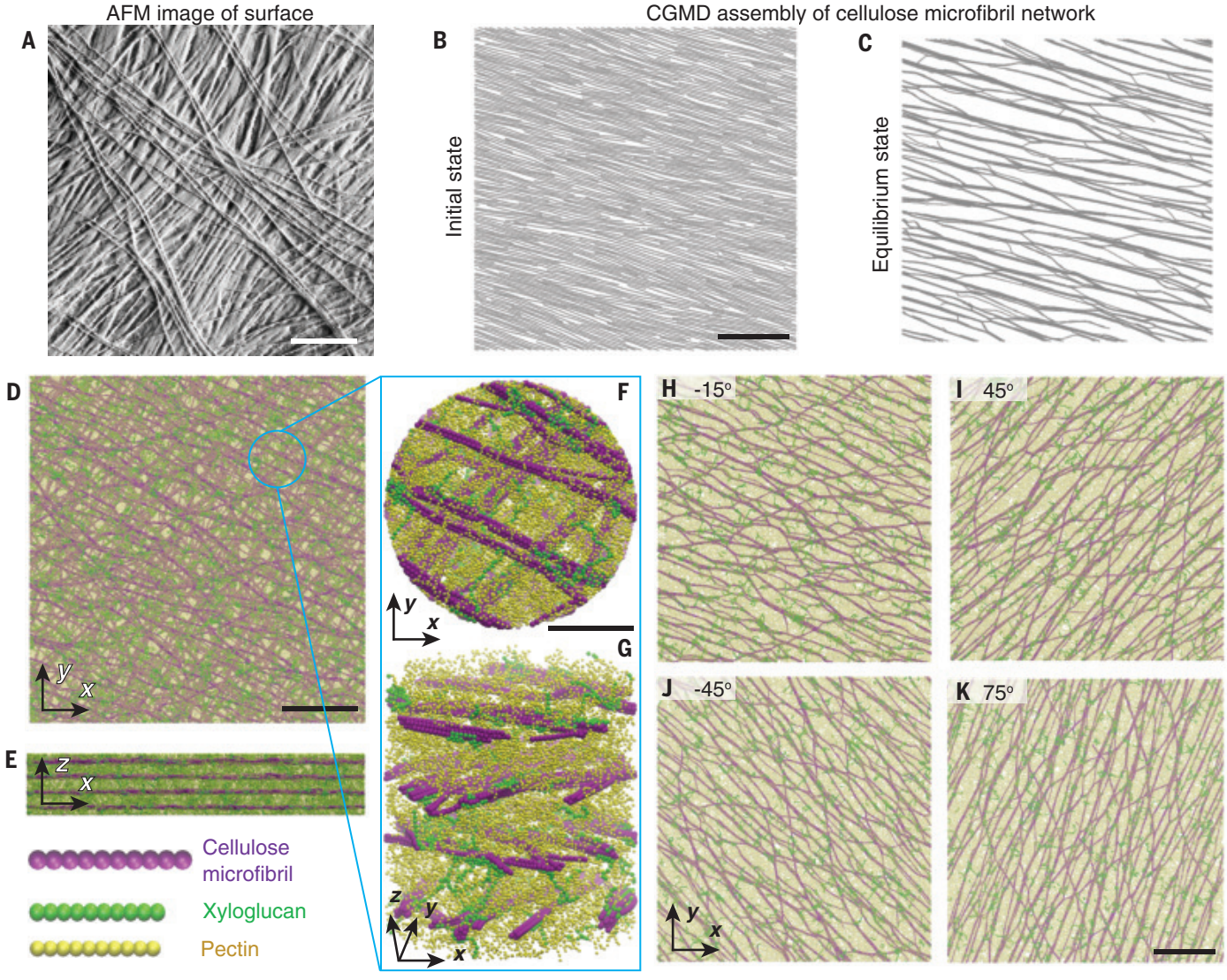

Fig. 1. Assembly of the CGMD model of a plant primary cell wall. (**A**) AFM image of newly deposited surface of outer epidermal wall of onion scale, showing the cross-lamellate organization of cellulose microfibrils [peak force error map, 1 × 1 μm; after (*20*)]. (**B** and **C**) Microfibril orientation in a single-lamella model before energy equilibration (B) and after (C), shown at the same scale. (**D** and **E**) Top (D) and side (E) views of the four-lamella wall after equilibration, shown at the same scale. (**F** and **G**) Close-ups of top and side views. (**H** to **K**) Top views of the four lamellae with varying initial cellulose orientation, shown at the same scale. Scale bars, 200 nm [(A) to (E) and (H) to (K)], 25 nm [(F) and (G)].

macromolecular morphologies resembling that of the actual wall can emerge from the collective physical interactions incorporated in the model.

Influence of cellulose on nonlinear mechanics

We used the model with four lamellae to represent the polylamellate epidermal wall and to compare its tensile responses to those of the actual wall. Cellulose orientations of the lamellae (−15°, +45°, −45°, +75°) were chosen to represent the range of cellulose angles while approximating a net isotropic structure (*30*). The structure was stretched uniaxially under constant-volume conditions; Fig. 2A shows the stress-strain result. The slope (modulus) was highly nonlinear (Fig. 2B): initially constant to ~1% strain, followed by a curvilinear region of increasing stiffness (increasing slope) to ~8% strain, and then a region of decreasing slope. As detailed below, the decrease in slope results from plastic yielding of selective wall components. The model's stress-strain behaviors closely recapitulated that of real epidermal walls (Fig. 2, A and B, and fig. S2) (*18*, *19*). These plots are characteristic of primary cell walls and are commonly used to assess wall extensibilities (*16*–*18*), although without microstructural insights.

Decomposition of wall stress into its components (Fig. 2C) (*24*) revealed that cellulose microfibrils carried most of the stress, despite the abundance of pectin and despite the frequent bridging of xyloglucans between microfibrils. This result is consistent with experimental observations that xyloglucanase and pectolyase digestions negligibly affect the tensile stiffness of onion epidermal walls (*21*). Increasing the binding energies between cellulose and matrix polysaccharides negligibly altered wall stiffness (Fig. 2E and fig. S5), whereas tuning of cellulose-cellulose interactions modulated stiffness at strains greater than 6% (Fig. 2F). Strengthening cellulose-cellulose interactions substantially reduced plasticity, manifested here as a declining stress-strain slope above 6% strain, delaying its onset to higher stresses. Additional simulations showed that xyloglucan length, pectin length, and pectin cross-linking had little effect on tensile responses, whereas the length, density,

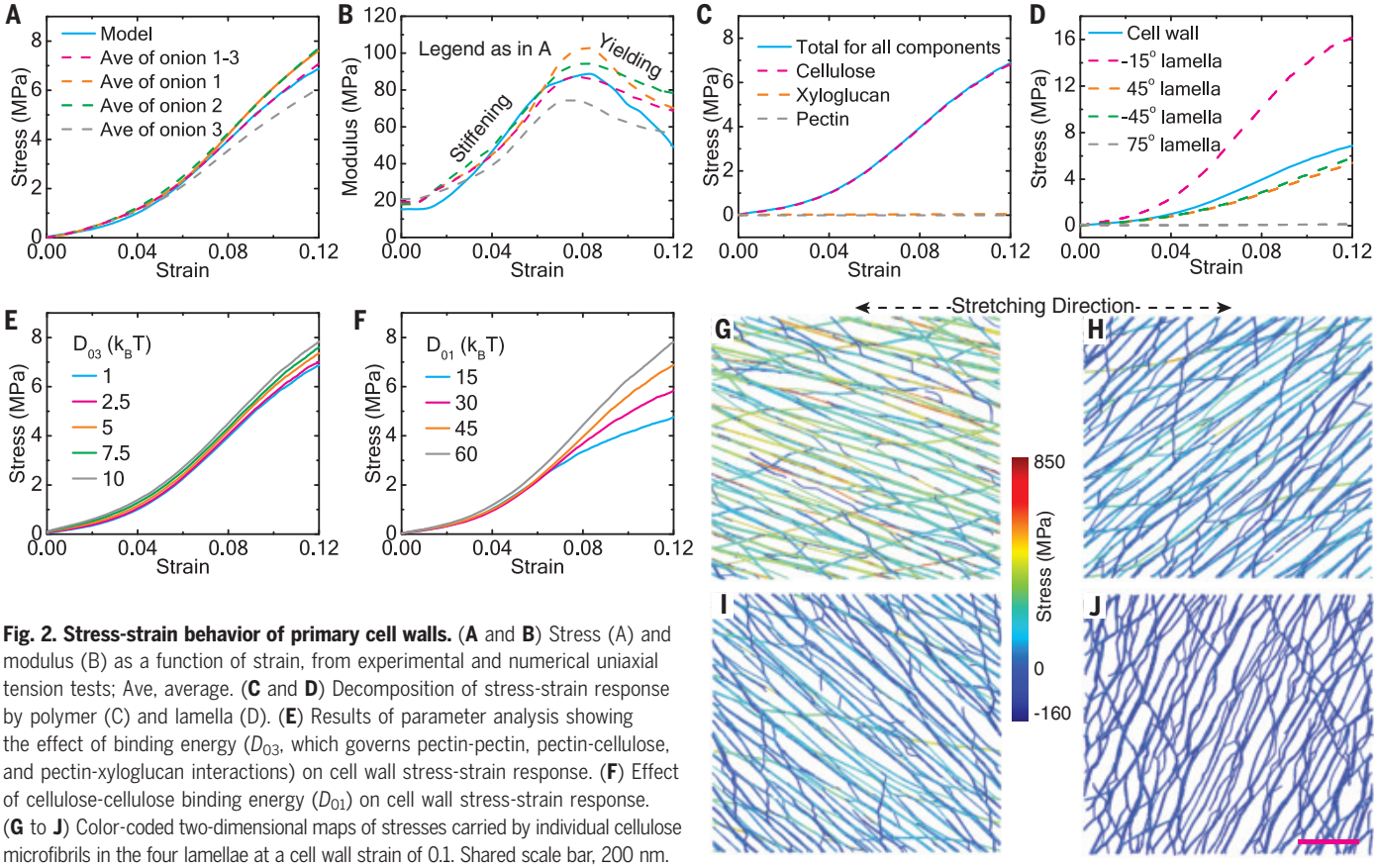

Fig. 2. Stress-strain behavior of primary cell walls. (**A** and **B**) Stress (A) and modulus (B) as a function of strain, from experimental and numerical uniaxial tension tests; Ave, average. (**C** and **D**) Decomposition of stress-strain response by polymer (C) and lamella (D). (**E**) Results of parameter analysis showing the effect of binding energy (D_{03}, which governs pectin-pectin, pectin-cellulose, and pectin-xyloglucan interactions) on cell wall stress-strain response. (**F**) Effect of cellulose-cellulose binding energy (D_{01}) on cell wall stress-strain response. (**G** to **J**) Color-coded two-dimensional maps of stresses carried by individual cellulose microfibrils in the four lamellae at a cell wall strain of 0.1. Shared scale bar, 200 nm.

and distribution of cellulose microfibrils had substantial effects (fig. S5). Thus, cellulose-cellulose interactions dominate the mechanical behaviors of this wall model, consistent with experimental results (*16*, *21*).

The dominance of cellulose results from its high axial stiffness, low bending stiffness, and strong lateral bonding. Together these properties enable cellulose microfibrils to aggregate extensively into laterally bonded bundles, forming strong, highly anisotropic planar networks that directly transmit tensile forces between microfibrils. In contrast, the entropic flexibility of matrix polysaccharides resulted in lower polymer stiffness (fig. S6), less stable networks, and smaller contributions to tensile mechanics.

Stress was greatest in the lamella (–15°) aligned most closely to the stretching direction, whereas the 75° lamella carried negligible stress (Fig. 2D). Lamellae with intermediate orientations developed small stresses at higher strains. The –15° lamella stiffened at low strains, whereas at high strains its stress-strain slope flattened as a result of microfibril sliding (see below). In contrast, the ±45° lamellae remained in the stiffening regime throughout the stretching process.

Stress responses were further analyzed by color-coded maps of microfibrillar stresses at 10% wall strain (Fig. 2, G to J). Stresses were heterogeneous, with the greatest variability in the –15° lamella, which also displayed the largest total stress and the largest yielding at high strains. Because the real wall consists of many lamellae of different cellulose orientations, collectively it appears approximately isotropic in-plane (*30*), yet individual lamellae are highly anisotropic and are predicted to bear very different stresses upon uniaxial stretch.

Microfibril movements during wall stretching

In simulations of single lamellae with varied cellulose orientations, we observed five distinctive cellulose microfibril movements: (i) straightening, where end-to-end length increased with stretching (Fig. 3A); (ii) curving, where end-to-end length decreased (Fig. 3B); (iii) sliding, where aligned microfibrils slipped past each other (Fig. 3C); (iv) angular reorientation, where microfibril direction changed (Fig. 3D); and (v) changes in bundling, where microfibrils altered their lateral associations (fig. S7 and movies S1 and S2). These movements replicated those detected in AFM analyses of stretching epidermal walls (*19*).

Changes in microfibril conformation were analyzed by plotting the average end-to-end length (L_E) as a function of strain (Fig. 3E). In lamellae with large orientation angles (60° and 90°), microfibrils became more curved as a result of wall compression transverse to the stretching direction. In lamellae with small and intermediate microfibril angles (0°, 30°, and 45°), microfibrils straightened, but this action ceased at a critical strain when microfibril sliding began (the transition from solid to dashed lines in Fig. 3E). This straightening-to-sliding transition point marks the yield threshold.

Cellulose reorientation was quantified as the change of the average orientation angle ($\Delta\beta$) during stretching (*24*). As expected from geometry, lamellae with intermediate microfibril angles (30° to 60°) experienced larger reorientations than those oriented close to 0° or 90° (Fig. 3F). Collective reorientation was associated with increased microfibril bundling at large strains as microfibrils were drawn into closer proximity (movie S2). For microfibrils at 90°, stretching caused microfibril curving but no net angular change.

Figure 3G shows stress-strain curves annotated to indicate the major modes of microfibril movements during stretching. Microfibril straightening occurred during lamellar stiffening (increasing slope), whereas microfibril sliding became dominant at the later stage of decreasing slope (yielding). The straightening-to-sliding transition occurred at a larger critical strain in lamellae with larger initial orientation angle, but at a similar stress threshold.

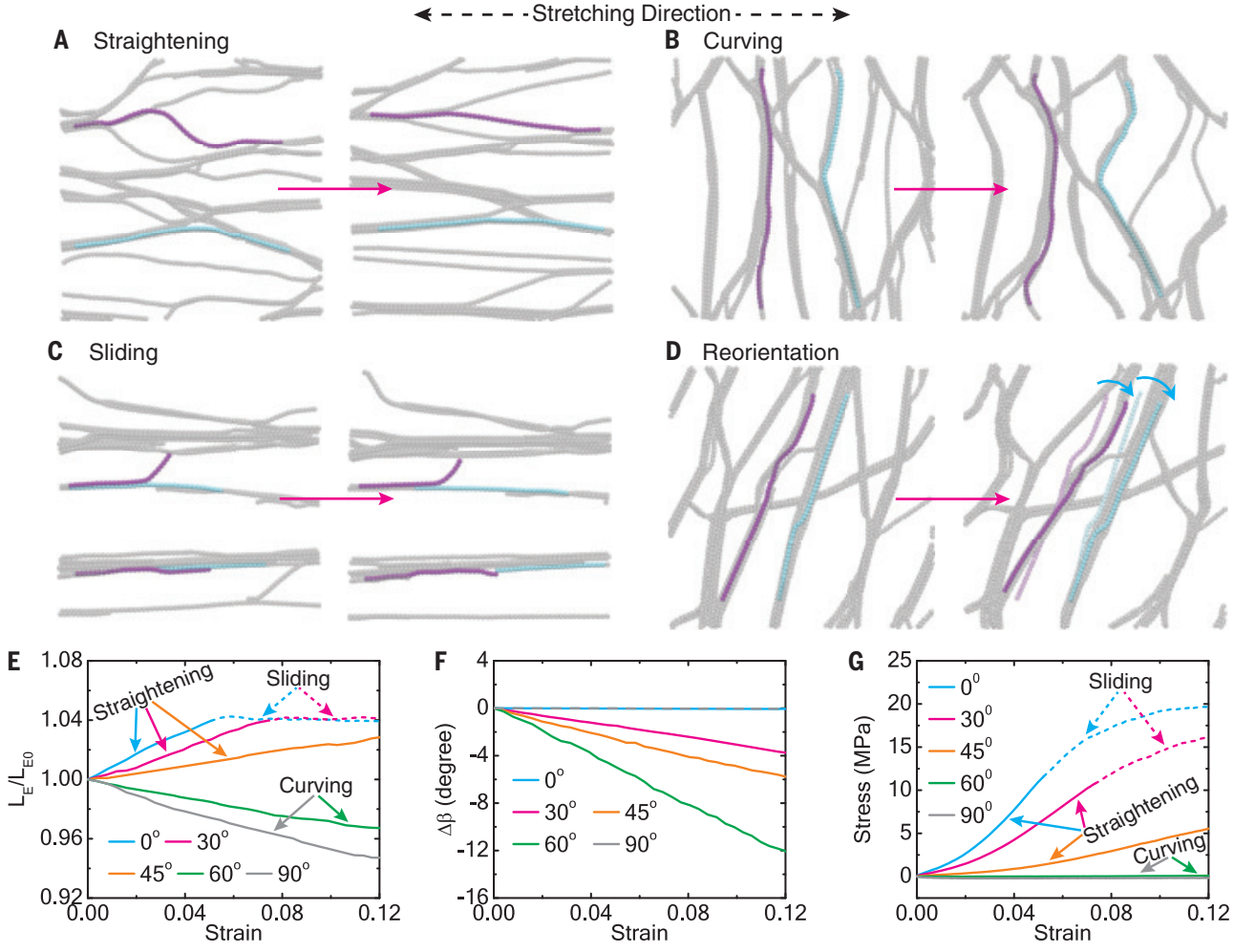

Fig. 3. Distinctive movements of cellulose microfibrils during uniaxial stretching of single lamellae. (**A** to **D**) Examples of microfibril movements (highlighted snapshots before and after movement), illustrating straightening (A), curving (B), sliding (C), and angular reorientation (D). (**E**) Normalized average end-to-end length of cellulose microfibrils, L_E/L_{E0}, as a function of wall strain for lamellae with different cellulose orientations. (**F**) Change in average orientation angle Δβ of cellulose microfibrils as a function of wall strain for lamellae with different cellulose orientations. (**G**) Wall stress as a function of strain for single-lamella wall model with various cellulose orientations, annotated to indicate the major modes of cellulose movement.

Energy dissipation and plasticity

We next investigated energy dissipation by stretching the walls (real and simulated) to the same stress value twice cyclically and measuring the loading and unloading stress-strain curves in both cycles. For real epidermal walls (Fig. 4A and fig. S8), loading and unloading curves in the first cycle followed different paths, revealing a large hysteresis and unrecoverable (plastic) deformation. Hysteresis indicates energy dissipation, represented by the area between the loading and unloading curves. Hysteresis is common in polymeric hydrogels, although its molecular basis varies in different materials (*31*, *32*). For the epidermal wall, the initial slope of the unloading curve was very steep, 290 MPa in this example, indicating high elastic stiffness despite the onset of plasticity.

The second loading curve followed a different path from the first, whereas the second unloading curve was nearly identical to the first. Subsequent cycles closely resembled the second cycle, indicating reversibility. This behavior contrasts with the progressive softening observed in animal tissues upon repeated stretching (*33*). From these results we distinguish two types of hysteresis: The second (reversible) cycle displays elastic hysteresis, whereas the first cycle includes an irreversible component due to plasticity (*17*).

In the corresponding model, cyclic extensions displayed similar behavior, including hysteresis and unrecoverable deformation (Fig. 4B). To elucidate the mechanisms underlying irreversible strain in the first cycle, we followed the evolution of L_E (straightening) of cellulose microfibrils as well as their average orientation β during the loading-unloading cycles. Both L_E and β in the four lamellae showed small irreversible changes at the end of the first cycle (Fig. 4, C and D, magenta arrows). We estimate (*24*) that microfibril sliding made the largest contribution (~63%) to irreversible extension of the −15° lamella, with smaller contributions from permanent microfibril straightening (~25%) and angular reorientation (~11%). At larger strains, cellulose sliding may account for a larger fraction of irreversible deformation. In the absence of sliding during the second cycle, cellulose straightening, curving, and reorientation were fully reversible. These results demonstrate coupling of the four modes of cellulose restructuring as well as different microfibril motions during loading and unloading.

The difference in hysteresis between the first and second stretch cycles for the model clarifies the energy dissipation mechanisms involved in wall stretching. In the first cycle, cellulose-cellulose sliding coupled to other conformational changes underlies irreversible deformation. Energy dissipation is largest in lamellae with cellulose aligned in the stretching direction (fig. S9), where fibril sliding is

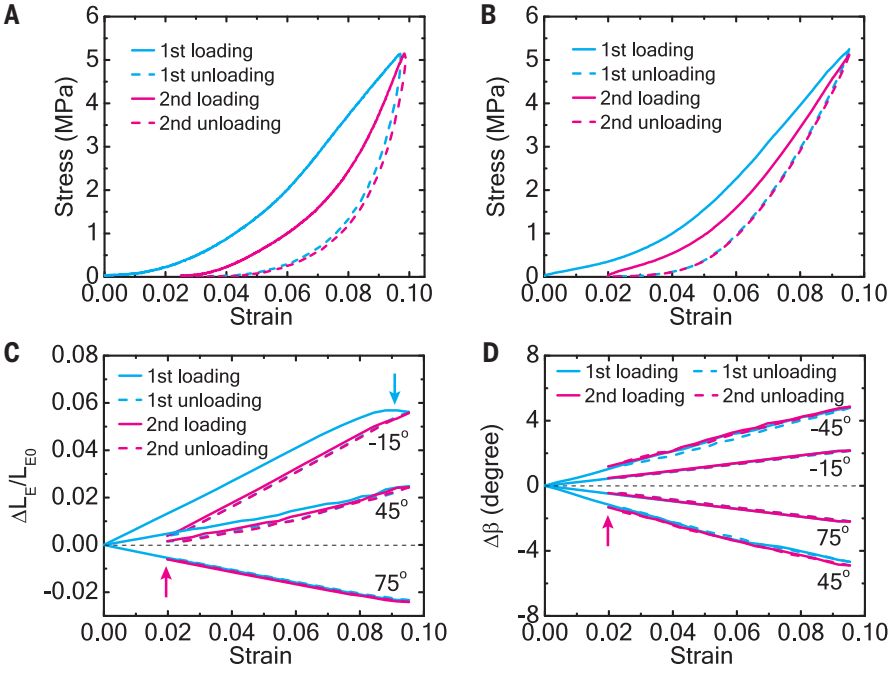

Fig. 4. Cell wall stress-strain responses during cyclic loading and unloading. (**A**) Experimental stress-strain response of onion epidermal strip (representative result of five trials). (**B**) Modeled numerical stress-strain response to strain matching the experimental data in (A) during cyclic loading and unloading. (**C**) Change in normalized average end-to-end length ($\Delta L_E/L_{E0}$) of cellulose microfibrils as a function of strain. The cyan arrow indicates the region where L_E reaches a plateau and sliding occurs in the −15° lamella. (**D**) Change in average orientation angle (β) of cellulose microfibrils as a function of strain. The magenta arrows in (C) and (D) indicate the unrecovered L_E and β, respectively, after the first stretch.

greatest. The second cycle exhibits only reversible hysteresis, likely arising from breaking and reforming noncovalent bonds between polysaccharides during loading and unloading (movie S2).

Calculations of cellulose bond lengths during the initial phase of unloading predict substantial elastic contraction of cellulose microfibrils aligned in the stretch direction, accounting for 80% of the initial wall contraction (fig. S9). This finding contrasts with a common view that cellulose is nearly inextensible in primary cell walls, but it is consistent with the steep slope of unloading (Fig. 4A) and the high axial stiffness of cellulose microfibrils (*14*, *15*, *34*).

Perspectives and outlook

Our physical model successfully assembled polysaccharides into a structure with supramolecular morphology and complex tensile behaviors resembling those of actual epidermal walls. The model shows how these traits, common to primary cell walls, may emerge from the collective elementary physical interactions between wall polysaccharides. Previous atomistic models simulated component interactions [e.g., xyloglucan binding to cellulose surfaces (*35*)], but this approach cannot reach the length scale needed to investigate the origins of wall mechanics or cellulose networks. In larger-scale finite-element wall models (*36*, *37*), cellulose was represented as stiff rods cross-linked at fixed points by thinner and stretchier rods, representing xyloglucan. In yet other studies (*38*, *39*), wall growth was modeled by continuum equations simulating insertion of pectins into the wall. Absent from these models are molecular processes central to our findings, including bundling and sliding of cellulose microfibrils, entropic effects on polymer conformations, and dynamic matrix-cellulose interactions. These realistic polysaccharide behaviors are enabled by the GCMD approach. What emerges from these interactions is a dynamic load-bearing network in which tensile forces are transmitted primarily through direct lateral contacts between microfibrils, rather than by matrix polysaccharides.

The CGMD simulations offer insights into the molecular bases of wall elasticity, plasticity above a yield threshold, stiffening at small strains, reduction in modulus at high strains, and energy dissipation during stretching. They clarify the mechanical contributions made by the three major wall polysaccharides, showing that complex cellulose movements dominate tensile mechanics. The results also offer a rationale for why enzymatic digestion of xyloglucan and pectin produced little effect on tensile stiffness or plasticity (*16*, *21*), contrary to expectations based on conventional tethered-network models of cell wall organization (*1*, *40*). With fewer lamellae than the actual wall and with polysaccharides simplified to CGMD representations, the model's behavior may differ from the actual wall in fine detail (e.g., in hysteresis and the exact shape of the loading and unloading curves). Moreover, the actions of expansins and other wall-modifying proteins (*1*) are not part of this model.

In a broader biological context, matrix polysaccharides likely influence tensile mechanics by modulating how cellulose microfibrils assemble into networks and by limiting the action of cellulose-modifying proteins. Microtubule dynamics and other cellular processes (*10*, *11*, *27*, *41*, *42*) ultimately influence wall mechanics by controlling patterns of cellulose microfibril deposition and the resulting network structure. These represent additional cellular mechanisms that control wall mechanics at a hierarchical level beyond the physical treatment presented here.

The highly nonlinear stress-strain behavior of primary cell walls has long been used to estimate empirical wall extensibilities for growth studies (*16*–*18*). Our results give a clearer basis for interpreting the meaning of such extensibilities. Cellulose sliding seen here resembles "slip-stick" deformation of wet wood (*43*–*45*), which also retains considerable stiffness after plastic yielding. Woody walls substantially differ from primary cell walls in composition, organization, and material properties, and their plasticity has been ascribed to viscous shearing of hemicelluloses between microfibrils (*23*, *43*, *45*). Direct sliding between microfibrils, as modeled here, may also contribute to the plastic deformation of woody cell walls, and this should be a subject of future investigation.

Finally, numerous studies in plant mechanobiology have implicated cell wall stress as an informational factor modulating microtubule organization and plant cell morphogenesis [e.g., (*10*–*12*, *42*)]. By clarifying how wall stresses are transmitted at the microscale and distributed within the wall, our study provides a physical framework for mechanistic investigations of how wall stresses relate to microtubule organization. Our results also clarify the distinctions among wall stress, lamellar stress, and stress in cellulose microfibrils (which can be two orders of magnitude greater than wall stress). The ingenious microstructural and architectural design of plant epidermal cell walls suggests ways to engineer strong and extensible fibrous materials with multifunctional applications.

REFERENCES AND NOTES

1. D. J. Cosgrove, *Nat. Rev. Mol. Cell Biol.* **6**, 850–861 (2005).
2. M. Lipowczan, D. Borowska-Wykret, S. Natonik-Bialon, D. Kwiatkowska, *J. Exp. Bot.* **69**, 4349–4362 (2018).
3. D. J. Cosgrove, *Curr. Opin. Plant Biol.* **46**, 77–86 (2018).
4. M. Vatankhah-Varnosfaderani *et al.*, *Science* **359**, 1509–1513 (2018).
5. H. Gao, B. Ji, I. L. Jager, E. Arzt, P. Fratzl, *Proc. Natl. Acad. Sci. U.S.A.* **100**, 5597–5600 (2003).

6. J. C. Weaver *et al.*, *Science* **336**, 1275–1280 (2012).
7. A. S. G. van Oosten *et al.*, *Nature* **573**, 96–101 (2019).
8. M. A. Meyers, J. McKittrick, P. Y. Chen, *Science* **339**, 773–779 (2013).
9. F. Barthelat, Z. Yin, M. J. Buehler, *Nat. Rev. Mater.* **1**, 16007 (2016).
10. O. Hamant, D. Inoue, D. Bouchez, J. Dumais, E. Mjolsness, *Nat. Commun.* **10**, 2360 (2019).
11. A. Sampathkumar *et al.*, *eLife* **3**, e01967 (2014).
12. S. Verger, Y. Long, A. Boudaoud, O. Hamant, *eLife* **7**, e34460 (2018).
13. K. Hu *et al.*, *Nat. Plants* **3**, 17009 (2017).
14. C. Chen *et al.*, *Nat. Rev. Mater.* **5**, 642–666 (2020).
15. J. Song *et al.*, *Nature* **554**, 224–228 (2018).
16. Y. B. Park, D. J. Cosgrove, *Plant Physiol.* **158**, 1933–1943 (2012).
17. R. Cleland, *Planta* **74**, 197–209 (1967).
18. A. J. Bidhendi, H. Li, A. Geitmann, *Botany* **98**, 49–64 (2020).
19. T. Zhang, D. Vavylonis, D. M. Durachko, D. J. Cosgrove, *Nat. Plants* **3**, 17056 (2017).
20. T. Zhang, Y. Zheng, D. J. Cosgrove, *Plant J.* **85**, 179–192 (2016).
21. T. Zhang, H. Tang, D. Vavylonis, D. J. Cosgrove, *Plant J.* **100**, 1101–1117 (2019).
22. H. I. Ingólfsson *et al.*, *Wiley Interdiscip. Rev. Comput. Mol. Sci.* **4**, 225–248 (2014).
23. D. C. Adler, M. J. Buehler, *Soft Matter* **9**, 7138–7144 (2013).
24. See supplementary materials.
25. Y. Zhang, E. P. DeBenedictis, S. Keten, *Soft Matter* **15**, 3807–3816 (2019).
26. P. Purushotham, R. Ho, J. Zimmer, *Science* **369**, 1089–1094 (2020).
27. J. Chan, E. Coen, *Curr. Biol.* **30**, 941–947.e2 (2020).
28. Y. Zheng, X. Wang, Y. Chen, E. Wagner, D. J. Cosgrove, *Plant J.* **93**, 211–226 (2018).
29. T. Wang, Y. B. Park, D. J. Cosgrove, M. Hong, *Plant Physiol.* **168**, 871–884 (2015).
30. K. Kafle *et al.*, *Cellulose* **24**, 3145–3154 (2017).
31. X. Zhao, *Soft Matter* **10**, 672–687 (2014).
32. Z. Wang *et al.*, *Proc. Natl. Acad. Sci. U.S.A.* **116**, 5967–5972 (2019).
33. K. M. Schmoller, A. R. Bausch, *Nat. Mater.* **12**, 278–281 (2013).
34. S. J. Eichhorn, *ACS Macro Lett.* **1**, 1237–1239 (2012).
35. Z. Zhao, V. H. Crespi, J. D. Kubicki, D. J. Cosgrove, L. H. Zhong, *Cellulose* **21**, 1025–1039 (2014).
36. H. Kha, S. C. Tuble, S. Kalyanasundaram, R. E. Williamson, *Plant Physiol.* **152**, 774–786 (2010).
37. R. Huang, A. A. Becker, I. A. Jones, *J. Eng. Math.* **95**, 121–154 (2015).
38. O. Ali, J. Traas, *Trends Plant Sci.* **21**, 398–409 (2016).
39. E. T. Smithers, J. Luo, R. J. Dyson, *J. Exp. Bot.* **70**, 3587–3600 (2019).
40. D. M. Cavalier *et al.*, *Plant Cell* **20**, 1519–1537 (2008).
41. A. R. Paredez, C. R. Somerville, D. W. Ehrhardt, *Science* **312**, 1491–1495 (2006).
42. A. Sampathkumar, *Development* **147**, dev177964 (2020).
43. L. Köhler, T. Speck, H. C. Spatz, *Planta* **210**, 691–700 (2000).
44. L. H. Thomas *et al.*, *Sci. Rep.* **11**, 453 (2021).
45. J. Keckes *et al.*, *Nat. Mater.* **2**, 810–814 (2003).
46. LAMMPS data and code are at Zenodo, DOI 10.5281/zenodo.4543822.

ACKNOWLEDGMENTS

We thank E. Coen and L. Petridis for discussions and L. Wilson for technical assistance. **Funding:** This work was supported as part of the Center for Lignocellulose Structure and Formation, an Energy Frontier Research Center funded by the US Department of Energy, Office of Science, Basic Energy Sciences under award DE-SC0001090. **Author contributions:** Y.Z.: investigation, methodology, formal analysis, software, writing–original draft; J.Y.: investigation; X.W.: investigation; D.M.D.: investigation, methodology; S.Z.: methodology, supervision, writing–review and editing; D.J.C.: conceptualization, supervision, writing–review and editing, project administration, funding acquisition. **Competing interests:** The authors declare no competing interests. **Data and materials availability:** All data are available in the main text or the supplementary materials, and at (*46*).

SUPPLEMENTARY MATERIALS

science.sciencemag.org/content/372/6543/706/suppl/DC1
Materials and Methods
Figs. S1 to S9
Tables S1 and S2
Movies S1 and S2
References (*47*–*95*)
MDAR Reproducibility Checklist

15 October 2020; accepted 29 March 2021
10.1126/science.abf2824

ATMOSPHERIC CHEMISTRY

Extreme oxidant amounts produced by lightning in storm clouds

W. H. Brune[1]*, P. J. McFarland[1], E. Bruning[2], S. Waugh[3], D. MacGorman[3,4,5], D. O. Miller[1], J. M. Jenkins[1], X. Ren[6,7], J. Mao[8], J. Peischl[9,10]

Lightning increases the atmosphere's ability to cleanse itself by producing nitric oxide (NO), leading to atmospheric chemistry that forms ozone (O_3) and the atmosphere's primary oxidant, the hydroxyl radical (OH). Our analysis of a 2012 airborne study of deep convection and chemistry demonstrates that lightning also directly generates the oxidants OH and the hydroperoxyl radical (HO_2). Extreme amounts of OH and HO_2 were discovered and linked to visible flashes occurring in front of the aircraft and to subvisible discharges in electrified anvil regions. This enhanced OH and HO_2 is orders of magnitude greater than any previous atmospheric observation. Lightning-generated OH in all storms happening at the same time globally can be responsible for a highly uncertain, but substantial, 2 to 16% of global atmospheric OH oxidation.

Lightning contributes to the atmosphere's ability to cleanse itself through the production of reactive nitric oxide (NO) followed by its subsequent chemistry. The atmosphere's two primary oxidants, the hydroxyl radical (OH) and ozone (O_3), are produced when lightning NO reacts with the hydroperoxyl radical (HO_2) to produce OH and nitrogen dioxide (NO_2). NO_2 then decomposes in sunlight, leading to O_3 formation. The direct generation of O_3 from lightning (LO_3) has been inferred, but not unambiguously observed, in the atmosphere (*1*–*3*). Lightning production of nitrogen oxides (LNO_x) was first suggested in the early 19th century (*4*) and, in the past four decades, has been studied intensively in the atmosphere, in the laboratory, and by model simulation (*5*–*18*). When global models of atmospheric chemistry include parameterized LNO_x emissions, tropospheric NO_x, O_3, and OH all increase substantially, primarily in the tropical to subtropical upper troposphere (*19*).

Electrified storms have charge distributions that are more horizontally stratified in anvils than in storm cores, but both anvils and cores contain granular electric field and charge distributions (*20*, *21*), resulting in a range of electrical currents, from subvisible discharges to visible flashes (*22*–*25*). Some subvisible discharges have sufficient energy to overcome the dissociation bond strengths of H_2O, producing OH, H, and HO_2, and of O_2, producing O_3. Only visible flashes have sufficient energy to also dissociate N_2, which has a bond dissociation energy almost twice that of H_2O and O_2, and to initiate the high-temperature chemistry that leads to NO formation (*26*). Previous modeling studies of lightning flash chemistry calculated that large amounts of OH and HO_2 ($OH + HO_2 = HO_x$) are produced by visible flashes, but the calculated OH lifetime is only milliseconds, too short for lightning HO_x (LHO_x) to contribute noticeably to atmospheric oxidation (*27*, *28*).

However, these studies did not consider OH exposure, which is the integral of the OH concentration multiplied by time:

$$\mathrm{OH_{exposure}} = \int [\mathrm{OH}]\,dt \qquad (1)$$

OH exposure multiplied by the reaction rate coefficient between OH and another trace gas determines how much of that gas will be destroyed. If each of the lightning flashes and subvisible electrical discharges occurring simultaneously around the globe produces large amounts of OH and HO_2, it is possible that even for short exposure times, LHO_x could make substantial contributions to the atmosphere's total OH exposure and therefore its oxidative capacity.

The NASA DC-8 aircraft flew through anvils of deep convective clouds during the Deep Convective Clouds and Chemistry (DC3) field study in the summer of 2012 (*29*). The aircraft carried instruments to measure in situ almost 100 atmospheric constituents, including OH and HO_2, which were measured by the Airborne Tropospheric Hydrogen Oxides Sensor (ATHOS; see supplementary materials). Typically, the DC-8 flew in the near-surface inflow

[1]Department of Meteorology and Atmospheric Science, Pennsylvania State University, University Park, PA, USA. [2]Department of Geosciences, Texas Tech University, Lubbock, TX, USA. [3]National Severe Storms Laboratory, National Oceanic and Atmospheric Administration, Norman, OK, USA. [4]Cooperative Institute for Mesoscale Meteorological Studies, University of Oklahoma, Norman, OK, USA. [5]School of Meteorology, University of Oklahoma, Norman, OK, USA. [6]Department of Atmospheric and Oceanic Science, University of Maryland, College Park, MD, USA. [7]Air Resources Laboratory, National Oceanic and Atmospheric Administration, College Park, MD, USA. [8]Department of Chemistry and Biochemistry and Geophysical Institute, University of Alaska, Fairbanks, Fairbanks, AK, USA. [9]Cooperative Institute for Research in Environmental Sciences, University of Colorado, Boulder, CO, USA. [10]NOAA Chemical Sciences Laboratory, Boulder, CO, USA.
***Corresponding author. Email: whb2@psu.edu**

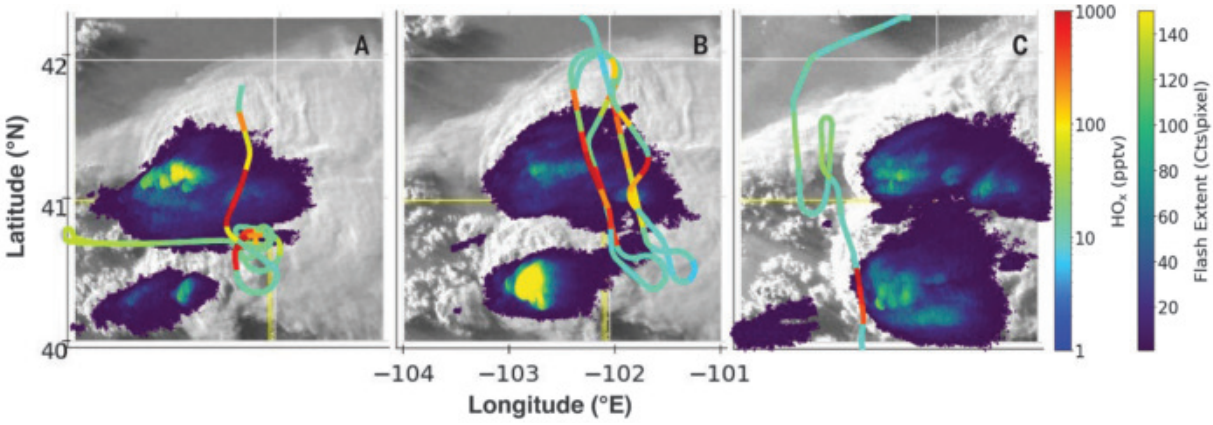

Fig. 1. Enhanced HO_x measured in an electrified anvil cloud. (**A** to **C**) HO_x abundances (indicated by colors and logarithmic scale) along the DC-8 flight track overlaid on LMA flash extent (*44*) and satellite anvil images during the flight on 22 to 23 June 2012 for three 1-hour periods: (A) 23:30 to 00:30 UTC; (B) 00:30 to 01:30 UTC; and (C) 01:30 to 02:30 UTC. The flash extent locations are shown for the entire hour as the storms moved from west to east. The storm cores are regions of the most intense flash extent. Cts/pixel, counts per pixel (each pixel is about 1 km^3).

region of a growing convective cell, spiraled up outside of it, and then sampled the convection outflow anvil. Simultaneously, a lightning mapping array (LMA) on the ground measured the position and intensity of the flashes within the convective storm and its anvil. Thus, DC3 presented an excellent opportunity to discover whether subvisible discharges and visible flashes produce substantial amounts of LHO_x.

Results from the 22 to 23 June flight

The DC-8 spent the most time in an anvil of active deep convection on 22 to 23 June over Colorado (Fig. 1). The DC-8 executed a low pass at 40.8°N latitude (Fig. 1A) before spiraling up beside the growing convective storm to 10-km altitude. HO_x was 5 to 20 parts per trillion by volume (pptv) outside of the anvil, which are typical amounts for these altitudes (*30*). The first instance of enhanced HO_x of ~700 pptv was measured in the cloud on the edge of the storm convective core at 7-km altitude during the spiral, but all the other enhanced HO_x was observed as the DC-8 passed back and forth through the electrified anvil at three different altitudes between 10 and 11 km (Fig. 1, A and B). Finally, after the DC-8 did a loop through a fire plume (Fig. 1C, upper left), it passed through the edge of another convective cell to the south, where enhanced HO_x was again observed. These coincidences between enhanced HO_x and electrified regions in the convection anvils indicate that electrical discharges were the source of enhanced OH and HO_2.

A time series of measured HO_x, NO_x, and O_3 shows that HO_x and NO_x were enhanced only within the convection anvil, which is indicated by the ice water content (IWC) (Fig. 2). The HO_x and NO_x enhancements varied substantially in terms of peak values and duration, with enhanced HO_x varying from tens to thousands of pptv and persisting for distances between 0.1 and 8 km along the flight track. The amount of OH was often about half that of enhanced HO_x (Fig. 2B).

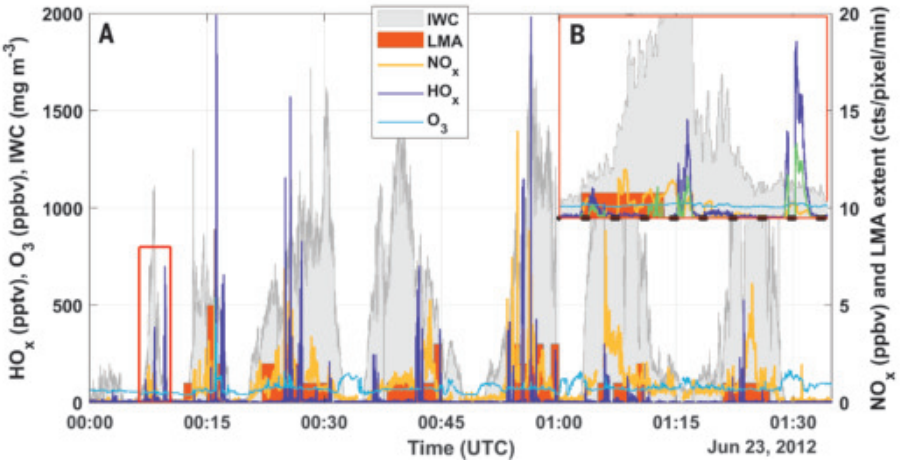

Fig. 2. HO_x, O_3, and NO_x during repeated flight passes through an electrified anvil cloud. Time series of HO_x (blue), NO_x (golden), O_3 (light blue), IWC (light gray), and LMA flash extent (orange) for the time period shown in Fig. 1. (**A**) Flash extents are given every minute, whereas NO_x and O_3 data are shown every 1 s and HO_x data every 0.2 s. (**B**) An expanded view of the region between 00:06:45 and 00:10:00 UTC. OH (green line) has been added to show that the amount of OH was often half that of HO_x. Black bars below zero indicate times when HO_x was not being measured. NO_x and O_3 were deemed to be unreliable between 00:16:00 and 00:16:13 UTC and were not reported.

Before this flight, the most HO_x ever observed in the atmosphere was about 150 pptv for HO_2 and a few pptv for OH (*30*, *31*). Thus, these discharge-generated OH and HO_2 amounts are orders of magnitude above any amounts ever observed before in the atmosphere.

The NO_x enhancements above background were a few parts per billion by volume (ppbv) to occasionally more than 10 ppbv, as has been observed before (*14*, *16*, *17*). The enhanced HO_x and enhanced NO_x sometimes coincided, but not always, for two reasons. First, the NO_x lifetime is at least several hours, whereas the HO_x lifetime is, at most, a few minutes. Thus, enhanced NO_x could have come from Earth's boundary layer or from visible flashes in the convection core or anvil several minutes before the DC-8 arrived, whereas any lightning-generated enhanced HO_x would have reacted away. Second, enhanced HO_x with little to no enhanced NO_x is generated by weak subvisible electrical discharges because the bond dissociation energies of H_2O and O_2 are about

half that of N_2 and NO production requires the high-temperature chemistry made possible by visible flashes (*26*).

About one-third of the time, HO_x was enhanced in anvil regions where no electrical activity was detected by the LMA (Fig. 2B). For instance, the enhanced HO_x on the right of Fig. 2B reached 700 pptv, whereas NO_x and O_3 were only a few times background, all in the anvil but outside of regions in which the LMA detected flashes. Thus, enhanced HO_x appears to be generated even by subvisible discharges too weak for the LMA to detect (*32*).

Some HO_x enhancements were accompanied by O_3 enhancements (Fig. 2). However, the DC-8 encountered stratospheric-like air that had wrapped itself around the outside of the anvil (*33*), and O_3 at the edge of the anvil often suddenly increased by as much as 100 ppbv, such as at 00:32 UTC in Fig. 2. Thus, it is difficult to say with certainty that these coincident O_3 enhancements were definitely produced by electrical discharges, even though our laboratory studies show that they can be (*26*).

A careful review of the NASA DC-8 forward camera revealed several subsecond instances of visible lightning, including one at 00:16:01 UTC and another at 00:16:11 UTC on 23 June. Less than a second after each visible lightning flash, large subsecond HO_x enhancements were measured. Enhancements were seen in NO_x and O_3, but they were considered spurious and thus were not included in the dataset (see supplementary materials for explanation). Both flashes occurred in front of the aircraft and were recorded by the aircraft forward camera as short white lines that lasted just one frame (<33 ms). The second flash is seen as the short, curved white line in the photograph in Fig. 3A and is just a small segment of a much larger flash, according to the LMA (fig. S1). A few tenths of a second later, observed HO_x was enhanced by 2000 pptv (Fig. 3B). The time delay between the flash in the video and the enhanced HO_x indicates that this flash segment occurred tens of meters in front of the aircraft, which traveled at 200 m s^{-1}. This result is consistent with the timing between the LMA flash and the enhanced HO_x spike in fig. S1 (*34*). Note that for the smaller, more diffuse HO_x spikes preceding and following these two flashes, no flashes were seen by either the forward or the nadir camera. Because in-flight and laboratory evidence demonstrates that these HO_x spikes were generated by atmospheric electrical discharges (see supplementary materials and fig. S2), these observations provide conclusive evidence that lightning produces extreme amounts of HO_x.

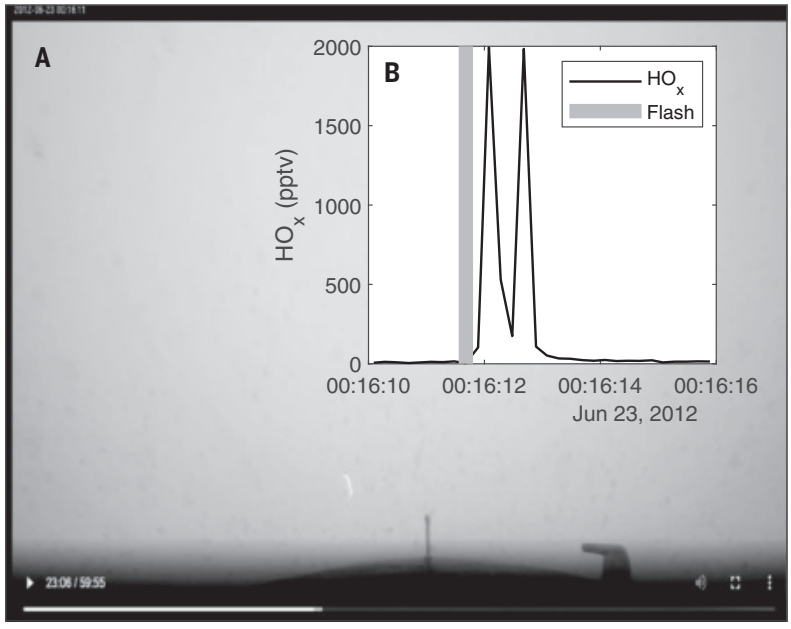

Fig. 3. A lightning flash and LHO_x. (**A**) Full-frame photograph shows lightning captured by the NASA DC-8 forward camera in a deep convection anvil at 00:16:11 UTC on 23 June 2012. (**B**) A time series plot of HO_x at 5 Hz (black line) and flash in video (gray vertical line). NO_x and O_3 data were not available during the flash.

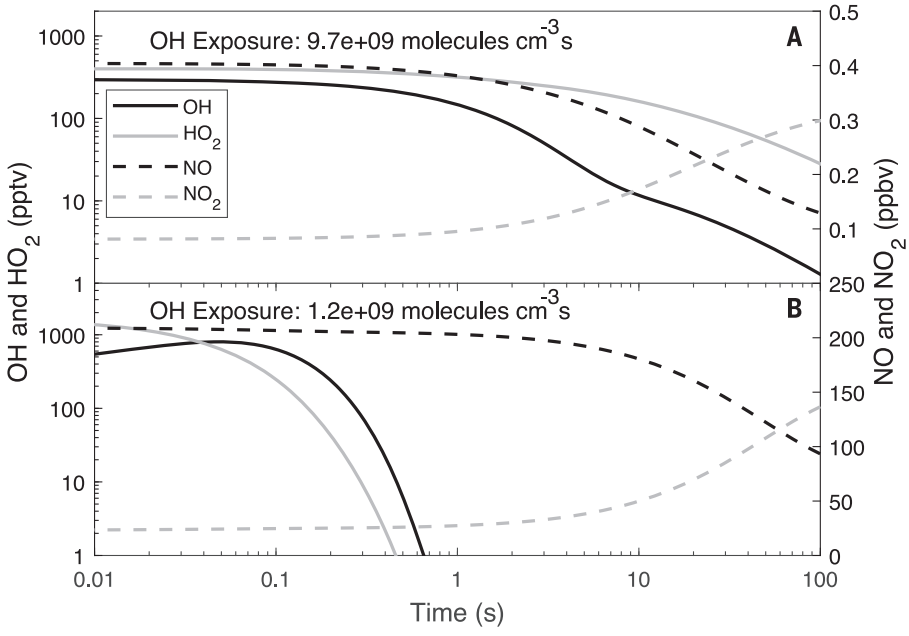

Fig. 4. Modeled behavior of OH, HO_2, NO, and NO_2. (**A** and **B**) Photochemical box model calculations of the changes in OH (solid black line), HO_2 (solid gray line), NO (dashed black line), and NO_2 (dashed gray line) for two cases: (A) 00:09:37 UTC, no visible flash, with measured values; and (B) 00:16:12 UTC, visible flash, with assumed values for NO, NO_2, and O_3 consistent with laboratory observations (*26*). The OH exposures were calculated using Eq. 1 and the modeled OH concentrations.

Modeling the evolution of HO_x and NO_x

Several observations of enhanced HO_x peaks were modeled with a photochemical box model that was constrained with other DC-8 measurements (*30*). Of these, two cases are shown in Fig. 4. For the first case at 00:09:37 UTC, no visible flash was observed and the model was initialized with 0.5 ppbv of NO_x, 70 ppbv of O_3, and 700 pptv of HO_x. For the second case at 00:16:11 UTC, the DC-8 sampled the air affected by the visible flash in Fig. 3 and the model was initialized with 230 ppbv of NO_x and 400 ppbv of O_3, which

were estimated from laboratory measurements, and 2000 pptv of HO_x. The names and numerical values for the other most important constraining chemical species are provided in the photochemical box modeling section of the supplementary materials.

Modeled OH and HO_2 decay to background levels within a few minutes for the subvisible discharge case and within a second for the visible flash case. NO_x is effectively constant because its lifetime is typically several hours (*18*), although NO reacts with O_3 to produce NO_2. For the low-NO_x case, the calculated OH and HO_2 decays are due primarily to the reaction $OH + HO_2 \rightarrow H_2O + O_2$, with a small contribution from $OH + NO + M \rightarrow HONO + M$, but for the high-$NO_x$ case, the OH and HO_2 decays are due primarily to the reactions $OH + NO + M \rightarrow HONO + M$ and $OH + NO_2 + M \rightarrow HNO_3 + M$, with only a small contribution from $OH + HO_2 \rightarrow H_2O + O_2$.

As a result, the calculated OH exposure is 9.7×10^9 molecules cm^{-3} s for the low-NO_x case and 1.2×10^9 molecules cm^{-3} s for the high-NO_x case. Note that the OH exposure is the result of all OH production and loss processes. Once an electrical discharge produces enhanced OH and HO_2, then OH will decay in a predictable way based on the rates of OH production, predominantly HO_2 reactions with NO and O_3, and the rates of OH loss to HO_2, NO, NO_2, CO, CH_4, and all other OH reactants. The OH exposure is just the integral of this decaying OH concentration over time (Eq. 1). Thus, for example, if a flash occurs once a second in the same volume of air, then the OH exposure (molecules cm^{-3} s) per flash multiplied by one flash per second will be the average OH concentration (molecules cm^{-3}) for that volume of air.

All flights into electrified anvils

Enhanced HO_x was observed on eight flights, always within electrified convective cores or anvils. On most flights, the DC-8 either flew inside the edge of the anvil or made only a few passes through it (figs. S3 and S4). For Table 1, the OH exposure was calculated for nine HO_x enhancements chosen to represent a range of initial HO_x and NO_x values, with four from the 22 to 23 June flight (Fig. 2). HO_x was enhanced by hundreds to thousands of pptv on all these flights, generally with little or no enhanced NO_x and O_3 and infrequent visible lightning. Peak OH was 125 to 600 pptv. As a result, the OH exposure calculated for these other flights was 3.3×10^9 to 11.8×10^9 OH molecules cm^{-3} s, consistent with that from the peaks on 22 to 23 June. Thus, the results from 22 to 23 June appear to be typical of the other DC3 flights in electrified storm anvils over Colorado or Oklahoma.

The electric field vertical structure was measured with balloon-borne electrometers in convection also sampled by the DC-8 over Oklahoma on 19 to 20 May and 29 May (figs. S3 and S4). These storms had negative electric field extrema of −20 and −80 kV m^{-1} and positive extrema of 10 to 40 kV m^{-1}, although the arrangement of negative and positive charge layers between these maxima was different between the two storms. These higher values are consistent with the breakdown electric fields that need to be exceeded before lightning can be initiated (*35*) and are fairly typical of the electric fields in electrified convection.

Discussion

Direct production of OH and HO_2 has now been observed in the anvils of deep convective clouds. The peak HO_x values were similar for subvisible discharges and the much less frequent visible flashes in regions where the LMA detected electrical discharges. In addition, about a third of enhanced HO_x was measured in the storm clouds outside of regions where the LMA detected flashes, indicating that low-energy subvisible electrical discharges not detected by the LMA also produced enhanced HO_x.

Global chemical transport models include parameterizations that use estimated LNO_x per visible flash (moles $flash^{-1}$ or molecules $flash^{-1}$) and thunderstorm visible flash distributions and then spread the LNO_x molecules throughout the grid cells affected by a visible flash to produce NO and NO_2 concentrations (*36*). Parameterizing LHO_x will be more complicated because subvisible discharges are such a substantial source. Our recent laboratory experiments have determined the LHO_x generated by individual sparks and subvisible discharges in terms of molecules per meter per discharge (*26*), but, in an electrified storm, LHO_x is likely generated by complex structures of subvisible discharges that vary in space and time but are currently unknown. At present, we can use only the OH mixing ratios measured during DC3 to estimate the LHO_x impact on atmospheric oxidation.

How important is LHO_x for atmospheric oxidation? For context, consider the global mean OH exposure per second, which is the same as the global mean number of OH molecules. Global model estimates of the mean [OH] are 1.03×10^6 to 1.15×10^6 molecules cm^{-3} (*37*–*42*), with an estimated uncertainty of ~25% with 68% confidence. Here, we use the global number of OH molecules calculated from a global chemistry-climate model, which is 4×10^{30} molecules (*42*).

Two methods for estimating the OH generated each second by LHO_x are described in the supplementary materials. Both methods assume that the amount of enhanced HO_x observed along the DC-8 flight path through the anvil represents the amount of enhanced HO_x generated throughout the electrified anvil region. Both use the typical LMA volume (table S1), the fraction of the flight track for which the electrical discharge occurred within the past second, and the typical OH exposure per electrical discharge. The first method uses flash rates in the anvil, and the second method uses the ratio of enhanced HO_x inside and outside of the regions in which the LMA detected electrical discharges but still inside the anvil. From these calculations, the convective cell

Table 1. Major HO_x peaks and resulting modeled OH exposure from six flights in 2012. These observed peaks may be lower than the initially generated peaks because the sampling is probably not always coincident with the electrical discharge.

Day	Time (UTC)	Peak HO_x (pptv)	Peak OH (pptv)	OH exposure (10^9 molecules cm^{-3} s)	Lightning visible?
18 May	23:18:34	1661.26	603.38	11.8	No
20 May	00:50:52	439.73	197.38	4.7	No
26 May	01:24:18	229.42	126.04	3.3	No
29 May	23:30:51	586.36	311.19	5.8	No
2 June	22:45:18	709.34	309.44	9.9	No
23 June	00:09:37	700.53	297.12	9.7	No
23 June	00:16:01	890.84	198.15	7.0	Yes
23 June	00:16:12	1992.62	334.34	1.2	Yes
23 June	00:56:27	1984.12	472.15	6.2	No

anvil on 22 to 23 June generated 2.7×10^{26} molecules for each second by the first method and 3.1×10^{25} molecules for each second by the second method.

The global number of active convective cells for each moment is thought to be 1800 (*16*). Thus, the electrically charged storm anvils would generate 4.9×10^{29} molecules each second by the first method and 5.6×10^{28} by the second method. The numbers are similar for the convective cell anvil sampled on 29 May (table S2). As a result, LHO_x in convective cell anvils could be responsible for 1.4 to 12% of global OH.

LHO_x further contributes to global OH in two other ways. First, much of the HONO produced from the reaction of enhanced OH and NO would eventually be photolyzed by sunlight, releasing OH and increasing the contribution of LHO_x to global OH. Second, from the DC3 LMA data, the convective core on 22 to 23 June contained 70% of the flashes (Fig. 1). During the spiral up on both 29 May and 23 June, the DC-8 flew through clouds associated with the convective core, encountering almost continuous enhanced HO_x in those clouds even though the DC-8 was kilometers from the nearest flashes. If total electrical activity is proportional to flash extent, then this core could have produced an OH exposure about a third that of the anvil, increasing the LHO_x contribution to global OH to 2 to 16%.

We emphasize that these estimates of the LHO_x contribution to global OH are highly uncertain by perhaps a factor of 10 (fig. S5). These storms, their electrical activity, or their LHO_x generation may be atypical of global storms because Colorado and Oklahoma storms have lightning characteristics different from those of the more numerous tropical and subtropical storms (*43*). In addition, LHO_x generation by subvisible discharges, as well as visible flashes, makes estimating LHO_x more uncertain than estimating LNO_x. Thus, the ratio of LHO_x to LNO_x varies from less than 0.01 for visible flashes to more than 1000 for subvisible discharges. Nonetheless, it may be possible to relate the amounts of LHO_x and LNO_x, but not from the DC3 data alone. These uncertainties must be narrowed before LHO_x can be included with any confidence in global chemical transport models and climate models.

Narrowing the LHO_x production uncertainty requires sampling a variety of electrified storms with an aircraft instrumented to measure environmental conditions, cloud particle properties, water vapor, electric fields and charge distributions, electrical discharge video and sound, OH, HO_2, NO, NO_2, O_3, and HONO at 5 Hz or faster. At a minimum, this aircraft should sample electrified anvils at different distances from the core, but optimally, it should penetrate the core itself at different altitudes. These storms should be observed simultaneously by an LMA and satellites. Such aircraft studies would determine the globally observed factors needed to parameterize LHO_x in models.

LHO_x is contributing to the global OH calculated from observations of atmospheric constituents that react with OH, such as methane or methyl chloroform (*37*–*42*), implying that the OH actually produced by standard atmospheric chemistry is less than that currently calculated. In addition, the impact of LHO_x on different atmospheric constituents depends on where it is generated. Our laboratory studies (*26*) indicate that LHO_x is generated in storm cores, cloud-to-ground lightning, and possibly even near high-voltage power lines, as well as in storm cloud anvils. Thus, LHO_x could be contributing to regional and global oxidation well beyond the storm cloud anvils. Furthermore, LHO_x may well be a larger contributor to global atmospheric oxidation than LNO_x. It is reasonable to assume that in a warmer climate, an increase in storm intensity and lightning will increase the importance of lightning-generated OH to regional and global atmospheric oxidation.

REFERENCES AND NOTES

1. R. E. Orville, *J. Geophys. Res.* **72**, 3557–3561 (1967).
2. H. Bozem *et al.*, *Atmos. Chem. Phys.* **14**, 8917–8931 (2014).
3. H. Huntrieser *et al.*, *J. Geophys. Res. Atmos.* **121**, 6600–6637 (2016).
4. J. von Liebig, *Ann. Chem. Phys.* **35**, 329–333 (1827).
5. A. F. Tuck, *Q. J. R. Meteorol. Soc.* **102**, 749–755 (1976).
6. W. L. Chameides, D. H. Stedman, R. R. Dickerson, D. W. Rusch, R. J. Cicerone, *J. Atmos. Sci.* **34**, 143–149 (1977).
7. E. Franzblau, C. J. Popp, *J. Geophys. Res.* **94**, 11089–11104 (1989).
8. C. Price, J. Penner, M. Prather, *J. Geophys. Res.* **102**, 5929–5941 (1997).
9. Y. Wang, A. W. DeSilva, G. C. Goldenbaum, R. R. Dickerson, *J. Geophys. Res.* **103**, 19149–19159 (1998).
10. A. J. DeCaria *et al.*, *J. Geophys. Res.* **105**, 11601–11616 (2000).
11. B. Ridley *et al.*, *J. Geophys. Res.* **109**, D17305 (2004).
12. A. J. DeCaria, K. E. Pickering, G. L. Stenchikov, L. E. Ott, *J. Geophys. Res.* **110**, D14303 (2005).
13. B. A. Ridley *et al.*, *J. Atmos. Chem.* **54**, 1–20 (2006).
14. L. E. Ott *et al.*, *J. Geophys. Res.* **115**, D04301 (2010).
15. H. Huntrieser *et al.*, *J. Geophys. Res. Atmos.* **121**, 6638–6668 (2016).
16. U. Schumann, H. Huntrieser, *Atmos. Chem. Phys.* **7**, 3823–3907 (2007).
17. I. B. Pollack *et al.*, *J. Geophys. Res. Atmos.* **121**, 2002–2028 (2016).
18. B. A. Nault *et al.*, *Geophys. Res. Lett.* **44**, 9479–9488 (2017).
19. L. J. Labrador, R. von Kuhlmann, M. G. Lawrence, *Atmos. Chem. Phys.* **5**, 1815–1834 (2005).
20. J. E. Dye *et al.*, *J. Geophys. Res.* **112** D11215 (2007).
21. S. A. Weiss, D. R. MacGorman, K. M. Calhoun, *Mon. Weather Rev.* **140**, 2064–2079 (2012).
22. D. Petersen, M. Bailey, W. H. Beasley, J. Hallett, *J. Geophys. Res. Atmos.* **113**, D17205 (2008).
23. D. Petersen, M. Bailey, J. Hallett, W. Beasley, *Q. J. R. Meteorol. Soc.* **141**, 1283–1293 (2014).
24. W. Rison *et al.*, *Nat. Commun.* **7**, 10721 (2016).
25. A. Y. Kostinskiy, T. C. Marshall, M. Stolzenburg, *J. Geophys. Res. Atmos.* **125**, e2020JD033191 (2020).
26. J. M. Jenkins, W. H. Brune, D. O. Miller, *J. Geophys. Res. Atmos.* 10.1029/2021JD034557 (2021).
27. R. D. Hill, R. G. Rinker, *J. Geophys. Res. Oceans* **86**, 3203–3209 (1981).
28. B. A. Bhetanabhotla, B. A. Crowell, A. Coucouvinos, R. D. Hill, R. G. Rinker, *Atmos. Environ.* **19**, 1391–1397 (1985).
29. M. C. Barth *et al.*, *Bull. Am. Meteorol. Soc.* **96**, 1281–1309 (2015).
30. W. H. Brune *et al.*, *Atmos. Chem. Phys.* **18**, 14493–14510 (2018).
31. D. Stone, L. K. Whalley, D. E. Heard, *Chem. Soc. Rev.* **41**, 6348–6404 (2012).
32. V. C. Chmielewski, E. C. Bruning, *J. Geophys. Res. Atmos.* **121**, 8600–8614 (2016).
33. L. L. Pan *et al.*, *Geophys. Res. Lett.* **41**, 7785–7790 (2014).
34. R. J. Thomas *et al.*, *J. Geophys. Res.* **109**, D14207 (2004).
35. T. C. Marshall, M. P. McCarthy, W. D. Rust, *J. Geophys. Res.* **100**, 7097–7103 (1995).
36. L. T. Murray, D. J. Jacob, J. A. Logan, R. C. Hudman, W. J. Koshak, *J. Geophys. Res.* **117**, D20307 (2012).
37. R. G. Prinn *et al.*, *Science* **269**, 187–192 (1995).
38. S. A. Montzka *et al.*, *Science* **288**, 500–503 (2000).
39. M. G. Lawrence, P. Jöckel, R. von Kuhlmann, *Atmos. Chem. Phys.* **1**, 37–49 (2001).
40. J. Lelieveld, S. Gromov, A. Pozzer, D. Taraborrelli, *Atmos. Chem. Phys.* **16**, 12477–12493 (2016).
41. M. Li *et al.*, *npj Clim. Atmos. Sci.* **1**, 29 (2018).
42. A. T. Archibald *et al.*, *Geophys. Res. Lett.* **38**, L05804 (2011).
43. E. Williams, V. Mushtak, D. Rosenfeld, S. Goodman, D. Boccippio, *Atmos. Res.* **76**, 288–306 (2005).
44. The flash extent is the number of flashes detected by the LMA in each grid cell (volume ~1 km^3) in each minute, whether it was initiated in that cell or just propagated through it; thus, flash extent is a reliable variable for determining the total region of electrical activity.
45. A. Aknan, G. Chen, NASA LaRC Airborne Science Data for Atmospheric Composition DC3 (2017); https://doi.org/10.5067/Aircraft/DC3/DC8/Aerosol-TraceGas.

ACKNOWLEDGMENTS

DC3 was sponsored by the U.S. National Science Foundation (NSF), the National Aeronautics and Space Administration (NASA), and the National Oceanic and Atmospheric Administration (NOAA). We thank the DC3 scientists, especially I. Pollack, T. Ryerson, and P. Lawson, for the use of their measurements; the DC-8 pilots and operations personnel; the DC3 weather forecasters; and NASA DC3 management for making the DC3 study possible. **Funding:** NSF AGS-1834711 supported this work; NASA NNX12AB84G supported the DC3 OH and HO_2 measurements; NSF AGS-1063945 supported the Oklahoma LMA work; and NSF-1063966 and AGS-1352144 supported the Colorado LMA work. **Author contributions:** W.H.B. and P.J.M. performed the formal analysis; W.H.B., D.O.M., X.R., J.M., J.P., E.B., S.W., and D.M. provided DC3 data; W.H.B. and P.J.M. wrote the initial draft; W.H.B., P.J.M., D.O.M., J.M.J., X.R., J.M., J.P., E.B., S.W., and D.M. reviewed and edited the manuscript; and W.H.B. supervised the research, analysis, and writing. **Competing interests:** The authors declare no competing interests. **Data and materials availability:** DC3 data, including the ATHOS 5-Hz OH and HO_2 data, are available at (*45*).

SUPPLEMENTARY MATERIALS

science.sciencemag.org/content/372/6543/711/suppl/DC1
Materials and Methods
Figs. S1 to S5
Tables S1 and S2
References (*46*–*63*)

16 December 2020; accepted 11 March 2021
Published online 29 April 2021
10.1126/science.abg0492

CELL DIFFERENTIATION

Cell-specific transcriptional control of mitochondrial metabolism by TIF1γ drives erythropoiesis

Marlies P. Rossmann[1,2], Karen Hoi[1,2], Victoria Chan[1,2], Brian J. Abraham[3]†, Song Yang[2], James Mullahoo[4], Malvina Papanastasiou[4], Ying Wang[5], Ilaria Elia[6], Julie R. Perlin[2], Elliott J. Hagedorn[2], Sara Hetzel[7], Raha Weigert[7], Sejal Vyas[6], Partha P. Nag[4], Lucas B. Sullivan[8], Curtis R. Warren[9]‡, Bilguujin Dorjsuren[1,2], Eugenia Custo Greig[1,2], Isaac Adatto[1,2], Chad A. Cowan[9], Stuart L. Schreiber[4], Richard A. Young[3,10], Alexander Meissner[1,4,7], Marcia C. Haigis[6], Siegfried Hekimi[5], Steven A. Carr[4], Leonard I. Zon[1,2]*

Transcription and metabolism both influence cell function, but dedicated transcriptional control of metabolic pathways that regulate cell fate has rarely been defined. We discovered, using a chemical suppressor screen, that inhibition of the pyrimidine biosynthesis enzyme dihydroorotate dehydrogenase (DHODH) rescues erythroid differentiation in bloodless zebrafish *moonshine (mon)* mutant embryos defective for transcriptional intermediary factor 1 gamma (*tif1γ*). This rescue depends on the functional link of DHODH to mitochondrial respiration. The transcription elongation factor TIF1γ directly controls coenzyme Q (CoQ) synthesis gene expression. Upon *tif1γ* loss, CoQ levels are reduced, and a high succinate/α-ketoglutarate ratio leads to increased histone methylation. A CoQ analog rescues *mon*'s bloodless phenotype. These results demonstrate that mitochondrial metabolism is a key output of a lineage transcription factor that drives cell fate decisions in the early blood lineage.

Vertebrate embryos produce circulating red blood cells (RBCs) that are required for oxygen and carbon dioxide transport (*1*). During embryonic development, three overlapping hematopoietic waves can be distinguished that all produce RBCs (*2*). In mammals, primitive erythroblasts that emerge in the blood islands within the extraembryonic yolk sac give rise to primitive erythrocytes of the first transient wave, and a second wave generates definitive erythroid-myeloid progenitors in the hemogenic endothelium of the yolk sac. Definitive erythrocytes of the third wave arise from multipotent hematopoietic stem cells that are born in the aortic endothelium of the aorta-gonad-mesonephros region and sustain hematopoiesis throughout the lifetime of the animal. Primitive erythrocytes supply the embryo with the oxygen needed for its rapid proliferation. Failure to initiate the first wave of erythropoiesis leads to embryonic lethality (*3*). Erythroid lineage differentiation is regulated by key transcription factors (*4*), but the cellular mechanisms that allow the generation and differentiation of the first erythroid progenitors remain largely unknown. Stem and descendent progenitor cells differ by their metabolic profiles (*5*), but there is little in vivo evidence for a link between transcriptional regulation and metabolic changes during cell fate decisions.

[1]Department of Stem Cell and Regenerative Biology, Harvard University, Cambridge, MA 01238, USA. [2]Stem Cell Program and Division of Hematology/Oncology, Boston Children's Hospital and Dana-Farber Cancer Institute, Howard Hughes Medical Institute, Harvard Stem Cell Institute, Harvard Medical School, Boston, MA 02115, USA. [3]Whitehead Institute for Biomedical Research, Cambridge, MA 02142, USA. [4]Broad Institute of MIT and Harvard, Cambridge, MA 02142, USA. [5]Department of Biology, McGill University, Montréal, Québec H3A 1B1, Canada. [6]Department of Cell Biology, Blavatnik Institute, Harvard Medical School, Boston, MA 02115, USA. [7]Department of Genome Regulation, Max Planck Institute for Molecular Genetics, 14195 Berlin, Germany. [8]Human Biology Division, Fred Hutchinson Cancer Research Center, Seattle, WA 98109, USA. [9]Beth Israel Deaconess Medical Center, Harvard Medical School, Boston, MA 02215, USA. [10]Department of Biology, Massachusetts Institute of Technology, Cambridge, MA 02139, USA.
†Present address: Department of Computational Biology, St. Jude Children's Research Hospital, Memphis, TN 38105, USA.
‡Present address: Cardiometabolic Disease Research, Boehringer-Ingelheim Pharmaceuticals Inc., Ridgefield, CT 06877, USA.
*Corresponding author. Email: leonard.zon@enders.tch.harvard.edu

DHODH inhibitors rescue defective *tif1γ*-dependent erythropoiesis

TIF1γ is essential for erythropoiesis from zebrafish to humans (*6*–*10*). Zebrafish *moonshine* (*mon*) mutant embryos defective for *tif1γ* do not make RBCs because of a transcription elongation block characterized by aberrantly paused RNA polymerase II (Pol II) (*9*–*11*). To uncover other factors required for *tif1γ*-dependent erythropoiesis, we performed a high-content chemical suppressor screen of 3120 compounds with known bioactivities to rescue erythropoiesis in the *mon* mutant. We incubated embryos with compounds from 5.3 hours post fertilization (hpf) until 22 hpf, the time of gastrulation and primitive erythropoiesis, and assayed embryonic *βe3 globin* expression using whole-mount in situ hybridization (WISH; Fig. 1A). This strategy identified the drug leflunomide as an inhibitor of dihydroorotate dehydrogenase (DHODH), the enzyme catalyzing the fourth step in the de novo pyrimidine biosynthesis pathway (*12*). Although *mon* embryos treated with leflunomide or its active metabolite, A771726 (*13*), showed increased *βe3 globin* expression, their wild-type and heterozygous siblings were blocked in erythroid differentiation (Fig. 1B and fig. S1, A and B). The fact that both leflunomide and A771726 rescued erythropoiesis in *mon* mutants ruled out an involvement of the aryl hydrocarbon receptor in this process, of which leflunomide has been described as an agonist (*14*). The structurally divergent DHODH inhibitor brequinar (*15*) similarly rescued the blood defect in *tif1γ*-depleted embryos, both at the level of *βe3 globin* expression (fig. S1C) and hemoglobin synthesis (Fig. 1C and fig. S1D), indicative of terminal erythropoiesis. In control embryos, DHODH inhibition led to a reduction in the number of hemoglobinized differentiated RBCs (Fig. 1C and fig. S1D). Modeling predicted the structures of zebrafish and human DHODH, including the binding pockets for A771726 and brequinar, to be highly conserved (fig. S2, A to C). These results demonstrate that inhibition of DHODH activity is required to rescue defective *tif1γ*-dependent erythropoiesis.

We performed time course studies to establish the developmental window during which DHODH is active in *mon* embryos. Treating embryos with leflunomide during gastrulation, but not later, was sufficient to rescue erythropoiesis in *mon* embryos (fig. S3). These results assign a critical early function for *tif1γ*, when specification of the erythroid lineage is initiated within mesoderm at the end of gastrulation. Blastula transplantation experiments showed a non-cell-autonomous role for *tif1γ* (fig. S4, A and B) in addition to its cell-autonomous role in erythropoiesis (fig. S4, C and D). During its development, mesoderm lies above the yolk sac, a metabolically active tissue that is a source of nutrients for the embryo proper and is analogous to the mammalian yolk sac and placenta (*16*, *17*). A non-cell-autonomous role of *tif1γ* could suggest a more direct metabolic function in the early embryo.

tif1γ loss leads to TCA cycle changes, DNA and histone hypermethylation

Because DHODH is the only enzyme of the pyrimidine de novo synthesis pathway located in mitochondria (*18*), we investigated whether mitochondrial metabolism was altered in *mon* mutant embryos. RNA-sequencing (RNA-seq) experiments for *tif1γ*-depleted embryos at 10 hpf (fig. S5 and data S1) revealed that 77% (182 genes) of genes encoding proteins with mitochondrial function (*19*) [95% (20 genes) when considering genes that encode for subunits of the respiratory chain] were transcriptionally down-regulated upon *tif1γ* loss of function (Fig. 2A, middle and right). By contrast, only 55% (or 1986 genes) of nonmitochondrial genes were transcriptionally down-regulated (Fig. 2A, left). Furthermore, mitochondrial genes were more significantly down-regulated compared with nonmitochondrial genes (fig. S6). These results indicate that mitochondrial gene expression specifically depends on *tif1γ*. DHODH inhibition did not alter the expression of p53 target genes (*20*), cell cycle genes, or genes involved in mitochondrial fission or fusion in *tif1γ*-depleted

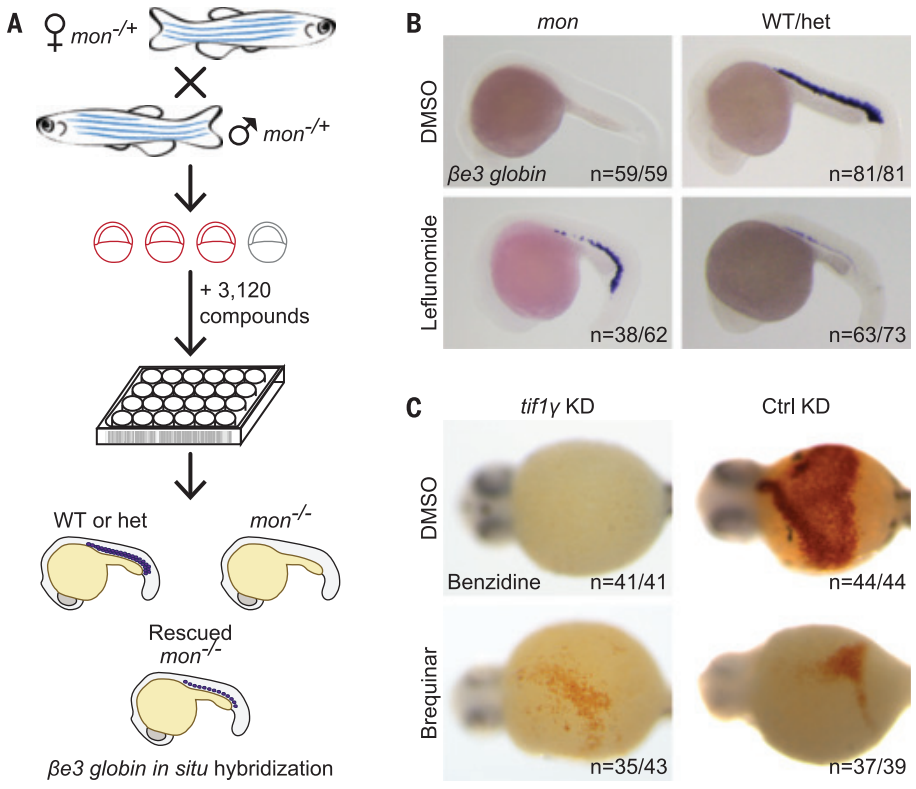

Fig. 1. Chemical suppressor screen for the *mon* zebrafish mutant identifies DHODH inhibitors to rescue primitive erythropoiesis. (**A**) Cartoon depicting chemical screening strategy. WT, wild type; het, *mon* heterozygous. (**B**) WISH for *βe3 globin* in *mon* and WT or het zebrafish embryos at 22 hpf treated with 7 μM leflunomide or DMSO. *N* (number of biological replicates) = 4. Cumulative results are shown. (**C**) Benzidine staining of embryos at 44 hpf after morpholino-mediated knockdown of *tif1γ* (*tif1γ* KD) or standard control knockdown (Ctrl KD) and treatment with 3.5 μM brequinar or DMSO from 5.3 hpf until 11.7 hpf. *N* = 3. Data from one representative experiment are shown. n = number of embryos with depicted phenotype/number of all embryos tested (see also fig. S1).

embryos (fig. S7, A and B; fig. S8; and data S2) but did promote differentiation processes including hematopoiesis specifically upon *tif1γ* loss, as shown by Metascape pathway analysis (fig. S9, A to D). Untargeted metabolomics analysis of *mon drl:EGFP* embryos at 22 hpf (Fig. 2B and fig. S10, A and B) or *tif1γ*-depleted embryos at 11 or 22 hpf (fig. S10, C and D) revealed reduced levels of several tricarboxylic acid (TCA) cycle metabolites, including citrate, its isomerization intermediate *cis*-aconitate, isocitrate, oxaloacetate, α-ketoglutarate (α-KG, also called 2-oxoglutarate), malate, and the TCA-cycle-related metabolite aspartate, suggesting a more general mitochondrial defect.

The activity of 2-oxoglutarate-dependent dioxygenases (OGGDs), which include DNA and histone demethylases, can be inhibited by an increased ratio of succinate, L-2-hydroxyglutarate (2HG), or fumarate to α-KG (*21*). Increased DNA and histone methylation levels have been observed after conditional knockout of mitochondrial complex III subunit Rieske iron-sulfur protein (encoded by UQCRFS1) in the hematopoietic system (*22*, *23*), and a biallelic variant in UQCRFS1 in humans has been recently described to cause anemia (*24*). In-depth TCA cycle metabolic analyses revealed that the succinate/α-KG ratio was significantly increased in *tif1γ*-depleted embryos (Fig. 2C), and the 2HG/α-KG and fumarate/α-KG ratios were elevated (fig. S10E). To address whether histone and DNA methylation levels were altered upon *tif1γ* loss, we profiled global chromatin modifications in histones extracted from *tif1γ*-depleted embryos at 22 hpf using quantitative targeted mass spectrometry (fig. S11, A and B). The absence of *tif1γ* led to significantly increased levels of the methylated histone species H3K27me1, H3K27me2, and H3K27me3, H3K36me2 and H3K36me3, as well as H4K20me2 (Fig. 2D and fig. S12, A and B), modifications that are removed by OGGDs (*25*). The levels of histone acetylation, phosphorylation, and ubiquitination remained unchanged (fig. S12A). The expression of histone demethylases in *tif1γ* knockdown and *mon* does not account for the changes in methylation (data S3). We next evaluated DNA methylation, which can be reversed by OGGDs. Reduced representation bisulfite sequencing (RRBS) experiments revealed significant hypermethylation of background (genome excluding CpG islands) CpG dinucleotides (CpGs; fig. S13, A and B, and data S4), which represented 94% of all CpGs covered by RRBS with at least 10 reads (fig. S13C). Our results indicate that the altered mitochondrial TCA cycle activity in the absence of *tif1γ* leads to an increased succinate/α-KG ratio that in turn results in changes in the epigenome with higher histone and DNA methylation levels.

Mitochondrial function is impaired upon *tif1γ* loss

To investigate whether *tif1γ* loss compromises mitochondrial function, we performed a high-throughput single-embryo analysis of the oxygen consumption rate (OCR). Embryos depleted for *tif1γ* exhibited a functional decrease in oxidative aerobic metabolism at 14 hpf compared with control embryos, as demonstrated by a significant decrease in the OCR at baseline (Fig. 3A and fig. S14A). Although DHODH inhibition by leflunomide treatment of wild-type embryos led to a reduced OCR, *tif1γ* depletion did not result in a further reduction. To estimate the reserve respiratory capacity, we treated embryos with the uncoupling agent carbonyl cyanide 4-(trifluoromethoxy)phenylhydrazone (FCCP), which abolishes the proton gradient and thus leads to an increase in oxygen consumption. Upon addition of FCCP, *tif1γ* depletion rescued the reduced OCR of DHODH-inhibited embryos (Fig. 3A and fig. S14B), showing that the function of DHODH in mitochondrial respiration is intimately linked to TIF1γ. In agreement with decreased baseline oxygen consumption of *tif1γ*-depleted embryos, we found that the ratio of oxidized to reduced nicotinamide adenine dinucleotides (NAD^+/NADH), which directly correlates with the OCR, was lowered in *mon* embryos (Fig. 3B). By comparison, embryos of the same age that were depleted for *gata1a*, the master transcription factor of the erythroid lineage and thus for RBCs (fig. S14C), showed an increased OCR over control-depleted embryos (fig. S14, D to F). *Gata1*$^-$ mouse embryonic stem cells give rise to an abnormal and highly proliferative blast population (*26*) that might exhibit high levels of mitochondrial respiration (*22*). These data show that mitochondrial respiration is required for blood formation and that *tif1γ* is required for normal mitochondrial function.

tif1γ drives erythropoiesis by affecting the electron transport chain

DHODH catalyzes the oxidation of dihydroorotate into orotate by transferring electrons to CoQ in the electron transport chain (ETC) (*27*). Thus, DHODH functionally links the production of pyrimidines with the mitochondrial respiratory chain (Fig. 4A). Uridine, which is converted through the salvage pathway into uridine monophosphate, can bypass the inhibition of de novo pyrimidine synthesis (fig. S15A). Although the erythroid differentiation block caused by DHODH inhibition in wild-type

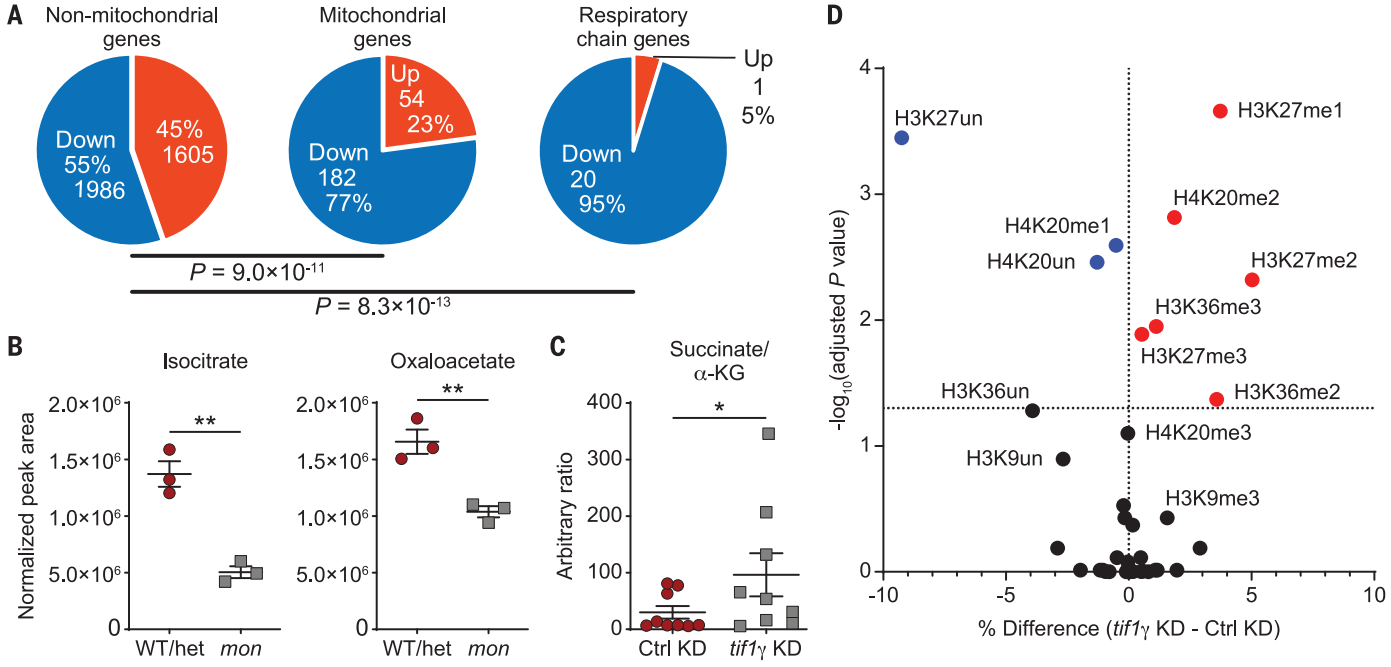

Fig. 2. *tif1γ* loss affects the TCA cycle and histone methylation. (**A**) RNA-seq data at 10 hpf showing all up- or down-regulated [FPKM (fragments per kilobase of transcript per million mapped reads) >1, $q < 0.05$] nonmitochondrial (left), mitochondrial (middle), and respiratory chain genes (right) in *tif1γ* KD or Ctrl KD embryos treated with DMSO from 5.3 hpf until 10 hpf. *P* values were determined by Pearson's chi-squared test with default parameters. (**B**) Levels of the indicated TCA cycle metabolites in *mon;Tg(drl:EGFP)* or sibling WT or het embryos at 22 hpf as measured by untargeted metabolomics. $N = 3$. Normalization by median correction. Data are shown as means ± SEM by two-tailed *t* test. (**C**) Succinate/α-KG ratio in *tif1γ* KD or Ctrl KD embryos at 22 hpf as measured by untargeted metabolomics. Data are shown as means ± SEM by two-tailed *t* test. (**D**) Volcano plot of percentage occupancy data of histone posttranslational modifications (PTMs) in *tif1γ* KD compared with Ctrl KD embryos at 22 hpf. Each dot represents a single modification at the amino acid level. *x*-axis shows the percentage difference between the means of *tif1γ* KD and Ctrl KD samples. Adjusted *P* values were determined by multiple *t* tests between all five replicates across the two conditions. Significantly enriched histone PTMs in *tif1γ* KD and Ctrl KD samples are shown in red and blue, respectively. $^{**}P < 0.01$; $^{*}P < 0.05$; ns, not significant (see also figs. S5 to S12).

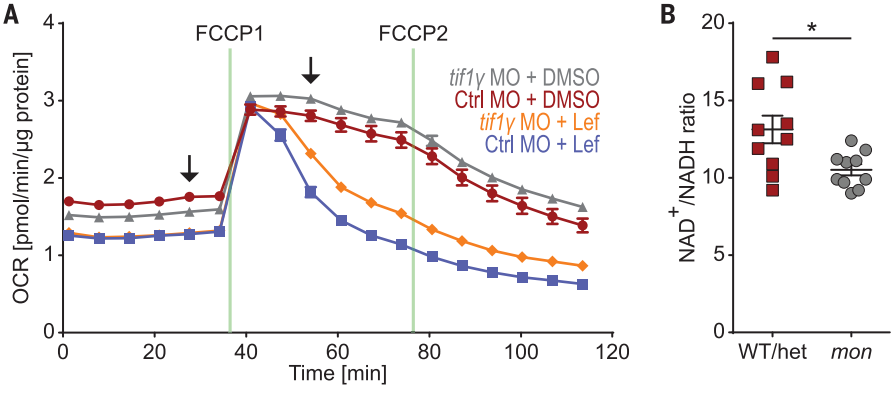

Fig. 3. *tif1γ* loss leads to a functional mitochondrial defect. (**A**) OCR as measured by Seahorse analysis of single *tif1γ* KD or Ctrl KD embryos at 16 hpf treated with 7 µM leflunomide or DMSO from 5.3 until 11 hpf. $N = 3$. Data from one representative experiment are shown. Data are shown as means ± SEM. Arrows indicate time points for which statistical analysis is shown in fig. S14, A and B. (**B**) Analysis of NAD^+/NADH ratio in *mon* and sibling WT or het embryos at 48 hpf using the NAD/NADH-Glo Assay. $N = 3$. Cumulative results are shown. One data point indicates one embryo. $^{*}P < 0.05$, two-tailed *t* test.

and heterozygous embryos could be partially reversed by the addition of uridine (fig. S15, B and C), the rescue of the *mon* blood defect by DHODH inhibition was not affected by uridine (Fig. 4B and fig. S15B), which could be caused by a "rewired metabolism" in *mon* mutants that may allow for more salvage pathway activity. To test whether the rescue of the *mon* blood defect by DHODH inhibition depends on DHODH's impact on mitochondrial electron transport, we cotreated *mon* embryos with leflunomide and rotenone, an inhibitor of complex I of the ETC. Indeed, rotenone reversed the rescue of *mon*'s blood defect by leflunomide, whereas on its own it did not rescue blood in *mon* (Fig. 4C). The antioxidant *N*-acetyl-L-cysteine did not rescue the *mon* blood defect (fig. S16). These results demonstrate that DHODH inhibition rescues the blood defect in *mon* embryos through its link to the ETC.

TIF1γ directly regulates CoQ levels in erythropoiesis

In the inner mitochondrial membrane, electrons are transferred from complex I or II to complex III in a manner dependent on CoQ, an electron carrier that cycles between three redox states (*28*). DHODH competes with complexes I and II of the ETC for CoQ as an electron acceptor (Fig. 4A). CoQ consists of a benzoquinone ring head group joined to a polyisoprenoid side chain (*29*), which is synthesized by an enzyme encoded by PDSS1 and PDSS2 in humans and zebrafish. The head group subsequently is modified by several COQ enzymes (fig. S17). *COQ2* deficiency in humans leads to pancytopenia and anemia in infancy, and quinone deficiencies can be rescued by an exogeneous ubiquinone analog (*30*). To

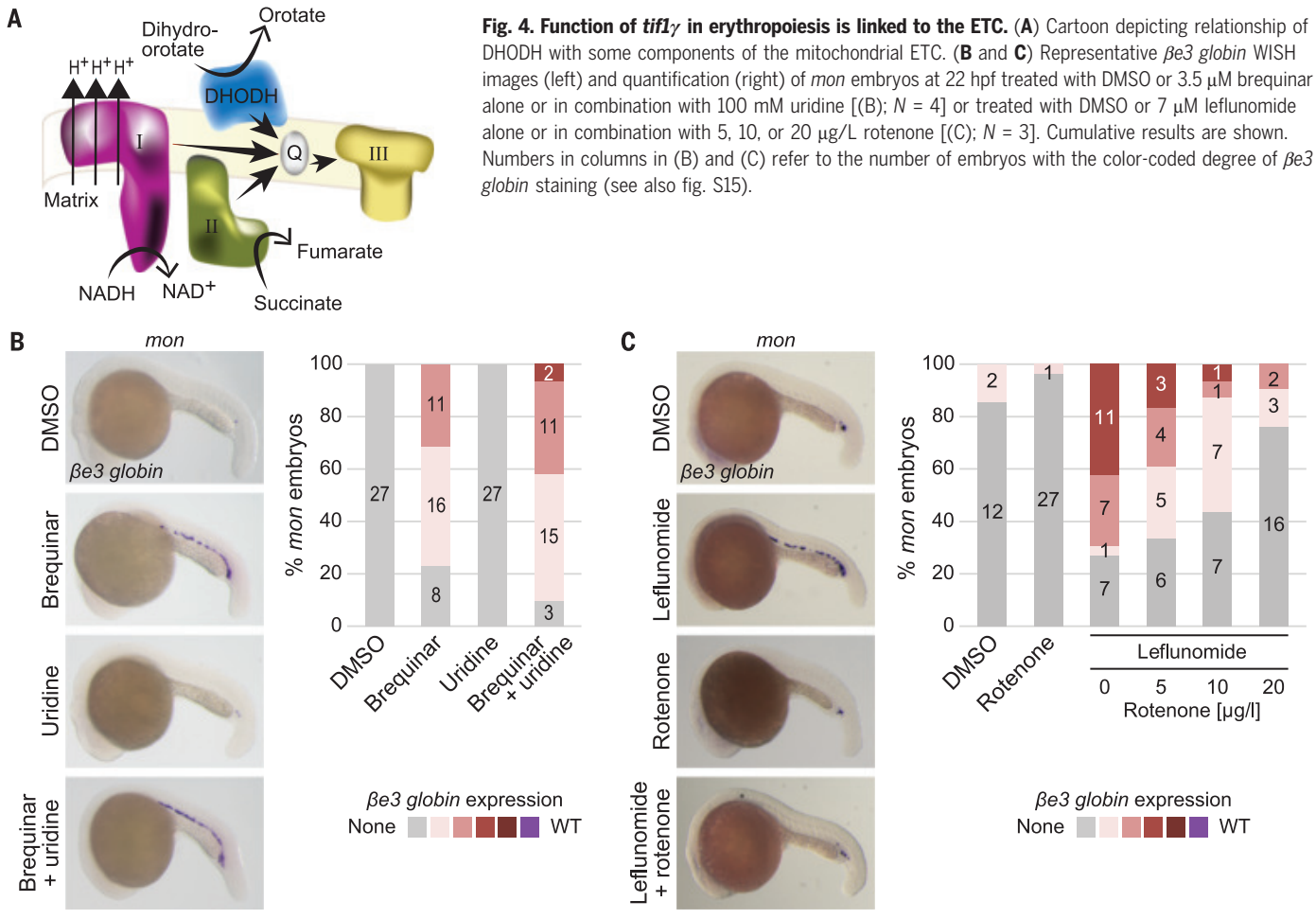

Fig. 4. Function of *tif1γ* in erythropoiesis is linked to the ETC. (**A**) Cartoon depicting relationship of DHODH with some components of the mitochondrial ETC. (**B** and **C**) Representative *βe3 globin* WISH images (left) and quantification (right) of *mon* embryos at 22 hpf treated with DMSO or 3.5 μM brequinar alone or in combination with 100 mM uridine [(B); *N* = 4] or treated with DMSO or 7 μM leflunomide alone or in combination with 5, 10, or 20 μg/L rotenone [(C); *N* = 3]. Cumulative results are shown. Numbers in columns in (B) and (C) refer to the number of embryos with the color-coded degree of *βe3 globin* staining (see also fig. S15).

evaluate the role of TIF1γ in the CoQ biosynthesis pathway, we generated stable human HepG2 cell lines that expressed one of two different *TIF1γ* shRNAs (shTIF1γ) or control shRNAs (shCtrl) under doxycycline control. We chose HepG2 cells as metabolically active cells akin to the yolk sac in the early zebrafish embryo. In these clonal cell lines, shTIF1γ-1 and shTIF1γ-2 induction specifically reduced *TIF1γ* expression by 98% and 50%, respectively, after 48 hours (Fig. 5A and fig. S18A), which correlated with reduced TIF1γ protein levels (fig. S18B). At this time point, we performed RNA-seq analysis, comparing both shTIF1γ with both shCtrl clones, in combination with chromatin immunoprecipitation-sequencing (ChIP-seq) analysis for TIF1γ chromatin occupancy, to identify differentially expressed genes that are also direct TIF1γ targets. Direct TIF1γ target genes frequently belonged to metabolic pathways (fig. S18C). In particular, several genes encoding CoQ pathway enzymes were significantly down-regulated upon shTIF1γ-1 and shTIF1γ-2 knockdown, including *PDSS1* by 88% and 35% and *COQ8A* by 42% and 69%, respectively, as well as *PDSS2* by 57% and *COQ2* by 84% in the more potent shTIF1γ-1 condition. Expression of the actin gene *ACTA2* remained unaffected by *TIF1γ* knockdown (fig. S18A). At the protein level, PDSS1 was down-regulated twofold upon *TIF1γ* knockdown (Fig. 5B). ChIP-seq analysis revealed that TIF1γ bound to the loci of these CoQ pathway genes and was often accompanied by the histone mark H3K27Ac, decorating active promoters and enhancers (Fig. 5C and fig. S19). These data establish that CoQ biosynthesis genes are direct targets of TIF1γ.

We hypothesized that down-regulation of CoQ pathway genes upon *TIF1γ* depletion and exhausted CoQ levels could be functionally relevant to the role of *tif1γ* in embryonic erythropoiesis. To test this idea, we measured CoQ levels in the zebrafish. We first determined that, as in humans but unlike in mice (*28*), the zebrafish CoQ isoprenoid side chain consists of 10 subunits (fig. S20A). Although the *mon* mutant is embryonically lethal, in rare cases, homozygous mutant *mon* fish survive into adulthood despite producing only very few mature RBCs (*9*). In other animals, livers have been described to contain normal levels of CoQ (*31*). In a large-scale effort, we generated sufficient numbers of *mon* fish, dissected their livers at 2 and 4.5 months, and found that CoQ_{10} levels were significantly reduced (Fig. 5D) and CoQ biosynthesis gene expression was down-regulated (fig. S20B and supplementary text). Treatment of *mon* embryos from the onset of gastrulation until 22 hpf with the CoQ analog decylubiquinone rescued *βe3 globin* expression in 26% (33/126) of *mon* embryos (Fig. 5E and fig. S21). We propose that in the absence of *tif1γ*, mitochondrial respiratory capacity is impaired because of insufficient electron transfer from complexes I and II to complex III of the ETC, thus shifting the balance in the hemogenic mesoderm to the undifferentiated cell state. Supplying *mon* embryos with CoQ boosts mitochondrial respiration and promotes erythroid differentiation.

Discussion

Tissue differentiation can be regulated by metabolic activities. It was previously unclear how lineage transcription factors induce distinct changes during cell fate specification and lineage differentiation. Our work demonstrates that the metabolic state of the tissue required for early erythroid lineage differentiation is under the direct transcriptional control of TIF1γ. CoQ is a critical downstream effector of TIF1γ transcriptional activity, regulating the balance between nucleotide synthesis and ETC activity

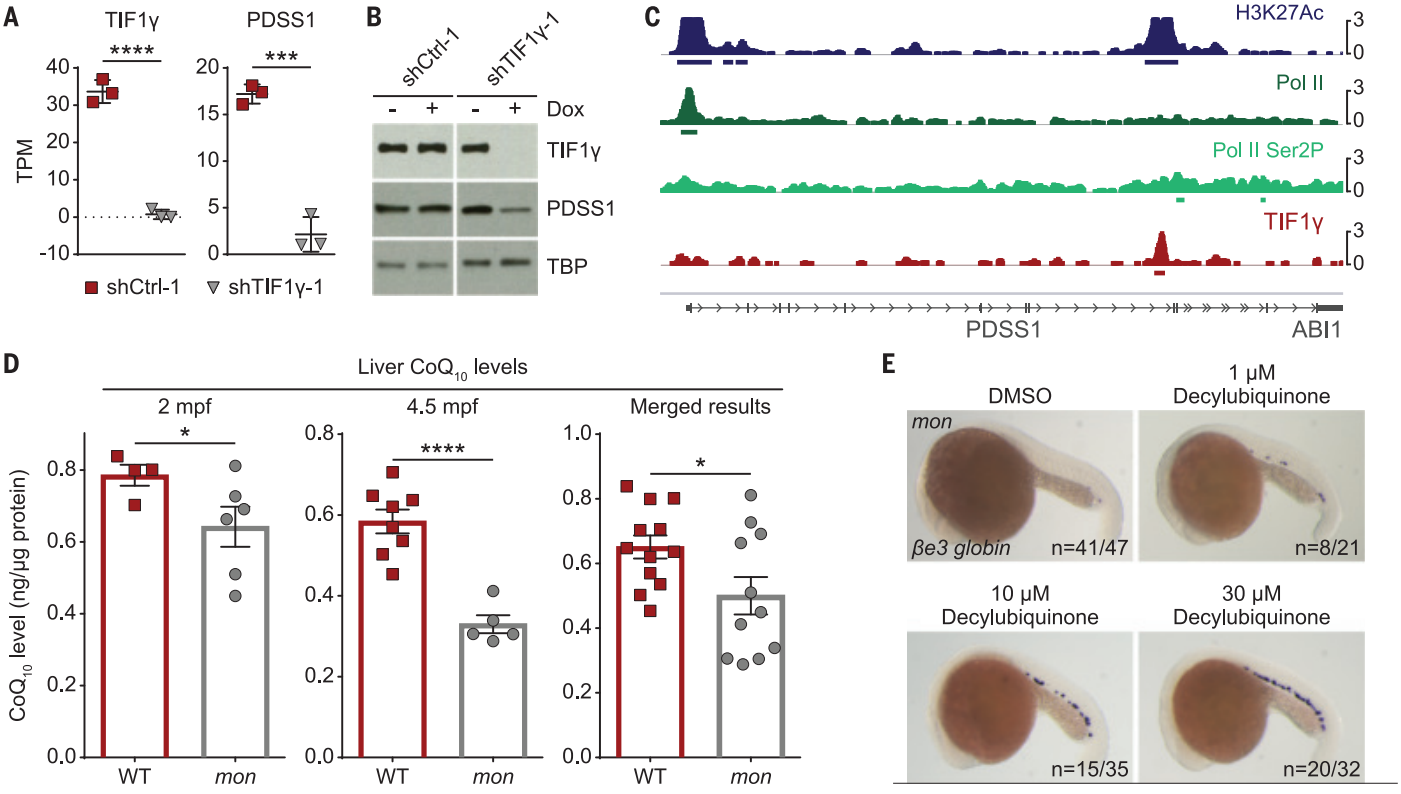

Fig. 5. CoQ is a functional target of *tif1γ* in primitive erythropoiesis. (**A**) RNA-seq data showing transcripts per kilobase million (TPM) of *TIF1γ* and *PDSS1* in two stable HepG2 clones carrying either an inducible shRNA targeting *TIF1γ* (shTIF1γ-1) or a control shRNA (shCtrl-1) 48 hours after induction with doxycycline. $N = 3$. Results were analyzed with two-tailed t test. (**B**) Western blot of TIF1γ and PDSS1 for the experiment described in (A). TBP was used as the loading control. (**C**) IGV output of a 52-kb genomic region around *PDSS1* on chromosome 10 showing the chromatin occupancy by ChIP-seq for H3K27Ac, Pol II, Pol II phosphorylated at serine 2 (Pol II Ser2P), and TIF1γ in HepG2 cells. (**D**) CoQ_{10} quantification of adult *mon* and WT livers at indicated time points by HPLC. mpf, months postfertilization. Merged results are shown on the right. Each dot represents five pooled livers (except for one sample per genotype at 4.5 mpf, which only contained three livers). Normalization to total protein amount per sample. (**E**) Representative *βe3 globin* WISH images of embryos at 22 hpf treated with DMSO or 1, 10, 20, or 30 µM decylubiquinone. $N = 3$. Cumulative results are shown. $^{****}P < 0.0001$; $^{***}P < 0.001$; $^{*}P < 0.05$ (see also figs. S18 to S21).

in embryonic erythropoiesis. This highlights a previously unappreciated role of mitochondrial respiration in driving the early commitment of the erythroid lineage. It has been proposed that transcriptional and metabolic processes influence each other (*32*, *33*). We demonstrate that this is the case in early erythropoiesis, where exogenous CoQ can drive erythroid differentiation in the *mon* mutant, including the expression of embryonic *globin* as a late lineage marker. This study thus offers the possibility for metabolic therapeutics that could be used to target otherwise difficult-to-treat deficiencies in transcriptional programs.

REFERENCES AND NOTES

1. M. H. Baron, *Stem Cells* **31**, 849–856 (2013).
2. J. Palis, *Front. Physiol.* **5**, 3 (2014).
3. M. W. Lensch, G. Q. Daley, *Curr. Top. Dev. Biol.* **60**, 127–196 (2004).
4. S. H. Orkin, L. I. Zon, *Cell* **132**, 631–644 (2008).
5. N. Cabezas-Wallscheid *et al.*, *Cell* **169**, 807–823.e19 (2017).
6. R. Aucagne *et al.*, *J. Clin. Invest.* **121**, 2361–2370 (2011).
7. X. Bai *et al.*, *Dev. Biol.* **373**, 422–430 (2013).
8. W. He *et al.*, *Cell* **125**, 929–941 (2006).
9. D. G. Ransom *et al.*, *PLOS Biol.* **2**, E237 (2004).
10. D. G. Ransom *et al.*, *Development* **123**, 311–319 (1996).
11. X. Bai *et al.*, *Cell* **142**, 133–143 (2010).
12. I. Lieberman, A. Kornberg, *Biochim. Biophys. Acta* **12**, 223–234 (1953).
13. R. A. Williamson *et al.*, *J. Biol. Chem.* **270**, 22467–22472 (1995).
14. E. F. O'Donnell *et al.*, *PLOS ONE* **5**, e13128 (2010).
15. S. Liu, E. A. Neidhardt, T. H. Grossman, T. Ocain, J. Clardy, *Structure* **8**, 25–33 (2000).
16. L. Carvalho, C. P. Heisenberg, *Trends Cell Biol.* **20**, 586–592 (2010).
17. A. Donovan *et al.*, *Nature* **403**, 776–781 (2000).
18. J. J. Chen, M. E. Jones, *Arch. Biochem. Biophys.* **176**, 82–90 (1976).
19. D. J. Pagliarini *et al.*, *Cell* **134**, 112–123 (2008).
20. M. Fischer, *Oncogene* **36**, 3943–3956 (2017).
21. I. Martínez-Reyes, N. S. Chandel, *Nat. Commun.* **11**, 102 (2020).
22. E. Ansó *et al.*, *Nat. Cell Biol.* **19**, 614–625 (2017).
23. S. E. Weinberg *et al.*, *Nature* **565**, 495–499 (2019).
24. M. Gusic *et al.*, *Am. J. Hum. Genet.* **106**, 102–111 (2020).
25. M. S. Islam, T. M. Leissing, R. Chowdhury, R. J. Hopkinson, C. J. Schofield, *Annu. Rev. Biochem.* **87**, 585–620 (2018).
26. D. L. Stachura, S. T. Chou, M. J. Weiss, *Blood* **107**, 87–97 (2006).
27. J. T. Madak, A. Bankhead 3rd, C. R. Cuthbertson, H. D. Showalter, N. Neamati, *Pharmacol. Ther.* **195**, 111–131 (2019).
28. Y. Wang, S. Hekimi, *Trends Cell Biol.* **26**, 367–378 (2016).
29. J. A. Stefely, D. J. Pagliarini, *Trends Biochem. Sci.* **42**, 824–843 (2017).
30. J. Mollet *et al.*, *J. Clin. Invest.* **117**, 765–772 (2007).
31. A. C. Casey, E. G. Bliznakov, *Cancer Res.* **33**, 1183–1186 (1973).
32. S. Donati, T. Sander, H. Link, *Wiley Interdiscip. Rev. Syst. Biol. Med.* **10**, e1396 (2018).
33. C. Guijas, J. R. Montenegro-Burke, B. Warth, M. E. Spilker, G. Siuzdak, *Nat. Biotechnol.* **36**, 316–320 (2018).

ACKNOWLEDGMENTS

We thank R. Mori and M. C. Nonato for generating the DHODH alignment and structural model; L. Krug for excellent care of our fish; C.-Y. Chiang, E. Lee, S. Kernet, W. Chaudhry, T. Schlaeger, D. Gupta, L. Rubin, T. Arvanites, K. Nybakken, and V. Oza for technical assistance with the chemical suppressor screen; S. Freyer, J. Weiss, and H. Moreau for other technical assistance; M. Prasad for help with RNA-seq data mapping; members of the Zon laboratory for discussions; and A. B. Cantor and B. Boettner for critical reading of the manuscript. **Funding:** This work was supported by the National Heart, Lung, and Blood Institute (grants 4R01HL048801, 5P01HL032262, 5U01HL134812, and 1P01HL131477 to L.I.Z.); the National Institute of Diabetes and Digestive and Kidney Diseases (grants 1U54DK110805 and 3R24DK092760 to L.I.Z.); Harvard Catalyst (L.I.Z.); the Canadian Institutes of Health Research (foundation grant FDN0159916 to S.H. and Y.W.); the National Cancer Institute (grant 5R01CA213062 to M.C.H.); the National Institute of General Medical Sciences (grant R35GM127045 to S.L.S.); the National Human Genome Research Institute (grant U54-HG008097 to M.P.); the Cancer Research Institute (I.E.); and the American Lebanese Syrian Associated Charities (B.J.A.). **Author contributions:** M.P.R. and L.I.Z. conceived the project; M.P.R. performed most of the experiments and analyzed the data. B.J.A. and S.Y. analyzed ChIP-seq and RNA-seq data. J.M., M.P., and S.A.C. performed histone modification analyses. Y.W. performed the CoQ measurements. I.E., S.V., and M.C.H. helped with metabolomics experiments. J.R.P. and E.J.H. helped with blastula transplantation experiments and imaging. S.H., R.W., and A.M. performed DNA methylation analyses. K.H., V.C., B.D., and E.C.G. provided research

assistance. P.P.N. and S.L.S. provided synthetic chemistry and chemical biology expertise. L.B.S. provided constructive suggestions and protocols. C.R.W. and C.A.C. provided the Seahorse and expertise. I.A. provided zebrafish husbandry expertise. R.A.Y. provided feedback on study design and experimental results. M.P.R. and L.I.Z. wrote the manuscript with input from B.J.A., S.Y., J.M., M.P., I.E., J.R.P., E.J.H., S.H., R.W., P.P.N., L.B.S., C.R.W., E.C.G., S.L.S., R.A.Y., A.M., M.C.H., and S.H. **Competing interests:** B.J.A. is a shareholder in Syros Pharmaceuticals. C.A.C. is a founder and Chief Scientific Officer of Sana Biotechnology. S.L.S. serves on the Board of Directors of the Genomics Institute of the Novartis Research Foundation (GNF), is a shareholder in and serves on the Board of Directors of Jnana Therapeutics, is a shareholder in Forma Therapeutics, is a shareholder in and advises Decibel Therapeutics and Eikonizo Therapeutics, serves on the Scientific Advisory Boards of Eisai Co., Ltd., Ono Pharma Foundation, Exo Therapeutics and F-Prime Capital Partners, and is a Novartis Faculty Scholar. R.A.Y. is a founder of and shareholder in Syros Pharmaceuticals, Camp4 Therapeutics, Omega Therapeutics and Dewpoint Therapeutics. M.C.H. serves on the Scientific Advisory Board of Pori Therapeutics. S.A.C. is a member of the scientific advisory boards of Kymera, PTM BioLabs and Seer, and is a scientific adviser to Pfizer and Biogen. L.I.Z. is a founder of and holds stock in Fate Therapeutics, Camp4 Therapeutics and Scholar Rock, and is a consultant to Celularity. All other authors declare no competing interests. **Data and materials availability:** The RNA-seq, ChIP-seq, and RRBS data of this study are deposited in the NCBI Gene Expression Omnibus (GEO) under accession number GSE136456.

SUPPLEMENTARY MATERIALS

science.sciencemag.org/content/372/6543/716/suppl/DC1
Materials and Methods
Supplementary Text
Figs. S1 to S21
Table S1
References (*34*–*75*)
Data S1 to S4
MDAR Reproducibility Checklist

26 August 2019; accepted 29 March 2021
10.1126/science.aaz2740

REPORTS

SUPERCONDUCTIVITY

Electric field control of superconductivity at the $LaAlO_3/KTaO_3(111)$ interface

Zheng Chen[1]†, Yuan Liu[1]†, Hui Zhang[2]†, Zhongran Liu[3], He Tian[3], Yanqiu Sun[1], Meng Zhang[1], Yi Zhou[4,5,6]*, Jirong Sun[4,5,7]*, Yanwu Xie[1,8]*

The oxide interface between $LaAlO_3$ and $KTaO_3(111)$ can harbor a superconducting state. We report that by applying a gate voltage (V_G) across $KTaO_3$, the interface can be continuously tuned from superconducting into insulating states, yielding a dome-shaped T_c-V_G dependence, where T_c is the transition temperature. The electric gating has only a minor effect on carrier density but a strong one on mobility. We interpret the tuning of mobility in terms of change in the spatial profile of the carriers in the interface and hence, effective disorder. As the temperature is decreased, the resistance saturates at the lowest temperature on both superconducting and insulating sides, suggesting the emergence of a quantum metallic state associated with a failed superconductor and/or fragile insulator.

Controlling superconductivity with an electric field is intriguing for both fundamental research and potential applications (*1*–*11*). Analogous to the case of semiconducting field-effect transistors (*9*), the two-dimensional (2D) carrier density n_{2D} of a superconductor can be tuned by applying an external gating voltage V_G. The attainable tuning ability can be estimated as $\delta n_{2D} = \varepsilon_0\varepsilon_r V_G/et$, where ε_0 is the vacuum permittivity, e is the elementary charge, and ε_r and t are the dielectric constant and the thickness of the dielectric material, respectively. To achieve prominent tuning of the superconductivity, particularly a transition from superconducting to insulating states, a δn_{2D} value that is comparable with n_{2D} is generally needed. However, the n_{2D} value of most superconductors is very high and far beyond the capability of typical electric gating (~10^{14} cm^{-2} or lower) (*9*). Therefore, it has been a long-standing challenge to control superconductivity electrostatically.

With recent advances in material fabrication and tuning technology, prominent tunings of superconductivity have been experimentally realized for a few systems, including oxide interfaces (*1*, *6*, *7*), electric-double-layer interfaces (*2*–*4*, *8*, *10*, *11*), and magic-angle graphene superlattices (*5*). These tunings were achieved by pushing the superconducting layer to an ultrathin limit to reduce n_{2D}, by developing technologies such as electric-double-layer gating to improve tuning ability (*3*, *11*), or— most often—by both (*2*, *12*). The tuning parameter in all these systems is n_{2D}.

$KTaO_3$(KTO) shares many common properties with $SrTiO_3$(STO) (*13*). In comparison with the well-known $LaAlO_3$(LAO)/STO interface (*14*), a 2D electron gas was observed at the LAO/KTO(001) (*15*) and $LaTiO_3$/KTO(001) (*16*) interfaces, but no superconductivity was reported. Superconductivity was observed at the electric-double-layer-gated KTO(001) surface; however, the transition temperature T_c was low (~0.05 K) (*4*). Very recently, it was found that the EuO/KTO(111) and LAO/KTO(111) interfaces can be superconducting with a T_c of up to ~2 K (*17*).

Here we demonstrate that the superconductivity at the LAO/KTO(111) interface can be tuned by applying V_G, and that, rather than n_{2D}, the key tuning parameter appears to be mobility, which can be associated with an "effective disorder."

We grew LAO films by pulsed laser deposition on 0.5-mm-thick single-crystalline KTO(111) substrates (*18*). The surfaces of these films were atomically flat (fig. S1). The microstructure of the interface was assessed by scanning transmission electron microscopy (STEM), which shows that LAO is homogeneous and amorphous (Figs. 1, A and B). The lack of epitaxial growth can be ascribed to the large lattice mismatch (*15*): The cubic lattice constants are 0.379 and 0.399 nm for LAO and KTO, respectively. The LAO films themselves are highly insulating; the conductance is in the KTO layer near the interface. A sketch of the field-effect device is shown in Fig. 1C. The gating voltage V_G is applied between the conducting LAO/KTO layer and a silver paste electrode at the back of the KTO. The active area of the device was patterned into a Hall bar configuration (Fig. 1D). All transport measurements in this study were performed on the same device.

The occurrence of superconductivity with a midpoint T_c ~2 K can be clearly seen in the temperature-dependent sheet resistance $R_{sheet}(T)$ (Fig. 1E). The thickness of the superconducting layer is estimated to be ~4 nm, and the estimated coherence length is ~18.8 nm (fig. S3). The comparison of these two length scales suggests a 2D superconductor. The 2D nature of the superconductivity can be further justified by the nonlinear current-voltage response [$V \sim I^3$

[1]Interdisciplinary Center for Quantum Information, State Key Laboratory of Modern Optical Instrumentation, and Zhejiang Province Key Laboratory of Quantum Technology and Device, Department of Physics, Zhejiang University, Hangzhou 310027, China. [2]School of Integrated Circuit Science and Engineering, Beihang University, Beijing, 100191, China. [3]Center of Electron Microscope, State Key Laboratory of Silicon Materials, School of Materials Science and Engineering, Zhejiang University, Hangzhou, 310027, China. [4]Beijing National Laboratory for Condensed Matter Physics and Institute of Physics, Chinese Academy of Sciences, Beijing 100190, China. [5]Songshan Lake Materials Laboratory, Dongguan, Guangdong 523808, China. [6]Kavli Institute for Theoretical Sciences and CAS Center for Excellence in Topological Quantum Computation, University of Chinese Academy of Sciences, Beijing 100190, China. [7]School of Physical Sciences, University of Chinese Academy of Sciences, Beijing 100049, China [8]Collaborative Innovation Center of Advanced Microstructures, Nanjing University, Nanjing 210093, China.
†These authors contributed equally to this work.
***Corresponding author. Email: yizhou@iphy.ac.cn (Y. Z.); jrsun@iphy.ac.cn (J. S.); ywxie@zju.edu.cn (Y. X.)**

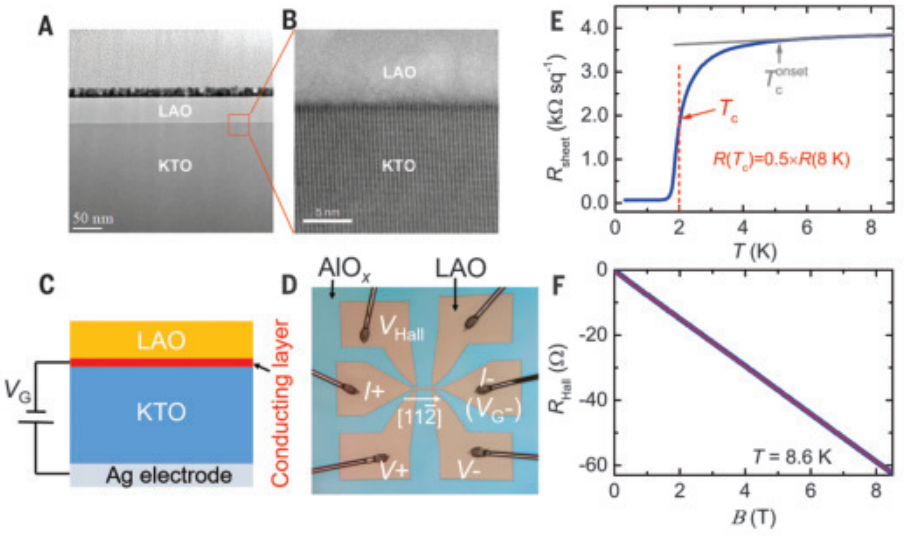

Fig. 1. Characterization of the LAO/KTO(111) device. (**A** and **B**) STEM images of a 40-nm LAO/KTO sample show that the LAO film is homogeneous and amorphous. (**C**) Cross-sectional view of the device structure. (**D**) Photograph of a typical device with bonded Al contacting wires. The device was fabricated in a six-probe Hall bar configuration. The conducting region is limited to the LAO/KTO interface (Hall bar area). The outside insulating region was obtained by coating amorphous AlO_x as a hard mask. The central Hall bar bridge is 20 μm in width and 100 μm in length (between V^+ and V^-). The current drain (I-) and the gating contact to the interface (V_G-) share the same probe. The electrical current flows along the [11$\bar{2}$] crystal axis. (**E**) Dependence of R_{sheet} on temperature and (**F**) dependence of R_{Hall} on the magnetic field for the 20-nm LAO/KTO device at V_G = 0.

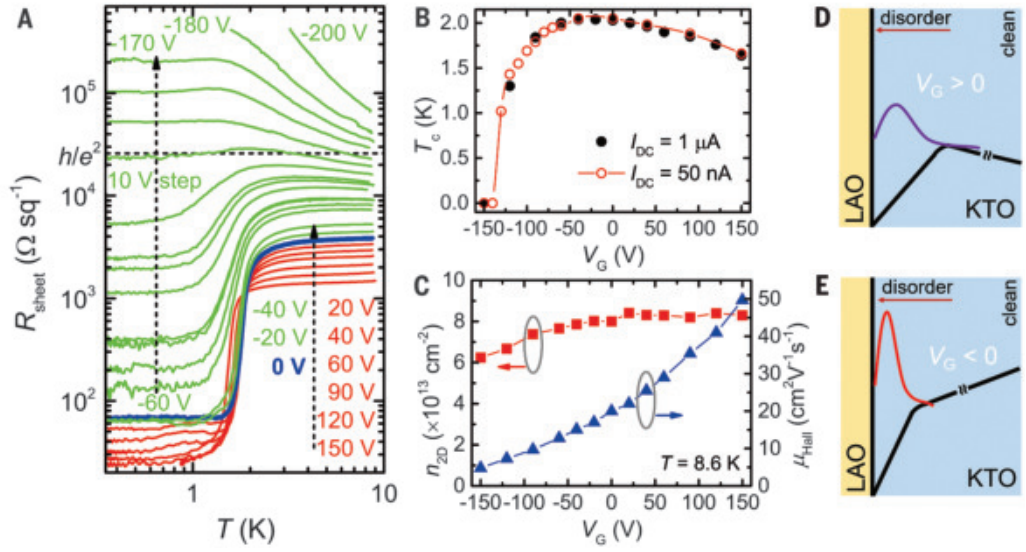

Fig. 2. Electric field control of transport properties. (**A**) Temperature-dependent $R_{sheet}(T)$, (**B**) midpoint T_c, and (**C**) carrier density n_{2D} and mobility μ_{Hall} at different V_G values. The dashed line in (A) indicates the position of the quantum resistance h/e^2. Two sets of data measured using different DC currents are shown in (B). The black filled circles represent the data measured in the same run as the Hall-effect measurements. (**D** and **E**) Schematic diagrams of the operations for V_G > 0 and V_G < 0, respectively. The purple and red lines represent the electron envelope wave function perpendicular to the interface, matching the potential well (thick solid lines) at the corresponding V_G. A higher degree of disorder is expected in the region closer to the interface.

dependence indicates a typical Berezinskii-Kosterlitz-Thouless (BKT) transition as shown in fig. S4], the large anisotropy of the upper critical field H_{c2} (fig. S3), and the magnetic-field–angle dependence of $R_{sheet}(T)$ (fig. S5).

The normal-state Hall resistance measured at 8.6 K (Fig. 1F) demonstrates that the charge carriers are electrons rather than holes, and the carrier density n_{2D} is ~8.5×10^{13} cm^{-2}. This value is much higher than that of a typical LAO/STO interface (*1*, *19*–*22*) and is not expected to be appreciably tuned by applying V_G. As an estimation, adopting a low-temperature ε_r of 5000 for KTO (*23*), a 300-V variation in V_G can induce a δn_{2D} value of only ~1.7×10^{13} cm^{-2} (~20% of the total n_{2D}). Given that ε_r in the interface region can be severely degraded by growth-induced defects and V_G-caused electric fields, the real attainable density δn_{2D} is expected to be even smaller, and thus insufficient to produce any prominent tuning. However, contrary to this expectation, the transport properties of the device were strongly tuned. When sweeping V_G from 150 V to −200 V, the device transits continuously from a superconductor to an insulator, and the normal-state resistance varies by more than two orders of magnitude (Fig. 2A). The V_G-tuned superconductor-insulator transition can also be convincingly seen in the evolution of the current-voltage behavior (Fig. 3). The midpoint T_c derived from the $R_{sheet}(T)$ values (Fig. 2A and figs. S6 and S7) exhibits an interesting dome-shaped dependence on V_G (Fig. 2B). This dependence resembles the dome-shaped superconducting phase diagram observed in many other systems (*1*, *4*, *11*), but the underlying mechanism is different because n_{2D} in the present device is not changed much by V_G, as shown below. It is worth mentioning that the present gate-tuned T_c does not obey the scaling relation $T_c \propto (V_G\text{-}V_c)^{2/3}$ that was observed in LAO/STO and attributed to V_G-induced carrier density changes (*1*) (fig. S8).

To characterize these tunable effects, we carried out normal-state Hall-effect measurements for different V_G values. To avoid any hysteresis effect, these measurements were made just before the $R_{sheet}(T)$ measurement for each V_G. The derived n_{2D} and Hall mobility μ_{Hall} are summarized in Fig. 2C. The data in the V_G range between 150 and −40 V are informative. In this range, n_{2D} changes only slightly, whereas μ_{Hall} decreases from ~50 to ~15 cm^2 V^{-1} s^{-1}. This strongly suggests that V_G mainly modulates the carrier mobility; we interpret this finding in terms of V_G tuning the effective

disorder in the conducting layer, which in turn modulates the electron scattering rate and thereby the charge carrier mobility. The relatively fast decrease in n_{2D} for $V_G < -40$ V is an indication of disorder-induced localization and cannot be attributed to δn_{2D} produced by the capacitance effect (note that varying V_G between −40 and −150 V can induce a $\delta n_{2D} \sim 0.6 \times 10^{13}$ cm^{-2} at best, which is only 37% of the experimentally observed value). It is convenient to characterize the effective disorder by the value of $k_F l$, where k_F is the Fermi wave vector and l is the electron mean-free path. By applying the data for R_{sheet} (8 K) and n_{2D} (8.6 K), we found that $k_F l$ was tuned from 17.5 ($k_F l \gg 1$, clean) to 0.4 ($k_F l \lesssim 1$, strongly disordered) by varying V_G (from 150 to −200 V, fig. S10). The corresponding value of the Drude conductivity is $\sigma_D^{(2D)} \sim (5-18) \times e^2/h$ at $k_F l > 5$.

As V_G varies from 150 to −80 V, the superconducting layer thickness decreases gradually from above 6 nm to below 2 nm (fig. S11). Supported by this observation, the V_G-induced modulation of effective disorder can be understood as sketched in Fig. 2, D and E: The electron envelope wave function is pushed away or compressed toward the interface by $V_G > 0$ or < 0. Because the disorder strength usually has a gradient from the disordered interface to the ordered interior, a variation in the spatial distribution of electrons equivalently causes a change in the average effective disorder. A similar modulation of the effective disorder by applying V_G was observed previously in the LAO/STO interface (*19*, *20*, *22*). Whereas the disorder effect generally plays a secondary role in LAO/STO, it dominates in our LAO/KTO device. This difference can be attributed to the following three factors: First, the dielectric constant of KTO (*23*) is smaller than that of STO (*1*); second, the n_{2D} of LAO/KTO is larger than that of LAO/STO (*1*, *19*–*22*); third, compared with LAO/STO (*19*–*22*), LAO/KTO has a much higher effective disorder, as indicated by the low-mobility μ_{Hall}, probably owing to the more disordered interface and the thinner electron gas.

Considering the framework above, the tuning achieved by V_G is concluded to be a natural disorder-driven effect. Disorder-driven superconductor-to-insulator quantum phase transitions (QPTs) have been intensely studied in disordered films (*24*–*27*). Compared with that configuration, the present device is distinctive because its effective disorder can be continuously tuned by V_G. Notably, although we observed an apparent superconductor-insulator transition and a large variation in R_{sheet}, a true superconducting ground state ($R_{sheet} = 0$) is absent. As shown in Fig. 2A [see also the Arrhenius plot of $R_{sheet}(T)$, fig. S12], on the superconducting side, the resistance $R_{sheet}(T)$ does not reach zero even at the lowest temperatures and saturates below ~1 K. Measured

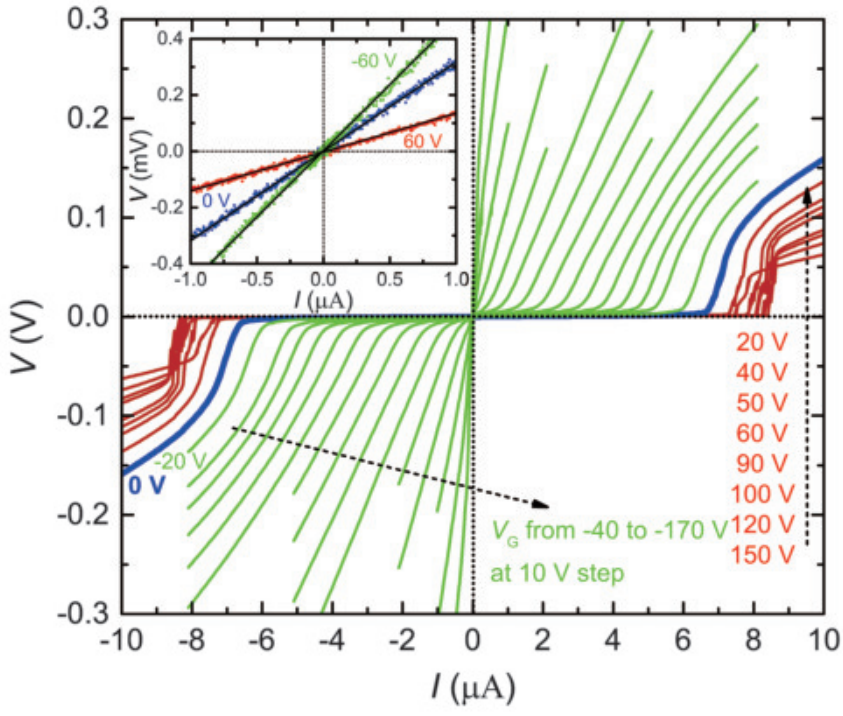

Fig. 3. Current (*I*)-voltage (*V*) behaviors of the central 20 μm by 100 μm bridge for V_G varying from 150 to −170 V. The measurements were performed at $T = 0.35$ K. The evolution from superconducting to insulating states is indicated from the gradual variation in the superconducting critical current. Inset: Three typical linear *I*-*V* dependences in the low current range.

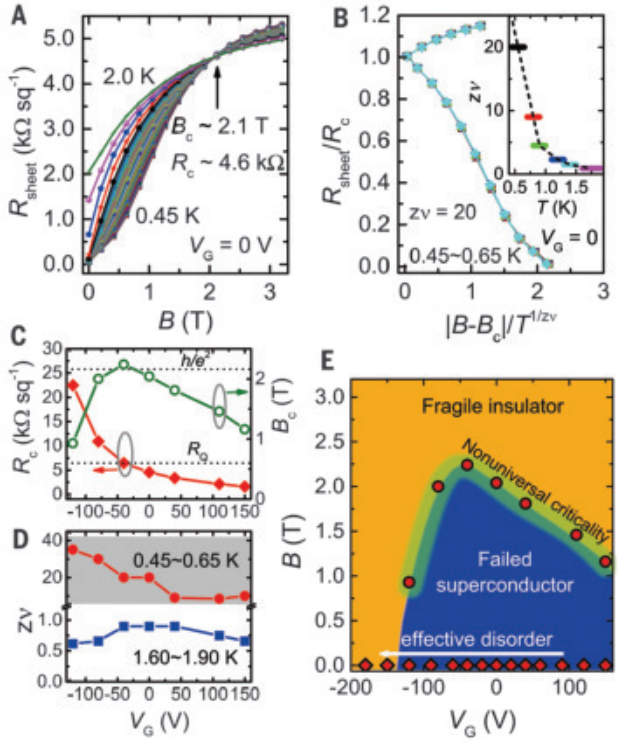

Fig. 4. V_G modulation during a QPT driven by a magnetic field perpendicular to the interface. (**A**) Dependence of R_{sheet} on the magnetic field B at fixed temperatures below 2 K. These curves were replotted from the temperature-dependent $R_{sheet}(T)$ data shown in fig. S5A. (**B**) Scaling of the data in 0.45 K ≤ T ≤ 0.65 K with respect to a single variable $|B - B_c|/T^{1/z\nu}$, with $z\nu = 20$. The inset shows the $z\nu$ values needed to scale the data in different temperature regimes (thick lines). (**C**) Dependences of R_c and B_c on V_G. The dashed lines indicate the positions of the quantum resistance h/e^2 and the pair quantum resistance R_Q. (**D**) Dependence of $z\nu$ on V_G for 0.45 K ≤ T ≤ 0.65 K (circles) and 1.60 K ≤ T ≤ 1.90 K (squares). The gray shadow highlights the large uncertainty in determining the $z\nu$ values in the low-temperature regime (see fig. S15). (**E**) A schematic V_G-B phase diagram for $T = 0$. The red dots correspond to the green circles in Fig. 4C; the red diamonds correspond to the data shown in Fig. 2A ($B = 0$). For $B > B_c$, in the insulating phase, R_{sheet} still saturates to a finite value (fig. S16).

with or without filters, the residual resistance is unchanged, which excludes the possibility of radiation thermalization (fig. S13). This intrinsic residual resistance, whose value spans a wide range from ~20 to above 10^3 ohms/square, can be tuned continuously with V_G.

The superconductivity in our system is verified not only by the large drop of the resistance at T_c, but also by the existence of a critical current. As illustrated in Fig. 3, at T = 0.35 K, the critical current is ~8.3 μA at V_G = 100 V and decreases as V_G decreases and eventually vanishes at the superconductor-insulator transition. For gating voltage V_G from 150 to −130 V, the resistance at temperatures below T_{BKT} (~1.7 K at V_G = 0) is measured by applying a DC current smaller than the critical current, where the linear *I-V* dependence (inset of Fig. 3) indicates an intrinsic ohmic resistance. As the temperature is lowered, the resistance falls at first and then saturates at a value that can be orders of magnitude smaller than its normal-state value and can be continuously tuned by varying V_G (Fig. 2A). The resistance saturation begins at a relatively high temperature (~1 K) (Fig. 2A), which together with the V_G dependence (Fig. 2A) and the linear *I-V* relation (Fig. 3, inset) excludes the possibility of Joule heating. Residual resistance saturation in the superconducting state has been observed in diverse 2D superconducting systems (*8*, *19*, *24*, *28*–*30*). The associated superconductors are called "failed superconductors" in the literature (*30*). The corresponding ground state is called an anomalous or quantum metallic state, whose origin is still under vigorous debate (*24*, *27*, *29*–*31*). The saturated resistance in the insulating state can be ascribed to the applied electric field–induced electron percolation on top of the insulating state. In this sense, the insulating state is fragile and can be called a "fragile insulator." Resistance saturation in the insulating state, although rare, was observed previously in disordered ultrathin Ga films (*32*), disorder-tuned LAO/STO interfaces (*19*), and graphene in a high magnetic field (*33*).

In disordered 2D superconductors, the magnetic-field–driven superconductor-to-insulator QPTs (*24*, *34*) is an interesting issue. The ability to continuously tune the effective disorder (from $k_F l \gg 1$ to $k_F l \sim 1$) in a single device enables us to monitor the disorder-dependent evolution of such QPTs. Figure 4A shows the plots of R_{sheet} as a function of a perpendicular magnetic field B for various temperatures below 2 K, at V_G = 0. These plots cross at approximately a single point, indicating a magnetic-field–driven superconductor-to-insulator QPT (*25*, *26*). The crossing point corresponds to the critical field B_c and the critical resistance R_c. To study the criticality of such QPTs, we analyzed the data with the scaling relation $R_{sheet}(\delta, T) = R_c f(\delta T^{-1/z\nu})$, where $\delta = |B - B_c|$, f is an arbitrary function with $f(0) = 1$, z is the dynamical critical exponent, and ν is the correlation length exponent (*7*, *25*, *27*, *34*, *35*). A notable observation is that the exponent product zν is not universal but diverges with decreasing temperature (Fig. 4B and its inset and figs. S14 and S15). A similar divergent $z\nu$ was observed previously in a few experimental studies (*35*, *36*) and has been discussed in recent theoretical work (*30*, *37*). One plausible explanation is that the disorder in the conducting layer gives rise to superconducting granularities, for which local quantum phase fluctuations, rather than large-scale superconducting fluctuations, are relevant (*38*).

As summarized in Fig. 4, C and D, by sweeping V_G from 150 to −120 V, the critical resistance R_c is tuned continuously from ~1/4 to ~4 R_Q (where $R_Q = h/4e^2 \approx 6.45$ kilohm is the quantum resistance of the Cooper pairs), and the critical magnetic field B_c exhibits a dome-shaped dependence on V_G, which evokes the dome-shaped T_c-V_G relation in the absence of an external magnetic field (Fig. 2B). All $z\nu$ values in the high-temperature regime (1.60 to 1.90 K) are within 0.7 ± 0.2, which is similar to those observed in STO-based 2D superconducting interfaces (*1*, *7*). In contrast, the $z\nu$ values in the low-temperature regime (0.45 to 0.65 K) are extremely large (divergent), implying that nonuniversal criticality generally exists. Finally, on the basis of all these observations, a schematic V_G-B phase diagram is produced in Fig. 4E.

In addition to the results presented in this report, we have fabricated and measured a total of 30 samples with different carrier densities and mobilities and found that the effective disorder-controlled tuning is quite general, although the tuning ability does depend on sample details, particularly the mobility (e.g., figs. S17 and S18). Our experiments show that a prominent low-temperature resistance saturation and a strong V_G-induced tuning tend to occur in low-mobility samples. Furthermore, strongly anisotropic transport behaviors have been observed in low-mobility samples (fig. S18). We emphasize that these anisotropic behaviors are different from the anisotropic superconductivity observed in EuO/KTO(111), because the latter is associated with high-mobility samples (*17*). Our work demonstrates that LAO/KTO(111) is an ideal platform to explore the rich physics of disordered 2D superconductors.

REFERENCES AND NOTES

1. A. D. Caviglia *et al.*, *Nature* **456**, 624–627 (2008).
2. A. T. Bollinger *et al.*, *Nature* **472**, 458–460 (2011).
3. K. Ueno *et al.*, *Nat. Mater.* **7**, 855–858 (2008).
4. K. Ueno *et al.*, *Nat. Nanotechnol.* **6**, 408–412 (2011).
5. Y. Cao *et al.*, *Nature* **556**, 43–50 (2018).
6. C. Richter *et al.*, *Nature* **502**, 528–531 (2013).
7. J. Biscaras *et al.*, *Nat. Mater.* **12**, 542–548 (2013).
8. Y. Saito, Y. Kasahara, J. Ye, Y. Iwasa, T. Nojima, *Science* **350**, 409–413 (2015).
9. C. H. Ahn, J.-M. Triscone, J. Mannhart, *Nature* **424**, 1015–1018 (2003).
10. J. T. Ye *et al.*, *Nat. Mater.* **9**, 125–128 (2010).
11. J. T. Ye *et al.*, *Science* **338**, 1193–1196 (2012).
12. C. H. Ahn *et al.*, *Science* **284**, 1152–1155 (1999).
13. J. R. Thompson, L. A. Boatner, J. O. Thomson, *J. Low Temp. Phys.* **47**, 467–475 (1982).
14. A. Ohtomo, H. Y. Hwang, *Nature* **427**, 423–426 (2004).
15. H. Zhang *et al.*, *ACS Appl. Mater. Interfaces* **9**, 36456–36461 (2017).
16. K. Zou *et al.*, *APL Mater.* **3**, 036104 (2015).
17. C. Liu *et al.*, *Science* **371**, 716–721 (2021).
18. Materials and methods and figs. S1 to S18 are available as supplementary materials.
19. Z. Chen *et al.*, *Nat. Commun.* **9**, 4008 (2018).
20. Z. Chen *et al.*, *Nano Lett.* **16**, 6130–6136 (2016).
21. N. Reyren *et al.*, *Science* **317**, 1196–1199 (2007).
22. C. Bell *et al.*, *Phys. Rev. Lett.* **103**, 226802 (2009).
23. Y. Fujii, T. Sakudo, *J. Phys. Soc. Jpn.* **41**, 888–893 (1976).
24. A. M. Goldman, *Int. J. Mod. Phys. B* **24**, 4081–4101 (2010).
25. N. Marković, C. Christiansen, A. M. Mack, W. H. Huber, A. M. Goldman, *Phys. Rev. B* **60**, 4320–4328 (1999).
26. A. Yazdani, A. Kapitulnik, *Phys. Rev. Lett.* **74**, 3037–3040 (1995).
27. N. Mason, A. Kapitulnik, *Phys. Rev. Lett.* **82**, 5341–5344 (1999).
28. A. W. Tsen *et al.*, *Nat. Phys.* **12**, 208–212 (2016).
29. C. Yang *et al.*, *Science* **366**, 1505–1509 (2019).
30. A. Kapitulnik, S. A. Kivelson, B. Spivak, *Rev. Mod. Phys.* **91**, 011002 (2019).
31. I. Tamir *et al.*, *Sci. Adv.* **5**, eaau3826 (2019).
32. C. Christiansen, L. M. Hernandez, A. M. Goldman, *Phys. Rev. Lett.* **88**, 037004 (2002).
33. J. G. Checkelsky, L. Li, N. P. Ong, *Phys. Rev. Lett.* **100**, 206801 (2008).
34. M. P. A. Fisher, *Phys. Rev. Lett.* **65**, 923–926 (1990).
35. Y. Xing *et al.*, *Science* **350**, 542–545 (2015).
36. Y. Saito, T. Nojima, Y. Iwasa, *Nat. Commun.* **9**, 778 (2018).
37. B. Spivak, P. Oreto, S. A. Kivelson, *Phys. Rev. B* **77**, 214523 (2008).
38. B. Sacépé, M. Feigel'man, T. M. Klapwijk, *Nat. Phys.* **16**, 734–746 (2020).
39. Y. Xie, Data for "Electric field control of superconductivity at the $LaAlO_3/KTaO_3$(111) interface," Zenodo (2021); https://doi.org/10.5281/zenodo.4626213.

ACKNOWLEDGMENTS

We thank S. A. Kivelson, H. Y. Hwang, H. Yao, and F. C. Zhang for fruitful discussions. Hall-bar devices were made at the Micro-Nano Fabrication Center of Zhejiang University. **Funding:** This work was supported by the National Key Research and Development Program of China (grant nos. 2017YFA0303002, 2016YFA0300202, 2016YFA0300204, 2016YFA0300701); National Natural Science Foundation of China (grant nos. 11934016, 11774306); the Strategic Priority Research Program of Chinese Academy of Sciences (grant no. XDB28000000); the Key R&D Program of Zhejiang Province, China (2021C01002, 2020C01019); and the Fundamental Research Funds for the Central Universities of China. J.S. thanks the support of the Science Center of the National Science Foundation of China (52088101) and the Project for Innovative Research Team of National Natural Science Foundation of China (11921004). **Author contributions:** Z.C., Y.L., H.Z., Y.S., and M.Z. prepared the samples; Z.C., Y.L., and Y.X. performed the transport measurements; Z.L. and H.T. performed the STEM measurements; and Y.Z., J.S., and Y.X. analyzed the data and wrote the manuscript with input from all authors. **Competing interests:** The authors declare no competing interests. **Data and materials availability:** Data for all graphs presented in this paper are available from Zenodo (*39*).

SUPPLEMENTARY MATERIALS

science.sciencemag.org/content/372/6543/721/suppl/DC1
Materials and Methods
Figs. S1 to S18
References (*40*)

29 March 2020; accepted 2 April 2021
10.1126/science.abb3848

RADIATION RISKS

Lack of transgenerational effects of ionizing radiation exposure from the Chernobyl accident

Meredith Yeager[1,2]*†, Mitchell J. Machiela[1]†, Prachi Kothiyal[1,3], Michael Dean[1,2], Clara Bodelon[1], Shalabh Suman[1,2], Mingyi Wang[1,2], Lisa Mirabello[1], Chase W. Nelson[4,5], Weiyin Zhou[1,2], Cameron Palmer[1,2], Bari Ballew[1,2], Leandro M. Colli[1,6], Neal D. Freedman[1], Casey Dagnall[1,2], Amy Hutchinson[1,2], Vibha Vij[1], Yosi Maruvka[7,8], Maureen Hatch[1], Iryna Illienko[9], Yuri Belayev[9], Nori Nakamura[10], Vadim Chumak[9], Elena Bakhanova[9], David Belyi[9], Victor Kryuchkov[11], Ivan Golovanov[11], Natalia Gudzenko[9], Elizabeth K. Cahoon[1], Paul Albert[1], Vladimir Drozdovitch[1], Mark P. Little[1], Kiyohiko Mabuchi[1], Chip Stewart[7], Gad Getz[7,8,12,13], Dimitry Bazyka[9], Amy Berrington de Gonzalez[1], Stephen J. Chanock[1]*

Effects of radiation exposure from the Chernobyl nuclear accident remain a topic of interest. We investigated germline de novo mutations (DNMs) in children born to parents employed as cleanup workers or exposed to occupational and environmental ionizing radiation after the accident. Whole-genome sequencing of 130 children (born 1987–2002) and their parents did not reveal an increase in the rates, distributions, or types of DNMs relative to the results of previous studies. We find no elevation in total DNMs, regardless of cumulative preconception gonadal paternal [mean = 365 milligrays (mGy), range = 0 to 4080 mGy] or maternal (mean = 19 mGy, range = 0 to 550 mGy) exposure to ionizing radiation. Thus, we conclude that, over this exposure range, evidence is lacking for a substantial effect on germline DNMs in humans, suggesting minimal impact from transgenerational genetic effects.

Nearly all inherited genetic variation is present in the germline DNA of at least one parent. However, a small number of transmitted variants are unique, having arisen from random mutations in gametes (sperm and oocytes), and are known as de novo mutations (DNMs). DNMs are critical building blocks of evolution and the only class of genomic variation that has not undergone extensive evolutionary purifying selection (purging of highly deleterious but nonlethal variants), making DNMs a distinctive form of inherited variation that differs from the genetic variation investigated in mapping complex traits and diseases (*1*). DNMs have been a topic of intense interest because of their role in human disease, particularly neurodevelopmental disorders (*2*, *3*).

Only recently has it been feasible to comprehensively investigate DNMs genome-wide at the population level in humans by using whole-genome sequencing (WGS) of mother-father-child trios. Recent reports of human DNMs characterized by WGS of trios estimate that between 50 and 100 new mutations arise per individual per generation (*2*, *4*–*8*), consistent with the population genetic estimate that the human mutation rate for single-nucleotide variants (SNVs) is ~1×10^{-8} per site per generation (*9*, *10*). The strongest predictor of DNMs per individual is paternal age at conception (*2*–*6*, *8*), with an increase of 0.64 to 1.51 mutations per 1-year increase in paternal age (*6*, *8*, *11*), whereas a maternal effect of ~0.35 mutations per 1-year increase in age was observed (*6*, *8*, *12*). Transgenerational studies of radiation exposure have primarily focused on disease (cancer, reproductive, and developmental) outcomes and have reported inconclusive results (*13*, *14*).

Exposure to ionizing radiation is known to increase DNA mutagenesis above background rates (*15*, *16*). Animal and cellular studies suggest that high doses of ionizing radiation can lead to DNMs in offspring, particularly through double-strand breaks (*13*, *17*). Human studies have sought a biomarker of prior radiation injury (*13*, *18*, *19*) but have examined a small number of minisatellites and microsatellites, yielding inconclusive results (*20*–*23*). A WGS study of three trios from survivors of the atomic bomb in Nagasaki, Japan, did not reveal a high load of DNMs (*20*), whereas a single-nucleotide polymorphism (SNP) array study of 12 families exposed to low doses of caesium-137 from the Goiânia accident in Brazil reported an increase in large de novo copy-number variants (*24*). No large-scale, comprehensive effort has explored DNMs genome-wide in children born to parents exposed to moderately high amounts of ionizing radiation, yet possible genetic effects have remained a concern for radiation-exposed populations, such as the Fukushima evacuees (*25*).

Herein, we examine rates of germline DNMs in children born to parents exposed to ionizing radiation from the 1986 Chernobyl (Chornobyl in Ukrainian) disaster, for which levels of exposure have been rigorously reconstructed and well documented (*26*). Our study focused on children born to enlisted cleanup workers ("liquidators") and evacuees from the town of Pripyat or other settlements within the 70-km zone around the Chernobyl Nuclear Power Plant in Ukraine (*27*) after the meltdown, some of whom had extremely high levels of radiation exposure and several of whom experienced acute radiation syndrome. We performed Illumina paired-end WGS (average coverage: 80×), SNP microarray analysis, and relative telomere length assessment on available samples from 130 children from 105 mother-father pairs. The parents had varying combinations of elevated gonadal ionizing radiation exposure from the accident (tables S1 to S3) and included a combination of exposed fathers, exposed mothers, both parents exposed, and neither parent exposed (*27*). The fathers' cumulative gonadal ionizing radiation dose (hereafter, "dose") at conception ranged from 0 to 4080 milligrays (mGy) [mean = 365 mGy, median = 29 mGy, standard deviation (SD) = 685 mGy], with 17 individuals exposed to >1000 mGy, whereas the mothers' dose ranged from 0 to 550 mGy (mean = 19 mGy, median = 2.1 mGy, SD = 72 mGy), with only 2 individuals exposed to >500 mGy (table S3). Paternal age at exposure ranged from 12 to 41 years and maternal from 10 to 33 years. Paternal mean age at conception was 29 (range = 18 to 52, SD = 5.7), whereas maternal mean age was 27 (range = 18 to 39, SD = 5.2). Of the children in our study, 58 (45%) were female and 72 (55%) were male. Children born at least 46 weeks after the Chernobyl accident were included; birth years were between 1987 and 2002 (52% born before 1992). There were 23 families with two or three siblings analyzed, but no twins. Principal component analysis revealed that nearly all parents shared common Eastern European heritage (fig. S1), and pairwise identity-by-descent analysis revealed four first-degree relative sets among the parents.

Two modified Mendelian inconsistency error (MIE) filtering strategies were applied after variant calling and determination of MIE

[1]Division of Cancer Epidemiology and Genetics, National Cancer Institute, Rockville, MD 20892, USA. [2]Cancer Genomics Research Laboratory, Frederick National Laboratory for Cancer Research, Frederick, MD 21701, USA. [3]SymbioSeq LLC, Arlington, VA 20148, USA. [4]Biodiversity Research Center, Academia Sinica, Taipei, 11529, Taiwan. [5]Institute for Comparative Genomics, American Museum of Natural History, New York, NY 10024, USA. [6]Department of Medical Imaging, Hematology, and Oncology, Ribeirao Preto Medical School, University of Sao Paulo, Ribeirao Preto, SP, 14049-900, Brazil. [7]Broad Institute of Harvard and Massachusetts Institute of Technology, Cambridge, MA 02142, USA. [8]Center for Cancer Research, Massachusetts General Hospital, Boston, MA 02114, USA. [9]National Research Centre for Radiation Medicine, 53 Yu. Illienka Street, Kyiv, 04050, Ukraine. [10]Department of Molecular Biosciences, Radiation Effects Research Foundation, 5-2 Hijiyama Park, Minami-ku, Hiroshima, 732-0815, Japan. [11]Burnasyan Federal Medical and Biophysical Centre, 46 Zhivopisnaya Street, Moscow, 123182, Russia. [12]Department of Pathology, Massachusetts General Hospital, Boston, MA 02114, USA. [13]Harvard Medical School, Boston, MA 02115, USA.
*Corresponding author. Email: chanocks@mail.nih.gov (S.J.C.); yeagerm@mail.nih.gov (M.Y.)
†These authors contributed equally to this work.

(*8*, *28*). All putative DNMs that passed the filtering criteria were examined manually, and the total number of DNMs was tallied for each of the following classes, reflecting distinct mutational mechanisms: (i) SNVs, (ii) small insertions or deletions (indels), (iii) complex variants (variants that arose from a complicated mutational event), and (iv) SNV-indel clusters [two or more variants that, by chance, occur in closer proximity than expected, as defined by Jónsson *et al.* (*6*)] (Table 1). Each instance of a complex variant or cluster was counted once, effectively assuming that clustered changes occurred together during one replication cycle. Length variants at microsatellite loci were examined separately because they have been previously reported as a potentially important class of mutation after radiation exposure (*21*, *22*, *29*–*31*). Although DNMs involving microsatellite loci were analyzed separately, they were tallied with indels overall. All variants are provided in table S1.

There was no evidence of an association between the total number of DNMs and the preconception ionizing radiation dose (cumulative estimated gonadal dose at 38 weeks before birth) for maternal [−0.02 DNM per mGy, 95% confidence interval (CI): −0.04 to 0.007, $P = 0.17$] or paternal (−0.0007 DNM per mGy, 95% CI: −0.003 to 0.002, $P = 0.56$) exposures (Table 2 and fig. S2). In an analysis restricted to DNMs with a known parent of origin (42%; Table 1), no effect of radiation

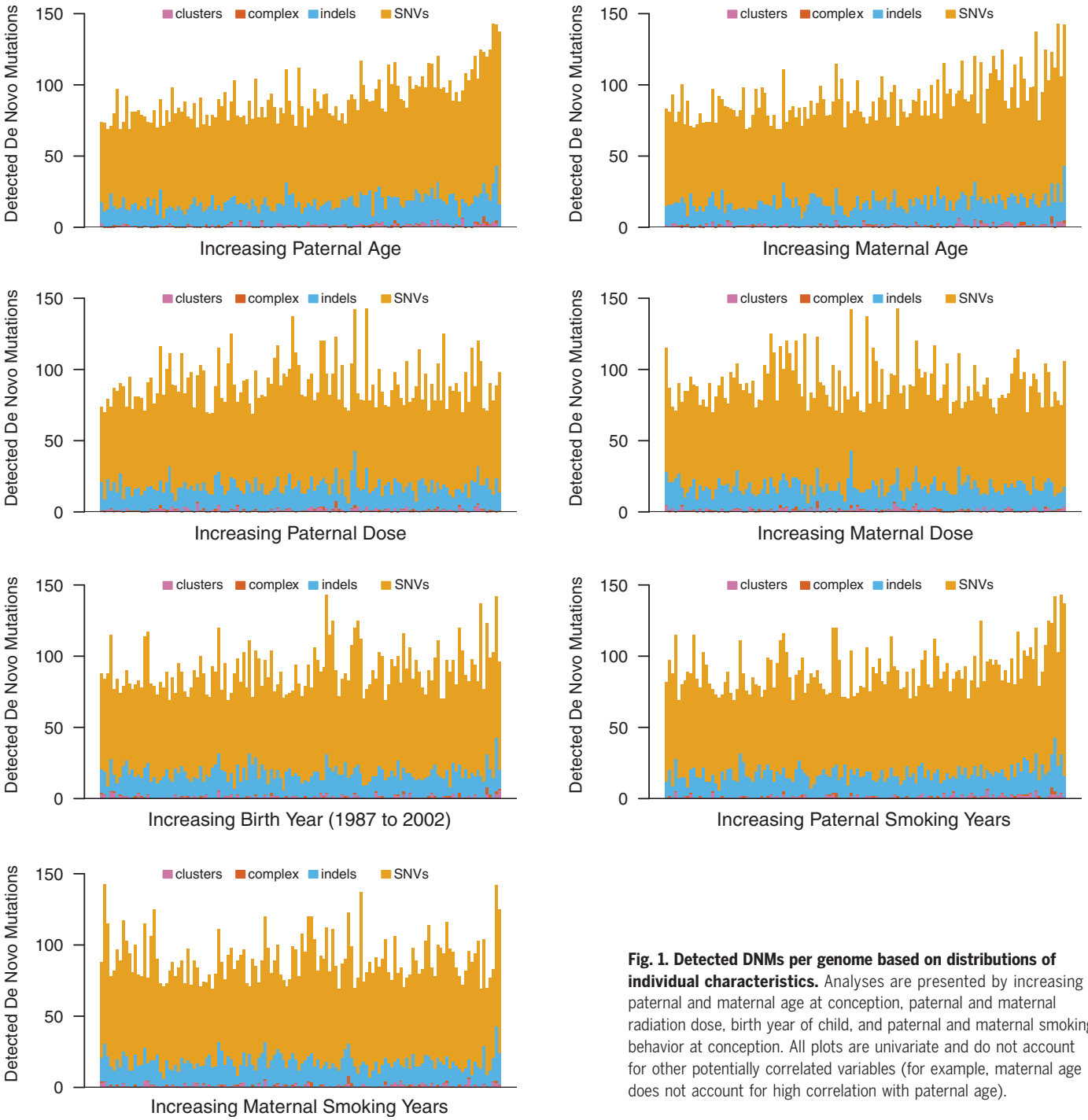

Fig. 1. Detected DNMs per genome based on distributions of individual characteristics. Analyses are presented by increasing paternal and maternal age at conception, paternal and maternal radiation dose, birth year of child, and paternal and maternal smoking behavior at conception. All plots are univariate and do not account for other potentially correlated variables (for example, maternal age does not account for high correlation with paternal age).

was observed (table S4), whereas the effect of parental age remained robust; the parent-of-origin point estimates for paternal and maternal age effects were 0.71 and 0.28, respectively. Further investigation did not reveal evidence for an effect of preconception dose for any individual class of DNMs evaluated (table S5). Sensitivity analysis conducted with doses truncated at 1000 mGy or log-transformed [ln(1 + dose(mGy))] did not reveal an impact of maternal and paternal dose modeling on association with DNMs (Table 3). We further investigated categorical dose levels and found no increase in DNMs for any dose category, even paternal doses ≥1000 mGy (table S6). No effect of time since exposure was observed between parental preconception ionizing radiation exposure and DNM count for children born in the years immediately after the Chernobyl accident (Fig. 1). Moreover, when restricting our analysis to SNVs, there was no difference in the distribution of nucleotide substitutions based on quartile of maternal and paternal dose (fig. S3). Furthermore, the rates and types (molecular spectra) of DNMs observed in the current study were similar to those observed in prior studies conducted in general populations (Fig. 2 and fig. S4) (*2*–*4*, *6*, *8*).

Because lifestyle exposures such as smoking have been associated with alterations of DNA [for example, mosaic loss of Y chromosome (*32*)], we also investigated possible effects of prenatal parental alcohol consumption and smoking on DNMs. We observed no association between the number of DNMs and either paternal (2.91 DNMs, 95% CI = −0.93 to 6.75, P = 0.14; Table 2 and Fig. 1) or maternal (5.31 DNMs, 95% CI = −0.18 to 10.81, P = 0.06; Table 2 and Fig. 1) tobacco smoking at conception. Similarly, no effect was observed for increasing levels of paternal (P = 0.12) or maternal (P = 0.12) alcohol consumption before conception. In addition, sequencing batch had no impact on the number of DNMs (3.28 DNMs, 95% CI = −0.25 to 6.82, P = 0.07).

Relative telomere length of participants was measured by quantitative polymerase chain reaction (*33*) to investigate the potential transgenerational impact of parental ionizing radiation on leukocyte telomere length in children. As expected, an overall relationship was observed between increasing age (at the time of blood draw) and shorter relative telomere length due to age-related telomere length attrition ($P = 4.49 \times 10^{-19}$; fig. S5). We did not observe an effect of paternal or maternal age at conception on relative telomere length in adult children (P = 0.95 and 0.06, respectively; table S7). Although our analysis did not find evidence for an effect of total paternal preconception ionizing radiation exposure on relative leukocyte telomere length (P = 0.88), we did observe a possible effect of total maternal preconception exposure (-2.75×10^{-4}, 95% CI = -5.20×10^{-4} to -2.90×10^{-5}, P = 0.03; table S7)—this finding will need to be confirmed in subsequent work. There was no evidence for a transgenerational effect of paternal or maternal smoking on telomere length in children (P = 0.91 and 0.22, respectively; table S7).

Although it is reassuring that no transgenerational effects of ionizing radiation were observed in adult children of Chernobyl cleanup workers and evacuees in the current study, additional investigation is needed to address the effects of acute high-dose parental gonadal exposure that occurred closer to conception. The upper 95% confidence bound suggests that the largest effect consistent with our data is <1 DNM per 100 mGy from paternal or maternal exposure (Table 3 and tables S8 and S9). Previously, Dubrova *et al.* (*22*, *29*) reported a twofold increase in minisatellite mutations in children born to parents living in a highly exposed region of Belarus. Weinberg *et al.* (*34*) reported an increase in the mutation rate at microsatellite loci among children born to cleanup workers. Subsequent small studies have not reported increased minisatellite or microsatellite mutation rate in children of cleanup workers, including those with low-dose exposure (0.09 to 0.23 Gy) (*21*, *30*, *35*), or in children of the atomic-bomb survivors of Hiroshima or Nagasaki, Japan (*31*).

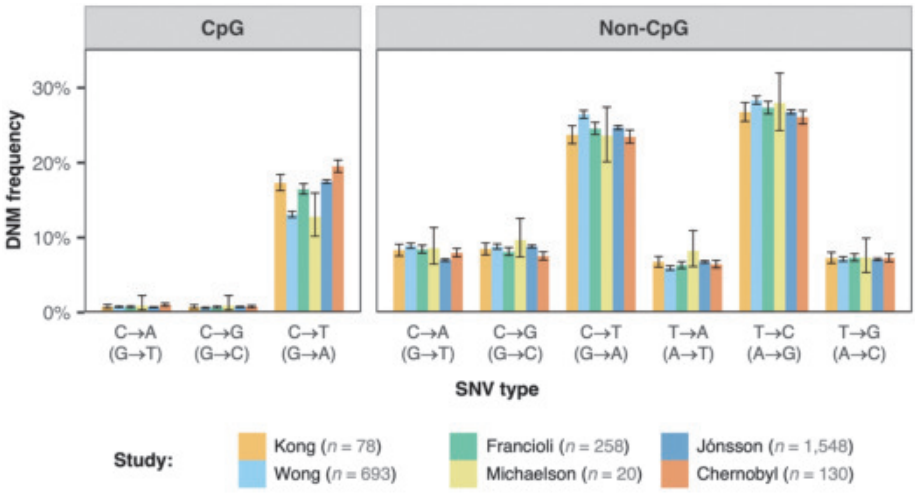

Fig. 2. Distribution of de novo SNVs by type of nucleotide change across six studies. Liftover was used to convert coordinates to hg38 (human reference genome 38) for all studies, and the reference for CpG sites was defined with respect to that reference sequence. Only autosomes were included. Error bars show binomial 95% CIs. Studies included those by Kong *et al.* (*2*), Wong *et al.* (*8*), Francioli *et al.* (*4*), Michaelson *et al.* (*3*), and Jónsson *et al.* (*6*), as well as the present study (Chernobyl). *n*, number of children sequenced. [Image adapted from (*39*).]

Table 1. Distribution of detected DNMs in the Chernobyl trios. Results reported as events per diploid genome per generation and proportion phased to paternal and maternal haplotypes. Microsatellites are a smaller group within indels; the mean microsatellite count (5.62) is part of the total mean indel count (16.18).

Detected DNM category	Mean	Median	Range	SD
Number of clusters	1.39	1	0–6	1.34
Number of complex variants	0.38	0	0–5	0.77
Number of indels	16.18	15	5–38	5.10
Number of microsatellites	5.62	5.5	0–13	2.49
Number of SNVs	72.22	69.5	47–121	13.36
Total number of DNMs	90.17	88	69–143	15.94
Phased to paternal haplotype	29.33	29	12–53	7.08
Phased to maternal haplotype	8.61	8	2–20	4.07
Proportion phased	42.1%	41.5%	27.6–55.8%	6.3%

Our study evaluated peripheral blood from adult children conceived months or years after the Chernobyl accident, so our ability to assess exposure closer to the time of conception was limited. However, there was no evidence of notable differences in DNMs in children born the year after the accident (1987). Because the families in our study were recruited several decades after the accident, we acknowledge potential survivor bias among sampled children—although this is unlikely because there is no consistent demonstration in humans of sustained clinical effects of preconception ionizing radiation exposure (*36*). The number of parental gonadal radiation-induced double-strand breaks could be lower than anticipated based on animal data, which often assesses acute exposure (as a single burst) at higher doses [2 to 4 Gy (*13*, *37*)]. Doses to which the Chernobyl liquidators were exposed were mostly lower and exposure was fractionated over an extended period of time, which could have decreased the probability of gonadal DNM events. Moreover, it is plausible that the balance between radiation-induced mutations and accurate repair over time favored the latter. Additionally, there could have been a loss of power owing to dose errors. Further human studies are needed to investigate the frequency of radiation-induced mutations and the subsequent response to address both the accuracy and efficiency of DNA repair. In a genomic landscape analysis of 440 cases of papillary thyroid cancer after the Chernobyl accident, increased radiation exposure was associated with a shift in tumor drivers from point mutations to small indels and nonhomologous end-joining events underlying fusions and other structural variants (*38*). Notably, there was no evidence of a radiation-specific single-base substitution signature, gene expression pattern, or methylation profile in cases of thyroid cancer with comparable radiation exposure history; instead, these were strongly associated with the tumor driver.

The rate, class distribution, and SNV type distribution of DNMs in adult children born to parents exposed to ionizing radiation, specifically of the type and amount relevant to Chernobyl cleanup workers and evacuees, are comparable to those reported in the general population. No effect of radiation on the specific classes of DNMs (SNVs, indels, complex variants, or clusters) was observed (table S5). Paternal age remains the strongest contributor to DNMs, although DNMs increase (albeit less so) with maternal age as well (Table 2 and table S4) (*12*). Our study sample did not include mothers with high exposure levels (>1 Gy), but lower maternal dose was not associated with elevated DNMs, consistent with animal studies (*13*). Furthermore, our analysis of 130 adult children from 105 couples, using 80× coverage of short-read technology, suggests that if such effects on human germline DNA occur, they are uncommon or of small magnitude. Our study represents an effort to systematically evaluate alterations in human mutation rates in response to a human-made disaster, such as accidental radiation exposure. Investigation of trios drawn from survivors of the Hiroshima atomic bomb could shed further light on this matter of public health. In summary, children of individuals exposed to either occupational or environmental radiation do not appear to experience elevated rates of DNMs from their parents' exposure. Thus, our study does not provide support for a transgenerational effect of ionizing radiation on germline DNA in humans.

Table 2. Associations of age at conception, cumulative ionizing radiation dose, and smoking history with DNM count. Multiple regression estimates for age and radiation dose are average changes in total DNMs per unit increase in the respective variables. Estimates for smokers are relative to those for individuals who have never smoked. The model was additionally adjusted by sequencing batch.

Variable	Estimate	95% CI	*P* value
Age at conception			
Maternal age	0.46	−0.02–0.93	0.06
Paternal age	1.94	1.51–2.36	3.65×10^{-15}
Cumulative radiation dose (per mGy)			
Maternal dose	−0.02	−0.04–0.007	0.17
Paternal dose	−0.0007	−0.003–0.002	0.56
Smoking history			
Maternal former smoker	−4.13	−10.74–2.49	0.22
Maternal current smoker	5.31	−0.18–10.81	0.06
Paternal former smoker	0.91	−5.16–6.97	0.77
Paternal current smoker	2.91	−0.93–6.75	0.14

Table 3. Sensitivity analyses of the impact of maternal and paternal cumulative radiation dose modeling on association with DNMs. All models are adjusted for sequencing batch, maternal and paternal age, and maternal and paternal smoking status. Additional analyses organized by dose category are in table S6.

Dose measure	Estimate	95% CI	*P* value
Cumulative radiation dose (per mGy)			
Maternal dose	−0.02	−0.04, 0.007	0.17
Paternal dose	−0.0007	−0.003, 0.002	0.56
Cumulative radiation dose truncated at 1000 (per mGy)			
Maternal dose	−0.02	−0.04, 0.009	0.21
Paternal dose	−0.003	−0.008, 0.001	0.17
Cumulative log radiation dose (per ln(1 + mGy))			
Maternal dose	−0.87	−2.12, 0.39	0.18
Paternal dose	−0.37	−1.07, 0.33	0.30

REFERENCES AND NOTES

1. V. Tam *et al.*, *Nat. Rev. Genet.* **20**, 467–484 (2019).
2. A. Kong *et al.*, *Nature* **488**, 471–475 (2012).
3. J. J. Michaelson *et al.*, *Cell* **151**, 1431–1442 (2012).
4. L. C. Francioli *et al.*, *Nat. Genet.* **47**, 822–826 (2015).
5. J. M. Goldmann *et al.*, *Nat. Genet.* **50**, 487–492 (2018).
6. H. Jónsson *et al.*, *Nature* **549**, 519–522 (2017).
7. R. Rahbari *et al.*, *Nat. Genet.* **48**, 126–133 (2016).
8. W. S. Wong *et al.*, *Nat. Commun.* **7**, 10486 (2016).
9. J. W. Drake, B. Charlesworth, D. Charlesworth, J. F. Crow, *Genetics* **148**, 1667–1686 (1998).
10. M. W. Nachman, S. L. Crowell, *Genetics* **156**, 297–304 (2000).
11. J. F. Crow, *Nat. Rev. Genet.* **1**, 40–47 (2000).
12. Z. Gao *et al.*, *Proc. Natl. Acad. Sci. U.S.A.* **116**, 9491–9500 (2019).
13. M. P. Little, D. T. Goodhead, B. A. Bridges, S. D. Bouffler, *Mutat. Res.* **753**, 50–67 (2013).
14. National Research Council, in *(US) Committee on Health Effects of Exposure to Low Levels of Ionizing Radiations (BEIR VII)* (2006).
15. H. J. Muller, *Proc. Natl. Acad. Sci. U.S.A.* **14**, 714–726 (1928).
16. *Lancet* **395**, 1012 (2020).
17. W. L. Russell, *Proc. Natl. Acad. Sci. U.S.A.* **74**, 3523–3527 (1977).
18. A. Fucic *et al.*, *Mutat. Res.* **658**, 111–123 (2008).
19. N. Nakamura, A. Suyama, A. Noda, Y. Kodama, *Annu. Rev. Genet.* **47**, 33–50 (2013).
20. M. Horai *et al.*, *J. Hum. Genet.* **63**, 357–363 (2018).
21. R. J. Slebos *et al.*, *Mutat. Res.* **559**, 143–151 (2004).
22. Y. E. Dubrova *et al.*, *Nature* **380**, 683–686 (1996).
23. C. Turner *et al.*, *Hum. Genet.* **112**, 303–309 (2003).
24. E. O. A. Costa *et al.*, *Sci. Rep.* **8**, 5914 (2018).
25. K. Kamiya *et al.*, *Lancet* **386**, 469–478 (2015).
26. V. Chumak *et al.*, *J. Radiol. Prot.* 10.1088/1361-6498/abf0f4 (2021).

27. D. Bazyka *et al.*, *Am. J. Epidemiol.* **189**, 1451–1460 (2020).
28. A. S. Allen *et al.*, *Nature* **501**, 217–221 (2013).
29. Y. E. Dubrova, G. Grant, A. A. Chumak, V. A. Stezhka, A. N. Karakasian, *Am. J. Hum. Genet.* **71**, 801–809 (2002).
30. A. Kiuru *et al.*, *Radiat. Res.* **159**, 651–655 (2003).
31. M. Kodaira *et al.*, *Radiat. Res.* **173**, 205–213 (2010).
32. W. Zhou *et al.*, *Nat. Genet.* **48**, 563–568 (2016).
33. R. M. Cawthon, *Nucleic Acids Res.* **37**, e21 (2009).
34. H. S. Weinberg *et al.*, *Proc. R. Soc. London Ser. B* **268**, 1001–1005 (2001).
35. L. A. Livshits *et al.*, *Radiat. Res.* **155**, 74–80 (2001).
36. J. D. Boice Jr., *Health Phys.* **119**, 494–503 (2020).
37. A. B. Adewoye, S. J. Lindsay, Y. E. Dubrova, M. E. Hurles, *Nat. Commun.* **6**, 6684 (2015).
38. L. Morton *et al.*, *Science* **372**, eabg2538 (2021).
39. T. C. A. Smith, P. F. Arndt, A. Eyre-Walker, *PLOS Genet.* **14**, e1007254 (2018).

ACKNOWLEDGMENTS

The authors gratefully acknowledge the participants in the study overseen by the National Research Centre for Radiation Medicine in Kiev (Kyiv in Ukrainian). This work utilized the computational resources of the NIH HPC Biowulf cluster (http://hpc.nih.gov). We thank G. Tobias (National Cancer Institute) for assistance with data posting and M.-H. Lin for assistance with data visualization. **Funding:** This research was supported by the Intramural Research Program of the Division of Cancer Epidemiology and Genetics of the National Cancer Institute. C.W.N. was supported by a Gerstner Scholars Fellowship from the Gerstner Family Foundation at the American Museum of Natural History and a postdoctoral research fellowship from Academia Sinica. This project has been funded in whole or in part with Federal funds from the National Cancer Institute, NIH, under contract no. 75N910D00024. The Radiation Effects Research Foundation (RERF), Hiroshima and Nagasaki, Japan, is a public interest foundation funded by the Japanese Ministry of Health, Labor and Welfare (MHLW) and the US Department of Energy (DOE). The opinions expressed by the authors are their own, and this material should not be interpreted as representing the official viewpoint of the National Cancer Institute of the US Department of Health and Human Services; US Department of Energy; or Japanese Ministry of Health, Labor and Welfare. **Author contributions:** D.Ba., A.B.d.G., S.J.C., P.K., and M.Y. conceptualized the study. D.Ba., A.B.d.G., S.J.C., V.C., D.Be., V.D., E.B., E.C., N.F., G.G., N.G., M.H., I.G., I.I., K.M., M.M., M.L., Y.M., N.N., P.A., P.K., C.S., V.K., Y.B., and M.Y. designed the study methodology. B.B., C.P., S.J.C., C.B., C.W.N., C.D., M.D., L.C., M.M., M.L., M.W., L.M., P.K., S.S., M.Y., and W.Z. analyzed the genomic data. D.Ba., A.B.d.G., V.C., C.D., D.Be., V.D., E.B., N.G., A.H., I.G., I.I., and Y.B. collected or generated the study data. B.B., D.Ba., A.B.d.G., V.C., C.D., D.Be., V.D., E.B., N.G., P.A., A.H., C.P., I.G., I.I., and Y.B. contributed resources (study materials, patients, computing resources, or other analysis tools). S.J.C., C.W.N., M.D., M.M., P.K., and M.Y. wrote the original draft. B.B., C.P., C.W.N., M.M., P.A., P.K., L.C., M.Y., and W.Z. visualized the data. A.B.d.G., S.J.C., G.G., and M.Y. supervised or managed the research. S.J.C. acquired funding for the study. All authors edited the final manuscript. **Competing interests:** G.G. receives research funds from IBM and Pharmacyclics and is an inventor on patent applications related to MuTect, ABSOLUTE, MutSig, MSMuTect, MSMutSig, MSIdetect, POLYSOLVER, and TensorQTL. G.G. is a founder and consultant of, and holds privately held equity in, Scorpion Therapeutics. All other authors declare no competing interests. **Data and materials availability:** Molecular data are available from the Genomic Data Commons: https://gdc.cancer.gov/about-data/publications/TRIO-CRU-2021, accessed through the database of Genotypes and Phenotypes (dbGaP, accession phs001163.v1.p1; www.ncbi.nlm.nih.gov/projects/gap/cgi-bin/study.cgi?study_id=phs001163.v1.p1). The MIE filtering pipeline code can be found at https://github.com/NCI-CGR/ChernobylDNMCalling.

SUPPLEMENTARY MATERIALS

science.sciencemag.org/content/372/6543/725/suppl/DC1
Materials and Methods
Figs. S1 to S7
Tables S1 to S10
References (*40*–*47*)
MDAR Reproducibility Checklist

22 December 2020; accepted 12 April 2021
Published online 22 April 2021
10.1126/science.abg2365

CHIRAL NANOMATERIALS

The chain of chirality transfer in tellurium nanocrystals

Assaf Ben-Moshe[1,2]†, Alessandra da Silva[3], Alexander Müller[4,5], Anas Abu-Odeh[1,5], Patrick Harrison[3], Jacob Waelder[6]‡, Farnaz Niroui[7]§, Colin Ophus[4], Andrew M. Minor[4,5], Mark Asta[1,5], Wolfgang Theis[3], Peter Ercius[4], A. Paul Alivisatos[1,2,8]*

Despite persistent and extensive observations of crystals with chiral shapes, the mechanisms underlying their formation are not well understood. Although past studies suggest that chiral shapes can form because of crystallization in the presence of chiral additives, or because of an intrinsic tendency that stems from the crystal structure, there are many cases in which these explanations are not suitable or have not been tested. Here, an investigation of model tellurium nanocrystals provides insights into the chain of chirality transfer between crystal structure and shape. We show that this transfer is mediated by screw dislocations, and shape chirality is not an outcome of the chiral crystal structure or ligands.

The formation pathway of crystals with chiral shapes has been a topic of controversy (*1*, *2*) for more than 170 years, ever since Pasteur (*3*) in 1848 reported the formation of chiral crystals from chiral tartarate molecules. Yet, Pasteur himself only ever obtained achiral shapes of one other chiral molecule, demonstrating that chirality of the crystal structure is not sufficient for the crystal shape to be chiral (*4*). Quartz (*5*, *6*), tellurium (*7*), and mercury sulfide (*8*, *9*) only occasionally form chiral shapes despite their intrinsically chiral crystal structures. For quartz in particular, it is often assumed that chiral shapes stem from the chiral molecular building blocks within the structure (*6*). Further complicating the matter, entirely achiral building blocks or materials with achiral crystal structures sometimes form chirally shaped crystals (*1*, *2*). Two broad classes of mechanisms for chiral shape formation have been discussed. The first attributes the formation of chiral crystal shapes to differential growth rates of chiral facets. This is possibly mediated by the presence of chiral ligands (*2*, *9*–*11*) but could also result from an intrinsic tendency that stems from the chiral crystal structure (*5*, *6*). The second starts from the observation that at very low supersaturation conditions, only nuclei of crystals that contain screw dislocations can grow further because these dislocations create a more reactive crystal growth front (*1*, *12*–*17*). Such screw-dislocation–mediated growth yields helical shapes and has in the past been considered as a formation mechanism for twisted nanowires (*1*, *12*–*17*). It has not been considered, however, as a formation pathway for distinct chiral polyhedral shapes of crystals.

Differentiating between these two mechanisms is difficult, but the advent of controlled colloidal synthesis has allowed for studies of nanocrystals that have chiral crystal structures and form both chiral and achiral shapes (*7*–*9*). Such nanostructures represent an embryonic stage in crystal growth and serve as convenient model systems to explore mechanisms of chiral shape formation (*7*, *9*, *18*, *19*). Previous studies concluded that chiral ligands are the cause for chiral shape formation. However, they did not explain why in many cases achiral shapes also formed in the presence of chiral ligands and did not address other observations of chiral shape formation in the absence of chiral ligands (*1*–*6*).

Our system consists of tellurium nanocrystals with chiral shapes that are a few hundred nanometers in size (*7*). Tellurium crystallizes in one of the two enantiomorphic chiral space groups, $P3_121$ or $P3_221$ (*7*). Growth of our nanocrystals involves reduction of tellurium dioxide in the presence of chiral thiolated penicillamine ligands and hydrazine that serves as a reducing agent, continuously supplying tellurium monomers for growth. Shapes of varying thickness were formed by blocking lateral growth at different stages of the reaction by using sodium dodecyl sulfate (SDS) (table S1). When added early in the reaction, thin twisted nanorods formed (Fig. 1A and fig. S1), and when added later, thick trigonal bipyramids formed (Fig. 1B and fig. S1). We

[1]Materials Sciences Division, Ernest Orlando Lawrence Berkeley National Laboratory, Berkeley, CA 94720, USA. [2]Department of Chemistry, University of California, Berkeley, CA 94720, USA. [3]Nanoscale Physics Research Laboratory, School of Physics and Astronomy, University of Birmingham, Edgbaston, Birmingham B15 2TT, UK. [4]National Center for Electron Microscopy, Molecular Foundry, Ernest Orlando Lawrence Berkeley National Laboratory, Berkeley, CA 94720, USA. [5]Department of Materials Science and Engineering, University of California, Berkeley, CA 94720, USA. [6]Department of Physics, University of Washington, Seattle, WA 98195, USA. [7]Miller Research Institute, University of California Berkeley, Berkeley, CA 94720, USA. [8]Kavli Energy NanoScience Institute, Berkeley, CA 94720, USA.
†Present address: Department of Physics of Complex Systems, Weizmann Institute of Science, Rehovot 7610001, Israel.
‡Present address: Applied Physics Program, University of Michigan, Ann Arbor, MI 48109, USA. §Present address: Department of Electrical Engineering and Computer Science, Massachusetts Institute of Technology, Cambridge, MA 02139, USA.
***Corresponding author: paul.alivisatos@berkeley.edu**

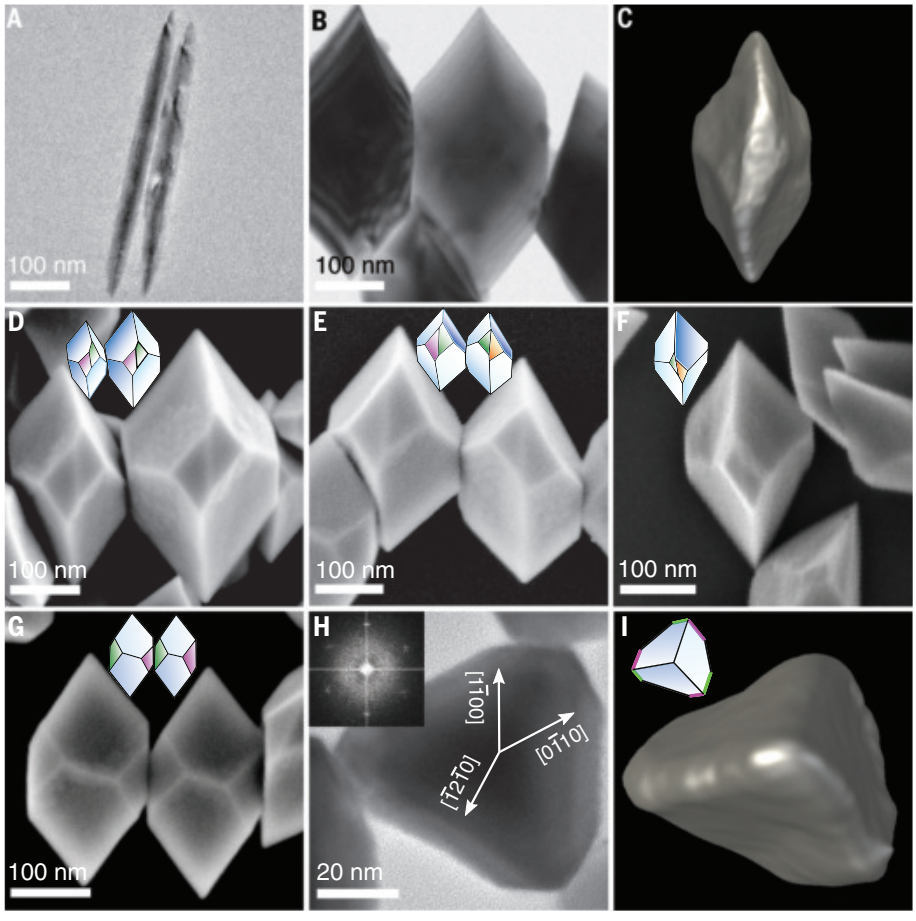

Fig. 1. Model system of morphologically chiral nanocrystals. (**A** and **B**) TEM images of (A) thin rods and (B) fully formed bipyramids. (**C**) A surface rendering of a STEM tomogram of a bipyramid observed along the $[\bar{1}2\bar{1}0]$ direction. (**D** to **F**) SEM images of (D) a pair of right-handed (P) bipyramids, (E) a right-handed (P) and a left-handed (M) bipyramid, and (F) a single left-handed (M) bipyramid all observed along the $[\bar{1}2\bar{1}0]$ direction for P and $[1\bar{2}10]$ for M. (**G**) A pair of right-handed (P) bipyramids observed along the $[1\bar{2}10]$ direction. (H) A TEM image of a bipyramid observed along the $[000\bar{1}]$ direction, with its corresponding fast Fourier transform. (I) A view along the $[000\bar{1}]$ direction of the tomogram in (C). The pair of facets used to assign handedness are marked pink, green, and orange on smaller inset models in (D) to (G) and (I).

further characterized the bipyramidal nanoparticles using scanning transmission electron microscopy (STEM) tomography and scanning electron microscopy (SEM), resolving the three-dimensional (3D) chiral morphology. 3D renderings of a representative bipyramid are presented in Fig. 1C and movie S1 as viewed along the $[\bar{1}2\bar{1}0]$ direction. Several facets can be seen with smoothing because of the tomographic reconstruction process. SEM is highly sensitive to edges, and we used the tomographic reconstructions of several nanoparticles to better interpret SEM images of the sharply faceted structure. Nanocrystals at the same orientation as in Fig. 1C are shown in Fig. 1, D to F, and fig. S2, and the bottom view is shown in Fig. 1G, giving a sense of the overall shape. The trigonal symmetry is observed along the nanoparticle's long axis ($[000\bar{1}]$ direction) in Fig. 1, H and I, by using a TEM projection and STEM tomography, respectively. This polyhedron possesses a D_3 point symmetry. STEM tomography and SEM images show that these nanoparticles present a distinct structure of flat facets with a chiral arrangement similar to chiral habits of macroscopic crystals (*2*, *3*, *5*, *6*). We assigned left-handedness (M) and right-handedness (P) nomenclature to the shapes using a convention that follows (*9*). In this approach, the 3D shape can be thought of as a set of 2D slices stacked and gradually rotating along the long axis ([0001]). Clockwise rotation is correlated with right-handedness, and counterclockwise is correlated with left-handedness (fig. S3). Further, the arrangement of two small facets in the center allows identifying the handedness because it is mirrored in crystals of opposite chirality. These facets can be determined from the relative directions identified in Fig. 1H, and their indexing depends on which mirror image of the crystal is observed (Fig. 2). In right-handed (P) particles, these are the $(0\bar{1}10)$ and $(1\bar{1}00)$ facets colored pink and green, respectively, in Fig. 1, D to I, insets. In left-handed (M) particles, these are the $(0\bar{1}10)$ and $(10\bar{1}0)$ colored green and orange, respectively, in Fig. 1, D to I, insets. Extra facets on the sides (fig. S4) are harder to assign but might be equivalent to those required in bulk chiral habits to lower shape symmetry, as in the case of quartz's s and x faces (*5*).

When the nanoparticles are prepared in the presence of one mirror image of the chiral ligand penicillamine, a large excess of one mirror image is formed as measured with circular dichroism (CD) (fig. S5) (*7*–*9*). CD does not allow quantification of the exact populations of mirror images; therefore, we used large-scale, automated SEM imaging and manual identification to distinguish the two forms from a large population of NPs (close to 300 in each sample).

In Fig. 2A, the distribution of both forms in samples made with pure D- and pure L- ligands is presented as a function of their length. In both samples, one mirror image formed in large excess (85%) but not 100%. The less-abundant particles are smaller in size, which indicates that chiral ligands affect the rates of both nucleation (affecting the population) and continuous growth (affecting the final size).

Next, we correlated the shape handedness with that of the crystal structure. For this purpose, aberration-corrected high angle annular dark field–STEM (HAADF-STEM) imaging at two stage tilts was performed. Low- and high-resolution HAADF-STEM images and an atomistic model viewed along the $[1\bar{2}10]$ tellurium nanocrystal direction are shown in Fig. 2B. A single 2D STEM image, even though it may appear to show chirality, does not decisively infer 3D handedness. Because of the projection nature of STEM, looking at the same particle from the opposite direction (corresponding to a 180° tilt) will reverse the sense of 2D handedness, and a single image is insufficient to tell which side of the bipyramid is viewed. To solve this problem, we acquired a focal series, as explained in the supplementary materials and fig. S6, which allows us to assign left-handedness (M) to the particle observed in Fig. 2B. The same particle was then imaged at the $[1\bar{1}00]$ zone axis. The low- and high-resolution STEM images at the new orientation, and a model, are presented in Fig. 2C. Dong and Ma recently demonstrated that atomic-resolution images at these two tilts are sufficient to resolve the handedness of the crystal structure (*20*). Figure 2C fits the model for the $P3_221$ space group (left-handed tellurium helices) and will not fit the $P3_121$ space group (right-handed tellurium helices), which at these tilt conditions will exhibit a mirror arrangement of atoms. A detailed comparison and description of the space groups along these two directions is presented in fig.

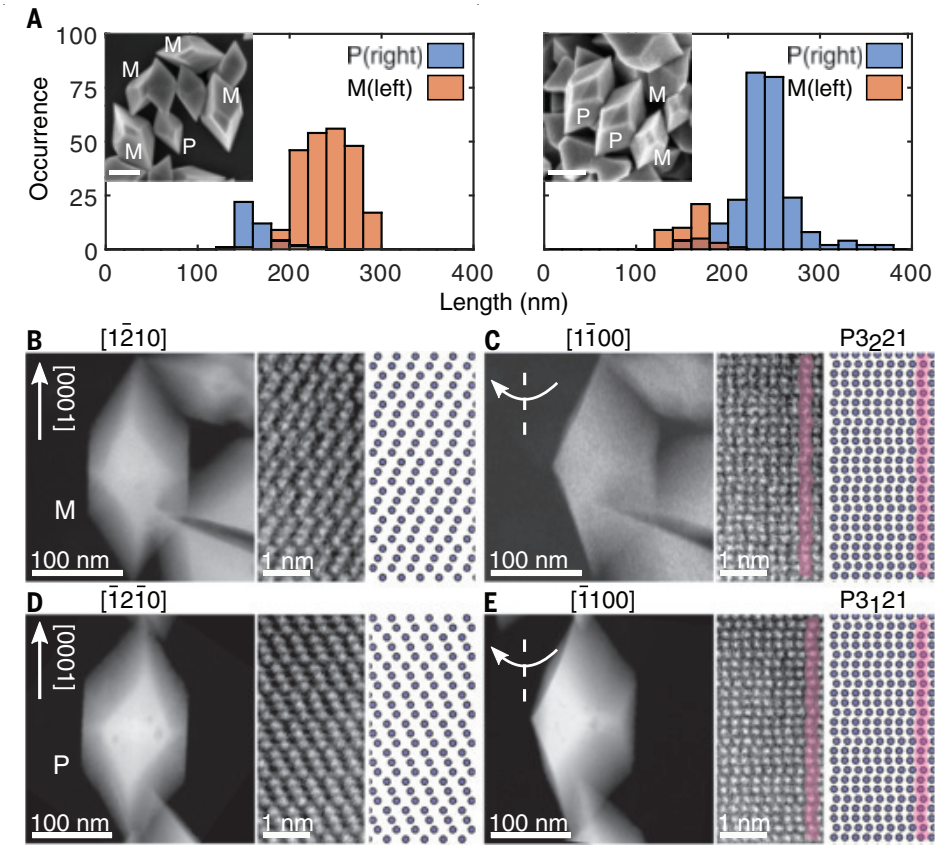

Fig. 2. Determination of crystal structure and shape handedness. (**A**) Distribution of bipyramid handedness when using only L- or D-penicillamine ligands in the reaction (left and right, respectively). Orange and blue columns represent left- and right-handed particles, respectively. Bottoms of columns that appear brown are where orange and blue overlap. (Insets) SEM images show the existence of both mirror images in each sample. Scale bars, 100 nm. (**B** and **C**) (Left) Low-resolution and (middle) high-resolution HAADF-STEM images and (right) a corresponding atomistic model observed along the (B) [1$\bar{2}$10] and (C) [1$\bar{1}$00] zone axes. Shape and crystal structure handedness were characterized as M and P3$_2$21 space group, respectively. Pink curved lines indicate atom columns to compare between the experiment and model. (**D** and **E**) A P-shaped nanocrystal observed along the (D) [$\bar{1}$2$\bar{1}$0] and (E) [$\bar{1}$100] directions. The crystal structure can be assigned to the P3$_1$21 space group.

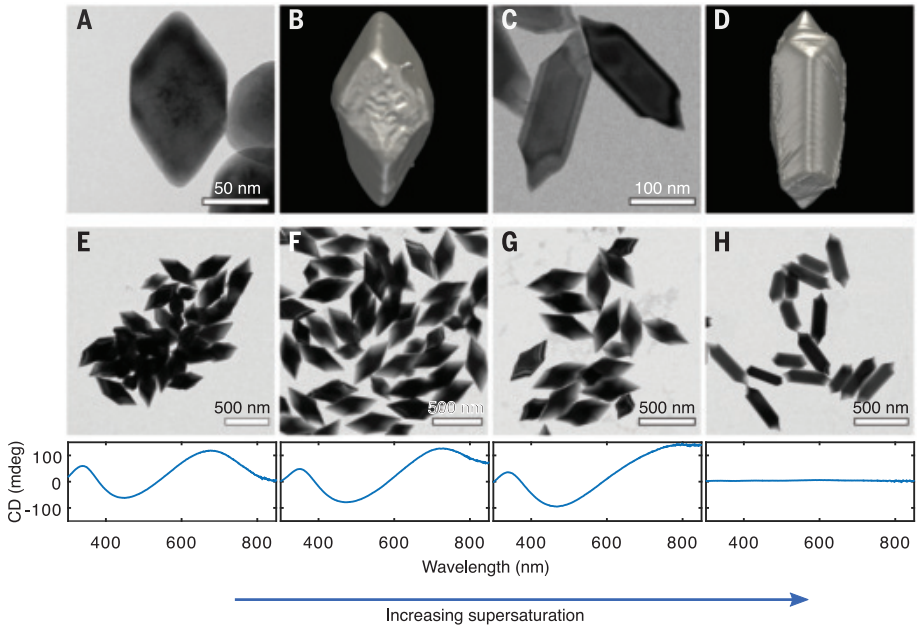

Fig. 3. Chiral ligands are neither necessary nor sufficient for chiral shape formation. (**A**) A TEM image and (**B**) a STEM tomogram of chiral bipyramids grown with achiral mercaptopropionic acid ligands. (**C**) A TEM image and (**D**) a STEM tomogram of achiral particles grown with chiral penicillamine ligands. (**E** to **H**) TEM images with the corresponding CD spectra below, of particles grown with (E) 1 ml, (F) 2 ml, (G) 4 ml, and (H) 6 ml of hydrazine. The transition from chiral to achiral morphology is observed between (G) and (H).

S7. In the same way, we determined that the particle observed along the [1$\bar{2}$10] direction in Fig. 2D and [$\bar{1}$100] in Fig. 2E is a right-handed (P) particle with a crystal structure belonging to the P3$_1$21 space group.

Both particles are from the sample depicted in Fig. 2A, right, where right-handed (P) nanocrystals are more common. Using this method, we measured seven right-handed (P) particles and two left-handed (M) particles and found that P shapes always had the P3$_1$21 space group, whereas M shapes had the P3$_2$21 space group.

These results seem to imply that the chain of chirality transfer starts with the ligands directing the handedness of the crystal structure formation and, in turn, the crystal structure handedness determines that of the shape. However, as shown in Fig. 3, even though chiral ligands strongly affect the relative abundance of mirror images, they are neither necessary nor sufficient for the formation of chiral shapes.

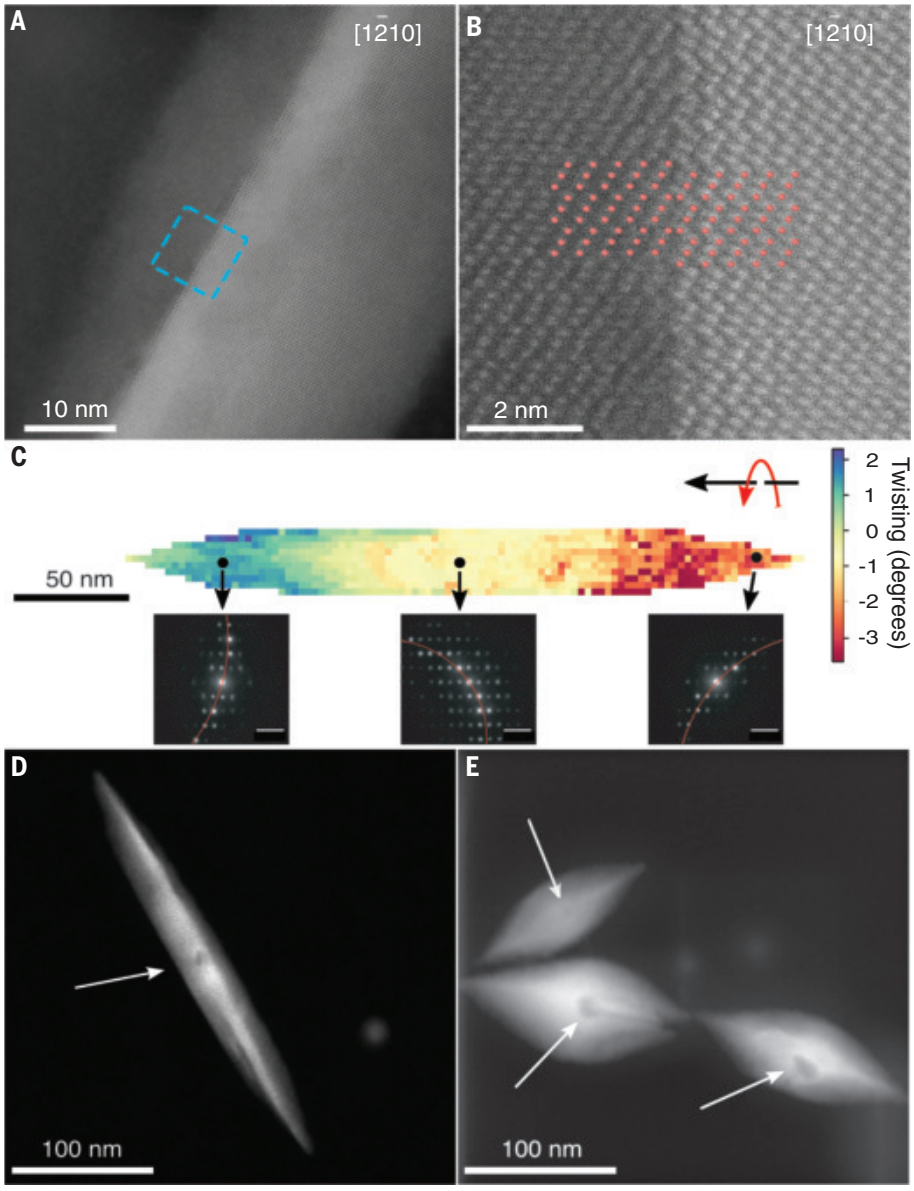

Fig. 4. Structural evidence of screw dislocations. (**A**) An atomic-resolution HAADF-STEM image of the center of a nanorod observed along the $[1\bar{2}10]$ direction. (**B**) The enlarged region marked by a cyan frame in (A) overlaid with a model for a dissociated dislocation (red dots). (**C**) Map of twist around the *c* axis extracted from 4D-STEM measurements. Electron diffraction patterns from different positions are overlaid with fits to a Laue circle (red lines). Twisting direction in this particle follows a left-handed screw rule. (**D** and **E**) HAADF-STEM images of (D) a nanorod and (E) bipyramids with voids (white arrows).

The reaction was conducted with achiral mercaptopropionic acid as the thiolated ligand, under similar conditions, and the nanoparticles still formed a chiral shape similar to the ones formed with penicillamine (Fig. 3, A and B, and movie S2). This sample exhibited no CD signal, indicating that an equal mixture of left- and right-handed nanocrystals formed. These results indicate that chiral ligands only serve to bias the synthesis in favor of one mirror image but do not cause chiral shape formation. This proves that past models of arrested growth by chiral additives (*2*, *9*–*11*) do not sufficiently describe the observations made here.

Next, we examined the other prominent mechanism that can lead to morphological chirality, screw-dislocation–mediated growth accompanied by "Eshelby twisting" of the crystal structure (*1*, *12*–*17*). Even though this mechanism is established as a source of shape chirality from twisting (*1*, *12*–*17*), we tested whether it also leads to the formation of the chiral polyhedrons. Classical crystal growth theory predicts that screw-dislocation–mediated growth is dominant at low monomer supersaturations (*12*–*16*). We therefore expected that if screw dislocations were involved, then higher tellurium dioxide reduction rates should produce achiral shapes. Achiral morphologies indeed formed in these conditions, even in the presence of chiral ligands at the same concentration as in the reactions that yielded chiral shapes (Fig. 3, C and D, and movie S3). Shown in Fig. 3 is the transition from chiral (Fig. 3, E to G) to achiral (Fig. 3H) shape formation as the rate of reduction, which sets supersaturation, is increased. Other than supersaturation, all synthetic conditions are identical between these samples. The TEM images show that particles in Fig. 3, E to G, have the chiral shape seen in Fig. 1B, and the ones in Fig. 3H have the achiral shape seen in Fig. 3, C and D. The CD response shown below each Fig. 3 TEM image (expected to be present only for chiral shapes) (*7*) is absent for the particles in Fig. 3H. This observation correlates with the model predicting a transition from screw-dislocation–driven growth to layer-by-layer growth (*12*–*16*).

We support these results, which strongly imply the involvement of screw dislocations in the growth process, with structural characterization. Aberration-corrected HAADF-STEM imaging allowed direct observation of atomic displacements induced by the dislocation, but two cases must be considered. First, a single screw dislocation line passes through the core of the nanorod (*12*–*17*). Second, as commonly observed in tellurium (*21*, *22*) and other systems (*22*, *23*), the screw dislocation dissociates into partials, lowering the crystal's overall energy. In the case of tellurium, a single screw dislocation with a Burgers vector b = [0001] can dissociate into three partials with $b = \frac{1}{3}[0001]$ (*20*, *21*). In Fig. 4A, a HAADF-STEM image of a thin rod observed along the $[1\bar{2}10]$ direction is presented. In Fig. 4B, the region marked by a cyan frame in Fig. 4A is magnified and compared with a model of a dissociated screw (supplementary materials, materials and methods, and fig. S8). A discontinuity in the rows of atomic columns is observed across the dislocation line. This is a signature of a dissociated screw and is not observed in a crystal with a nondissociated screw (fig. S8). Images of another nanoparticle and direction also show the atomic column displacements of the line defect (fig. S9).

Another indication of screw dislocations is the Eshelby twisting of the lattice (*12*–*17*), which we measured using 4D-STEM (*24*), a technique that allows extraction of local twisting with high spatial resolution (supplementary materials, materials and methods, and fig. S10). In brief, a measurement of 2D electron diffraction patterns is acquired at a 2D set of scanning positions, and Laue circle fitting for each scan position maps the local lattice orientation relative to the [0001] axis (Fig. 4C). Representative diffraction patterns with red fit

lines from three beam positions are presented. The measured twisting along the *c* axis of 0.02° nm^{-1} is similar to other measurements of Eshelby twisting (*12*–*14*). Existence of this twist further reduces the possibility that chirality of the shape originates from differential growth rates of facets induced by chiral ligands or by the chiral crystal structure because this would not be accompanied by lattice twisting.

Screw dislocations can also lead to void formation because of the strain energy associated with the dislocation exceeding the surface energy required to form an inner surface (*14*). In Fig. 4, D and E, representative HAADF-STEM images of rods and bipyramids, respectively, show these voids as dark regions. STEM tomography shows that these voids are inside the nanoparticle (fig. S11). As expected, voids were not found in achiral shapes (fig. S12) but were found in chiral shapes grown in the absence of chiral ligands (fig. S13).

Combined, our results strongly suggest a chain of chirality transfer from crystal structure to shape that is not a result of the chiral crystal structure or chiral ligands. Instead, chiral shapes form when grown in sufficiently low supersaturation so that they are the result of screw-dislocation–mediated growth. That the handedness of the shape seems to be dictated by that of the crystal structure is probably a result of screw dislocations of opposite handedness being favored in crystal structures of opposite handedness (*25*, *26*). In this way, screw dislocations also mediate correlation of handedness between the two hierarchies. Even though chiral ligands do not give rise to chiral shapes in our system, they can bias the population of both mirror images, leading to an abundance of one mirror image over the other, as well as a difference in average size. This suggests that chiral ligands unevenly affect opposite mirror images of chiral crystals in both the nucleation and growth stages. Although screw-dislocation–mediated growth has been studied in relation to twisting, it has rarely been considered as the source of habits of single crystals that present a chiral arrangement of facets. It is not surprising that such a mechanism has been overlooked in bulk crystals that present chiral nontwisted habits because the signature of these dislocations in growth would have been very hard to identify.

REFERENCES AND NOTES

1. A. G. Shtukenberg, Y. O. Punin, A. Gujral, B. Kahr, *Angew. Chem. Int. Ed.* **53**, 672–699 (2014).
2. L. Addadi, M. Geva, *CrystEngComm* **5**, 140–146 (2003).
3. L. Pasteur, *Ann. Chim. Phys.* **24**, 442–459 (1848).
4. J. Gal, *Chirality* **20**, 5–19 (2008).
5. R. M. Hazen, D. S. Sholl, *Nat. Mater.* **2**, 367–374 (2003).
6. K.-H. Ernst, *Surf. Sci.* **613**, 1–5 (2013).
7. A. Ben-Moshe *et al.*, *Nat. Commun.* **5**, 4302 (2014).
8. A. Ben-Moshe, A. O. Govorov, G. Markovich, *Angew. Chem. Int. Ed.* **52**, 1275–1279 (2013).
9. P.-P. Wang, S.-J. Yu, A. O. Govorov, M. Ouyang, *Nat. Commun.* **8**, 14312 (2017).
10. I. Weissbuch, L. Addadi, L. Leiserowitz, *Science* **253**, 637–645 (1991).
11. C. A. Orme *et al.*, *Nature* **411**, 775–779 (2001).
12. M. J. Bierman, Y. K. A. Lau, A. V. Kvit, A. L. Schmitt, S. Jin, *Science* **320**, 1060–1063 (2008).
13. J. Zhu *et al.*, *Nat. Nanotechnol.* **3**, 477–481 (2008).
14. S. A. Morin, M. J. Bierman, J. Tong, S. Jin, *Science* **328**, 476–480 (2010).
15. F. Meng, S. A. Morin, A. Forticaux, S. Jin, *Acc. Chem. Res.* **46**, 1616–1626 (2013).
16. Y. Liu *et al.*, *Nature* **570**, 358–362 (2019).
17. L. H. G. Tizei *et al.*, *Phys. Rev. Lett.* **107**, 195503 (2011).
18. A. Ben-Moshe, B. M. Maoz, A. O. Govorov, G. Markovich, *Chem. Soc. Rev.* **42**, 7028–7041 (2013).
19. J. Yeom *et al.*, *Nat. Mater.* **14**, 66–72 (2015).
20. Z. Dong, Y. Ma, *Nat. Commun.* **11**, 1588 (2020).
21. J. Di Persio, J. C. Doukhan, G. Saada, *J. Phys. France* **28**, 661–666 (1967).
22. B. Escaig, *J. Phys. Colloq.* **35**, C7-151–C7-166 (1974).
23. S. Ismail-Beigi, T. A. Arias, *Phys. Rev. Lett.* **84**, 1499–1502 (2000).
24. C. Ophus, *Microsc. Microanal.* **25**, 563–582 (2019).
25. A. G. Shtukenberg *et al.*, *Cryst. Growth Des.* **15**, 921–934 (2015).
26. B. Sung, A. de la Cotte, E. Grelet, *Nat. Commun.* **9**, 1405 (2018).
27. dasilvaale, dasilvaale/4D-STEM-Analysis: Initial release. Zenodo (2021); doi:10.5281/zenodo.4587925.

ACKNOWLEDGMENTS

We are very grateful to M. G. Cho for her help with HR imaging, to K. Bustillo for help with 4D-STEM data collection, C. Song for assistance in STEM imaging, and to C. Nixon and S. Marquesee for graciously allowing us to use their group's CD spectrometer and supporting us in the process. A.B.-M. is grateful to A. Teitelboim for useful discussions and her support. We are very grateful to Y. Ma for useful discussion regarding determination of crystal structure handedness in STEM. **Funding:** This work was primarily supported by the U.S. Department of Energy, Office of Science, Office of Basic Energy Sciences, Materials Sciences and Engineering Division, under contract DE-AC02-05-CH11231 within the Characterization of Functional Nanomachines Program (KC1203). Work at the Molecular Foundry, Lawrence Berkeley National Laboratory, was supported by the U.S. Department of Energy under contract DE-AC02-05CH11231. J.W. acknowledges support from the U.S. Department of Energy, Office of Science, Office of Workforce Development for Teachers and Scientists (WDTS) under the Science Undergraduate Laboratory Internship (SULI) program. F.N. was supported by the Miller Research Institute. A.B.-M. acknowledges support from a Fulbright fellowship. A.d.S. acknowledges funding from the Brazilian National Council of Technological and Scientific Development (CNPq). A.A. and M.A. acknowledge support for the computational modeling from a fellowship through the National Science Foundation Graduate Research Fellowship Program (grant DGE 1752814), and the U.S. Department of Energy, Office of Science, Office of Basic Energy Sciences, Materials Sciences and Engineering Division, under contract DE-AC02-05-CH11231 within the Damage-Tolerance in Structural Materials (KC 13) program, respectively. **Author contributions:** A.B.-M. and A.P.A. conceived of the idea for the project. A.B.-M. performed synthesis of nanocrystals, TEM characterizations, and CD measurements. A.d.S. performed data acquisition and analysis for STEM tomography, supervised by P.E. 4D-STEM data was collected by A.d.S. and analyzed by A.d.S and P.H., supervised by C.O., W.T., and P.E.; A.M. acquired large-scale SEM scans and HR-SEM, and the data was analyzed by A.M., J.W., and A.B.-M.; F.N. performed additional SEM characterizations. P.E. performed HR-STEM imaging. A.M.M., W.T., and P.E. supervised all the electron microscopy work. A.A. developed the continuum elasticity models, supervised by M.A.; A.B.-M. and A.P.A. wrote the manuscript, with critical contributions and edits from all authors. A.P.A. directed the project. **Competing interests:** The authors declare no competing interests. **Data and materials availability:** All data are available in the main text or the supplementary materials. Computer code and files used for extraction of twisting from 4D-STEM measurements are permanently archived in Zenodo (*27*).

SUPPLEMENTARY MATERIALS

science.sciencemag.org/content/372/6543/729/suppl/DC1
Materials and Methods
Figs. S1 to S13
Table S1
References (*28*–*38*)
Movies S1 to S3

3 December 2020; accepted 23 March 2021
10.1126/science.abf9645

EVOLUTIONARY ECOLOGY

Macroevolutionary stability predicts interaction patterns of species in seed dispersal networks

Gustavo Burin*†, Paulo R. Guimarães Jr., Tiago B. Quental*

Assessing deep-time mechanisms affecting the assembly of ecological networks is key to understanding biodiversity changes on broader time scales. We combined analyses of diversification rates with interaction network descriptors from 468 bird species belonging to 29 seed dispersal networks to show that bird species that contribute most to the network structure of plant–frugivore interactions belong to lineages that show higher macroevolutionary stability. This association is stronger in warmer, wetter, less seasonal environments. We infer that the macroevolutionary sorting mechanism acts through the regional pool of species by sorting species on the basis of the available relative differences in diversification rates, rather than absolute rates. Our results illustrate how the interplay between interaction patterns and diversification dynamics may shape the organization and long-term dynamics of ecological networks.

Seed dispersal by animals is a fundamental property of ecosystems (*1*). This mutualism between angiosperms and, mainly, vertebrates started about 80 million years ago (*2*), and currently between 70 and 90% of woody species rely on vertebrates to disperse their seeds (*3*). Accordingly, many vertebrate groups have fruits as part of their diet [56% of bird families and many species of mammals, reptiles, fishes, and even amphibians (*3*–*4*)]. The radiations of seed-dispersing birds and mammals are hypothesized to be linked to the rise and dominance of angiosperms during the Cenozoic era (*2*), although the causal links

Departamento de Ecologia, Instituto de Biociências, Universidade de São Paulo, Sao Paulo, Brazil.
***Corresponding author. Email: gustavoburin@usp.br (G.B.); tbquental@usp.br (T.B.Q.)**
†Present address: Department of Life Sciences, Natural History Museum, Cromwell Road, London SW7 5BD, UK.

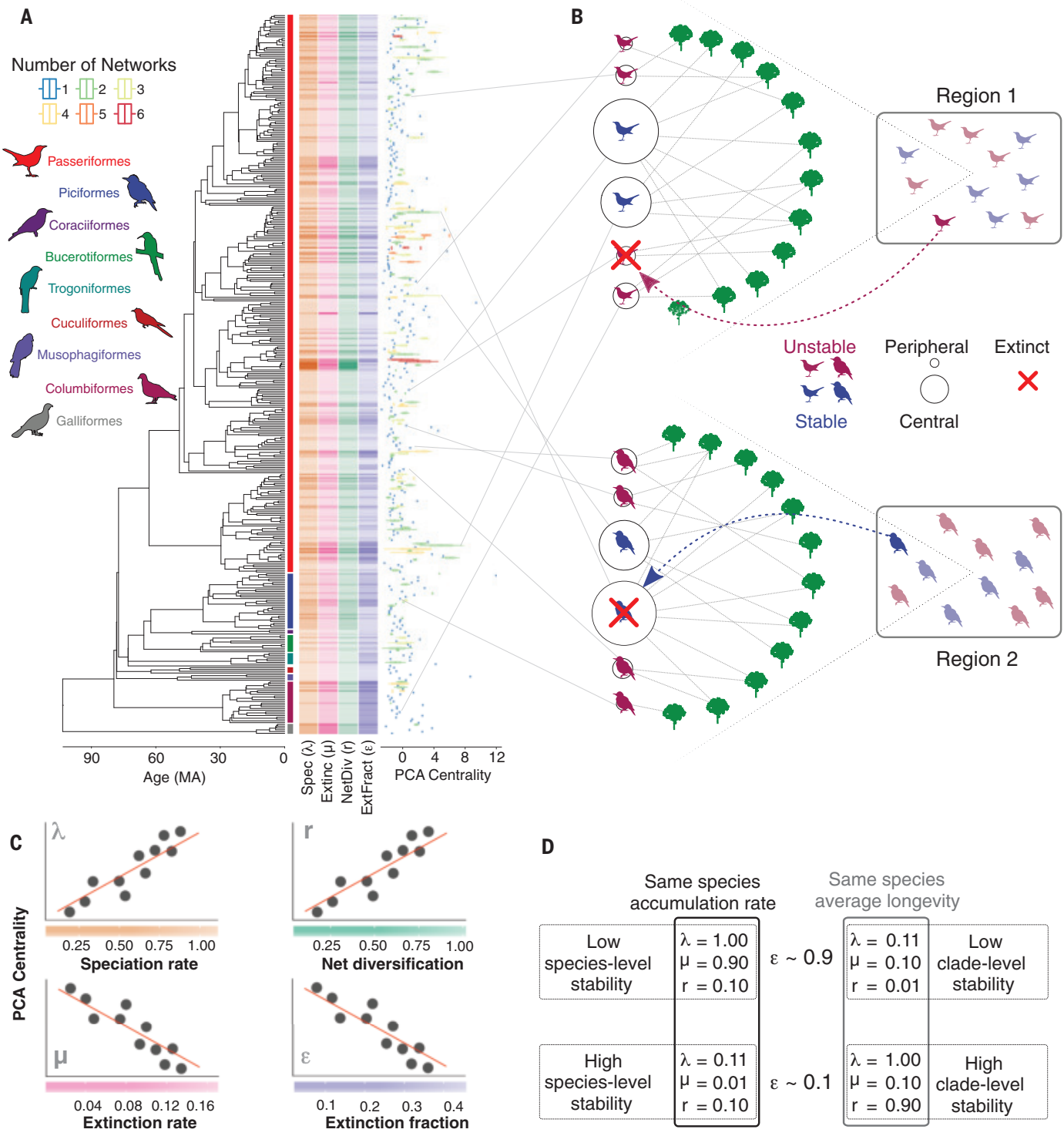

Fig. 1. Conceptual framework and data used. (**A**) Exemplar pruned phylogeny with indicated bird orders, along with the speciation rates (λ) (orange lines), extinction rates (μ) (pink lines), net diversification rates (r) (green lines), extinction fraction (ε) (purple lines), and the PCA centrality values for each of the species, of all species used in the analyses; PCA centrality scores resulted from defining interaction patterns when using three different network descriptors. Some species were present in more than one ecological network, and this information is displayed by points or bars of different colors in the PCA centrality graph. The color scheme on the *x* axis in (C) acts as a legend for the rate values here. MA, millions of years. (**B**) Cartoon example of two networks, showing the suggested patterns of network assembly with respect to macroevolutionary rates shown in (A) and the potential replacement from another species in the regional pool of species (indicated by the dashed line) in case a given species in a particular network goes extinct. (**C**) Expected correlations between PCA centrality and all four rates considered in this study. (**D**) Illustrative combination of speciation and extinction rates, showing different degrees of species- and clade-level stability. The accumulation rate is described by the rate of diversification, whereas average species longevity is the reciprocal of extinction rate (1/μ).

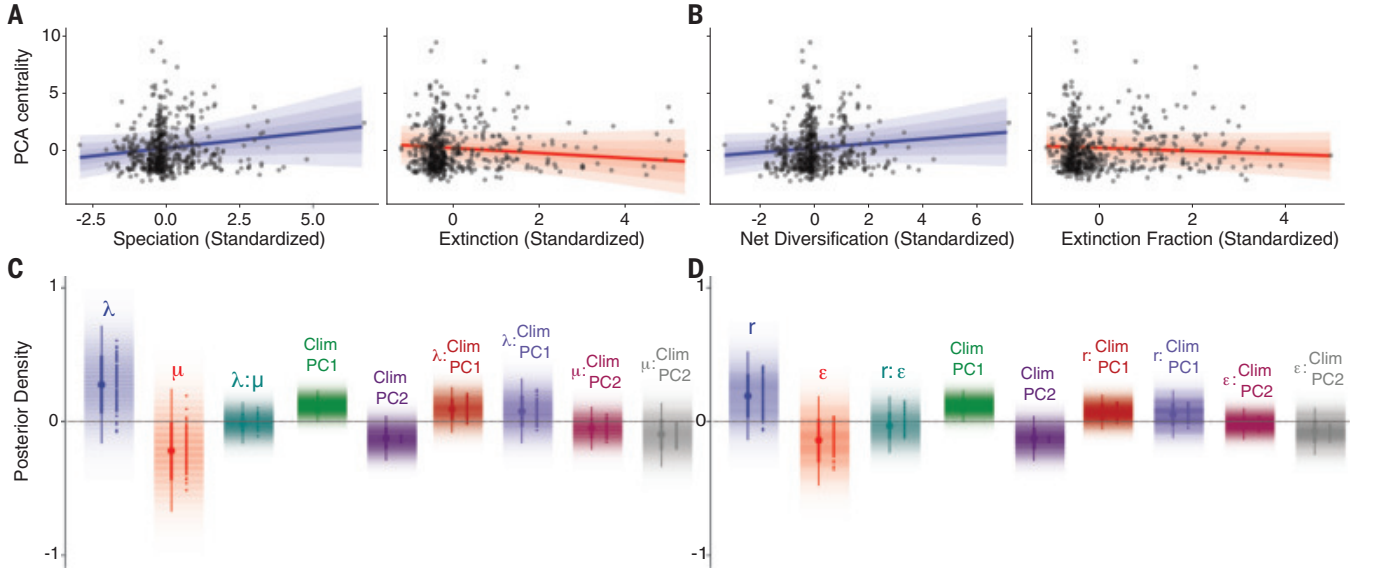

Fig. 2. Association between network centrality and macroevolutionary stability. (**A**) Exemplar association between PCA centrality values (a PCA score based on three centrality descriptors) and speciation and extinction rates estimated from one phylogenetic tree. The blue and red lines are the median intercept and slope values from the combined posterior distribution of each parameter, and the shaded areas (from darker to lighter) represent the 50, 80, and 95% credibility intervals, respectively. (**B**) Exemplar association between PCA centrality scores and extinction fraction and net diversification rates estimated from one phylogenetic tree. The blue and red lines are the median intercept and slope values from the combined posterior distribution of each parameter, and the shaded areas (darker to lighter) represent the 50, 80, and 95% credibility intervals, respectively. In (A) and (B), the points are not independent because of phylogenetic structure, and therefore visual inspection of results could be misleading. (**C**) Posterior distributions of all slopes for Bayesian generalized linear mixed model analysis between use of speciation (λ) and extinction (μ) rates as predictors. (**D**) Posterior distributions of all slopes for the Bayesian generalized linear mixed model analysis between use of net diversification (r) and extinction fraction (ε) rates as predictors. Posterior distributions of most slopes are off-center from a slope of zero (positive for speciation and net diversification and negative for extinction and extinction fraction), indicating that species belonging to macroevolutionarily more stable lineages are more central in the networks. In (C) and (D), the density of color represents the posterior density of each parameter; the point-and-range lines on the left of each variable represent the median (point), 66% highest posterior density (HPD) interval (thick line), and 95% HPD (thin line); the dots on the right of each variable represent the median of the posterior distribution of each individual tree used in the analyses. ClimPC1 and ClimPC2 refer to the principal component of climatic variables, with ClimPC1 mainly representing variation in average annual temperature and temperature seasonality and ClimPC2 representing total annual precipitation and precipitation seasonality (see fig. S9 for the loadings).

are elusive. In particular, some bird groups are consistently recognized as specialized frugivores across broad ranges of spatial and temporal scales (*1*, *5*–*7*).

Most studies on seed dispersal networks have focused on understanding patterns and processes at ecological time scales (*8*–*9*), with few studies looking at broader temporal scales (*2*, *10*–*14*). We are now beginning to understand how diversification dynamics may affect the assembly process, and consequently, the structure of interaction networks [e.g., (*15*, *16*)]. Although interaction networks as a whole might be plastic both in time and space (*17*–*19*), evidence suggests that the core of seed dispersal networks is robust to yearly fluctuations of fruit availability and bird species presence (*20*). Moreover, theory suggests that species that show higher persistence across time and space should interact with more partners (*21*, *22*), supporting the idea that at least the core of the network might show some temporal stability. This temporal stability in interaction patterns may be observed at longer temporal scales, because closely related frugivores often interact with similar coteries of plants (*12*, *23*). In this context, a fundamental problem to solve is whether and how patterns of interaction observed in the networks formed by plants and their seed dispersers at ecological scales are associated with macroevolutionary dynamics operating at deeper temporal scales.

Here, we explore this problem by integrating macroevolutionary information, ecological data on species interactions, and network analysis. We hypothesized that lineages that contain long-lived species or lineages that can quickly accumulate many species of birds (here, macroevolutionarily stable lineages) are more likely to contribute with species to the core of ecological networks, providing an explicit macroevolutionary mechanism for network assemblage (see Fig. 1 for a schematic version of our general approach and the data used).

Here, we define macroevolutionary stability at two different levels. At the species level, we define stable species as species that typically last longer (lower extinction rates imply longer longevities) or species that are more likely to produce new daughter species (those species with higher speciation rates). In the latter case, the continuation of the "species" amid extinctions would be through the production of daughter species that likely share traits associated with the interaction [this case could be also seen as a higher-level effect (see below)]. At higher phylogenetic levels (e.g., a monophyletic lineage with multiple species), we define stable lineages as lineages that either have a low extinction fraction (i.e., relatively low extinction compared to speciation) and/or higher net diversification (i.e., lineages that can accumulate species at a faster pace), which would allow more efficient replacement of a given extinct species by a closely related one that would show similar patterns of interaction (*12*, *23*).

Starting from a molecular phylogeny (Fig. 1A), we estimated rates of speciation, extinction, net diversification rate (speciation minus extinction), and extinction fraction (extinction divided by speciation rate) for all species in the networks. We then estimated species' interaction patterns (how they were connected) within each of the 29 networks (Fig. 1B), using three different network descriptors to characterize interaction patterns of each species, which were then combined into a single descriptor index for each species by using principal component analysis (PCA) (*24*). We then used a hierarchical Bayesian phylogenetic framework to test for relationships between macroevolutionary stability and

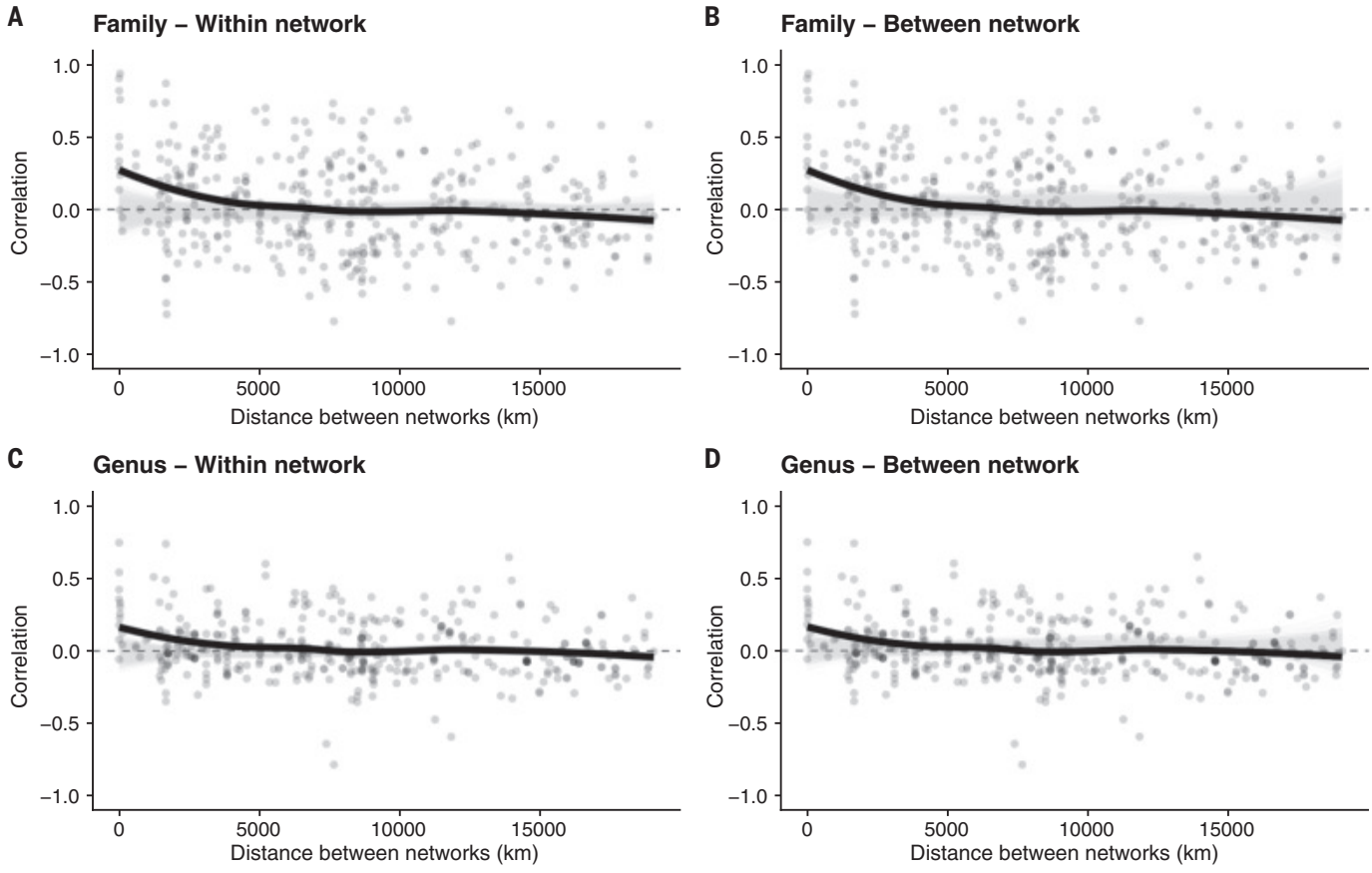

Fig. 3. Association between mean PCA centrality for each family or genus and geographical distance. (**A** to **D**) Each point represents a pairwise correlation between interaction patterns in two different networks, and the thick black lines are a loess smoothing showing the general trend of the data. The gray areas represent the null models that were built by randomizing centrality values for each species within networks (A) and (C) or by randomizing the identity of networks for each geographical distance (B) and (D). Regardless of the null model selected, the associations between mean centrality of families and genera are higher than expected by the null model for geographically close networks, and this similarity dissipates with distance, suggesting there is no single group driving the association between macroevolutionary stability and interaction patterns.

interaction patterns of bird species (Fig. 1C) (*24*). This workflow naturally incorporated phylogenetic and ecological uncertainties, along with environmental factors, to address how the interplay between biotic and abiotic factors affects the assembly of local networks according to macroevolutionary dynamics. We jointly tested whether the sorting of different macroevolutionary diversification dynamics (speciation and extinction rates and combinations of these two rates) (Fig. 1) takes place at the regional or global scale by using raw absolute rates and standardized rates (rescaled for each network). The absolute rates allow us to explore a global sorting mechanism which selects for specific diversification dynamics (specific absolute rate values) irrespective of the pool of available clades. Conversely, standardized rates allow us to explore a sorting mechanism that would act on the relative rank of rates available at the regional scale. Owing to the lack of comprehensive species-level phylogenies for plants, we performed the analysis only for bird species.

We found that central bird species in seed dispersal networks tend to belong to macroevolutionarily stable lineages. Standardized speciation and extinction rates show, respectively, positive and negative associations with species' patterns of interaction (Fig. 2A). The negative association between interaction pattern and extinction rates highlights that the sorting process takes place at the species level (because longevity is an inherent property of a species), with longer-lasting species occupying more central positions within networks. We also found that extinction fraction is negatively correlated with species' interaction patterns, whereas net diversification rates are positively correlated (Fig. 2B). In all cases, the posterior distributions are not centered on a slope value of zero. These correlations suggest that species that occupy central positions in networks tend to belong to lineages that are either less volatile [sensu (*25*)] and/or generate multiple species in a short time span. Hence, central species are more likely both to persist in time (negative correlation with extinction rate) and to belong to clades that are more likely to provide a replacement species if one goes extinct (correlations with extinction fraction and diversification rate).

We also found a positive relationship between speciation rate and centrality measures. This association reinforces the idea of a clade-level stability mechanism, because high speciation rates indicate that those species are more likely to produce daughter species that might replace a species if it goes extinct. One important assumption for the higher-level sorting mechanism, which finds support in previous knowledge (*12*), is that the replacement species has similar ecological attributes that allow them to perform similar ecological dispersal services. All these results hold after accounting for multiple sources of uncertainty (figs. S1 and S2). Median standardized effects for speciation, extinction, extinction fraction, and net diversification were 0.275, −0.218, −0.140, and 0.191, respectively, indicating that the two higher-level components of macroevolutionary stability contribute with similar intensity to

the structuring of the networks. Sensitivity analysis based on the medians of the posterior distributions for most parameters for each individual tree (Fig. 2, C and D) suggests that this signal holds irrespective of phylogenetic uncertainty.

Our results provide evidence that this macroevolutionary sorting of diversification dynamics is predominantly a regional-scale phenomenon, because we only observed evidence for sorting when analyzing the rates standardized within networks (Fig. 2) and not for the raw absolute rates (figs. S5 and S6). This suggests that the macroevolutionary sorting mechanism acts at a regional scale, sorting the species within each region through their relative rank of stability, rather than on absolute values of speciation, extinction, extinction fraction, or net diversification rates. Our results indicate that representatives of important seed-dispersers groups across multiple localities indeed have high relative macroevolutionary stability, as the result of either fast species accumulation (e.g., thraupid genera, such as *Tangara* and *Thraupis*) or long-lived lineages (e.g., species of Turdidae) (*5*–*7*). Ecological factors such as species abundance distributions (*26*) and the presence of invasive species (*27*) also influence network organization. Unfortunately, the lack of data prevents us from further testing if macroevolutionary consequences to network structure are modulated by those factors.

To evaluate if species within the same lineage have similar interaction patterns in different networks, we calculated the average centrality value for each different lineage (either family or genus) for all networks. The association between the mean centrality value of each lineage in different networks decays as a function of the geographical distances between those networks (Fig. 3 and fig. S7), suggesting that geographically close networks tend to have similar lineages with similar interaction patterns but that similar patterns of interaction are shown by different lineages in different places. This reinforces previous findings that different networks along a geographical range are structured with similar functional roles within their structures (*28*). This result also reinforces that the assembly process occurs at the regional scale, in accordance with the existence of a relationship between centrality and macroevolutionary stability for the standardized rates but not for the absolute rates.

We also found that environmental conditions affect the relationship between interaction patterns in a seed dispersal network and macroevolutionary stability, with warmer, wetter, nonseasonal environments showing a stronger sorting (here, revealed by an interaction with environmental descriptors, which suggests a steeper slope between macroevolutionary rates and centrality descriptors), favoring the building of the network around macroevolutionarily stable species and lineages (Fig. 2). These environments harbor the highest frugivorous species richness (*7*), and we hypothesize that such species-rich environments allow for a finer subdivision of network roles on which this macroevolutionary sorting of stable species and lineages can act. In fact, networks in these tropical forest–like environments often show higher variation in centrality values across species than networks found on colder, drier, and seasonal environments (Fig. 2, C and D). This variation, however, was not simply a consequence of variation in species richness. Body size disparity data show that niche space in warmer, more humid environments is more homogeneously occupied without increasing either total niche space or niche overlap (using body size as a proxy for ecology) between species (figs. S10 and S11). Furthermore, we found that not only do central species interact with more partners, but also these partners belong to more distinct phylogenetic groups (figs. S12 to S15). Thus, higher variation in species richness, niche occupation, and diversity of partners provide the raw material that allows macroevolutionary sorting of stable species to occur.

Our results provide evidence for a macroevolutionary sorting mechanism (species selection in a broad sense) (*29*) on network assembly, where central species tend to have longer longevities (the inverse of extinction rate) and belong to evolutionary lineages that are more stable over deep time. Furthermore, we found that not only do central species interact with a large number of connected species (directly or indirectly), but also that associated species belong to more distinct plant families (figs. S12 to S15). Although the relationship between macroevolutionary rates and network centrality metrics may reflect the role of macroevolutionary stability on the sorting of interaction patterns during network assembly, we note that the causal relationship might also act in the opposite direction, and species network position might eventually affect the rates of diversification. For instance, increased frugivory may fuel diversification within some vertebrate lineages, such as primates (*13*). We are only beginning to understand how macroevolutionary effects relate to the ecological organization of species interactions networks. In this sense, it is hard to infer causality direction when experiments are not an option. Nevertheless, our study shows evidence of the importance of species turnover on the structure of ecological networks in geological time, expanding the temporal scale to the ones addressed in previous studies (*17*, *19*). By now, our results suggest potential multilevel selective regimes involving interaction patterns and diversification dynamics, which might shape the fate of groups of very distantly related lineages (e.g., birds and plants) linked through ecological interactions.

REFERENCES AND NOTES

1. T. H. Fleming, W. J. Kress, *The Ornaments of Life: Coevolution and Conservation in the Tropics. Interspecific Interactions*. (Univ. of Chicago Press, 2013).
2. O. Eriksson, *Biol. Rev. Camb. Philos. Soc.* **91**, 168–186 (2016).
3. P. Jordano, "Fruits and frugivory" in *The Ecology of Regeneration in Plant Communities*, M. Fenner, Ed. (CAB International, ed. 2, 2000), pp. 125–166.
4. C. I. Donatti *et al*., *Ecol. Lett.* **14**, 773–781 (2011).
5. D. W. Snow, *Biotropica* **13**, 1 (1981).
6. T. H. Fleming, R. Breitwisch, G. H. Whitesides, *Annu. Rev. Ecol. Syst.* **18**, 91–109 (1987).
7. W. Daniel Kissling, K. Böhning-Gaese, W. Jetz, *Glob. Ecol. Biogeogr.* **18**, 150–162 (2009).
8. J. Bascompte, P. Jordano, *Annu. Rev. Ecol. Evol. Syst.* **38**, 567–593 (2007).
9. M. Galetti *et al*., *Science* **340**, 1086–1090 (2013).
10. L. J. Harmon *et al*., *J. Evol. Biol.* **32**, 769–782 (2019).
11. G. Burin, W. D. Kissling, P. R. Guimarães Jr., Ç. H. Şekercioğlu, T. B. Quental, *Nat. Commun.* **7**, 11250 (2016).
12. J. M. Gómez, M. Verdú, F. Perfectti, *Nature* **465**, 918–921 (2010).
13. J. M. Gómez, M. Verdú, *Syst. Biol.* **61**, 567–577 (2012).
14. M. G. Weber, A. A. Agrawal, *Proc. Natl. Acad. Sci. U.S.A.* **111**, 16442–16447 (2014).
15. S. L. Nuismer, L. J. Harmon, *Ecol. Lett.* **18**, 17–27 (2015).
16. P. D. Roopnarine, K. D. Angielczyk, A. Weik, A. Dineen, *Earth Sci. Rev.* **189**, 244–263 (2019).
17. M. M. Pires *et al*., *Oecologia* **175**, 1247–1256 (2014).
18. L. C. Ponisio, M. P. Gaiarsa, C. Kremen, *Ecol. Lett.* **20**, 1261–1272 (2017).
19. P. J. CaraDonna *et al*., *Ecol. Lett.* **24**, 149–161 (2021).
20. M. Plein *et al*., *Ecology* **94**, 1296–1306 (2013).
21. J. M. Olesen, J. Bascompte, H. Elberling, P. Jordano, *Ecology* **89**, 1573–1582 (2008).
22. S. Yang, R. Albert, T. A. Carlo, *Ecosphere* **4**, art147 (2013).
23. E. L. Rezende, J. E. Lavabre, P. R. Guimarães, P. Jordano, J. Bascompte, *Nature* **448**, 925–928 (2007).
24. Materials and methods are available as supplementary materials.
25. N. L. Gilinsky, *Paleobiology* **20**, 445–458 (1994).
26. A. Krishna, P. R. Guimarães Jr., P. Jordano, J. Bascompte, *Oikos* **117**, 1609–1618 (2008).
27. E. C. Fricke, J.-C. Svenning, *Nature* **585**, 74–78 (2020).
28. D. M. Dehling *et al*., *Ecology* **101**, e03028 (2020).
29. D. Jablonski, *Evolution* **62**, 715–739 (2008).
30. A global phylogeny of birds; http://birdtree.org/.
31. A. L. Pigot *et al*., *Proc. Biol. Sci.* **283**, 20161597 (2016).
32. A. L. Pigot *et al*., Data from: Quantifying species contributions to ecosystem processes: A global assessment of functional trait and phylogenetic metrics across avian seed-dispersal networks, Dryad (2016); https://doi.org/10.5061/dryad.2br2b.
33. G. Burin, P. R. Guimaraes Jr., T. B. Quental, Macroevolutionary stability predicts interaction patterns of species in seed dispersal networks, zenodo (2019); https://doi.org/zenodo.org/record/3560680.
34. G. Burin, github github.com/gburin/macroevoNet.

ACKNOWLEDGMENTS

We thank E. Santos, M. Melo, M. Aguiar, P. Morelatto, M. Gaiarsa, D. Caetano, N. Cooper, S. Alewijnse, T. Park, and all the researchers in LabMeMe, Guimarães Lab, and the EvolClub-BR for their insightful comments during several steps of this work. **Funding:** All authors thank FAPESP (Fundação de Amparo à Pesquisa do Estado de São Paulo) for funding (G.B.: grants #2014/03621-9 and #2018/04821-2; P.R.G.: grant #2018/14809-0; T.B.Q.: grants #2012/04072-3 and #2018/05462-6); G.B. also thanks CAPES for a PhD fellowship. **Author contributions:** G.B.: Conceptualization, Methodology, Data Curation, Investigation, Writing - Original Draft & Review & Editing, Visualization; P.R.G.: Conceptualization, Methodology, Writing - Review & Editing; T.B.Q.: Conceptualization, Methodology, Writing - Original Draft & Review & Editing, Supervision. **Competing interests:** The authors declare no competing interests. **Data and materials availability:** Bird phylogenies were obtained from birdtree.org (*30*), and ecological networks were compiled by Pigot *et al.* (*31*) and can be directly downloaded from Dryad (*32*). All data and code used in this study are available for download at zenodo (*33*). Codes are also available at github (*34*).

SUPPLEMENTARY MATERIALS INCLUDE

science.sciencemag.org/content/372/6543/733/suppl/DC1
Materials and Methods
Figs. S1 to S15
Tables S1 to S7
References (*35*–*50*)

30 September 2020; accepted 24 March 2021
10.1126/science.abf0556

CORONAVIRUS

Shared B cell memory to coronaviruses and other pathogens varies in human age groups and tissues

Fan Yang[1]*, Sandra C. A. Nielsen[1], Ramona A. Hoh[1], Katharina Röltgen[1], Oliver Fabian Wirz[1], Emily Haraguchi[1], Grace H. Jean[1], Ji-Yeun Lee[1], Tho D. Pham[1,2], Katherine J. L. Jackson[3], Krishna M. Roskin[4,5,6], Yi Liu[7], Khoa Nguyen[1], Robert S. Ohgami[8], Eleanor M. Osborne[9], Kari C. Nadeau[10,11], Claus U. Niemann[12,13], Julie Parsonnet[14,15], Scott D. Boyd[1,10]*

Vaccination and infection promote the formation, tissue distribution, and clonal evolution of B cells, which encode humoral immune memory. We evaluated pediatric and adult blood and deceased adult organ donor tissues to determine convergent antigen-specific antibody genes of similar sequences shared between individuals. B cell memory varied for different pathogens. Polysaccharide antigen–specific clones were not exclusive to the spleen. Adults had higher clone frequencies and greater class switching in lymphoid tissues than blood, while pediatric blood had abundant class-switched convergent clones. Consistent with reported serology, prepandemic children had class-switched convergent clones to severe acute respiratory syndrome coronavirus 2 with weak cross-reactivity to other coronaviruses, while adult blood or tissues showed few such clones. These results highlight the prominence of early childhood B cell clonal expansions and cross-reactivity for future responses to novel pathogens.

The clonal identity of a B cell can be traced by the sequence of its B cell receptor (BCR), which determines its antigen specificity (*1*). Immunoglobulin (Ig) sequences are formed via irreversible variable, diversity, and joining (VDJ) gene segment rearrangement and can be diversified through somatic hypermutation (SHM) and class-switch recombination (CSR) (*2*). Convergent BCRs with high sequence similarity in individuals exposed to the same antigen reflect antigen-driven clonal selection and form shared immunological memory between individuals (*3*–*5*). It is still unclear, however, how B cell memory to different antigens distributes in human tissues and changes during an individual's life span.

Humoral immune responses can differ between children and adults; for example, children use more B cell clones to achieve neutralizing antibody breadth to HIV-1 (*6*). Children usually have milder disease following severe acute respiratory syndrome coronavirus 2 (SARS-CoV-2) infection than adults do (*7*–*10*), potentially owing to differences in viral receptor expression and immune responses (*11*, *12*). SARS-CoV-2–infected children, in contrast to adults, show lower antibody titers and more IgG specific for the spike (S) protein over the nucleocapsid (N) protein. The faster viral clearance and lower viral antigen loads in children have been attributed to these differences (*13*). Whether B cell clones specific for coronaviruses and other pathogens differ between children and adults is unclear. Blood-based studies survey only a fraction of an individual's BCR repertoire. The lymph nodes, spleen, and gastrointestinal tract harbor greater numbers of B cells and are major sites for SHM and CSR (*14*, *15*). Specialized responses in particular tissues have been reported, such as for polysaccharide antigen–specific B cells in functional splenic tissue (*16*, *17*).

To study changes in antigen-specific B cell memory over the human life span and across tissues, we characterized convergent Ig heavy chain (IGH) repertoires specific to six common pathogens as well as two viruses not encountered by the participants, Ebola virus (EBOV) and SARS-CoV-2, in pre-COVID-19 pandemic individuals. We analyzed 12 cord blood (CB) samples; 93 blood samples from 51 children aged 1 to 3 years (*18*); 114 blood samples from healthy human adults aged 17 to 87 years (*18*); and blood, lymph node, and spleen samples from eight deceased organ donors (table S1). Children were vaccinated against *Haemophilus influenzae* type b (Hib), *Pneumococcus pneumoniae* (PP), and tetanus toxoid (TT) at 2, 4, 6, and 12 to 15 months, had influenza virus (flu) vaccination, and were very likely exposed to respiratory syncytial virus (RSV) but were not vaccinated against *Neisseria meningitidis* (NM) (*19*). Adult vaccination histories were unknown. Convergent IGHs were identified by clustering with pathogen-specific reference IGH (table S2) sharing IGH variable domain (IGHV) and joining region (IGHJ) gene segment usage, complementarity-determining region H3 (CDR-H3) length, and minimum 85% CDR-H3 amino acid sequence identity.

B cell clones fell into three groups: (i) naïve clones containing only unmutated IgM or IgD (hereafter, unmutM/D); (ii) antigen-experienced IgM or IgD with median SHM over 1% and without class-switched members (hereafter, mutM/D); and (iii) antigen-experienced clones with class-switched members (hereafter, CS). As we hypothesized, CB samples showed the lowest convergent IGH frequencies, consistent with limited fetal pathogen or vaccine exposures (Fig. 1A). Convergent clones in children and adults were largely mutM/D or CS (Fig. 1A and fig. S1). In adult blood, convergent clones for Hib, NM, and RSV were predominantly mutM/D clones, whereas PP, TT, and flu clones were predominantly CS (fig. S2A). Adults over 45 years of age had elevated mutM/D B cell clone frequencies to NM, potentially from exposures preceding widespread NM vaccination (*20*). Unexpectedly, children had higher frequencies than adults of CS convergent clones for Hib, PP, TT, and RSV (fig. S2B), with mutated IgM or IgD also found in these clones (Fig. 1B). Convergent clone frequency in children's blood was not significantly associated with vaccination timing (figs. S3 to S5 and table S3), indicating persistently elevated frequencies. Flu-specific convergent clone frequencies were comparable in children and adults (Fig. 1A), with age-related increases in IgG SHM potentially due to frequent exposures via vaccination or infection (Fig. 1C) (*18*).

To test whether low frequencies of CS convergent clones in adult blood reflect preferential localization of clones in lymphoid tissues, we analyzed the blood, spleen, mediastinal lymph nodes (MDLN), and mesenteric lymph nodes (MSLN) of eight adult deceased organ donors. Lymph nodes and spleen showed greater clonal sharing with each other than with blood (fig. S6A), suggesting larger clone sizes in lymphoid tissues and limited recirculation. Each tissue was dominated by different clones (fig. S6B), and SHM correlated with the number of tissues a clone occupied (fig. S7), consistent with greater prior antigen exposure leading to wider tissue distribution (*21*). Convergent clone frequencies for Hib, NM, PP, TT, RSV, and flu were higher in adult lymph nodes and spleen than in blood (Fig. 2A). Adult lymph nodes and child blood shared more convergent clones than did adult and child blood, showing differing distributions of

[1]Department of Pathology, Stanford University, Stanford, CA 94305, USA. [2]Stanford Blood Center, Stanford University, Stanford, CA 94305, USA. [3]Garvan Institute of Medical Research, Darlinghurst, NSW 2010, Australia. [4]Department of Pediatrics, University of Cincinnati, Cincinnati, OH 45267, USA. [5]Division of Biomedical Informatics, Cincinnati Children's Hospital Medical Center, Cincinnati, OH 45229, USA. [6]Division of Immunobiology, Cincinnati Children's Hospital Medical Center, Cincinnati, OH 45229, USA. [7]Calico Life Sciences, South San Francisco, CA 94080, USA. [8]Department of Pathology, University of California, San Francisco, CA 94143, USA. [9]Sarah Cannon Cancer Center, Tennessee Oncology, Smyrna, TN 37167, USA. [10]Sean N. Parker Center for Allergy and Asthma Research, Stanford University, Stanford, CA 94305, USA. [11]Division of Pulmonary, Allergy and Critical Care Medicine, Stanford University, Stanford, CA 94305, USA. [12]Department of Anesthesia and Perioperative Care, University of California, San Francisco, CA 94143, USA. [13]Department of Surgery, Division of Transplantation, University of California, San Francisco, CA 94143, USA. [14]Department of Medicine, Stanford University, Stanford, CA 94305, USA. [15]Epidemiology and Population Health, Stanford University, Stanford, CA 94305, USA.
*Corresponding author. Email: sboyd1@stanford.edu (S.D.B.); fyang90@stanford.edu (F.Y.)

these clones in children and adults (Fig. 2B and fig. S8; P = 0.0001181, Fisher's exact test). B cells specific for bacterial capsular polysaccharides are reported to be enriched in the spleen, and splenectomized patients are vulnerable to these bacteria (*16*, *17*). However, frequencies of convergent clones for Hib, NM, and PP are similar or higher in lymph nodes than in the spleen. Moreover, estimated B cell numbers are greater in human lymph nodes than the spleen (*22*, *23*), indicating that the spleen is not the sole reservoir of these clones. Convergent IGH for polysaccharides were usually IgM or IgD, with some CS clones for PP in lymph nodes and spleen (Fig. 2C). Thus, memory to these antigens spans a diversity of both lymphoid tissues and isotype expression.

Recent reports describe SARS-CoV-2–binding antibodies in prepandemic children's blood (*12*, *24*). Such antibodies and other physiological distinctions are under investigation in adults and children (*25*) and could contribute to the generally milder COVID-19 disease in children. SARS-CoV-2 S-binding B cells in unexposed individuals have been analyzed in a former SARS-CoV patient (*26*), naïve B cells of healthy individuals (*27*), and memory B cells in prepandemic donors (*26*, *28*). We detected rare convergent clones for EBOV, as unmutM/D in blood or tissues (Fig. 3A and fig. S9A). By contrast, convergent clones for SARS-CoV-2 (table S4) were more common in children's blood. In 37 of 51 children, these clones displayed SHM with or without CS, indicating prior antigen experience (Fig. 3, A and B). Adult frequencies of SARS-CoV-2 convergent clones were lower in blood and lymphoid tissues compared with children's blood, with few CS examples (Fig. 3A and fig. S9). Convergent clones specific for SARS-CoV-2 receptor binding domain (RBD) and other S domains showed similar distributions (fig. S10). Reference antibodies for SARS-CoV-2, EBOV, and the pathogens in Fig. 1 used a wide diversity of IGHV genes (fig. S11).

Three convergent clones from five children in this study, but none from adults, had IGH sequences highly similar to SARS-CoV-2 S-binding clones isolated from a prepandemic donor that were reported to weakly bind other human coronavirus (HCoV) spikes (*26*) (Fig. 3C). Three other clones from six children had IGHs identical to known SARS-CoV-2 binders (fig. S12). We expressed 19 monoclonal antibody (mAb) clones for SARS-CoV-2 (table S5) with IGH from participants in this study and reference light chains, and we identified 17 binders for SARS-CoV-2 S and S domains (Table 1). Four RBD binders showed >90% blocking of angiotensin-converting enzyme 2 (ACE2) binding to SARS-CoV-2 S (table S6). mAb FY11H1 showed evidence of S2 binding and did not block ACE2 binding. We characterized the breadth of mAb binding using a

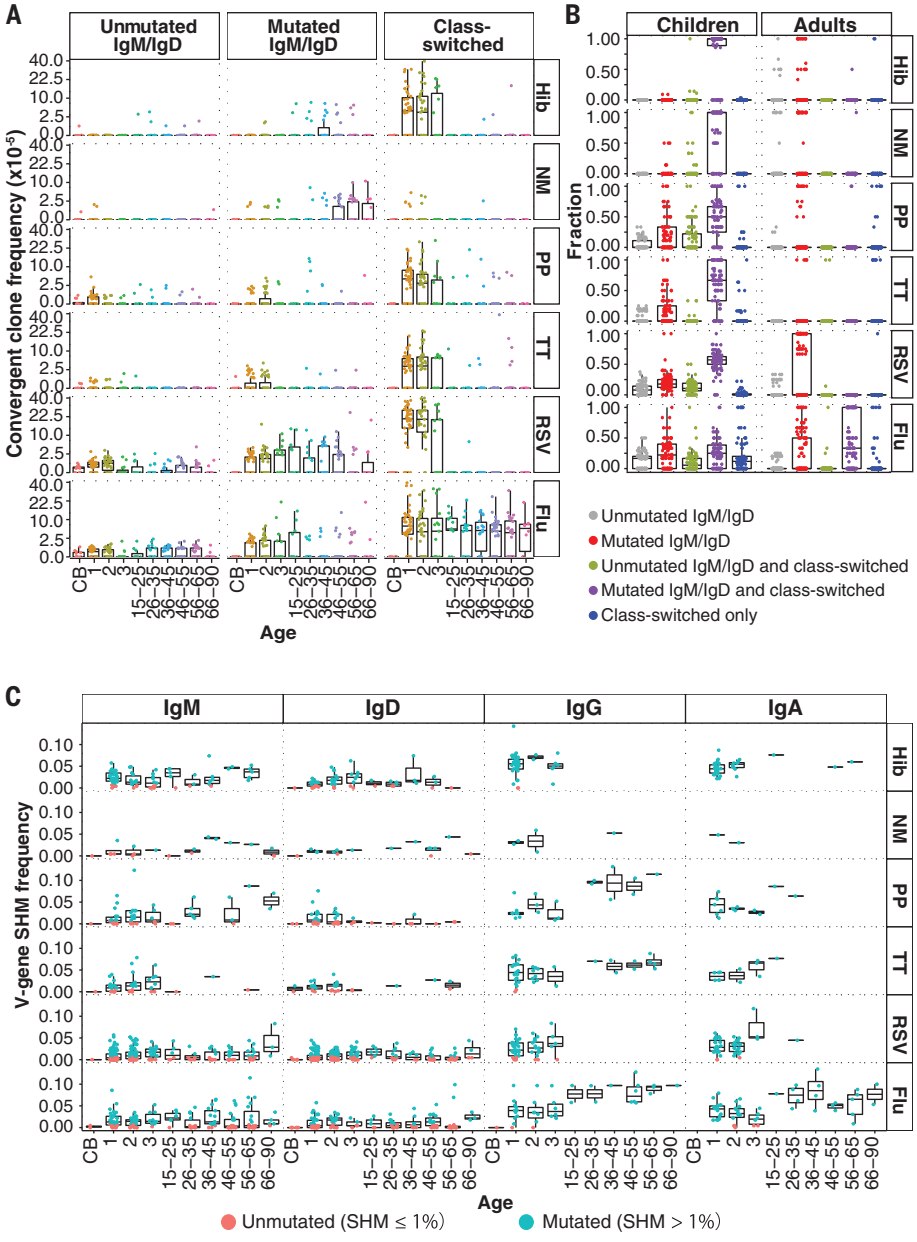

Fig. 1. Frequency, class switching, and SHM of pathogen-specific convergent clones in children and adults. (**A**) Convergent clone frequencies for each pathogen, plotted on a square root scale. Ages given in years. CB, cord blood. (**B**) Fractions of convergent clones expressing unmutated IgM or IgD, mutated IgM or IgD, class-switched, or combinations of these. Children have significantly larger fractions of class-switched convergent clones with mutated IgM/IgD clone members (colored in purple) than do adults [$P = 5.08 \times 10^{-32}$, 6.66×10^{-29}, 2.39×10^{-29}, 3.45×10^{-34}, and 1.71×10^{-41} for Hib, NM, PP, TT, and RSV, respectively, by Wilcoxon-Mann-Whitney (WMW) test]. (**C**) Median IGHV gene SHM frequencies of each convergent clone in participants of different ages indicated in years. SHM frequencies of convergent clones expressing IgG or IgA were lower in children than in adults ($P = 6.50 \times 10^{-13}$ and 1.96×10^{-8}, respectively; WMW test).

panel of HCoV spikes and SARS-CoV-2 viral variant RBDs and spikes. Three child-derived mAbs (FY7H1, FY7H2, and FY1H2) and one adult mAb (FY4H1) showed the strongest binding to B.1.1.7, B.1.351, and P.1 S and RBD variants (table S7). Cross-reactive binding to endemic HCoV spikes was very weak to absent for all mAbs, as previously noted for reference mAb-154 (similar to mAb FY13H1) isolated from a sorted cross-reactive B cell (*26*). The child-derived mAbs FY13H1 and FY9H2 had a higher, although still weak, signal for binding HKU1. Thus, children's convergent coronavirus-binding B cells may have greater cross-reactivity than those of adults, in addition to having higher frequencies.

Childhood immune responses are particularly important in an individual's life, as they

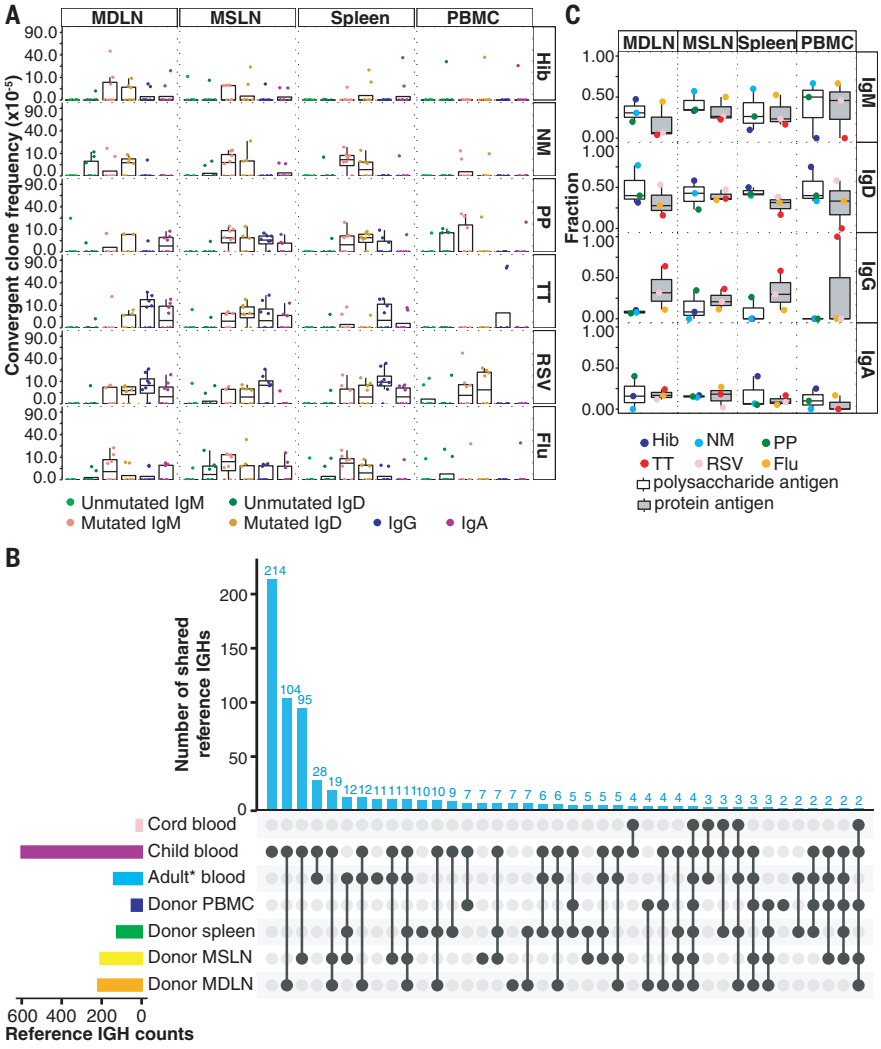

Fig. 2. Convergent B cell clone distribution in tissues. (**A**) Convergent clone frequencies in adult blood (PBMC), MDLN, MSLN, and spleen. Frequencies are on a square root scale. Frequencies in tissues were higher than in blood (P = 0.00049, 0.0037, 0.016, 6.71×10^{-7}, 0.012, and 0.00017 for Hib, NM, PP, TT, RSV, and flu, respectively; WMW test). (**B**) Convergent antigen-specific IGH in CB and blood of children; healthy adults (Adult* blood); deceased organ donors (Donor PBMC); and donor spleen, MSLN, and MDLN. Vertical bars: reference antigen–specific IGH sequences per specimen combination. Left bars: total convergent IGH unique sequences per tissue. (**C**) Fraction of convergent clones containing the indicated isotypes in tissues. Some clones contain multiple isotypes. Compared with protein antigen–specific clones, polysaccharide-specific clones more frequently express IgM/D and less often express IgG (P = 0.035 and 0.0058, respectively; WMW test).

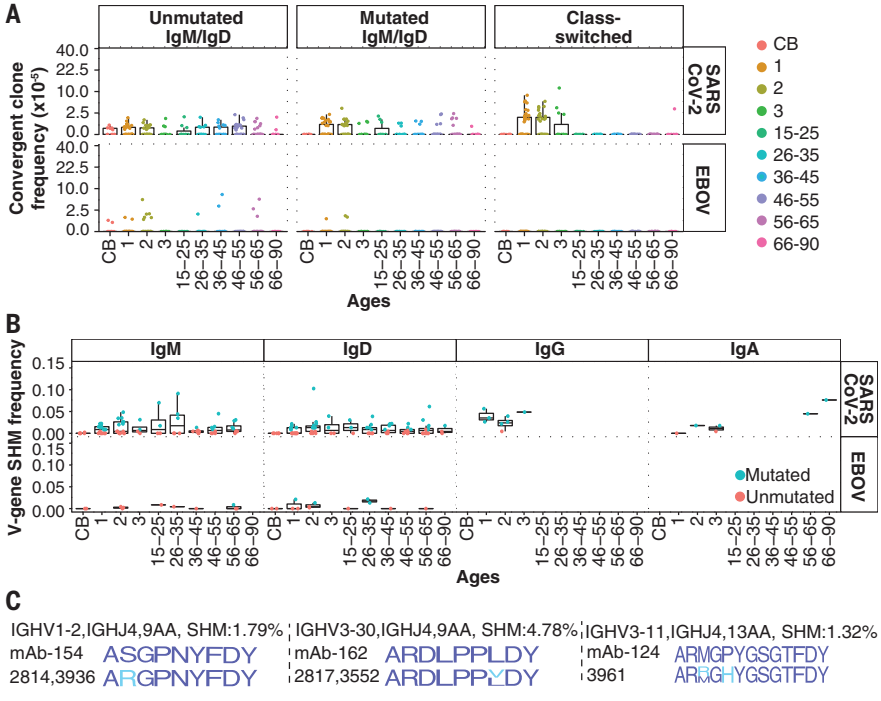

Fig. 3. Convergent clones for SARS-CoV-2 and EBOV. (**A**) Convergent clone frequencies on a square root scale. CS and mutM/D convergent clone frequencies for SARS-CoV-2 are higher in children than in adults ($P = 1.22 \times 10^{-13}$ and 0.0089, respectively; WMW test). (**B**) SHM frequencies of convergent clones for each isotype in participants of different ages (x axis). (**C**) CDR-H3 amino acid sequences of convergent IGH cross-reactive to SARS-CoV-2 and other HCoVs. Top row: CDR-H3 sequence logos for reported antigen-specific clones. Second row: sequence logos for convergent clones from children (blue indicates a match, cyan indicates sequence differences).

Table 1. Convergent mAb binding data for SARS-CoV-2 spike, RBD, and nucleocapsid (N) and endemic HCoV spikes. Testing by electrochemiluminescence immunoassay in duplicate wells, with the average arbitrary unit per milliliter (AU/ml) values displayed in the table. Antibodies with binding signal at least five standard deviations above the average of negative control antibodies (Neg1 to Neg5) are listed.

mAb	CoV-2 S	CoV-2 RBD	CoV-2 S2	CoV-2 N	CoV S	HKU1 S	OC43 S	NL63 S	229E S	Source
FY1H3	161.84	132.42	0.12	2.42	4.62	0.22	0.30	0.30	0.22	Children
FY3H1	158.05	130.83	0.08	0.89	1.00	0.10	0.17	0.17	0.11	Both
FY3H3	153.27	123.26	0.26	6.33	2.91	0.38	0.69	0.61	0.45	Children
FY3H2	150.57	127.35	0.24	0.87	1.18	0.10	0.16	0.14	0.09	Adults
FY7H1	149.78	125.82	0.12	1.41	4.21	0.10	0.19	0.19	0.13	Children
FY1H2	148.44	119.56	2.39	1.92	18.00	0.47	0.63	0.58	0.50	Children
FY13H1	147.29	119.22	0.15	3.55	0.39	1.41	0.47	0.29	0.25	Children
FY7H2	146.59	120.11	0.06	1.94	4.29	0.24	0.15	0.16	0.12	Children
FY4H1	131.23	116.83	0.19	2.27	1.32	0.25	0.39	0.27	0.23	Adults
FY8H1	114.20	107.56	0.03	0.80	2.08	0.12	0.09	0.07	0.04	Adults
FY9H1	91.02	94.74	1.39	3.62	5.87	0.75	0.56	0.31	0.30	Children
FY11H1	79.65	41.41	13.59	0.78	44.62	0.13	0.09	0.06	0.12	Both
FY6H1	79.09	71.33	0.54	5.22	2.88	0.45	0.27	0.21	0.24	Both
FY14H1	78.73	63.10	3.91	2.43	9.56	0.30	0.45	0.35	0.29	Adults
FY5H1	69.60	45.71	0.33	3.27	1.71	0.49	0.50	0.25	0.23	Children
FY9H2	53.53	13.86	3.83	2.42	10.03	1.46	0.35	0.23	0.25	Children
FY10H1	9.96	8.69	0.02	0.18	0.27	0.02	0.08	0.02	0.02	Adults
Neg5	0.52	0.01	0.00	0.00	0.02	0.00	0.00	0.00	0.00	Controls
Neg4	1.63	0.02	0.00	0.90	0.09	0.01	0.00	0.00	0.00	Controls
Neg3	1.22	0.02	0.00	0.03	0.07	0.00	0.00	0.00	0.00	Controls
Neg2	1.37	0.02	0.00	0.02	0.08	0.01	0.00	0.00	0.00	Controls
Neg1	0.87	0.02	0.00	0.01	0.04	0.00	0.00	0.00	0.00	Controls

form the initial memory B cell pool that shapes future responses (*29*). We find that in comparison to adults, children have higher frequencies of convergent B cell clones in their blood for pathogens they have encountered. Notably, prepandemic children also had class-switched convergent clones to SARS-CoV-2 and its viral variants, but not EBOV, at higher frequencies than adults. We hypothesize that previous HCoV exposures may stimulate cross-reactive memory, and that such clonal responses may have their highest frequencies in childhood. The caveats of our analysis are that convergent clones may not fully represent the properties of all pathogen-specific clones in an individual and that binding affinities for cross-reactivity that would be relevant in vivo are not known. Further study of the role of cross-reactive memory B cell populations in primary immune responses to related but divergent viruses as well as better understanding of the determinants of long-lived B cell memory and plasma cell formation will be important for ongoing improvement of vaccines to SARS-CoV-2, its viral variants, and other pathogens.

REFERENCES AND NOTES

1. S. D. Boyd, J. E. Crowe Jr., *Curr. Opin. Immunol.* **40**, 103–109 (2016).
2. D. D. Dudley, J. Chaudhuri, C. H. Bassing, F. W. Alt, *Adv. Immunol.* **86**, 43–112 (2005).
3. K. J. Jackson *et al.*, *Cell Host Microbe* **16**, 105–114 (2014).
4. J. Trück *et al.*, *J. Immunol.* **194**, 252–261 (2015).
5. I. Setliff *et al.*, *Cell Host Microbe* **23**, 845–854.e6 (2018).
6. L. Goo, V. Chohan, R. Nduati, J. Overbaugh, *Nat. Med.* **20**, 655–658 (2014).
7. F. Götzinger *et al.*, *Lancet Child Adolesc. Health* **4**, 653–661 (2020).
8. X. Lu *et al.*, *N. Engl. J. Med.* **382**, 1663–1665 (2020).
9. C. Jiehao *et al.*, *Clin. Infect. Dis.* **71**, 1547–1551 (2020).
10. I. Liguoro *et al.*, *Eur. J. Pediatr.* **179**, 1029–1046 (2020).
11. R. Carsetti *et al.*, *Lancet Child Adolesc. Health* **4**, 414–416 (2020).
12. K. W. Ng *et al.*, *Science* **370**, 1339–1343 (2020).
13. S. P. Weisberg *et al.*, *Nat. Immunol.* **22**, 25–31 (2021).
14. C. Berek, C. Milstein, *Immunol. Rev.* **96**, 23–41 (1987).
15. J. Jacob, G. Kelsoe, K. Rajewsky, U. Weiss, *Nature* **354**, 389–392 (1991).
16. C. G. Vinuesa, C. de Lucas, M. C. Cook, *Postgrad. Med. J.* **77**, 562–569 (2001).
17. I. C. MacLennan, Y. J. Liu, *Res. Immunol.* **142**, 346–351 (1991).
18. S. C. A. Nielsen *et al.*, *Sci. Transl. Med.* **11**, eaat2004 (2019).
19. S. R. Dunn *et al.*, *Clin. Vaccine Immunol.* **20**, 1654–1656 (2013).
20. M. P. Broderick, D. J. Faix, C. J. Hansen, P. J. Blair, *Emerg. Infect. Dis.* **18**, 1430–1437 (2012).
21. W. Meng *et al.*, *Nat. Biotechnol.* **35**, 879–884 (2017).
22. V. V. Ganusov, R. J. De Boer, *Trends Immunol.* **28**, 514–518 (2007).
23. M. Langeveld, L. E. Gamadia, I. J. ten Berge, *Eur. J. Clin. Invest.* **36**, 250–256 (2006).
24. E. M. Anderson *et al.*, *Cell* **184**, 1858–1864.e10 (2021).
25. S. Bunyavanich, A. Do, A. Vicencio, *JAMA* **323**, 2427–2429 (2020).
26. A. Z. Wec *et al.*, *Science* **369**, 731–736 (2020).
27. S. I. Kim *et al.*, *Sci. Transl. Med.* **13**, eabd6990 (2021).
28. G. Song *et al.*, bioRxiv 2020.09.22.308965 [Preprint]. 23 September 2020. https://doi.org/10.1101/2020.09.22.308965.
29. C. P. Arevalo *et al.*, *Proc. Natl. Acad. Sci. U.S.A.* **117**, 17221–17227 (2020).

ACKNOWLEDGMENTS

We thank all staff members of the California Transplant Donor Network (now Donor Network West), especially S. Swain. We thank A. Z. Fire, E. A. Hope, and J. D. Merker for helpful discussions and contributions to the research. We thank Meso Scale Diagnostics for helpful collaboration and material support in this study. **Funding:** This work was supported by NIH/NIAID R01AI127877, R01AI130398, U19AI057229, and U19AI090019 and NIH/NCI U54CA260517 (S.D.B.); NIH R01 HD063142 (J.P.); and an endowment from the Crown Family Foundation (S.D.B.). **Author contributions:** F.Y. and S.D.B. conceived of the project. F.Y., S.C.A.N., K.J.L.J., Y.L., and K.M.R. performed data analyses. F.Y., S.C.A.N., and S.D.B. verified the analyses. F.Y., S.C.A.N., R.A.H., K.R., E.H., O.F.W., G.H.J., R.S.O., E.M.O., J.-Y.L., K.N., and T.D.P. contributed to sample preparation and carried out the experiments. T.D.P., K.C.N., C.U.N., J.P., and S.D.B. provided samples and supported the project. F.Y., S.C.A.N., and S.D.B. wrote the initial manuscript. All authors provided critical feedback and contributed to the final manuscript. **Competing interests:** S.D.B.: consulting for Regeneron, stock ownership in AbCellera Biologics, and collaboration with Meso Scale Diagnostics. K.N.: director of the World Allergy Organization (WAO) Center of Excellence at Stanford; advisor at Cour Pharma; co-founder of Before Brands, Alladapt, Latitude, and IgGenix; national scientific committee member at Immune Tolerance Network (ITN) and the National Institutes of Health (NIH) clinical research centers; and data and safety monitoring board member for NHLBI. **Data and materials availability:** All data are available in the main text or the supplementary materials. Previously generated IGH repertoire data are available under BioProject numbers PRJNA503602 (child dataset) and PRJNA491287 [114 healthy human adult dataset was previously reported (*18*)]. The IGH sequences for mAbs tested in this study were deposited in GenBank (MW821491 to MW821509). The IGH repertoire data for the deceased organ donors and the cord blood infant samples are available under BioProject number PRJNA674610. This work is licensed under a Creative Commons Attribution 4.0 International (CC BY 4.0) license, which permits unrestricted use, distribution, and reproduction in any medium, provided the original work is properly cited. To view a copy of this license, visit https://creativecommons.org/licenses/by/4.0/. This license does not apply to figures/photos/artwork or other content included in the article that is credited to a third party; obtain authorization from the rights holder before using such material.

SUPPLEMENTARY MATERIALS

science.sciencemag.org/content/372/6543/738/suppl/DC1
Materials and Methods
Figs. S1 to S12
Tables S1 to S9
References (*30*–*84*)
MDAR Reproducibility Checklist

13 November 2020; accepted 7 April 2021
Published online 12 April 2021
10.1126/science.abf6648

NUCLEAR ASTROPHYSICS

^{60}Fe and ^{244}Pu deposited on Earth constrain the r-process yields of recent nearby supernovae

A. Wallner[1,2]*, M. B. Froehlich[1], M. A. C. Hotchkis[3], N. Kinoshita[4], M. Paul[5], M. Martschini[1]†, S. Pavetich[1], S. G. Tims[1], N. Kivel[6], D. Schumann[6], M. Honda[7]‡, H. Matsuzaki[8], T. Yamagata[8]

Half of the chemical elements heavier than iron are produced by the rapid neutron capture process (r-process). The sites and yields of this process are disputed, with candidates including some types of supernovae (SNe) and mergers of neutron stars. We search for two isotopic signatures in a sample of Pacific Ocean crust—iron-60 (^{60}Fe) (half-life, 2.6 million years), which is predominantly produced in massive stars and ejected in supernova explosions, and plutonium-244 (^{244}Pu) (half-life, 80.6 million years), which is produced solely in r-process events. We detect two distinct influxes of ^{60}Fe to Earth in the last 10 million years and accompanying lower quantities of ^{244}Pu. The ^{244}Pu/^{60}Fe influx ratios are similar for both events. The ^{244}Pu influx is lower than expected if SNe dominate r-process nucleosynthesis, which implies some contribution from other sources.

All naturally occurring nuclides heavier than iron are produced in stellar environments, almost exclusively by nuclear processes involving the successive captures of neutrons to build up heavier masses. About half of these nuclides are synthesized slowly as a by-product of steady stellar fusion. The other half, including all actinide elements, require a very short but intense flux of neutrons, resulting in a rapid neutron capture process (r-process). The sites and yields of the r-process remain a topic of debate (*1*–*6*). It is expected to occur in explosive stellar environments such as certain types of supernovae (SNe) or neutron-star mergers (NSMs), the latter of which has been supported by observations of the gravitational-wave event GW170817 (*7*). The abundance patterns of r-process nuclides can be used to constrain the production site. Radioactive isotopes (radionuclides) provide additional time information resulting from their decay over time following their synthesis. Such radionuclides should be scattered through the interstellar medium (ISM) and could be deposited on Earth.

The Solar System (SS) is located inside a large ISM structure [the Local Superbubble (LB)] that was shaped by supernova (SN) explosions during the last ~12 million years (Myr) (*8*). Earth has therefore been exposed to both ejecta from the SNe and swept-up interstellar material that traversed the SS during this time period (*9*, *10*). Dust particles from the ISM pass through the SS (*11*) and contain nucleosynthetic products of stellar events (e.g., stellar winds and SNe) (*10*, *12*, *13*). Earth's initial abundance of the ^{60}Fe radionuclide [half-life ($t_{1/2}$) = 2.6 Myr (*14*, *15*)] has decayed to extinction over the 4.6 billion years (Gyr) since the SS's formation. ^{60}Fe, however, is produced in massive stars and ejected in SN explosions. Evidence for the deposition of extraterrestrial ^{60}Fe on Earth has been found in deep-sea geological archives dated to between 1.7 and 3.2 million years ago (Ma) (*16*–*20*), at recent times (*21*, *22*), and possibly also around 7 Ma (*19*). ^{60}Fe has also been detected in lunar samples (*23*), in astronomical observations of gamma rays associated with its radioactive decay (*24*), and in galactic cosmic rays (*25*). SN activity in the last ~2 Myr is suggested by an excess in the local cosmic-ray spectrum (*26*). Other radionuclides are also produced and ejected in such explosions (*9*, *27*–*30*). If substantial r-process nuclei are produced in SNe this would also have enriched the local ISM with actinides, such as ^{244}Pu. With a half-life of 80.6 Myr, ^{244}Pu is much longer lived than ^{60}Fe, so it can be contributed by older r-process events, not limited to those that formed the LB. Either as part of the SN direct

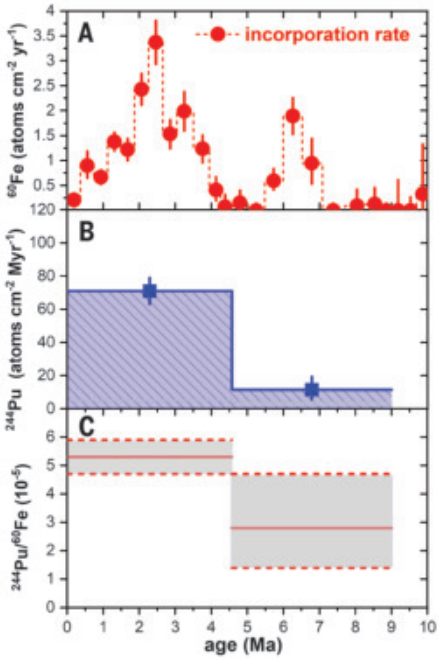

Fig. 1. Influx of interstellar ^{60}Fe and ^{244}Pu. (**A**) ^{60}Fe incorporation rates for Crust-3. The data (red points) have been decay corrected, and each layer is equivalent to 400 thousand years. The absolute ages have an uncertainty of ~0.3 to 0.5 Myr (*27*). (**B**) ^{244}Pu incorporation rates for the three layers after subtraction of the anthropogenic ^{244}Pu fraction (*27*). (**C**) ^{244}Pu$_{ISM}$/^{60}Fe number ratio in the crust sample with layers 1 and 2 combined (horizontal solid lines with shaded error bars). All error bars show 1σ Poisson statistics.

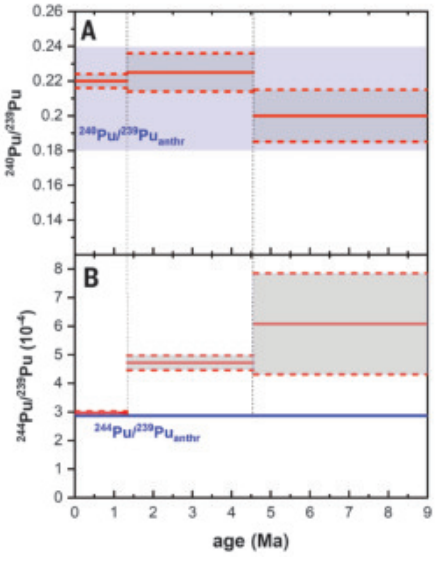

Fig. 2. Measured Pu isotope ratios and comparison with global fallout values. (**A** and **B**) Variations of the measured ^{240}Pu/^{239}Pu ratio (A) and the ^{244}Pu/^{239}Pu ratio (B) across the three layers (solid red lines). The dashed red lines and gray shading indicate 1σ uncertainties. The blue shaded area and solid line represent the expected ratios for Pu from nuclear weapons fallout (*27*). ^{240}Pu/^{239}Pu remains constant across the three layers, whereas ^{244}Pu/^{239}Pu is enhanced in the deeper (older) layers. We attribute the excess above anthropogenic (anthr) levels to extraterrestrial ^{244}Pu. Equivalent data for ^{241}Pu/^{239}Pu are shown in fig. S4.

[1]Department of Nuclear Physics, Research School of Physics, Australian National University, Canberra, ACT 2601, Australia. [2]Helmholtz-Zentrum Dresden-Rossendorf, Institute of Ion Beam Physics and Materials Research, 01328 Dresden, Germany. [3]Australian Nuclear Science and Technology Organisation, Lucas Heights, NSW 2234, Australia. [4]Institute of Technology, Shimizu Corporation, Tokyo 135-8530, Japan. [5]Racah Institute of Physics, The Hebrew University of Jerusalem, Jerusalem 91904, Israel. [6]Laboratory of Radiochemistry, Department for Nuclear Energy and Safety, Paul Scherrer Institute, 5232 Villigen, Switzerland. [7]Graduate School of Pure and Applied Sciences, University of Tsukuba, Ibaraki 305-8577, Japan. [8]Micro Analysis Laboratory, Tandem Accelerator, The University Museum, The University of Tokyo, Tokyo 113-0032, Japan.
***Corresponding author. Email: anton.wallner@hzdr.de or anton.wallner@anu.edu.au**
†Present address: Vienna Environmental Research Accelerator Laboratory, Faculty of Physics, University of Vienna, Vienna 1090, Austria.
‡Present address: Nuclear Science Research Institute, Japan Atomic Energy Agency, Ibaraki 319-1195, Japan.

Table 1. ^{60}Fe/Fe ratios from AMS measurements of layered samples of Crust-3. Twenty-four individual samples, distributed equally across 10 Myr, were analyzed and combined into four sections (individual data are listed in table S1). The stable Fe content was measured separately through inductively coupled plasma mass spectrometry (ICP-MS) (table S4). Ages are derived from ^{10}Be measurements (table S5) and have an uncertainty of ±0.3 Myr (*27*).The number of ^{60}Fe background events expected was calculated by scaling (in measurement time and beam intensity) measurements of terrestrial Fe blank samples. $^{60}Fe/Fe_{d.c.}$ denotes background- and decay-corrected data (*27*). Dashes in otherwise empty cells indicate not applicable.

Section	Depth (mm)	Time period (Ma)	^{60}Fe detector events	^{60}Fe background events expected	^{60}Fe/Fe (10^{-15})	$^{60}Fe/Fe_{d.c.}$ (10^{-15})	^{60}Fe incorporation (10^6 atoms cm^{-2} per section)	^{60}Fe incorporation rate (atoms cm^{-2} yr^{-1})
I	0 – 9.2	0 – 4.2	379	10	1.10 ± 0.06	1.87 ± 0.12	6.10 ± 0.31	1.46 ± 0.07
II	9.2 – 12	4.2 – 5.5	3	2	0.05 ± 0.03	$0.06^{+0.14}_{-0.06}$	$0.09^{+0.23}_{-0.09}$	$0.07^{+0.16}_{-0.07}$
III	12 – 15	5.5 – 7.0	49	3	0.40 ± 0.06	1.96 ± 0.31	1.77 ± 0.25	1.12 ± 0.16
IV	15 – 24	7.0 – 10.0	4	5	0.02 ± 0.01	<0.05	<0.2	<0.07
Total	0 – 24	0 – 10	435	20	0.56 ± 0.03	0.56 ± 0.03	7.96 ± 0.38	0.79 ± 0.04
Blank	terrestrial Fe	–	2	–	0.03 ± 0.02	–	–	–

ejecta or as continuous ISM influx, we expect dust particles containing ^{244}Pu to enter the SS, similarly to ^{60}Fe, but probing different nucleosynthetic processes. Previous measurements in terrestrial or lunar archives have provided only upper limits on actinide influx (*12*, *31*–*33*).

We searched for extraterrestrial ^{60}Fe and ^{244}Pu incorporated into a deep-sea sample on Earth—a ferromanganese crust (which we refer to as Crust-3) that spans the last 10 Myr, sampled at ~1500 m below sea level in the Pacific Ocean, with 115-cm^2 cross-sectional area and ~25-mm thickness (*27*). The radionuclides were identified and counted using accelerator mass spectrometry (AMS) (*27*). For ^{60}Fe, a time-resolved depth profile of ~1-cm^2 area was analyzed, subdivided into 24 layers, each ~1-mm thick, corresponding to a time resolution of ~0.4 Myr per layer [crust growth-rate of ~2.4 mm Myr^{-1}, dated with terrestrial ^{10}Be (*27*)]. The remaining part of Crust-3 (114-cm^2 area), after separating the aliquots used for ^{60}Fe analysis, was split into three thick, horizontal layers designated 3/A (extending from 0 to 3 mm, equivalent to 0 to 1.3 Ma, with a mass of ~20 g), 3/B (3 to 10 mm, 1.3 to 4.6 Ma, 179 g), and 3/C (10 to 20 mm, 4.6 to 9.0 Ma, 208 g), given the anticipated low abundance of ^{244}Pu. We expected the top layer to contain anthropogenic Pu from atmospheric nuclear weapons tests performed during the 20th century.

The ^{60}Fe content was measured as the isotope ratio ^{60}Fe/Fe, where single ^{60}Fe atoms were counted in a particle detector and normalized to the stable Fe content in the sample (*15*, *19*, *27*). We obtained a measurement background of $^{60}Fe/Fe = (3 \pm 1) \times 10^{-17}$, equivalent to one identified background event over ~1 day of measurement (fig. S1). A total of 435 ^{60}Fe detector events were registered over the 24 samples of the crust (Table 1). Two distinctly separated ^{60}Fe signals are observed, with maxima at 2.5 and 6.3 Ma (Fig. 1). No ^{60}Fe above the background was observed between 4.2 and 5.5 Ma and for samples older than 7 Ma. The absolute ^{60}Fe flux and its time profile confirm previous results in sediment, crust, and nodule samples (fig. S2). The ^{60}Fe incorporation was $(6.10 \pm 0.31) \times 10^6$ atoms cm^{-2} and $(1.77 \pm 0.25) \times 10^6$ atoms cm^{-2} for the younger and older signals, respectively, consistent with previous reports [$(5.9 \pm 0.8) \times 10^6$ and $(3.5 \pm 1.4) \times 10^6$ atoms cm^{-2}, respectively] (*19*) (all uncertainties are given as 1σ values). Unlike sediments, crusts have incorporation efficiencies for Fe and Pu of <100% (see supplementary text). By comparing with sediment data (*19*), we deduce an incorporation efficiency for ^{60}Fe into Crust-3 of 17% [previously measured crusts had efficiencies of 17 and 6% (*17*, *19*)]. We found a similar efficiency for ^{244}Pu incorporation (*27*).

The three larger aliquots for ^{244}Pu analysis were completely dissolved and spiked with a known amount of ^{242}Pu to monitor the chemical yield of Pu (*27*). Pu abundances were measured using an AMS system that was specifically optimized for Pu measurements (*34*).

We observed an anthropogenic Pu signal in the top layer of Crust-3, which has ^{240}Pu/^{239}Pu and ^{241}Pu/^{239}Pu isotope ratios that are consistent with the expected values for nuclear weapons fallout (supplementary text). ^{239}Pu, ^{240}Pu, and ^{244}Pu events were observed in all three crust layers, and ^{241}Pu was observed in the first two layers. The ^{240}Pu/^{239}Pu and ^{241}Pu/^{239}Pu ratios are constant over these layers. The ^{244}Pu/^{239}Pu ratio shows an excess over anthropogenic levels in the two deeper layers (Fig. 2 and fig. S4). Assuming that the ^{244}Pu abundance is dominated by the anthropogenic contribution in the top layer, we correct the deeper layers for this contribution and attribute the additional ^{244}Pu to extraterrestrial deposition. The amount of short-lived anthropogenic Pu in the deeper layers indicates some anthropogenic Pu penetrated below the top layer (with concentrations relative to the top layer A of 1.5 and 0.1% in layers B and C, respectively), possibly as a result of pore water–induced redistribution into the deeper layers (*27*). If ^{60}Fe also migrates in crusts, our observed time profile (Fig. 1A) could have been slightly broadened by this effect.

We attribute 181 detector events to extraterrestrial ^{244}Pu in the three layers of Crust-3, compared with about one ^{244}Pu event for blank samples (*27*). The averaged extraterrestrial ^{244}Pu incorporation rate was (71 ± 8) and $\left(11.5^{+7.8}_{-5.8}\right)$ atoms cm^{-2} Myr^{-1} for 0 to 4.6 Ma and 4.6 to 9 Ma, respectively. These results are consistent with previous 2σ limits of <188 (0.5 to 5 Ma) and <66 atoms cm^{-2} Myr^{-1} (5 to 12 Ma) based on zero and one ^{244}Pu event, respectively (*12*) (fig. S8). Combining the decay-corrected ^{244}Pu and ^{60}Fe concentrations in Crust-3, we find an atom ratio of ^{244}Pu/^{60}Fe = $(5.3 \pm 0.7) \times 10^{-5}$, averaged over the last ~4.6 Myr, and $\left(2.8^{+1.9}_{-1.4}\right) \times 10^{-5}$ for 4.6 to 9 Ma, consistent with each other within the uncertainties (Table 2).

We attribute the two peaks in the ^{60}Fe deposition profile (Fig. 1A) to multiple nearby SN explosions during the last 10 Myr. Earth may have been exposed to separate waves of SN ejecta, or alternatively, the SS may have traversed clouds of ^{60}Fe-enriched dust. There are several potential explanations for the 3 to 4× higher ^{60}Fe influx for the younger time period: a SN at about half the distance of the older event, a more massive star that produced substantially more ^{60}Fe, more than one SN explosion (compatible with the broader peak), or different ISM conditions affecting dust survival and penetration into the SS.

After decay correction (*27*), our measured ^{60}Fe fluence is equivalent to a 10-Myr-averaged ^{60}Fe local concentration of (0.3 to 0.6) × 10^{-12} ^{60}Fe atoms cm^{-3} at Earth's orbit [with an incorporation efficiency of 17% (see above) and assuming a relative velocity of the SS in the ISM between 10 and 20 km s^{-1} (supplementary text)]. Two SNe, with a ^{60}Fe-yield of 2×10^{-5} solar masses ($M_\odot$) each (*19*, *35*), would enrich the ISM within a volume of 75-parsecs

Table 2. ^{60}Fe and ^{244}Pu data for three time periods during the last 10 Myr from three crust layers. Crust-3 data are from this work, and Crust-0 data are from (*12*, *19*). For details on the ISM (extraterrestrial) flux and fluence calculations, see (*27*). The FeMn-crust sample was split into three layers A, B, and C for ^{244}Pu (18, 179, and 208 g, respectively). The individual ^{60}Fe data (background-corrected) from table S1 were combined to cover the same time periods as ^{244}Pu. All uncertainties are 1σ [we converted the 2σ values for Crust-0 (*12*) to 1σ]. The bolded lines (Crust-$3_{0\text{-}4.6}$ and Crust-$0_{0.5\text{-}5.0}$) cover the time periods of the younger ^{60}Fe influx (0 to 4.6 Ma and 0.5 to 5.0 Ma, respectively). The italicized lines (Crust-$3_{0\text{-}9.0}$ and Crust-$0_{0.5\text{-}12}$) represent the time integral over the 9 Myr covered by Crust-3 as well as the similar time span of 0.5 to 12 Ma investigated for Crust-0 (*12*). Dashes in otherwise empty cells indicate not applicable.

Layer	Depth (mm)	Time period (Myr)	$^{60}Fe_{ISM}$ atoms detected	^{60}Fe rate (atom cm^{-2} yr^{-1})	^{60}Fe layer incorporation (10^6 atoms cm^{-2})
Crust-3/A	0 – 3	0 – 1.34	88 ± 9	0.72 ± 0.08	0.97 ± 0.10
Crust-3/B	3 – 10	1.34 – 4.57	282 ± 17	1.61 ± 0.09	5.19 ± 0.31
Crust-3/C	10 – 20	4.57 – 9.0	46 ± 7	0.42 ± 0.04	1.82 ± 0.26
Crust-$3_{0\text{-}4.6}$	**0 – 10**	**0 – 4.57**	**370 ± 19**	**1.35 ± 0.07**	**6.14 ± 0.31**
Crust-$3_{0\text{-}9.0}$	*0 – 20*	*0 – 9.0*	*415 ± 20*	*0.89 ± 0.04*	*7.96 ± 0.38*
blank	–	–	2	–	–

Layer	Time period (Myr)	$^{244}Pu_{ISM}$ atoms detected	^{244}Pu rate (atoms cm^{-2} Myr^{-1})	^{244}Pu layer incorporation (atoms cm^{-2})	$^{244}Pu_{ISM}$ flux at Earth orbit (10^3 atoms cm^{-2} Myr^{-1})	$^{244}Pu_{ISM}$ fluence at Earth orbit 10^3 atoms cm^{-2}	^{244}Pu/^{60}Fe (10^{-6} at/at)
Crust-3/A	0 – 1.34	34 ± 17	38 ± 19	51 ± 26	0.90 ± 0.48	1.2 ± 0.6	52 ± 26
Crust-3/B	1.34 – 4.57	141 ± 19	85 ± 11	274 ± 37	1.99 ± 0.44	6.4 ± 1.4	53 ± 7
Crust-3/C	4.57 – 9.0	$6.3^{+4.3}_{-3.2}$	$11.5^{+7.8}_{-5.8}$	51^{+35}_{-26}	$0.27^{+0.18}_{-0.14}$	$1.2^{+0.8}_{-0.6}$	28^{+19}_{-14}
Crust-$3_{0\text{-}4.6}$	**0 – 4.57**	**175 ± 19**	**71 ± 8**	**325 ± 40**	**1.67 ± 0.35**	**7.7 ± 1.6**	**53 ± 6**
Crust-$3_{0\text{-}9.0}$	*0 – 9.0*	*181 ± 19*	*42 ± 4*	*376 ± 40*	*0.98 ± 0.18*	*8.9 ± 1.8*	*47 ± 5*
Blank	–	1	–	–	–	–	–
Crust-$0_{0.5\text{-}5.0}$	**0.3 – 5.0**	**0**	**<100**	**<420**	**<2.2**	**<10.0**	**<170**
Crust-$0_{0.5\text{-}12}$	*0.3 – 12*	*1*	*<40*	*<440*	*<1*	*<10.0*	–
Crust-$0_{0.5\text{-}25}$	0.3 – 25	2	<30	<700	<0.6	<15.0	–

(pc) radius to $\lesssim 10^{-11}$ ^{60}Fe atoms cm^{-3}, if distributed homogeneously and taking into account radioactive decay. The Galaxy-averaged concentration of ^{60}Fe is ~4×10^{-12} atoms cm^{-3}, deduced from the average SN rate for the Milky Way and gamma-ray astronomical observations (*22*) (supplementary text). Assuming that ^{60}Fe only reaches Earth when adsorbed on dust grains, comparison of the measured local ^{60}Fe concentration and typical SN yields lead to a probability of dust formation and SS penetration for SN-produced ^{60}Fe of ~*3* to *6*% in mass, close to the measured fraction of interstellar dust grains reaching the inner SS at present times of ~(*6* ± *3*)% (*11*, *12*). This *3* to *6*% (in mass) probability of dust reaching Earth reflects the selective filtering of interstellar dust particles that favors larger dust grains (supplementary text). We conclude that the ^{60}Fe fluence reaching Earth ~*2.5* and *6.5* Ma is compatible with two to four SN events at distances of 50 to 100 pc.

The extraterrestrial ^{244}Pu, deposited concomitantly with SN-produced ^{60}Fe, shows an approximately constant ^{244}Pu/^{60}Fe ratio of (*3* to *5*) × 10^{-5} (Fig. 1). Assuming no fractionation between ^{244}Pu and ^{60}Fe, these values represent their atom ratio in the ISM. If ^{244}Pu and ^{60}Fe originate from the same SN events, this ratio can be used to deduce ^{244}Pu SN yields (*36*) (supplementary text), though the absolute yield estimates in those models have large uncertainties for ^{60}Fe and ^{244}Pu. Unusual types of SNe are improbable if there were two consecutive local SN events. If the ^{244}Pu was already present in the ISM from older r-process events, any actinide yields from the recent SN explosions would be accordingly lower.

We next consider alternative scenarios for the origin of extraterrestrial ^{244}Pu. The 30× longer half-life of ^{244}Pu compared with that of ^{60}Fe means that it could have been produced in older events than the SNe that produced the ^{60}Fe. The ^{244}Pu influx during the past 9 Myr could be a remainder of an older r-process event if it was incorporated into dust that survived the LB formation (>10 to 15 Ma) and was swept up by the more recent SN ejecta, together with freshly produced ^{60}Fe. Depending on the rate of actinide production, older ^{244}Pu (and other actinides) could be present in the ISM in (i) a steady-state concentration, if produced with high frequency compared with its lifetime (e.g., in SNe), or (ii) as the remaining fraction of an earlier rare event [such as NSMs, collapsars, or magneto-rotational SNe (*3*–*5*)], after radioactive decay has lowered an initially high actinide nucleosynthesis yield. Alternatively, the SS could have moved through two separate dust clouds containing SN-produced ^{60}Fe and older ^{244}Pu.

We calculate whether our data are compatible with ^{244}Pu having a steady-state concentration in the local ISM, assuming ^{244}Pu and ^{60}Fe are similarly adsorbed onto dust particles. Combining the Galaxy-averaged concentration of ^{60}Fe, 4×10^{-12} atoms cm^{-3} (*24*) (supplementary text), with the measured ^{244}Pu/^{60}Fe ratio leads to a concentration (c) of ^{244}Pu in the local ISM $c_{^{244}\mathrm{Pu,ISM}} = (1.2 \text{ to } 2.0) \times 10^{-16}$ atoms cm^{-3}. Assuming that $c_{^{244}\mathrm{Pu,ISM}}$ is associated with ISM dust particles of a composition similar to that of the early SS, we calculate (supplementary text) that steady-state conditions lead to an expected dust mass concentration of ~(1 to 2) × 10^{-28} g cm^{-3}. This value is one-hundredth the size of—and is inconsistent with—the measured local (within a few parsecs) dust mass density at the present time, which is ~1.5×10^{-26} g cm^{-3} (*37*) (supplementary text). However, it is consistent with the recent SNe exploding inside the LB, a region of very low-density ISM. Earlier SN ejecta could have reached Earth prior to the more recent SNe; if so, they would have swept up older ISM material and erased any existing steady-state ^{244}Pu inside the newly forming LB.

Our measurements of extraterrestrial ^{244}Pu and ^{60}Fe confirm an influx of interstellar material into the inner SS through two or more local and transient SN events over the last ~10 Myr, and they are compatible with some production of actinides in core-collapse SNe, possibly of common type. Combining these data with previous results of ^{244}Pu influx over the past 25 Myr (*12*) (extending prior to the

formation of the LB) indicates that SN actinide yields seem insufficient to account for the overall abundance of r-process nuclides in the Galaxy (fig. S8). These yields can be compared with the total r-process inventory calculated by SN actinide nucleosynthesis simulations, which, however, is limited by model uncertainties. The present data are compatible with the LB being a local disturbance of a large-scale Galactic steady-state (from SN enrichment of the ISM occurring more frequently than the radioactive half-life), with less-frequent injections from rarer r-process sources that nevertheless dominate the production of r-process elements, such as NSMs. The data are also consistent with the hypothesis of a nearby rare event before the time of SS formation that supplied the majority of the SS known inventory of the primordial actinides Th, U, and Pu (*12*, *38*) (fig. S9 and supplementary text).

REFERENCES AND NOTES

1. Y.-Z. Qian, *Prog. Part. Nucl. Phys.* **50**, 153–199 (2003).
2. M. Arnould, S. Goriely, K. Takahashi, *Phys. Rep.* **450**, 97–213 (2007).
3. F. K. Thielemann *et al.*, *Prog. Part. Nucl. Phys.* **66**, 346–353 (2011).
4. J. J. Cowan *et al.*, *Rev. Mod. Phys.* **93**, 015002 (2021).
5. J. M. Lattimer, D. N. Schramm, *Astrophys. J.* **210**, 549–567 (1976).
6. A. P. Ji, A. Frebel, A. Chiti, J. D. Simon, *Nature* **531**, 610–613 (2016).
7. D. Kasen, B. Metzger, J. Barnes, E. Quataert, E. Ramirez-Ruiz, *Nature* **551**, 80–84 (2017).
8. D. Breitschwerdt *et al.*, *Nature* **532**, 73–76 (2016).
9. J. Ellis, B. D. Fields, D. N. Schramm, *Astrophys. J.* **470**, 1227 (1996).
10. B. J. Fry, B. D. Fields, J. R. Ellis, *Astrophys. J.* **827**, 48 (2016).
11. N. Altobelli *et al.*, *J. Geophys.* **110**, A07102 (2005).
12. A. Wallner *et al.*, *Nat. Commun.* **6**, 5956 (2015).
13. G. Korschinek, T. Faestermann, K. Knie, C. Schmidt, *Radiocarbon* **38**, 68 (1996).
14. G. Rugel *et al.*, *Phys. Rev. Lett.* **103**, 072502 (2009).
15. A. Wallner *et al.*, *Phys. Rev. Lett.* **114**, 041101 (2015).
16. K. Knie *et al.*, *Phys. Rev. Lett.* **83**, 18–21 (1999).
17. K. Knie *et al.*, *Phys. Rev. Lett.* **93**, 171103 (2004).
18. C. Fitoussi *et al.*, *Phys. Rev. Lett.* **101**, 121101 (2008).
19. A. Wallner *et al.*, *Nature* **532**, 69–72 (2016).
20. P. Ludwig *et al.*, *Proc. Natl. Acad. Sci. U.S.A.* **113**, 9232–9237 (2016).
21. A. Wallner *et al.*, *Proc. Natl. Acad. Sci. U.S.A.* **117**, 21873–21879 (2020).
22. D. Koll *et al.*, *Phys. Rev. Lett.* **123**, 072701 (2019).
23. L. Fimiani *et al.*, *Phys. Rev. Lett.* **116**, 151104 (2016).
24. R. Diehl, *Rep. Prog. Phys.* **76**, 026301 (2013).
25. W. R. Binns *et al.*, *Science* **352**, 677–680 (2016).
26. M. Kachelrieß, A. Neronov, D. V. Semikoz, *Phys. Rev. Lett.* **115**, 181103 (2015).
27. Materials and methods are available as supplementary materials.
28. J. Feige *et al.*, *Phys. Rev. Lett.* **121**, 221103 (2018).
29. G. Korschinek *et al.*, *Phys. Rev. Lett.* **125**, 031101 (2020).
30. B. J. Fry, B. D. Fields, J. R. Ellis, *Astrophys. J.* **800**, 71 (2015).
31. C. Wallner *et al.*, *New Astron. Rev.* **48**, 145–150 (2004).
32. M. Paul *et al.*, *Astrophys. J.* **558**, L133–L135 (2001).
33. P. R. Fields *et al.*, *Science* **167**, 499–501 (1970).
34. M. A. C. Hotchkis *et al.*, *Nucl. Instrum. Methods Phys. Res. B* **438**, 70–76 (2019).
35. M. Limongi, A. Chieffi, *Astrophys. J.* **647**, 483–500 (2006).
36. S. Goriely, H.-Th. Janka, *Mon. Not. R. Astron. Soc.* **459**, 4174–4182 (2016).
37. A. Li, *J. Phys. Conf. Ser.* **6**, 229–248 (2005).
38. K. Hotokezaka, T. Piran, M. Paul, *Nat. Phys.* **11**, 1042 (2015).

ACKNOWLEDGMENTS

We thank JOGMEC for supplying the crust and M. G. Froehlich for assisting in sample preparation. **Funding:** A.W., M.B.F., M.P., M.M., and S.P. were supported by the Australian Research Council's Discovery scheme, project numbers DP140100136, DP180100495, and DP180100496. N.Kin. was supported by the Japan Society for the Promotion of Science (JSPS) KAKENHI grant no. 17K05722. We also acknowledge financial support from the Australian government for the Heavy Ion Accelerator Facility at ANU and for the Centre for Accelerator Science at ANSTO through the National Collaborative Research Infrastructure Strategy (NCRIS). **Author contributions:** A.W. and M.P. wrote the manuscript, and all authors were involved in the project and commented on the paper. A.W. initiated the study. N.Kin. acquired the crust sample. M.B.F. and N.Kin. prepared the sample. A.W., S.G.T., S.P., M.M., and M.B.F. performed the AMS measurements for ^{60}Fe at the ANU; M.A.C.H. and A.W. performed the ^{244}Pu measurements at VEGA; and N.Kin., T.Y., and H.M. organized the ^{10}Be measurements at MALT. N.Kin. and M.H. analyzed stable elements with ICP-MS. N.Kiv. and D.S. produced the ^{60}Fe standard. A.W. and M.A.C.H. performed the data analysis. **Competing interests:** The authors declare no competing interests. **Data and materials availability:** Our Fe measurements are listed in table S1 and the Pu measurements in tables S2 and S3. The stable element concentrations and the ^{10}Be data used for the dating of the individual layers are given in tables S4 and S5. The Crust-3 sample was collected by the Japan Oil, Gas and Metals National Corporation (JOGMEC) in 1995 and acquired through an intermediary (Takashi Nakanishi, Kanazawa University) (see supplementary text). The sample location has not been revealed by JOGMEC for resource-protection reasons. The sample was consumed during our experiments. We expect samples from other locations to contain the same interstellar signals (supplementary text).

SUPPLEMENTARY MATERIALS

science.sciencemag.org/content/372/6543/742/suppl/DC1
Materials and Methods
Supplementary Text
Figs. S1 to S9
Tables S1 to S6
References (*39*–*104*)

21 March 2019; accepted 12 April 2021
10.1126/science.aax3972

DROUGHT

Watersheds may not recover from drought

Tim J. Peterson[1,2]*, M. Saft[2]†, M. C. Peel[2]†, A. John[2]

The Millennium Drought (southeastern Australia) provided a natural experiment to challenge the assumption that watershed streamflow always recovers from drought. Seven years after the drought, the runoff (as a fraction of precipitation) had not recovered in 37% of watersheds, and the number of recovered watersheds was not increasing. When recovery did occur, it was not explained by watershed wetness. For those watersheds not recovered, ~80% showed no evidence of recovering soon, suggesting persistence within a low-runoff state. The post-drought precipitation not going to runoff was found to be likely going to increased evapotranspiration per unit of precipitation. These findings show that watersheds can have a finite resilience to disturbances and suggest that hydrological droughts can persist indefinitely after meteorological droughts.

Watersheds are widely assumed to always recover from droughts, whereby recovery is simply a function of duration after the drought (*1*–*4*). Although our understanding of watershed drought recovery is limited (*3*) and often overlooked (*5*, *6*), theoretical studies show that recovery can be uncertain and may occur only after a wet period, rather than a given duration after a drought (*7*). This nonrecovery occurs because of the interaction between a disturbance and a positive feedback, which produces more than one dynamic equilibrium, or steady state, and hence a finite resilience (*8*). Recent observations show that prolonged droughts can cause unexpectedly large reductions in streamflow in Australia (*9*), the US (*10*), and China (*11*). This further suggests that watersheds may have multiple steady states, but confirming this requires evidence of persistence in the alternate state after drought (*7*, *12*). Whether or not watersheds always recover from prolonged droughts has major implications for global long-term water resource planning and aquatic environments, especially under climate change. In this study, we used the Australian Millennium Drought as a natural experiment to empirically assess watershed recovery from prolonged droughts.

The Millennium Drought was the longest uninterrupted period of low rainfall in southeast Australia since at least 1900, and although its start date is ambiguous (~1997 to 2001), it ended with a strong La Niña event in early 2010 (*13*). We investigated recovery from this drought by statistically analyzing the annual and seasonal streamflow and precipitation of 161 unregulated watersheds with high-quality data within Victoria, Australia (figs. S1 to S4 and tables S1 and S2)—this region, which was most severely affected by the Millennium Drought, is approximately the area of the UK, or half of California. Each watershed has at least 15, 7, and 5 years of streamflow observations before, during, and after the Millennium Drought,

[1]Department of Civil Engineering, Monash University, Clayton, Victoria, Australia. [2]Department of Infrastructure Engineering, University of Melbourne, Parkville, Victoria, Australia.
*Corresponding author. Email: tim.peterson@monash.edu
†These authors contributed equally to this work.

respectively, and has no major upstream reservoirs or river extractions. The streamflow observation record mean start date was 1960, 89% of gauges had at least 40 complete years of observations (fig. S3), and the rating curves were generally updated during and after the drought (fig. S4).

To illustrate the nonrecovery, Fig. 1A shows that at gauge 224206, the conversion of annual precipitation to runoff did not change during or after the drought. At 405217, the runoff reduced during the drought (for a given precipitation) but then recovered to predrought conditions after the drought (Fig. 1C). Conversely, at 221201 the runoff reduced during the drought, but after the drought the reduction has persisted (Fig. 1E), despite some above-average rainfall years, and hence appears to have not recovered.

Hidden Markov models (HMMs) (*14*) are well suited to understanding this persistence (*15*) and its cessation and hence the timing of recovery or otherwise. For this study, we developed 64 annual and 32 seasonal homogeneous HMMs for each watershed, with the former informing annual runoff changes and having a simpler structure, but one that allows the inclusion of up to 3 years serial correlation, and with the latter informing whether annual runoff changes are explained by recent shifts in seasonal rainfall (*16*) and having four times the observed data (compare with annual). The HMM states are analogous to the shifting *y*-axis intercepts in Fig. 1, A, C, and E, and to separate the runoff variability from the precipitation variability, precipitation was a covariate (see materials and methods and figs. S19 to S180). The most parsimonious model at each watershed was identified by using the Akaike information criterion (AIC) and compared against the best one-state model (figs. S6 and S181 to S398 and tables S3 and S4). The results show that watersheds can have one runoff state (Fig. 1B), two runoff states but quick recovery after the Millennium Drought (Fig. 1D), two states and nonrecovery after the drought (Fig. 1F), or variants of each (figs. S19 to S180). In combination, Fig. 1, B, D, and F, provides empirical evidence for the conceptual models of watershed resilience (*7*, *12*).

Across all 161 watersheds, we found that 8 years into the drought, 51% of watersheds switched into a low (or very low) runoff state (Fig. 2, A and B). When the drought ended in 2010, predominantly only the eastern watersheds shifted back to a normal-runoff state (Fig. 2C). Notably, 7 years after the drought, 37% (n = 55) of watersheds remained within a low-runoff state (Fig. 2D). This nonrecovery is not explained by the stream-gauge method (fig. S7). Also, most watersheds in the central region remained within a low-runoff state, whereas many in the southwest and the wetter southeast and northeast recovered (movies S1 and S2). Within these regions, however, the response was heterogeneous, which suggests the importance of watershed attributes in addition to the regional climate. The evidence ratio (*17*), which was calculated from the AIC (*18*) for the most parsimonious model (i.e., lowest AIC) and divided by the AIC for the best one-state model, shows that 55% (n = 30) of the watersheds that did not recover had an evidence ratio ≥log(100) (Fig. 2E). This suggests that there is little evidence (*17*) to support there only being one runoff state before, during, and after the drought in these watersheds.

The nonrecovery reduced the post-drought runoff by 37.2% [mean (μ) = 92 mm/year decline, standard deviation (σ) = 101 mm/year] and, because of the higher precipitation after the drought, this reduction was generally greater than that during the drought (table S4). This change in runoff, as well as that during the drought, was found to be uncorrelated with the remotely sensed time series of land-cover change (figs. S8 to S10). Although the impact of other anthropogenic changes cannot be ruled out, the impact of farm dams is likely to explain <5% of the post-drought runoff reduction (*19*). Given that the reduced runoff is also not explained by precipitation because the variability in precipitation is accounted for in the HMMs, this reduction can be thought of as precipitation missing from the stream gauge.

The number of watersheds within a low (or very low) runoff state increased rapidly

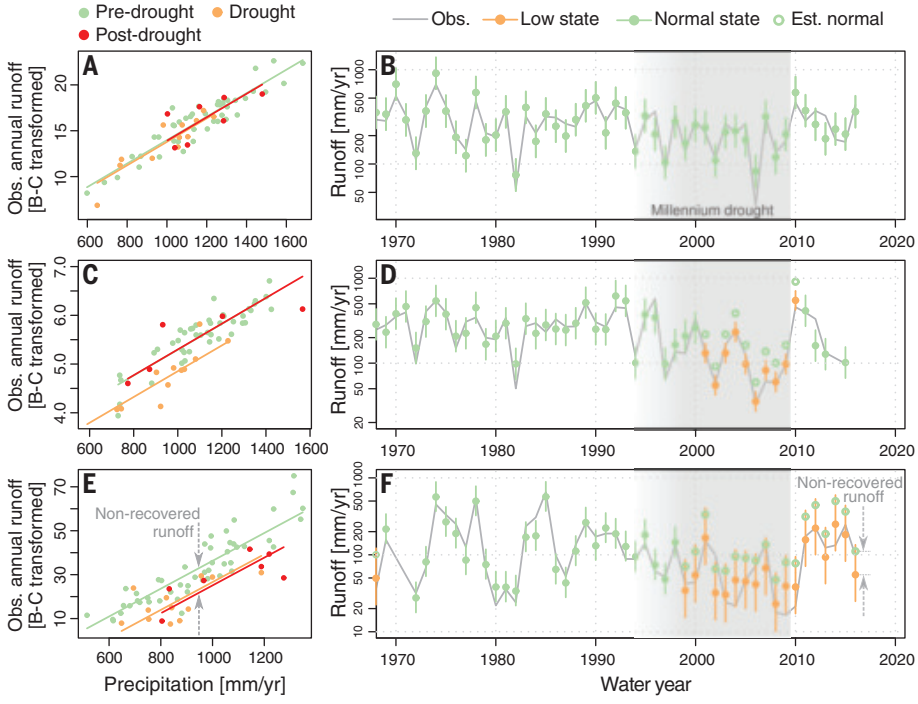

Fig. 1. Three examples of how watersheds may respond and recover (or otherwise) from a drought. (**A** and **B**) Wonnangatta River (224206) rainfall-runoff did not change during or after the Millennium Drought. (**C** and **D**) Yea River (405217) rainfall-runoff declined during the drought and appears to have recovered. (**E** and **F**) Cann River (221201) rainfall-runoff declined during and after the drought and appears not to have recovered. The left column shows scatterplots of the annual precipitation against Box-Cox (BC)–transformed annual runoff colored by before the Millennium Drought (≤1997), during the drought (>1997 and <2010), and after the drought (≥2010). The lines were fitted by extending the analysis in (9) to include post-drought years. The right column shows the hidden Markov modeling results and the observed annual runoff (note: log *y* axis). Panel (B) shows that the watershed was found to have only one runoff state. Panel (D) shows that the watershed was found to have two runoff states and to have shifted into a low-runoff state in water year 2001 and recovering 1 year after the Millennium Drought ended in water year 2010. Panel (E) shows that the watershed also was found to have two runoff states and to have shifted into a low-runoff state in water year 1999 and had not recovered by the final year of analysis. Panels (D) and (F) show estimates of the normal runoff had the watershed not been in the low-runoff state. The dashed arrows in (E) and (F) denote the nonrecovered runoff. The years of the Millennium Drought are graduated to denote that it generally started in Victoria in 1997, but in some parts of Victoria, it may have started in 1994. The vertical bars in (B), (D), and (F) denote the 5th and 95th percentile estimates of runoff. Est., estimated; Obs., observed.

from water year 1996 and peaked at the end of the meteorological drought in summer 2010 (Fig. 3). By 2011, only 15% (n = 25) of watersheds had recovered (seasonal: n = 27, 17%). Over the 7 years after the drought, there was no trend of increasing recovery, and by 2017, 38% (n = 62) of watersheds remained within a low-runoff state (seasonal: n = 56, 34%). This persistence within a low state does not support the argument that watershed recovery is controlled by the post-drought duration (*2*). The consistency between the annual and seasonal results and the seasonal shifts that persist for years (figs. S19 to S180), rather than seasonally flickering between states, suggests that the redistribution of within-year precipitation (*16*) does not explain the nonrecovery.

To understand whether recovery will occur soon, as it did in 1983 (Fig. 3), we estimated the 3-year trend in the low-state conditional probability of each watershed in a nonrecovered and recovered state. Specifically, for the former, we derived the slope from the final 3 years of analysis, and for the latter, we derived the slope from the 3 years before the recovery from the Millennium Drought, for which 3 years was a pragmatic choice that placed greater weight on the most recent post-drought years, rather than the wet years immediately after the drought, while having sufficient points to derive a multiyear trend. For the recovered watersheds, the slope was <0 for 82% (seasonal: 76%) of sites (Fig. 4A). Conversely, for the nonrecovered watersheds, the slope was <0 for 16% of sites (seasonal: 28%). Hence, the watersheds that have recovered displayed prior warning of recovery, whereas the watersheds that have not yet recovered displayed no such warning. This suggests that most of the watersheds that have not recovered show no evidence of recovering soon and appear to be persisting within the low-runoff state.

However, the persistent nonrecovery may simply be caused by insufficient precipitation to refill subsurface storages (soil moisture and groundwater). To explore whether wetness does drive recovery, we identified periods when a watershed switched from a normal state to a subnormal state and then recovered. The change in wetness was then approximated from the cumulative rainfall residual, CRR (see materials and methods), at recovery minus that when it switched into the subnormal state (ΔCRR), divided by the standard deviation of the rainfall residuals, σ_r. We found that 86% (seasonal: 70%) of periods had a lower CRR at recovery than when the subnormal period began (Fig. 4B), and a one-sided Mann-Whitney test indicated that there is insufficient evidence to reject the null hypothesis that ΔCRR < 0. Watershed wetness, therefore, appears to be lower at recovery than before switching into a subnormal state. This indicates that recovery

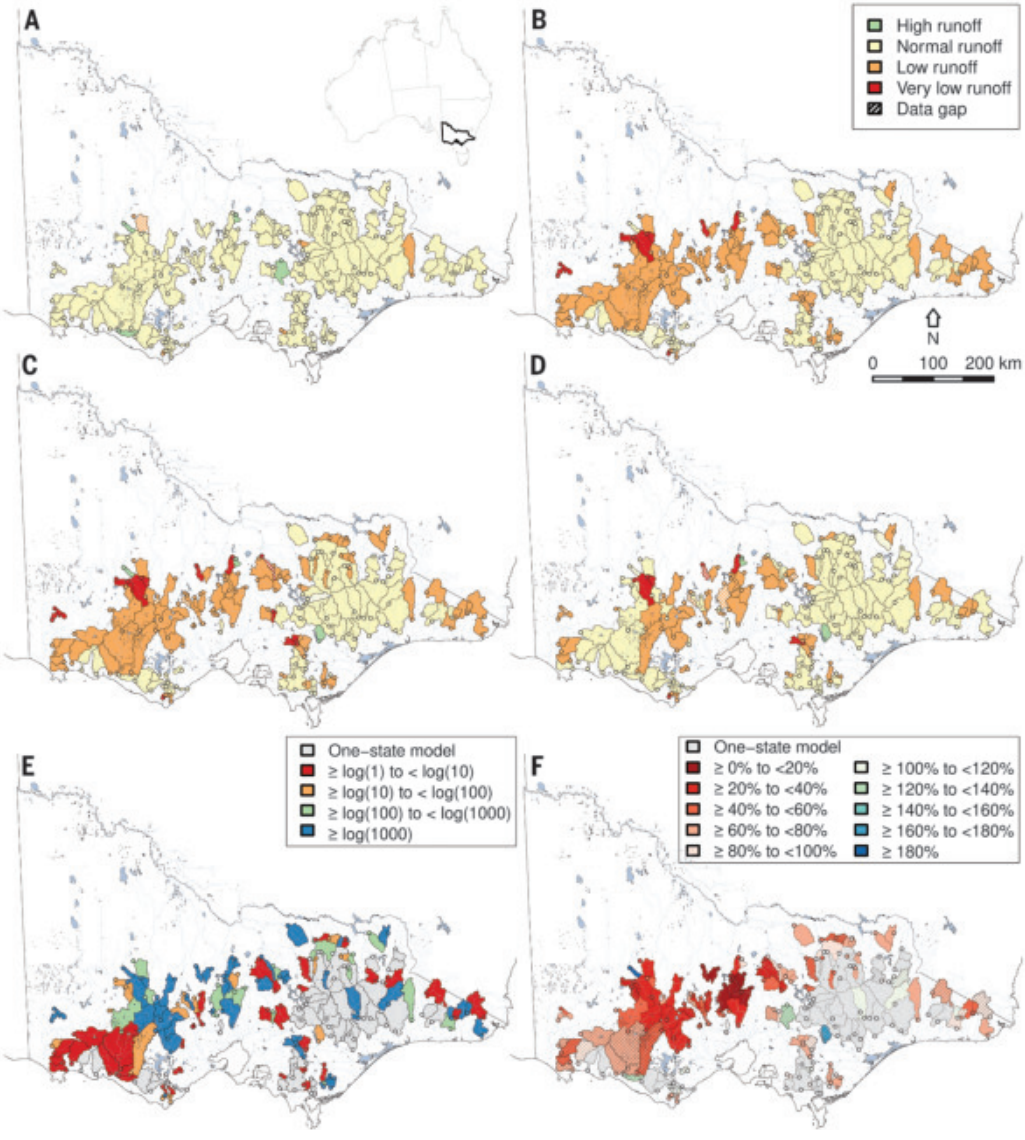

Fig. 2. Maps of the change in runoff state before, during, and after the Millennium Drought, and the evidence ratio and percentage change in runoff. (**A** to **F**) Rainfall-runoff states from the hidden Markov modeling at 161 streamflow gauges in Victoria, Australia, at (A) the approximate start of the Millennium Drought in 1995 (note that 1997 is considered the general start, but in some parts of Victoria, it may have started in 1994), (B) ~8 years into the drought (2005), (C) the first year after the end of the drought (2010), and (D) 7 years after the end of drought (2016), with (E) the evidence ratio of multistate models and (F) the mean post-drought runoff as a percentage of the estimated normal-state runoff, in which cross-hashing denotes an evidence ratio <log(100), which suggests lower evidence for multiple states. Note that the years are at the start of water year, which started in March. The inset in (A) shows the study area of Victoria, Australia.

is not always controlled by refilling of subsurface storages and suggests mechanisms other than post-drought duration.

The post-drought precipitation that is missing from the streamflow can only be going to increased vadose zone storage, increased rainfall interception, groundwater recharge, groundwater outflow, or evapotranspiration. Increased interception is unlikely to explain the missing streamflow of 92 mm/year, given that the leaf area index (LAI) did not change during the drought (*20*, *21*). Similarly, the constancy or decline of the groundwater head after drought (figs. S17 and S18) suggests that the missing streamflow is not going to increased recharge. At the watershed outlet, the subsurface groundwater outflow may have changed, but, given that we see no evidence that the lateral head gradient at the outlet increased, the lower heads likely reduced the aquifer lateral transmissivity, and hence, the groundwater outflow rate probably also declined. Therefore, the missing streamflow is most likely to have infiltrated but appears not to have produced a year-on-year increase in vadose zone storage, given the lower recharge. We postulate that the missing streamflow is most likely going to increased evapotranspiration (ET), per unit of precipitation, relative to that before the drought.

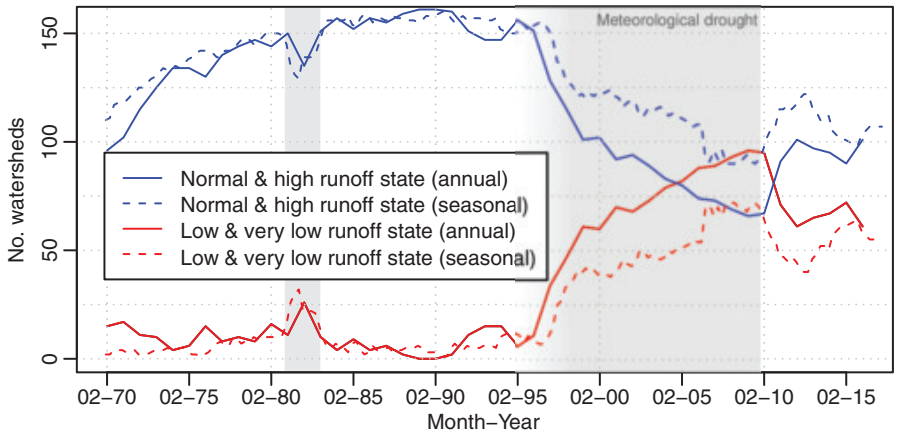

Fig. 3. Number of watersheds within a low (or very low) runoff state and within a normal (or high) runoff state, as derived from the annual and the seasonal HMMs. Gray shading denotes meteorological droughts. A Mann-Kendall trend test of the annual low-flow results from 2010 to 2017 found no significant declining trend (P = 0.18). Analysis of seasonal results found a weakly significant rising trend (P = 0.07) but with a slight correlation (τ = 0.24). Note that results for a water year or season are plotted at the start of each analysis period.

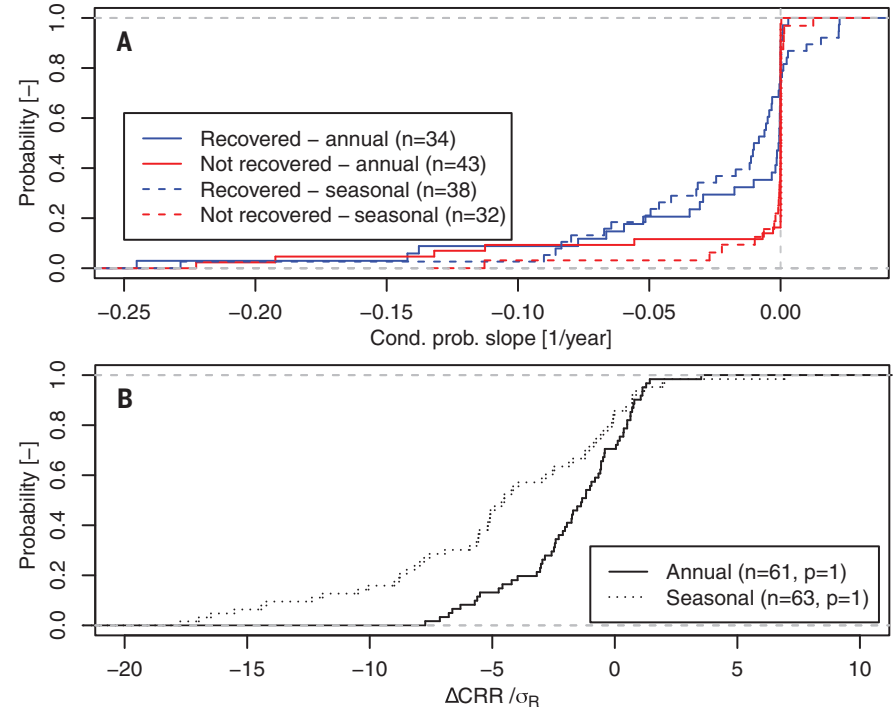

Fig. 4. Cumulative probabilities of the change in the runoff state probabilities at or before recovery and the change in the cumulative rainfall residuals. (**A**) Slope in the conditional probability of being in a low (or very low) runoff state over the 3 years before recovery (dashed) and over the final 3 years in which recovery had not occurred (solid) for the annual and seasonal analysis. (**B**) CRR at recovery from a low-runoff state minus the CRR when switching into the low-runoff state (normalized by the SD in the rainfall residuals, σ_r) for both the annual and seasonal analysis.

Practically, this implies that in response to the Millennium Drought, the vegetation in many watersheds responded by maintaining similar rates of transpiration, given that LAI did not decline and despite the reduced precipitation. To examine this, we used Horton's index (*22*), H, to estimate the mean watershed evapotranspiration as a fraction of the precipitation that wetted the watershed (i.e., excluding precipitation that went quickly to streamflow) before, during, and after the drought. Although the approach assumes zero change in annual water storage, given that this assumption has been found to produce a water balance error of <5% of precipitation when >5 years are averaged (*23*) and that we average periods of ≥7 years, we argue that this assumption is acceptable. Furthermore, given the groundwater level decline during the drought (figs. S17 and S18), the change in storage during the drought is likely to be negative. Hence, the mean H during the drought, and its change relative to before the drought, is likely to be an underestimate.

We found that the mean H was statistically significantly higher after the Millennium Drought than before the drought at 40 to 42% (n = 64 to 67) of watersheds (fig. S14) and that this change was statistically significantly greater in watersheds that had not recovered by water year 2016 (fig. S15) and was moderately correlated with the fractional change in post-drought streamflow (fig. S16). Mechanistically, it appears that the increased evapotranspiration (as a fraction of precipitation) reduced recharge, which lowered the water table and increased the vadose zone soil moisture capacity. With increased capacity, a greater fraction of precipitation could be evapotranspired before being lost to streamflow or recharge, which further lowered the water table. Attributing the change in actual ET to increased transpiration (as a fraction of precipitation) does, however, remain problematic, given the difficulties in estimating watershed transpiration (*24*), whereas drought-induced changes in soil hydraulics (*25*) and vegetation phenology (*26*) may further explain the mechanisms.

In summary, we conclude that the annual and seasonal runoff in approximately one-third

of Victoria's gauged unregulated watersheds has not recovered from the Millennium Drought, that the nonrecovery is not explained by shifts in the seasonal precipitation, and that ≈80% of nonrecovered watersheds appear to be persisting within a low-runoff state. Evidence suggests that the vegetation responded to the drought by increasing the fraction of precipitation going to transpiration. Overall, these findings are consistent with the theoretical evidence of watersheds having multiple stable states and a finite resilience (*1*, *7*) and climate variability driving watersheds between alternate persistent states (*7*). It is not proof of such, but it does provide empirical evidence that recovery can be driven by the occurrence of wet periods perturbing a nonrecovered watershed past some as-yet-unknown threshold and not just the post-drought duration. More broadly, we have demonstrated that multiple states can be identified from observation data and hence have overcome a major limitation in the use of resilience for natural resource management (*27*).

Our findings suggest that hydrological droughts can persist indefinitely after meteorological droughts and that the mechanism for recovery remains an open question. Like other natural systems with multiple stable states (*8*), this persistence may be caused by a biophysical adaption to disturbances, specifically transpiration, that results in a positive feedback. Current rainfall-runoff models do not include positive feedbacks, and this may be one reason for their often-poor simulation of prolonged droughts (*28*). This has particularly important implications for understanding the runoff response in drying regions under climate change. Although climate change may not yet have increased global drought severity or frequency (*29*), given the future predictions of increased meteorological droughts (*30*), then where multiple runoff stable states exist, climate change could increase the probability of switching into a low-runoff period and reduce the probability of recovery (*7*). This amplification of climate change impacts could present substantial additional challenges to the already-threatened sustainable use of water resources for human and ecological outcomes.

REFERENCES AND NOTES

1. T. J. Peterson, R. M. Argent, A. W. Western, F. H. S. Chiew, *Water Resour. Res.* **40**, W03406 (2009).
2. A. F. Van Loon, H. A. J. Van Lanen, *Hydrol. Earth Syst. Sci.* **16**, 1915–1946 (2012).
3. A. F. Van Loon, *WIREs Water* **2**, 359–392 (2015).
4. Y. Yang *et al.*, *Water Resour. Res.* **53**, 4821–4837 (2017).
5. T. R. Ault, *Science* **368**, 256–260 (2020).
6. T. J. Brodribb, J. Powers, H. Cochard, B. Choat, *Science* **368**, 261–266 (2020).
7. T. J. Peterson, A. W. Western, R. M. Argent, *Water Resour. Res.* **50**, 3010–3029 (2014).
8. M. Scheffer, S. Carpenter, J. A. Foley, C. Folke, B. Walker, *Nature* **413**, 591–596 (2001).
9. M. Saft, A. W. Western, L. Zhang, M. C. Peel, N. J. Potter, *Water Resour. Res.* **51**, 2444–2463 (2015).
10. F. Avanzi *et al.*, *Hydrol. Earth Syst. Sci.* **24**, 4317–4337 (2020).
11. W. Tian, X. Liu, C. Liu, P. Bai, *J. Hydrol.* **565**, 95–105 (2018).
12. R. Q. Grafton *et al.*, *Nat. Sustain.* **2**, 907–913 (2019).
13. A. van Dijk *et al.*, *Water Resour. Res.* **49**, 1040–1057 (2013).
14. W. Zucchini, I. L. MacDonald, *Hidden Markov Models for Time Series: An Introduction Using R* (Monographs on Statistics and Applied Probability 110, CRC Press, 2009).
15. M. Thyer, G. Kuczera, *J. Hydrol.* **275**, 12–26 (2003).
16. N. J. Potter, F. H. S. Chiew, *Water Resour. Res.* **47**, W00G10 (2011).
17. K. P. Burnham, D. R. Anderson, K. P. Burnham, *Model Selection and Multimodel Inference: A Practical Information-Theoretic Approach* (Springer, 2002).
18. H. Akaike, *IEEE Trans. Automat. Contr.* **19**, 716–723 (1974).
19. L. Lowe, R. Nathan, R. Morden, *Aust. J. Water Resour.* **9**, 13–26 (2005).
20. Y. Sawada, T. Koike, *J. Geophys. Res. Biogeosci.* **121**, 2312–2327 (2016).
21. A. M. Ukkola *et al.*, *Nat. Clim. Chang.* **6**, 75–78 (2016).
22. P. A. Troch *et al.*, *Hydrol. Processes* **23**, 2409–2414 (2009).
23. J. Han *et al.*, *Water Resour. Res.* **56**, e2020WR027392 (2020).
24. Z. Wei *et al.*, *Geophys. Res. Lett.* **44**, 2792–2801 (2017).
25. J. S. Caplan *et al.*, *Sci. Adv.* **5**, eaau6635 (2019).
26. X. Ma, A. Huete, S. Moran, G. Ponce-Campos, D. Eamus, *J. Geophys. Res. Biogeosci.* **120**, 2036–2052 (2015).
27. A. C. Newton, *Conserv. Lett.* **9**, 369–376 (2016).
28. K. J. A. Fowler, M. C. Peel, A. W. Western, L. Zhang, T. J. Peterson, *Water Resour. Res.* **52**, 1820–1846 (2016).
29. J. Sheffield, E. F. Wood, M. L. Roderick, *Nature* **491**, 435–438 (2012).
30. L. Xu, N. Chen, X. Zhang, *Int. J. Climatol.* **39**, 2375–2385 (2019).

ACKNOWLEDGMENTS

We thank Q. Grafton for his review of the presubmission manuscript; A. Mohammadi for application of the Lyne-Hollick baseflow filter; the Victorian Department of Environment, Land, Water and Planning for providing the stream-gauge control data (fig. S4); and the two anonymous reviewers. **Funding:** The majority of funding was received from the Victorian Government Department of Environment, Land, Water and Planning under the Victorian Water and Climate Initiative with recent supplemental support from the Australian Research Council (FT120100130 and LP180100796). **Author contributions:** T.J.P. conceived and developed the HMM code and the post-HMM analysis (Figs. 3 and 4), applied and analyzed the Horton's index, assessed land-cover change, and drafted the manuscript and supplementary materials. M.S. and M.C.P. supported the analysis, provided ideas and material for figures, and reviewed the manuscript. T.J.P., M.C.P., and M.S. prepared the data, sourced the funding, and managed the project. A.J. undertook preliminary application and refinement of the HMM concepts and commented on the manuscript. **Competing interests:** None of the authors have any conflicts of interest. **Data and materials availability:** Data and code are available at https://github.com/peterson-tim-j/HydroState.

SUPPLEMENTARY MATERIALS

science.sciencemag.org/content/372/6543/745/suppl/DC1
Materials and Methods
Supplementary Text
Figs. S1 to S398
Tables S1 to S5
References (*31*–*38*)
Movies S1 and S2

26 June 2020; accepted 5 April 2021
10.1126/science.abd5085

CALL FOR PAPERS

SPJ
SCIENCE PARTNER JOURNALS

Energy Material Advances

Energy Material Advances is an online-only, Open Access journal published in affiliation with **Beijing Institute of Technology (BIT)** and distributed by the **American Association for the Advancement of Science (AAAS)**. The journal publishes, research articles, review articles, short communications, perspectives, and editorials. *Energy Material Advances* covers multiple fields from cutting-edge material to energy science, investigating theoretical, technological as well as engineering aspects.

Submit your research to *Energy Material Advances* today!

Learn more at **spj.sciencemag.org/energymatadv**

The Science Partner Journal (SPJ) program was established by the American Association for the Advancement of Science (AAAS), the nonprofit publisher of the *Science* family of journals. The SPJ program features high-quality, online-only, Open Access publications produced in collaboration with international research institutions, foundations, funders and societies. Through these collaborations, AAAS furthers its mission to communicate science broadly and for the benefit of all people by providing top-tier international research organizations with the technology, visibility, and publishing expertise that AAAS is uniquely positioned to offer as the world's largest general science membership society.

Visit us at: **spj.sciencemag.org**

@SPJournals **@SPJournals**

OPEN ACCESS

ARTICLE PROCESSING CHARGES WAIVED UNTIL JULY 2023

BioProcess Container

Bioprocess researchers undertaking high-density mammalian, bacterial, or microbial cell culture separations can now benefit from a next-generation single-use, sterilized, closed-system BioProcess Container (BPC) designed to offer a highly efficient alternative for harvesting by centrifugation. The CentriPAK BPC, developed specifically for use with the Thermo Fisher Scientific Sorvall BIOS 16 centrifuge, enables optimal protection of critical sterile liquids from cross-contamination typically associated with reusable containers. The CentriPAK can be used to process culture volumes of between 3 L and 500 L, facilitating high-throughput and high-efficiency cell biomass or clarified supernatant harvesting to maximize laboratory productivity. Furthermore, there are no time-consuming, labor-intensive, and costly preparation and post-use cleaning steps involved. To ensure it meets the high standards expected in the bioprocessing industry, the unit is subject to thorough quality-control procedures, in compliance with current good manufacturing practice and ISO 13485:2016. The CentriPAK is available in various configurations and comes with a full suite of accessories, including adapters, racks, clips, and spacers.

Thermo Fisher Scientific
For info: 435-792-8500
www.thermofisher.com

GMP-Ready Helper Plasmids for AAV Production

Manufactured in dedicated cleanrooms with mandated changeovers before new production cycles, AMS Biotechnology's new pHelper-Kan plasmid DNA is optimized for adeno-associated virus (AAV) manufacturing. AAV is a nonenveloped virus that can be engineered to efficiently deliver DNA sequences of interest into target cells with a low immunogenicity. Because of these unique characteristics, AAV-mediated genome editing has emerged as a highly promising gene-delivery method. The robust virus packaging productivity of pHelper-Kan plasmid has been tested in almost all AAV serotypes. It is proven for use in daily AAV production, for both good manufacturing practice (GMP)- and research-grade batches. Immediately available and premanufactured in stock, pHelper-Kan reduces the optimization work required to obtain high efficacy when producing your viral vectors. Its high reproducible quality is maintained and verified by our standardized manufacturing technology. We also provide a custom service to make ready-to-use AAV for any specific gene, short hairpin RNA, or microRNA.

AMS Biotechnology
For info: 617-945-5033
www.amsbio.com

Single-Microplate Evaporator

Porvair Sciences announces its new-generation Ultravap Levante nitrogen blowdown sample evaporator. Operated via an intuitive graphical color LED touchscreen, the software includes up to five stored alphanumerically named programs and multistep evaporation programs. This functionality, combined with real-time run displays showing actual gas temperature, gas flow rate, and stage height, puts you in full control of the evaporation process. The Levante is supplied with an evaporator head of your choice, which may be interchanged quickly as your workflow demands. The precision-engineered mechanism uses a standard ANSI/SLAS plate nest to accept most microplate formats and tube racks. It can accommodate tubes up to 50 mm in height in a variety of configurations to allow the use of 2-dram vials, 1.5-mL HPLC vials, barcoded tubes in racks, and many other common formats. Evaporator heads are available for efficient drydown of 24-, 48-, 96-, and 384-well microplates at temperatures up to 80°C.

Porvair Sciences
For info: 800-552-3696
www.porvair-sciences.com

Nanoparticle Measurement

Izon Science announces the worldwide launch of its latest nanoparticle measurement device, the Exoid. This new-generation instrument improves the existing and widely used Tunable Resistive Pulse Sensing (TRPS) measurement method by automating many of the previously manual user inputs and adding new central processing units and electronics. Measuring particle size, concentration, and charge with much higher resolution and precision than traditional light-based systems, TRPS enables researchers to analyze complex samples of nanobioparticles, including extracellular vesicles, viruses, liposomes, and nanomedicine products. The Exoid also comes with updated, more intuitive software that guides the researcher through the measurement process. By continually monitoring the baseline current, applied pressure, and blockade size, the system can carry out optimizations without the need for user intervention. The unit's combined hardware and software improvements also allow for 3D modeling of particle size, concentration, and zeta potential.

Izon Science
For info: 617-945-5936
www.izon.com

Ultra-Low Temperature Freezer

Eppendorf continues to follow the path of sustainability by redesigning the CryoCube F570 (all voltages). The well-known standard-sized ultra-low temperature (ULT) freezer is now completely equipped with future-proof green cooling liquids and green insulation foam. Combining longevity and quality with sustainability aspects, the CryoCube F570 is the well-accepted standard-format ULT freezer for the lab. Its 570-L capacity can be filled with up to 400 freezer storage boxes. Low-energy consumption of down to 7.4 KWh/day (−80°C) is integrated with powerful pull down to −80°C within 210 min and fast recovery back to −80°C after door opening. The F570 is the perfect solution for freezers that are used in the lab on a daily basis, keeping valuable samples safe at constant conditions.

Eppendorf
For info: 800-645-3050
www.eppendorf.com/freezers

Viral Nucleic Acid Extraction Kit

BioChain has successfully provided enough reagents to test over 3 million people across the United States for COVID-19 infection. This is due to the recent launch of their vamPure Viral Nucleic Acid Extraction kit, which allows for fast and efficient total nucleic acid extraction from human swab samples. The final extract is ideal for subsequent detection of various viral species, including the novel coronavirus responsible for COVID-19 disease. BioChain's new kit has been hailed as a high-quality, cost-effective, sensitive, and reliable tool by clinical labs that need to process tens of thousands of test samples per day. vamPure is easy to use and ideal for application on automation platforms, which greatly facilitates acquisition of test results. The kit can be purchased in small quantities or bulk packaging depending on the customer's needs.

BioChain Institute
For info: 888-762-2568
www.biochain.com/product/vampure-viral-nucleic-acid-extraction-kit

Electronically submit your new product description or product literature information! Go to www.sciencemag.org/about/new-products-section for more information.

Newly offered instrumentation, apparatus, and laboratory materials of interest to researchers in all disciplines in academic, industrial, and governmental organizations are featured in this space. Emphasis is given to purpose, chief characteristics, and availability of products and materials. Endorsement by *Science* or AAAS of any products or materials mentioned is not implied. Additional information may be obtained from the manufacturer or supplier.

Who's the top employer for 2020?

Science Careers' annual survey reveals the top companies in biotech & pharma voted on by *Science* readers.

Read the article and employer profiles at sciencecareers.org/topemployers

Science 2020
TOP EMPLOYER

Director, Immune and Molecular Profiling (IMP) Facility
Researcher/Scientist IV
Immunobiology (T)
College of Medicine, University of Arizona Health Sciences

The UA Immune and Molecular Profiling (IMP) facility, serving the University of Arizona Health Sciences as well as the broader UArizona community, is seeking an outstanding scientist in the general area of immune and molecular profiling to serve as its director. The IMP is a part of the University's "Personalized Defense" Strategic Initiative. The position will be in charge of the overall operations of the IMP, including day-to-day operations as well as its function to promote the UAHS and UArizona strategic plan. This position will be hired via the Department of Immunobiology at University of Arizona College of Medicine-Tucson (UACoM-T). The UACoM and the Department of Immunobiology recognize the power of a diverse community and strongly encourage individuals with varied experiences, perspectives, and backgrounds to apply.

The successful candidate will join the UA Department of Immunobiology at the rank of Researcher/Scientist IV and could be considered for Research-track appointment following demonstration of successful performance and scholarly promise.

The successful candidate should have strong immunology and multi-omics training and understanding and a demonstrated expertise in high-throughput, high-resolution flow cytometry. RNASeq expertise, particularly at the single-cell level, will be a plus.

Applicants must have a PhD in biological sciences, preferably in immunology. Successful candidates will be able to manage the IMP as its chief scientist and supervise staff of one or more technicians; to consult with other scientists regarding their projects and to help plan, design and execute scientific projects within the scope of IMP services (chiefly multicolor spectral flow cytometry and single cell and bulk transcriptome). Co-writing of manuscripts and grants and participating in scientific projects as a collaborator would be a plus. Salary and start-up funds are attractive and commensurate with qualifications and experience.

The University of Arizona has been recognized on *Forbes* 2015 list of America's Best Employers in the United States and has been awarded the 2016 Work-Life Seal of Distinction by World@Work! For more information about working at the University of Arizona, see **https://talent,arizona.edu**.

For full details and qualifications, and to complete an on-line application, see **req4379** at **talent.arizona.edu**. Outstanding UA Benefits!

The University of Arizona is an Equal Opportunity Employer Minorities/Women/Vets/Disabled.

University of Minnesota-Twin Cities
Tenure Track Positions in Structural Biology and Biophysics

The University of Minnesota (UMN) invites applications for **two tenure-track faculty positions** in the Department of Biochemistry, Molecular Biology and Biophysics within the University of Minnesota Medical School. We seek applications in all areas of structural biology and biophysics including CryoEM, NMR, X-ray crystallography and spectroscopy. Of particular interest are applications of structural biology relating to immunology and cancer biology.

Responsibilities: We seek dynamic individuals who will lead federally-funded research programs, contribute to medical, graduate and/or undergraduate education programs through instruction and research mentorship, and contribute to academic service on the campus and/or professionally.

Required Qualifications: An earned doctorate, MD or equivalent.

Preferred Qualifications: A record of research in an area of biomedically-relevant biochemistry that complements departmental strengths. Applications at the Assistant Professor level are encouraged, but candidates at a higher level will be considered if there is evidence of continuous extramural research funding, high impact publications and excellence in teaching and service expected of tenured faculty at a research-intensive university. A record of successful post-doctoral research; ability to communicate effectively in a research and educational setting; and evidence of past research collaborations or a willingness to work in related research areas is anticipated.

Application: Please send a full CV, a 2-page research overview, a 1-page teaching statement, and a diversity statement to **sbsearch@umn.edu**. Three letters of recommendation that consider both research and teaching potential should be sent directly from the referee to the Faculty Search Committee at **sbsearch@umn.edu**.

University of Minnesota is an Equal Opportunity/Affirmative Action employer and is dedicated to creating and fostering a diverse academic environment. We encourage applications from individuals belonging to groups underrepresented in their respective fields, and others who would enrich and add unique perspectives to the University.

Smithsonian National Museum of Natural History

DEPUTY DIRECTOR

The Smithsonian's National Museum of Natural History (NMNH) is seeking an experienced executive to work with the Director and Executive Team to lead and manage a wide portfolio of programs and activities spanning the Museum's scientific, public and operational programs. The successful candidate will bring extensive experience in leadership and management of museums or similar organizations, strategic planning, financial, operational and personnel management, and policy formulation to the NMNH, which has over 450 employees plus large student and volunteer bodies. Working in collaboration with the Sant Director, this high-profile leader will formulate and implement strategic directions for the science, public and operational programs of the Museum; lead the management of the research departments, collections programs, exhibits, education, outreach and visitor experience, finances, operations, facilities, specialized laboratories, field stations, and other similar programs and partnerships; assure the quality and breadth of all Museum activities; and provide institutional leadership in broader national and international programs.

The National Museum of Natural History is a public-facing, science-based museum within the Smithsonian Institution's complex of museums and research organizations. The NMNH is dedicated to understanding and explaining the natural world and is one of the most visited natural history museums in the world, reaching more than 4 million museum visitors each year and millions more through its education programs and digital channels. With over 146 million specimens and objects, the Museum's collections represent over 90% of the holdings of the Smithsonian and are the largest of its kind in the world. These collections, and the work of the scientific staff, form the foundation for the Museum's extensive public programs, and include exhibitions, education, and citizen science.

This is a full-time, permanent position to be filled as Trust (private sector, U.S. citizenship not required, proof of eligibility to work in the U.S. required). Salary commensurate with experience. The Smithsonian Institution offers a comprehensive package of benefits. For complete requirements and application procedures, please visit: **www.si.edu/ohr** and refer to Announcement # **EX-21-09**. Applications must be received online by **5/31/2021**. Applicants will be notified by email when their applications are received.

We encourage all qualified candidates to apply.

The Smithsonian Institution is an Equal Opportunity Employer.

By **Johana Goyes Vallejos**

What's in a name?

"I think it is ready to submit," one of my Ph.D. committee members said. I was incredulous; the manuscript overflowed with red ink. But she was my biggest fan and my harshest critic; if she said it was ready, then it must be true. Now I needed to ask the question that had been nagging me since I began to work on the manuscript: "How should I publish my name?" "However you want," she replied. "It is time for people to understand that Latin American scientists have two last names."

Since I moved to the United States to pursue my Ph.D., my colleagues have had trouble pronouncing my first name, let alone my two very Hispanic-sounding surnames—my father's first and then my mother's, as is standard in most Spanish-speaking countries. And English-language publishing systems are often not designed for two last names. Using just one surname or connecting them with a hyphen, as many Hispanic scientists publishing their work in English do, would certainly make matters "easier." But easier for whom? Growing up, I never met anyone whose last name was hyphenated. I have always been proud to use my two surnames, honoring both of my parents and my cultural heritage.

"I worried that I would face a career-long battle to publish my name as I want it."

Still, I worried that I would face a career-long battle to publish my name as I want it. Should I just get over it and use a hyphen? Yet the support from my mentor, who was born in the United States and whose name fits the "standard" first-name last-name format, gave me courage. I decided I would publish my paper using my two surnames—no hyphen.

When the "last name" box showed up during the submission process, I typed my two surnames, with a space, holding my breath while waiting to see whether the electronic system would allow it. Submit. No warning popped up. Victory. I had to reassure the editor that, yes, those are indeed my two surnames, but several months later the paper was published with my name in its authentic form.

Since then, the path hasn't always been as smooth. In one instance, a colleague offering feedback on a manuscript went through all the citations of my previous work—in which I had (correctly) listed myself as "Goyes Vallejos, J."—and added a hyphen. When I mentioned that I do not use the hyphen, he replied, "Yeah, that is not going to fly. You will be mis-cited for the rest of your days. Mark my words, you will have to call me and apologize for not following my advice." An editor-in-chief made a similar comment, stating, "You decide how your name should be spelled, but the options are your two surnames with a hyphen or just one of them." I refused and ultimately published without the hyphen. Still, in the journal's table of contents, my name appears incorrectly as "Vallejos, J.G." And because other researchers sometimes cite my name incorrectly, my metrics—for example on Web of Science, Scopus, and Google Scholar—vary greatly, which could affect future job prospects and promotions.

"Two last names are too much for 'them' to handle, and they will butcher them anyway," my Latin American friends say when explaining why they hyphenate or use a single last name for their publications. I support their decisions to publish as they choose. But those of us who decide to maintain our heritage in the form of our names also deserve support. This is not an isolated issue for Latino and Hispanic scientists; it also affects members of other groups whose names do not conform to a "first-name last-name" norm. And insisting on being able to present our names as we choose is not "picky" or "capricious." It is a matter of respect for our identities as scientists and as citizens of the world.

Simple steps from the community can make a big difference. When in doubt, ask scientists how they would like to be addressed. When you cite their work, check their previous publications, their ORCID account, and their web pages. Next time you add a paper to your reference manager, double check the author line to ensure the system has imported it correctly. Above all, make sure researchers from all backgrounds have the opportunity to claim their identities and feel validated in their workplaces. ■

Johana Goyes Vallejos is a postdoctoral fellow at the University of Missouri in Columbia. Send your career story to SciCareerEditor@aaas.org.

ILLUSTRATION: ROBERT NEUBECKER